Split-filter dual-energy CT: investigation of tumor visibility, spectral separation, and dose allocation

By

Lianna D. DiMaso-Myers

A dissertation submitted in partial fulfillment of
the requirements for the degree of

Doctor of Philosophy
(Medical Physics)

at the
University of Wisconsin – Madison
2020

Date of final oral examination: June 18, 2020

This dissertation is approved by the following members of the Final Oral Committee:
Larry A. DeWerd, Professor, Medical Physics
Jessica R. Miller, Associate Professor, Department of Human Oncology
Bryan P. Bednarz, Associate Professor, Medical Physics
John E. Bayouth, Professor, Department of Human Oncology
Timothy P. Szczykutowicz, Associate Professor, Radiology
Jessie Huang-Vredevoogd, Assistant Professor, Department of Human Oncology (non-voter)

"The roots of education are bitter, but the fruit is sweet."

Aristotle

Abstract

Department of Medical Physics

Split-filter dual-energy CT: investigation of tumor visibility, spectral separation, and dose allocation

Lianna D. DiMaso-Myers

Split-filter dual-energy computed tomography (DECT) has recently been implemented for clinical use as an added feature to the Siemens SOMATOM Definition Edge CT scanner. This split-filter technique is referred to as TwinBeam (Siemens Healthcare, Forchheim, Germany). TwinBeam is a novel modality performed with an x-ray source operated at 120 kVp and a removable split-filter made of adjacent 0.05 mm of gold and 0.6 mm of tin. This dissertation explores the use of TwinBeam for imaging pancreas and liver tumors for radiation therapy applications. This dissertation also compares the new split-filter system to other DECT modalities based on spectral separation and dose allocation.

Accurate tumor delineation is crucial for stereotactic body radiation therapy. Unfortunately, tumor delineation using conventional single-energy CT (SECT) images can be a challenge for pancreatic adenocarcinomas and liver tumors where contrast between the tumor and surrounding healthy tissue is low. The first part of this work investigates the utility of TwinBeam to improve pancreas and liver tumor visibility as quantified by contrast and contrast-to-noise-ratio (CNR) for radiation therapy applications. The visibility of pancreatic adenocarcinomas was found to substantially increase with TwinBeam virtual monoenergetic images (VMIs), while the increase in visibility of liver tumors was not universal but was observed for certain patients. The investigation of other dual-energy images, including relative electron density and effective atomic number images, were also explored for tumor delineation. The difference between tumor and healthy tissue based on these images varied by tumor location but still provided additional information to complement VMIs and aid in tumor delineation.

The accuracy of TwinBeam iodine-enhanced images was investigated and used to quantify the iodine concentration within pancreas and liver tumors and surrounding healthy tissue during bi-phasic imaging for radiation therapy simulation. The accuracy was found to be dependent on patient size; therefore, a methodology to determine the iodine concentration within 3D contours from patient datasets was established. First order

texture analysis was also performed using TwinBeam VMIs and analyzed as a function of reconstruction energy. Mean CT number and standard deviation increased with decreasing energy for virtual monoenergetic images (VMIs), while skewness and kurtosis were seen to be stable and did not change as a function of reconstructed energy.

A subjective contouring study with split-filter DECT images was performed to investigate the current implementation of TwinBeam for delineating pancreas and liver tumors for radiation therapy applications. Three contouring sessions were conducted several days apart. Four clinicians were asked to contour the pancreas or liver gross target volume (GTV) on one of three different TwinBeam DECT images (VMI, iodine-enhanced, or virtual SECT image). Tumor conspicuity, tumor edge sharpness, contouring confidence, and image quality were also scored on a five-point scale. The GTVs were compared using Jaccard coefficient (JC), Dice similarity coefficient (DSC), Hausdorff distance (HD), and overall volume. Tumor edge sharpness score negatively correlated with HD for both the pancreas and liver cases. The intra-clinician and inter-clinician variability were analyzed across the different image types. For some pancreas and liver cases, the TwinBeam VMIs decreased the variability of the GTVs compared to the virtual SECT image.

Monte Carlo models of split-filter DECT with peak tube voltages of 120 kVp and 140 kVp were developed based on measurement of half value layer and beam profile from the Siemens SOMATOM Definition Edge scanner. These two models were used to characterize split-filter DECT based on spectral separation and dose allocation and to investigate the potential benefits of increased tube voltage. Overall, the spectral separation increased with peak tube voltage, and dose allocation was unchanged with increased tube voltage for larger phantom sizes. The impact of the spectral differences caused by the split-filter on CT dosimetry was also investigated; the energy dependence across the beam was found to vary with ionization chambers used for CT dosimetry.

Acknowledgements

I am unbelievably grateful for the many people who have made the past five difficult years the most rewarding and overall amazing years of my life. All of them deserve so much more than an acknowledgement.

I could not have asked for a better graduate experience than what I had during my time at the University of Wisconsin-Madison. It has been a privilege to be a part of the Calibration Laboratory (Cal Lab). I must thank my advisor and University of Wisconsin Medical Radiation Research Center (UWMRRC) director, Professor Larry DeWerd for seeing my potential and accepting me into the lab. Dr. DeWerd provides his students with what seems like an unlimited amount of opportunities and resources to ensure the success of our medical physics research projects. With Dr. DeWerd's support, guidance, and wisdom, I have become a more confident and independent researcher, and for that I will never be able to repay him.

This project would not have come to fruition without my co-advisor and dual-energy expert, Professor Jessica Miller. She spent countless hours answering my questions and reviewing manuscripts, and she was always available to lend an open ear. She inspires me with her professionalism, kindness, and intelligence. I am grateful for her amazing mentorship both in life and medical physics.

Next, I would like to acknowledge my other co-advisor, Professor Jessie Huang-Vredevoogd, who was integral to the success of this project. I am indebted to her for presenting for me at AAPM while I was on maternity leave and for spending so much time offering edits and suggestions to every manuscript, abstract, and thesis chapter. I have been so lucky to have to have such an articulate and intelligent advisor whose knowledge and direction has made me a better scientific writer.

I would like to thank my committee members, Dr. Larry DeWerd, Dr. Jessica Miller, Dr. Bryan Bednarz, Dr. John Bayouth, and Dr. Timothy Szczykutowicz for all of their guidance, critique, and enthusiasm towards this project. Their involvement has been crucial in defining the direction of this thesis.

I would also like to thank the University of Wisconsin Accredited Dosimetry Calibration Lab (UWADCL) director, Dr. Wesley Culberson who has guided me through my time as a graduate student. Thank you to the past Cal Lab students for paving the way, especially Dr. Sameer Taneja and Dr. Michael Lawless for their invaluable mentorship. Thanks to the current students, specifically Blake Smith, Autumn Walter, Leah Turner,

Wil Ferris, and Emily King for their unforgettable friendship and edits to this thesis. The staff of the UWMRRC has been an invaluable resource unique to the Cal Lab. Thank you, Jennifer Hull for dedicating your time to answer my questions, help me with the 3D printer, and calibrate the ionization chambers. Thank you, Cliff Hammer for all of the laughs and TLD help during my early graduate career. Thank you, Benjamin Palmer for being someone to talk parent stuff with and for the delish food once my daughter, Evadora, was born. I looked forward coming into work and going to weekly lab meetings because of all of you.

Thank you to the physicians (Dr. Michael Bassetti, Dr. Adam Burr, Dr. Grace Blitzer, Dr. Megan Lubner, and Dr. Sangjune Laurence Lee) who spent many hours contouring. Thank you to the physicists and dosimetrist from the Department of Human Oncology. It has been such a joy working beside all of them and I cannot wait to continue to during residency.

Thank you to Kailtin Woo and Lu Mao from biostatstics who helped with the statistical analysis of this thesis. Thank you to Drs. Nilesh Mistry and Jainil Shah from Siemens Healthineers for their contributions.

To my father and grandparents for enduring unimaginable hardships and for leaving their country to come to this one for the sole reason of trying to make a better life for their family, and for never letting me forget the value and privilege of an education. None of this would be possible without my mom and dad, Marisa and Lorenzo DiMaso whose never ending unconditional love and support carried me through every stage of my life so far, and even when I doubted myself, I never doubted their faith in me. I recognize and appreciate all of the sacrifices made to ensure I had all of the opportunities to truly be whoever I wanted to be in life. My sister, Sabrina, whom I strive to be every day. They see me at my absolute worst, and I will never be able to thank them enough for loving me anyway.

Last but not least, I must thank my wonderful husband, Charlie for always believing in me and being my main motivation. He would listen (and stay awake) while I practiced my research talks and made sure I spoke with poise and confidence. He has endured all of my complaints and late nights and has been there to celebrate every victory. I am eternally grateful for his love and support. I appreciate his hard work to provide for me and Evadora while I strived towards my dreams. For all of that and more, thank you, "you are the best thing that ever happened to me".

Contents

List of Figures

List of Tables

Abbreviations

ADMIRE	advanced modeled based iterative reconstruction
Al	Aluminum
Au	Gold
ANOVA	analysis of variances
CF	conversion factor
CNR	contrast-to-noise ratio
CPE	charged particle equilibrium
CT	computed tomography
CTDI	computed tomography dose index
CTTA	computer tomography texture analysis
DECT	dual-energy computed tomography
DS	dual spiral
DSC	Dice similarity coefficient
ED	effective diameter
FWHM	full width half max
FBP	filtered back projection
GTV	gross target volume
HCC	hepatocellula carcinoma
HD	Hausdorff distance
HU	Hounsfield unit
HVL	half-value layer
IRB	Institutional Review Board
JC	Jaccard coefficient

keV	kiloelectron volt
kVp	kilovoltage peak
LOD	limit of detection
LOQ	limit of quantification
MC	Monte Carlo
MCNP	Monte Carlo n-particle transport
MCTN	mean computed tomography number
mg I/ml	milligram of iodine per milliliter
mm Al	millimeter of aluminum
nMERA	novel monoenergetic algorithm
OAR	organ at risk
RMSE	root mean squared error
ROI	region of interest
SBRT	stereotactic body radiotherapy
SD	standard deviation
SECT	single-energy computed tomography
SF	split filter
Sn	Tin
TASMICS	tungsten anode spectral model using interpolating cubic splines
TASMIP	tungsten anode spectral model using interpolating polynomials
TB	TwinBeam
UWADCL	University of Wisconsin Accredited Dosimetry Calibration Lab
UWMRRC	University of Wisconsin Medical Radiation Research Center
VMI	virtual monoenergetic image
VNC	virtual non-contrast
mGy	milli-Gray
cm	centimeter
mm	millimeter
Gy/C	Gray per coulomb

To my daughter, Evadora, you are my sunshine.

Chapter 1

Introduction and outline

1.1 Overview

Computed tomography (CT) is the most common imaging modality which uses a narrow beam of x-rays to create a detailed image of internal organs, bones, soft tissue, and blood vessels of a patient. The first single-energy CT (SECT) scanner was introduced in the early 1970's by Godfrey Hounsfield and Allan Cormack, whom later received a Nobel Prize for their discovery [5]. Though CT imaging technology has made great advances, materials with different elemental compositions can still be difficult to differentiate, as they are often represented by the same or very similar, CT numbers. For example, calcified plaques, bone, and iodine-containing tissue may appear identical on a SECT image. The measured CT number for a given image voxel is determined based on the linear attenuation coefficient, $\mu(E)$ which is not specific to the given material but rather a function of the material's composition, material's density, and the energy of the x-rays

interacting with the material [6].

Unlike SECT, dual-energy CT (DECT) acquires images with two x-ray spectra; therefore, two linear attenuation coefficients of the same anatomical location are obtained. The intrinsic energy dependence of a material's attenuation coefficients allows DECT to utilize material decomposition to generate material-specific images, virtual monoenergetic images (VMIs), and effective atomic number and electron density maps. Therefore, materials that were hard to differentiate in SECT can now be easily identified. The use of DECT images has been shown to aid in tumor segmentation and tissue characterization in the abdomen [7–11], to assess tumor response after radiotherapy [12, 13], and to aid in functional tissue segmentation [7, 14–19].

Despite the availability of several commercial DECT techniques and the many applications of their resulting images, DECT has not gained widespread use within the radiation oncology community. Prior to radiation therapy treatment planning, CT images are acquired and used to identify the tumor location and differentiate tumor from healthy tissue. SECT is an integral component to the radiation therapy workflow, as density information derived from CT images is needed for many dose calculation algorithms. However, SECT is not an optimal imaging modality for soft tissue contrast. Poor soft-tissue contrast can lead to inaccuracies in tumor and organ-at-risk (OAR) segmentation resulting in greater uncertainties in the radiation therapy process [20–22].

Abdominal cancers, specifically in the liver and pancreas, suffer from poor soft-tissue contrast. Radiation therapy is a localized treatment option for the majority of pancreatic and liver cancer patients; therefore, confident and accurate tumor delineation is vital to

successful treatment [23, 24]. Fortunately, DECT has shown to aid in the delineation and visualization of abdominal tumors. An increase in conspicuity of iodine in low-energy VMIs and iodine-material decomposition images can aid in the detection and characterization of abdominal tumors [25–27]. The increase in visualization of these tumors, in conjunction with advanced treatment techniques, may lead to the applicability of dose-escalated radiation therapy, which has shown to provide long-term patient survival [23, 24, 28–33].

While many DECT modalities require extensive hardware upgrades, such as a second x-ray source or unique detectors, split-filter DECT is a more cost-effective technique which has the potential to increase the accessibility of DECT in radiation therapy. Split-filter DECT is a single-source DECT modality which is currently only manufactured with a 120 kVp initial x-ray spectrum and a split filter made of gold and tin and is referred to as TwinBeam (Siemens Healthineers, Forchheim, Germany). Although split-filter DECT is known to have inferior spectral separation compared to other DECT modalities [34, 35], the nearly simultaneous acquisition of the low- and high-energy data gives TwinBeam the capability to image dynamic contrast, making this modality a candidate for imaging pancreatic and liver cancer. Dynamic contrast imaging uses an iodine contrast agent to enhance the tumor with respect to the surrounding soft tissue, and multiple phases are typically imaged for pancreas and liver tumors.

As mentioned, radiation therapy is a localized treatment option for the majority of pancreatic and liver cancer patients. However, confident and accurate tumor delineation is a challenge with conventional SECT [36–40]. Therefore, this work characterizes the

individual spectra of the TwinBeam system and investigates the ability of TwinBeam DECT images to improve visualization of pancreas and liver tumors for radiation therapy applications.

Since, TwinBeam is a novel DECT modality the split beam has not been well characterized in the literature. Characterization of the spectra and x-ray fluence is necessary to optimize the beam configuration, filter construction, and determine optimal scanning parameters. Furthermore, understanding the effects of the split beam on ionization chamber response is required for accurate dosimetry. Therefore, an equivalent source model of the TwinBeam system was created to characterize split-filter DECT by quantifying the spectral separation, effective energies, and dose allocation. The dosimetric impact of these parameters on CT ionization chamber response was determined and an additional source model was created at a peak tube voltage of 140 kVp to investigate the potential benefits of increased tube voltage.

1.2 Aims of this work

The current implementation of split-filter DECT with TwinBeam is hypothesized to increase the visualization of certain anatomical sites, such as pancreas and liver tumors. Several quantitative imaging studies and subjective contouring studies with TwinBeam DECT images were performed to investigate the current implementation of TwinBeam for delineating pancreas and liver tumors for radiation therapy applications.

TwinBeam is a novel split-filter DECT modality; therefore, the spectral separation, effective energy, and dose allocation of the low- and high-energy beams are not well

characterized. Two Monte Carlo (MC) models of split-filter DECT were created to characterize the modality with different peak tube voltages. The models were benchmarked against dosimetric measurements, and results were compared to other DECT techniques.

The goal of this thesis work was to explore split-filter DECT as a function of peak tube voltage and characterize it based on spectral separation, effective energy, and dose allocation as well as determine if TwinBeam split-filter DECT can increase the visibility and delineation accuracy of pancreas and liver tumors over conventional SECT for radiation therapy applications. To achieve this goal, three aims were developed and pursued: (1) characterize the low- and high-energy beams from split-filter DECT by quantifying the spectral separation, effective energy, and dose allocation using validated MC models (2) quantify and compare image metrics from TwinBeam DECT and virtual SECT images to assess visibility of pancreas and liver tumors, and (3) analyze the clinician agreement of pancreas and liver GTVs to determine the reproducibility and accuracy of tumor delineation from TwinBeam DECT and virtual SECT images. It is believed that the information gained from this work will increase the understanding of how DECT can be utilized in radiation therapy for pancreas and liver tumors, as well as enhance split-filter DECT acquisition.

1.3 Description of upcoming chapters

The following chapters are organized in such a way to best present the clinical implementation of split-filter DECT.

Chapter 2 provides a brief background on the characterization of DECT, the different single-source and dual-source techniques, the types of DECT images, and their applications in medicine. This chapter also introduces pancreas and liver tumors and the research that has already been done to improve their conspicuity.

Chapter 3 characterizes split-filter DECT by creating an equivalent MC model to investigate the spectral separation, effective energy, and dose allocation of the modality and to determine the impact peak tube voltage has on the overall system. The impact of these parameters on ion chamber response was calculated.

Chapters 4-7 outline the methods, results, and conclusions of several imaging studies investigating the visibility of pancreas and liver tumors using TwinBeam DECT images.

Chapter 4 investigates the visibility of pancreas tumors using TwinBeam DECT images through the quantification of GTV contrast and contrast-to-noise ratio (CNR). The entirety of this chapter has been peer reviewed and published in the Journal of Applied Clinical Medical Physics.

Chapter 5 investigates the ability of TwinBeam DECT images to visualize liver tumors through GTV contrast and CNR. This chapter explains the different enhancement properties of liver tumors and the impact of these properties on quantitative image metrics. The entirety of this chapter has also been peer reviewed and published in the Journal of Applied Clinical Medical Physics.

Chapter 6 describes the methodology used to quantify iodine concentration from TwinBeam iodine-enhanced images, which was used to further quantify the iodine uptake of

pancreas and liver tumors and healthy tissue to assist with tumor delineation. This chapter also performs CT texture analysis on TwinBeam DECT images to quantify differences between tumor and healthy tissue and determine trends as a function of VMI energy.

Chapter 7 provides an investigation of TwinBeam effective atomic number and relative electron density images to visualize pancreas and liver tumors. The effective atomic number and relative electron density images are reconstructed from the same raw patient data used in Chapters 3-7.

Chapter 8 provides the outline and results of two contouring studies investigating the inter- and intra-clinician agreement of pancreas and liver tumor contours using TwinBeam DECT images. A qualitative assessment on the image quality and confidence in tumor delineation is also performed.

Chapter 9 summarizes the results of this work and states the final conclusions of this investigation. Potential future directions of split-filter DECT within the field of radiation oncology are discussed.

Chapter 2

Background

2.1 Dual-energy computed tomography

DECT originated during the 1970s and utilizes low- and high-energy photon spectra to image the same anatomical location [41]. Though the idea of DECT has been around since the 1970s, it has not been until recently that advances in scanner technology have allowed for the clinical use of DECT [26]. DECT has significant advantages over conventional SECT, specifically when imaging the abdomen because DECT allows for the differentiation of tissues with similar density but different elemental compositions [34]. Some DECT applications in the abdomen include depicting small liver lesions, differentiating renal cysts from tumors, and improving the depiction of pancreas tumors [22]. DECT imaging can be achieved with either a dual-source or single-source scanner. Dual-source DECT utilizes two x-ray sources and two separate detector arrays placed roughly

90° apart on the same bore. Siemens SOMATOM Definition (Siemens, Forchheim, Germany) is a dual-source scanner where the low-energy data is obtained at 80 kVp or 100 kVp and the high-energy data is obtained at 120 kVp or 140 kVp with the option of added filtration to improve spectral separation. An advantage of dual-source imaging is the ability to adjust kVp, imaging dose, and filtration independently on the two sources. Additionally, the short time separation between the acquisition of the low- and high-energy data is beneficial for dynamic contrast imaging. Since the acquisition of low- and high-energy data for the same anatomical location are only separated by a quarter rotation, this DECT technique has high temporal coherence. One disadvantage to dual-source DECT is the limited field of view of 35 cm restricting the ability to evaluate and calculate dose on the entire anatomy for large patients.

There are several single-source DECT modalities on the market today. Single-source fast kVp-switching DECT utilizes a single x-ray source that rapidly switches between a low- and high-energy spectra. GE's fast kVp-switching technique (GE Healthcare, Milwaukee, Wisconsin) uses a single detector layer to acquire both the low- and high-energy data. The x-ray source rapidly switches between 80 kVp and 140 kVp within 0.5 msec time intervals. The exposure time ratio of the low- and high-energy is 65% and 35% respectively to account for the higher tube output of the 140 kVp [26]. Like dual-source DECT, fast kVp-switching allows for high temporal coherence, as the low- and high-energy data are only separate by 0.5 ms. One disadvantage to fast kVp-switching DECT is that the low- and high-energy tube potentials are fixed and the addition of filtration to further increase the spectral separation is not available.

Single-source sequential scan DECT is performed with a low-energy scan followed by a high-energy scan. Siemens' specific sequential scan technique is called Dual Spiral and is achievable on several Siemens' CT models, including the SOMATOM Definition Edge CT scanner (Siemens, Forchheim, Germany). This modality is most similar to dual-source DECT as the peak tube voltages, current, and filtration can be individually changed. Unfortunately, due to the low temporal coherence between the low- and high-energy scans, large motion artifacts are associated with the resulting DECT images.

Another single-source DECT modality is achieved with a dual layer detector. Philips Brilliance CT (Philips Healthcare, Andover, Massachusetts) uses a 120 kVp x-ray spectrum and has a modified detector array with two layers of scintillators. The top layer captures the low-energy data while the bottom layer captures the high-energy data. This technique is beneficial for simultaneous acquisition of the low- and high-energy spectra. However, Dual-layer DECT has low spectral separation compared to dual source because the sensitivity profiles of the scintillator materials between the two layers are considerably overlapped [42]. Schematics of these four dual-energy techniques are illustrated in Figure 2.1.

2.1.1 Split-filter DECT

Split-filter DECT is another single source DECT modality that creates the low- and high-energy photon spectra using a filter made of two adjacent material compositions of different thicknesses. This concept was first introduced in 1981 by Brian Rutt and Aaron Fenster [43]. A diagram of the split-filter DECT technique is depicted by the two colors

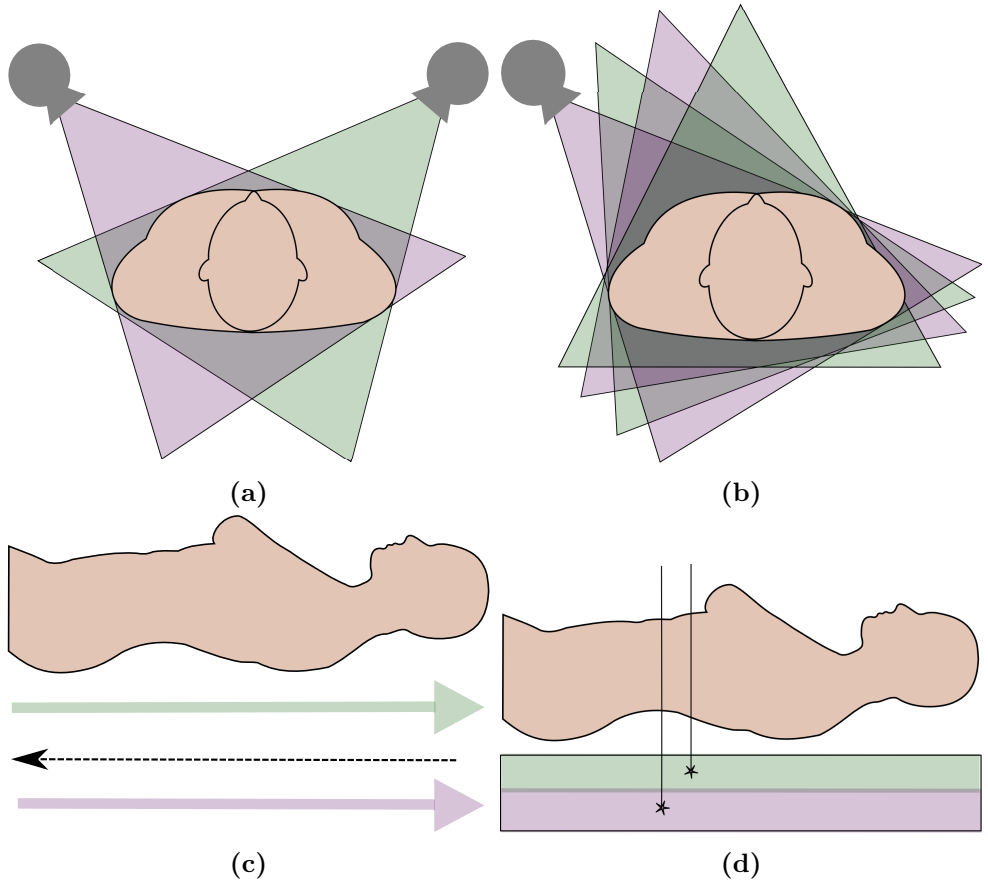

Figure 2.1: Schematic of dual-source (a), fast kVp-switching (b), sequential scan (c), and dual-layer (d) DECT. The purple and green regions represent the acquisition of the low- and high-energy spectra, respectively.

in Figure 2.2. The split-filter DECT concept was recently implemented for clinical use as a cost-efficient additive feature to the Siemens SOMATOM Definition Edge CT scanner and is referred to as TwinBeam, with a removable split filter made of adjacent 0.05 mm gold and 0.6 mm tin. This DECT scanner will be the main focus of this work.

Within the past four years, several researchers have compared the imaging capabilities of TwinBeam to other DECT modalities and to conventional SECT. The spatial resolution of TwinBeam images was similar to dual-source DECT but TwinBeam images demonstrated poorer CT number separation and inferior contrast and contrast-to-noise

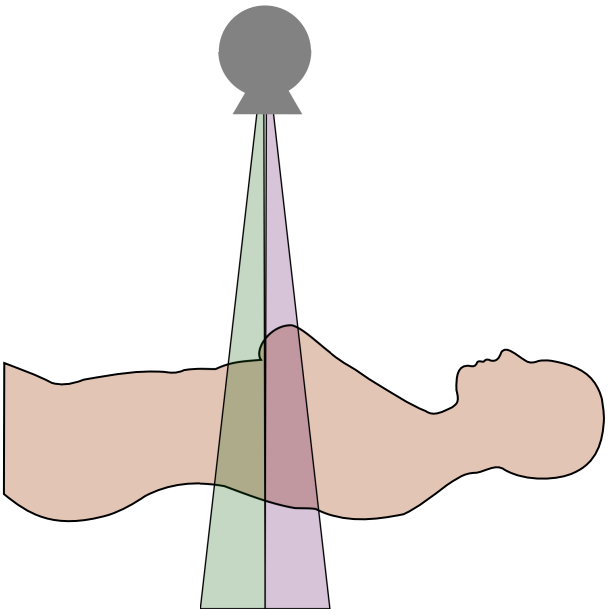

Figure 2.2: Schematic of split-filter DECT.

ratio (CNR) of iodine inserts [34]. TwinBeam images demonstrated similar image noise [35] and higher liver parenchyma to fat CNR compared to conventional SECT images [44]. The optimal energy of TwinBeam VMI has also been determined to better visualize OARs based on CNR in head-and-neck radiation therapy [45].

2.1.2 Types of DECT images

The acquisition of two CT datasets at two different energies allows for the reconstruction of multiple DECT images. Some but not all possible images that can be reconstructed from DECT include: VMIs, iodine-enhanced images, effective atomic number, electron density, virtual non-contrast images, and SECT equivalent images. Since this work is limited to the TwinBeam system, which is unique to the Siemens SOMATOM Definition Edge CT scanner, the following data sets will be discussed in light of Siemens' image-based reconstruction techniques.

Arguably the most popular DECT images are VMIs. The weighted sum of the low- and high-energy CT datasets generated from DECT can be used to create VMIs at energies ranging from 40 keV to 190 keV. VMIs are virtual CT images that are reconstructed as if they were created from a series of monoenergetic x-ray sources. VMIs reconstructed at low energies offer greater enhancement capabilities compared to SECT because SECT can only create one CT image based on a single x-ray photon spectrum [46]. Most enhancements of DECT VMIs are due to the injected iodine contrast. Iodine (Z=53, k-edge = 33.7 keV) is predominately attenuated by the photoelectric effect and is used as a radio-contrast agent to enhance certain soft tissues. The total attenuation of iodine increases at lower energies and provides contrast between tissues with varying iodine uptake. The difference in attenuation of iodine and soft tissue is shown in Figure 2.3.

In the Siemens implementation of DECT, the VMIs are calculated as a linear combination of the low- and high-energy CT images with the weighting factor being a function of energy [46]. The calibration of the weighting factor is performed using scans of a 15 mgI/mL cylindrical vial scanned in air, in a 20 cm phantom, and in a 30 cm phantom. In addition to the linear combination of the low- and high-energy datasets, Siemens performs an image-based recombination to decrease the image noise at low-energy reconstructions by using the image noise at the average effective energy of the low- and high-energy beams (approximately 70 keV) [1, 46, 47]. This method is referred to the novel monoenergetic reconstruction algorithm (nMERA or Mono+). An illustration of this method is shown in Figure 2.4 and an investigation of these images compared to the standard monoenergetic reconstruction algorithm has been completed by Grant et al. [1].

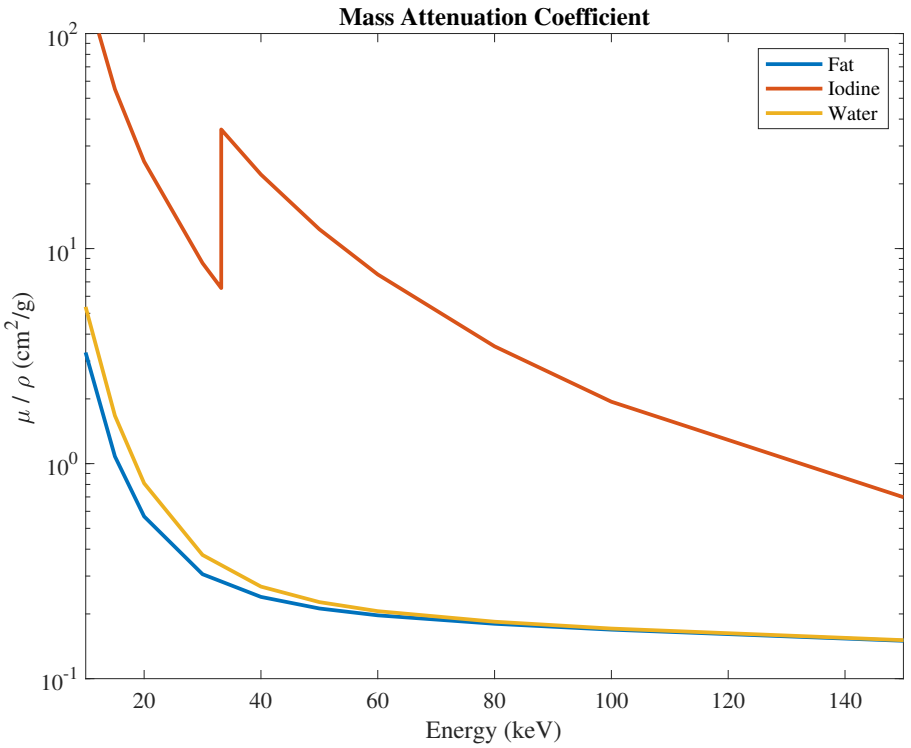

Figure 2.3: Attenuation coefficient of fat, iodine, and muscle as a function of energy. As energy decreases the difference in attenuation between iodine and human tissue increases.

Iodine-enhanced images are derived using the concept of material decomposition. Material decomposition relies on the assumption that everything in the body is made up of some combination of basis pair materials, such as iodine and soft tissue. In iodine-material decomposition, a voxel of unknown material can be decomposed into known amounts of iodine and soft tissue as shown in Figure 2.5. A weighted sum of the two basis pairs, a_1 and a_2 are used to determine the attenuation coefficient of an unknown sample.

The blue line in Figure 2.5 is called the identity line. In a plot of the low- and high-energy attenuation coefficients, the identity line intersects the attenuation coefficients of fat and soft tissue. The red line follows the attenuation coefficients of iodine at different concentrations. The slope of the red line is referred to as the dual-energy (DE) ratio, and

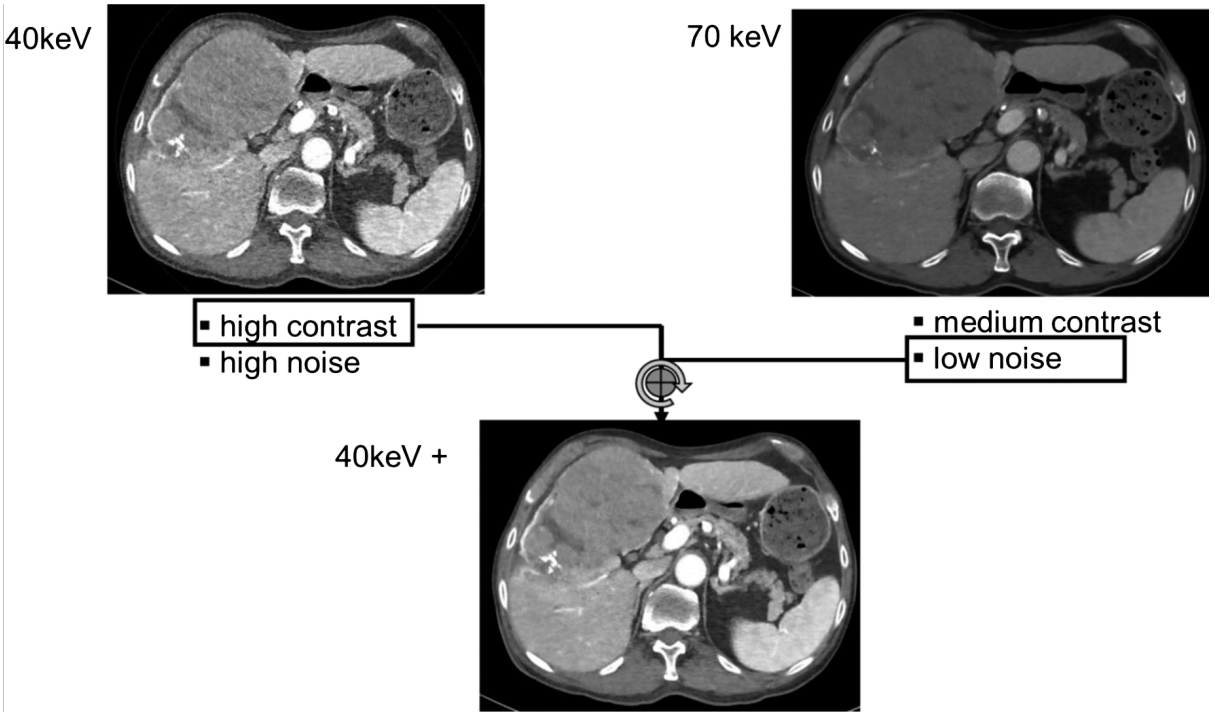

Figure 2.4: Schematic illustrating the method used to create the Mono+ images. Images with high contrast and high noise (40 keV) are mixed with images at lower contrast and lower noise (70 keV). [1].

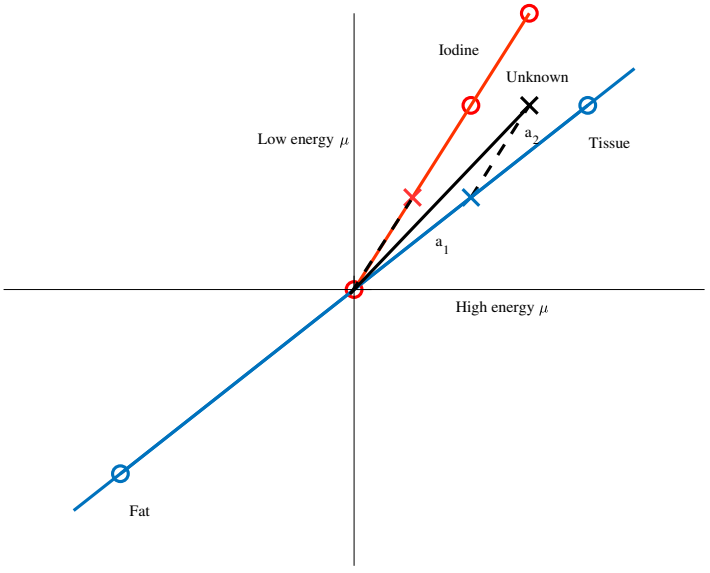

Figure 2.5: Material composition of an unknown voxel into amounts of tissue (a_1) and iodine (a_2).

it is a metric used to quantify the spectral separation of a dual-energy system. The DE ratio changes with different DECT modalities [48–50]. The dual-energy ratio is typically calculated by plotting the Hounsfield Units (HUs) as a function of iodine concentration for the low- and high-energy data separately, as shown in Figure 2.6. The ratio of m_1 and m_2 is equivalent to the DE ratio, were m is the slope of the HU versus iodine concentration plots. Not only does the DE ratio depend on the DECT modality, but it is also a function of phantom/patient thickness as discovered by Lambert et al. and suggested by Jacobsen et al. [50, 51]. As the red and blue curves become more precise or in other words the noise of the low- and high-energy images decreases, the DECT ratio and the basis pairs used for material decomposition becomes more accurate [41].

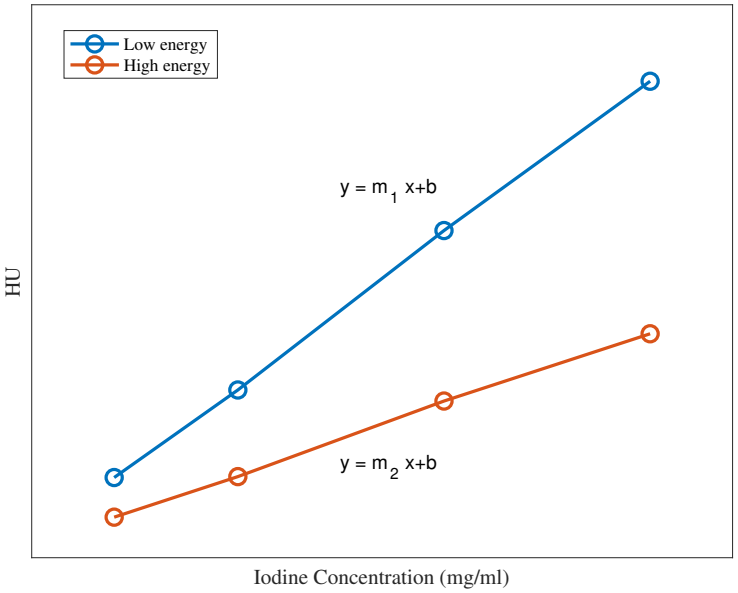

Figure 2.6: Schematic of HU as a function of iodine concentration for a low- and high-energy scan used to determine the DE ratio of a system.

The DE ratio along with the reference HUs of iodine, soft tissue, and fat from Figure

2.5 are used to generate iodine-enhanced and virtual non-contrast images in Siemens' Syngo.via software. These images allow for the viewer to visualize the underlying soft tissue and distribution of the iodine concentration separately as shown in an example in Figure 2.7. The accuracy of the material decomposition and the overall accuracy of these types of images have been investigated for various manufacturers and dual-energy modalities [51, 52].

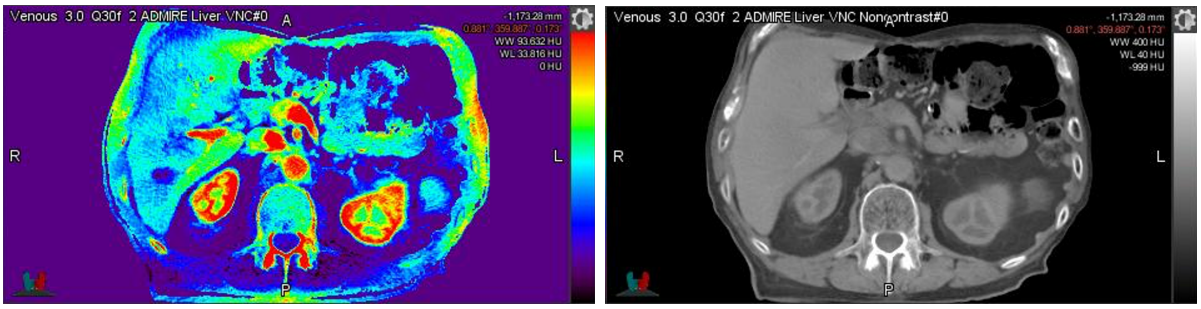

(a) **(b)**

Figure 2.7: Axial slice of an iodine-enhanced image (a) and virtual non-contrast image (b).

Specific to Siemens, the summation of the virtual non-contrast and the iodine-enhanced image is equivalent to a virtual 120 kVp SECT image. Siemens virtual SECT images are called mixed images, as they are a direct weighted sum of the low- and high-energy datasets to create a virtual 120 kVp-equivalent image based on HU, image noise, contrast, and patient dose.

Effective atomic number and electron density data sets are two additional types of DECT images that are created using basis pair decomposition. Since the attenuation coefficient of a material is dependent on the contribution from the photoelectric effect and Compton scatter, the attenuation coefficient from the low- and high-energy datasets

of DECT can be approximated using the following equations,

$$\mu(E_{low}) = b_1(\frac{1}{E_{low}^3}) + b_2 KN(E_{low}) \tag{2.1}$$

$$\mu(E_{high}) = b_1(\frac{1}{E_{high}^3}) + b_2 KN(E_{high}) \tag{2.2}$$

where b_1 is proportional to the electron density and atomic number ($\rho_e Z^3$) and b_2 is only proportional to the electron density (ρ_e). Using basis pair decomposition, the electron density and atomic number can be determined and mapped for each image voxel. The primary application for these images has been in the derivation of stopping power ratios for dose calculations for heavy-ion therapy [53].

The accuracy of determining iodine uptake, electron density, and effective atomic number has been investigated through phantom studies with TwinBeam, dual-source, and fast kVp-switching DECT. It was concluded that TwinBeam had significantly less accurate iodine quantification compared to the other DECT modalities [51]. Iodine quantification from the iodine-enhanced images is generally accurate to within 10% regardless of the vendor and scanner type, except for split-filter dual-energy CT system where errors up to -37% have been demonstrated [51]. The accuracy of TwinBeam electron density and effective atomic number images were also inferior [34].

Many studies have determined the contribution of CT texture analysis (CTTA) in the field of radiation oncology and investigated the reliability of CTTA parameters [54–56]. Dual-energy CTTA has been used to investigate urinary stone fragility, hepatic fibrosis, and pulmonary embolism detection, and results concluded that dual-energy images

were superior and more accurate compared to conventional SECT [54, 56]. CTTA can be performed retrospectively and is an objective way to assess lesion heterogeneity and characteristics beyond what is possible with subjective visual interpretation [57, 58]. This work quantifies first order CTTA parameters of pancreas and liver tumors as a function of VMI energy using TwinBeam DECT images. First order CTTA parameters include mean CT number, standard deviation, skewness, and kurtosis which all assess the distribution of a given histogram. A CTTA study with TwinBeam has never been done before and is novel as it can determine if TwinBeam DECT images can provide additional tumor information for delineation that is not available with conventional SECT images.

2.1.3 Spectral separation, effective energy, and dose allocation

Although DECT has the capability to provide additional information compared to conventional SECT, the accuracy and quality of virtual DECT images depend on the spectral separation and dose allocation (also known as dose partitioning) of the low- and high-energy photon beams [43, 46]. Spectral separation can be defined as

$$\Delta E = \int_0^{E_2} S_{\text{high}}(E) E \mathrm{d}E - \int_0^{E_1} S_{\text{low}}(E) E \mathrm{d}E \tag{2.3}$$

where S is the incident photon spectra and E_1 and E_2 are the maximum energies of the low- and high-energy beams, respectively [59]. Greater spectral separation results in more accurate virtual DECT images and is commonly achieved by adding tin filtration to the high energy beam [46, 60]. With all DECT modalities, the two photon spectra have significant overlap as each are continuous up until the peak tube voltage. Greater

spectral overlap is inefficient and is a limitation for material decomposition techniques. Spectral overlap also reduces dose efficiency as the higher energy beam contains a significant amount of low-energy photons that contribute to dose but do not contribute to the accuracy of the DECT images [60].

Dose allocation is defined as

$$A = \frac{\epsilon_{\text{low}}}{\epsilon_{\text{low}} + \epsilon_{\text{high}}}, \tag{2.4}$$

where ϵ can be entrance surface dose, effective dose, imparted energy, or dose at a specified depth of a patient from the low- and high-energy beams [61, 62]. Dose allocation can range from 0-1, and studies have shown that CNR of dual-energy CT modalities such as fast kVp-switching and dual source is optimized when the dose allocation is roughly 30% [59, 61–63]. Vilches-Freixas et al. investigated stopping power ratio accuracy as a function of dose allocation and found that dose allocation from 0.30-0.70 resulted in the most accurate DECT images, while the precision of the stopping power ratio was slightly shifted towards the lower dose allocation range [59].

CT specific ionization chambers can have up to a 5% energy response within kilovoltage x-ray energies, and are, therefore, calibrated based on the effective energy of the beam [64]. The accuracy of DECT dosimetry relies on a knowledge of the effective energies of the low- and high-energy photon beams [64]. A beam's effective energy is defined as the energy of a mono-energetic photon beam with the same half-value layer (HVL) and is used in the calibration of ionization chambers used in CT dosimetry. Effective energy

can be calculated using the following equations,

$$\frac{1}{2} = e^{-(\frac{\mu}{\rho})\cdot \mathrm{HVL}\cdot\rho} \tag{2.5}$$

$$(\frac{\mu}{\rho}) = \frac{ln(2)}{\rho \cdot \mathrm{HVL}} \mathrm{cm}^2/\mathrm{g} \tag{2.6}$$

where the mass attenuation coefficient, μ/ρ is used to interpolate the beams effective energy from a list of known values specific to the attenuating material [65]. The effective energy is used to determine the calibration coefficients for ionization chambers. During ion chamber calibration at a primary or secondary standards lab, calibration coefficients, N_k are determined from using NIST traceable beams with well characterized effective energies. Before the ion chamber is used clinically, a new N_k value is interpolated based on the effective energy of the clinical beam. Therefore, the knowledge and accuracy of a CT beam's effective energy is crucial for accurate dosimetry. To our knowledge, there is no literature investigating or characterizing the spectral separation, dose allocation, and effective energy for the TwinBeam split-filter modality.

2.2 Pancreas and liver tumors

Pancreatic and liver cancer are the fourth and fifth leading cause of cancer related death for men and women in the United States (excluding uterus cancer), and although surgery

is the established curative treatment option for these cancers, the majority of these patients are not surgical candidates [66]. Radiation therapy offers another localized treatment option and recent studies have shown that accurately focused dose-escalated radiation therapy of these cancers may increase median survival [24, 30, 36, 67]. Accurate tumor delineation is crucial for successful dose-escalated radiation therapy [33, 39]. Unfortunately, delineating pancreas and liver tumors using conventional SECT can be a challenge because these tumors have poor contrast with surrounding healthy parenchyma even with iodine-enhanced imaging techniques [40, 68]. Several dual-energy CT modalities have shown to improve the visualization of these tumors [7, 9, 11, 38, 40, 69, 70]. DECT images generated from fast kVp-switching DECT and dual-source DECT have exemplified greater lesion contrast [11] and lesion CNR [47] of pancreatic adenocarcinomas. DECT images generated from dual-source DECT were more sensitive in detecting hyper-vascular liver lesions compared to conventional single-energy 140 kVp images [7] and had greater CNR of hypo-vascular liver metastases compared to virtual 120 kVp-equivalent images [71]. The use of iodine-enhanced images has also been shown to aid in the visibility of pancreas and liver tumors for radiological purposes as the iodine uptake of these tumors differ from surrounding healthy tissue [8, 72]. Within the past decade, a significant amount of work has been dedicated to applying DECT for the visualization of pancreas and liver tumors through contrast and CNR calculations, but this work has not been applied to the TwinBeam system.

Contouring studies are commonly used to assess the accuracy of a new image modality for tumor delineation. Gupta et al. performed a contouring study that investigated the

geometric uncertainty of pancreatic tumor measurements by analyzing the repeatability of the measurements on DECT images [73]. It was concluded that tumor measurements were highly reproducible on fast kVp-switching DECT images and that clinicians preferred to use the DECT VMIs and iodine maps rather than conventional SECT images [73]. Although contouring studies have been conducted for pancreas tumors with fast kVp-switching DECT images, no one has investigated the reproducibility of pancreas and liver tumor segmentation with TwinBeam images. Furthermore, no studies have quantitatively determined inter- and intra-clinician contour variability on DECT images compared to conventional SECT.

At the University of Wisconsin-Madison Department of Human Oncology, every pancreas and liver cancer patient who will receive radiation therapy is imaged with the Siemens SOMATOM Definition Edge prior to treatment planning. During the simulation procedure, a dual-phase imaging protocol with TwinBeam split-filter is acquired. The pancreatic and portal venous phase scans are acquired for the pancreas cases and the arterial and venous phase scans are acquired for the liver cases. The iodine contrast medium is administered via bolus tracking to account for differences in cardiac output. The type of DE images used for tumor delineation is up to the physician's discretion but usually consist of VMI at 57 keV and the mixed 120 kVp-equivalent image.

After Institutional Review Board (IRB) approval for this thesis work, the raw imaging data and diagnostic information from 20 pancreas and 20 liver cancer cases acquired between June 2016 and August 2018 at the University of Wisconsin-Madison were collected. A total of 20 patients for each tumor site was deemed an adequate number of

cases based on statistical analysis of the preliminary data of overall tumor contrast (difference in HU). A power calculation was performed and determined that a sample size of 20 pancreas cases achieved 82% power to detect a mean of paired differences of at least 10 HU with an estimated standard deviation (SD) of differences of 14.7 and alpha = 0.05 using a two-sided, paired t-test. A sample size of 9 liver cases achieved 80% power to detect a mean of paired differences of at least 10 HU with an estimated SD of differences of 8 and alpha = 0.05 using a two-sided, paired t-test.

2.3 Project motivation and goals

Though the role of DECT imaging is fairly well-established in diagnostic imaging, the benefit of DECT is less well known for radiation therapy. This thesis explored whether TwinBeam can improve tumor visibility as quantified by contrast and CNR for pancreas and liver tumors and whether an increase in these metrics translates to more accurate tumor delineation. The image studies of this thesis analyzed the visibility and texture of pancreas and liver tumors. A contouring study was also performed to compare the variability of GTV contours for TwinBeam images. Also, it is known that TwinBeam has lower spectral separation compared to other DECT techniques, which may limit its benefit in radiation therapy for contouring of difficult tumors. Therefore, another aim of this study was to develop a Monte Carlo model to investigate the characteristics of the split beam and quantify the benefit of increasing peak tube voltage on spectral separation, effective energy, and dose allocation.

Our institution is one of the first clinics in the world to install the Siemens SOMATOM Definition Edge CT scanner with TwinBeam split-filter DECT and the first to use the system for radiation therapy purposes. Similar to other DECT modalities, the current implementation of TwinBeam is hypothesized to increase the visualization of anatomical sites, specifically in the pancreas and liver, that are not well visualized using conventional single-energy CT [40]. Therefore, several quantitative imaging studies of this thesis work used TwinBeam VMIs and mixed 120 kVp-equivalent DECT images to investigate the current implementation of TwinBeam for delineating pancreas and liver tumors for radiation therapy applications. This work used the entire tumor gross target volumes (GTVs) to assess pancreas and liver tumor visibility, which is unlike other published work that have used small region of interests (ROIs) optimally placed within tumors to assess parenchyma-to-tumor contrast and CNR [9, 11, 40]. The results of this study clarified the benefit of TwinBeam compared to conventional SECT in radiation therapy as the investigation of GTV CNR is more applicable to radiotherapy, which requires the entire tumor to be delineated rather than simply identified and measured as in diagnostic imaging.

Although the accuracy of iodine concentration determined from TwinBeam spit-filter iodine-enhanced images has previously been investigated, the results were not applied to actual patient data for the investigation of tumor delineation. This work investigated the iodine concentration in-vivo through size-specific calibration curves. Iodine concentration calibration curves were calculated from TwinBeam DECT images as a function

of phantom size. This information is important first to verify that the iodine concentration calculated by Siemens' Syngo.via software properly accounts for size-specific beam-hardening artifacts, and second to investigate concentrations in-vivo where calculations from volumetric contours are required. At the time of this work, Syngo.via only provided concentration values derived from 2D circular ROIs [51]. This methodology has not been published and can provide information to correlate concentration of iodine with tumor contrast.

The contouring study investigated the reproducibility of pancreas and liver tumor GTVs among clinicians on several TwinBeam DECT images. As previously mentioned, accurate tumor delineation is crucial for successful dose-escalated radiation therapy [23, 24, 30, 33]. Therefore, this contouring study is important because the results can be used to determine whether TwinBeam images can more accurately delineate pancreas and liver tumors for dose-escalated radiation therapy.

CT dose is the biggest contribution to public radiation exposure, and it is suggested that 2% of all cancers in the US are caused by radiation exposure from CT [74]. Although DECT may provide better image quality compared to SECT, the total dose should be equal to or less than the dose from conventional SECT and must be accurately measured for DECT to be beneficial in the clinical workflow. Recent efforts have investigated TwinBeam CT dose index (CTDI) metrics and reported that it provides lower values compared to SECT [44]. Although TwinBeam provided lower CTDI metrics, validation of these metrics through traceable measurements and simulations has not been performed. Accurate CTDI measurements require the knowledge of the beams' effective energy (i.e.

beam quality) to correct the ion chamber reading into true exposure [75].

The effective energies of the low- and high-energy beams of TwinBeam have not been determined. Even though CTDI metrics do not represent patient absorbed dose like the small ion chamber method does, they both still require accurate ion chamber calibration and knowledge of the beams' effective energies [76]. The effective energies and spectral separation of the low- and high-energy spectra of TwinBeam DECT have not been investigated using empirical methods nor optimized with respect to peak tube voltage. The effect of peak tube voltage on spectral separation, dose allocation, and effective energy of split-filter DECT was investigated in this thesis work and the energy response of CT ionization chambers across the split-beam was also quantified. The benchmarked Monte Carlo (MC) model of this study evaluated the individual spectra from the split beam of split-filter DECT based on these three parameters and investigate the impact of increased peak tube voltage.

The overall goal of this project was to explore whether TwinBeam can increase the visibility and delineation accuracy of pancreas and liver tumors over conventional SECT and to characterize split-filter DECT based on spectral separation, effective energy, and dose allocation.

Chapter 3

Spectral separation, effective energy, and dose allocation

3.1 Introduction

As a reminder, dual-energy CT (DECT) is an imaging modality where two x-ray spectra are used to image the same anatomical location and reconstruct a single DECT image. Although DECT was first introduced in the 1970's, the first clinical DECT machine did not become available until 2005 as a dual-source DECT scanner. Since then, there has been several different DECT modalities created that are now used clinically. The two most common modalities are dual-source and fast kVp-switching DECT. Dual-source is just as its name suggests. It is a CT scanner with two x-ray tubes that are operated at a low- and high-energy. Fast kVp-switching is a DECT scanner with one x-ray tube that rapidly switches between the low- and high-energy spectra. Fast kVp-switching has been

characterized and optimized for abdominal imaging and is operated at an 80 kVp and 140 kVp [46, 49, 59, 77]. Dual-source DECT allows for a variety of tube potentials and the ability for additional filtration [4]. The kVp of the low-energy spectra can range from 80 kVp to 100 kVp while the high-energy spectra is operated at 140 kVp or 150 kVp with an additional tin filter. Split-filter (SF) DECT is modality where a single x-ray spectrum is spatially split into a low- and high-energy component. This modality has recently been implemented for clinical use as an additive feature to the Siemens SOMATON Definition Edge CT scanner and is referred to as TwinBeam. TwinBeam has a removable 0.05 cm gold and 0.6 mm tin split filter and is operated at a 120 kVp, which is lower than the peak tube voltage of other DECT scanners.

Common parameters used to optimize a dual-energy CT modality are spectral separation and dose allocation as the accuracy and quality of DECT images depend on these two parameters [43, 46, 49]. Spectral separation is essentially the difference in effective energies and can be calculated with the known energy spectra using Equation 3.1

$$\Delta E = \int_0^{E_2} S_{\text{high}}(E) E \mathrm{d}E - \int_0^{E_1} S_{\text{low}}(E) E \mathrm{d}E \tag{3.1}$$

where S is the incident photon spectra and E_1 and E_2 are the maximum energies of the low- and high-energy beams [59]. Greater spectral separation is desired as it results in more accurate dual-energy ratio, better differentiation of materials, and overall, more accurate virtual DECT images [46, 48, 49]. Specifically, a paper by Alvarez and Mac demonstrated that noise from DECT images decrease when the basis function are more different, or in other words, the spectral separation is large [41].

Abujazar et al. investigated the effect of spectral separation on the contrast and contrast-to-noise ratio (CNR) of different contrast materials such as iodine and gadolinium and found that from the specific kVps investigated (80 kVp, 100 kVp, 120 kVp, and 140 kVp), 80 kVp and 140 kVp provide the best differentiation of these materials [49]. Kruass et al. also investigated the result of different spectral separations on dual-source DECT by investigating different kVp pairs as well as the addition of filters for several phantom sizes. The low- and high-energy beams with the greatest spectral separation for the largest phantom investigated was 80 kVp and 150 kVp with an additional Sn filter. This combination resulted in the greatest dual-energy ratio and the lowest image noise [48]. In the literature, spectral separation is sometimes calculated as the difference in kVp between the low- and high-energy beams; therefore, the actual spectra are not required. But with SF DECT, the kVp of the low- and high-energy beam is the same at 120 kVp. Therefore, the actual determination of the spectra to calculate Equation 3.1 is desired for accurate comparison to other DECT modalities.

Overall, greater spectral separation increases the accuracy and separation of the basis pair vectors introduced in Chapter 2 which is beneficial for image noise. Greater spectral separation also leads to lower dose to the patient as overlapping photons have no value in material decomposition but does increase the effective dose.

Although the effective patient dose is important to determine, the main goal of this work is to determine the dose to a point for the calculation of dose allocation. As previously mentioned, dose allocation is used to characterize a DECT modality and is defined

as Equation 3.2

$$A = \frac{\epsilon_{\text{low}}}{\epsilon_{\text{low}} + \epsilon_{\text{high}}} \tag{3.2}$$

where ϵ can be entrance surface dose, effective dose, imparted energy, CT dose index (CTDI), or dose at a specified depth of a patient from the low- and high-energy beams [61, 62]. Dose allocation can range from 0-1, and studies have shown that CNR of dual-energy CT modalities, such as fast kVp-switching and dual-source, is optimized when the dose allocation is about 30% [59, 61–63]. The dose allocation from TwinBeam DECT has never been investigated. The only type of dosimetry that has been done with TwinBeam is through measurements of CTDI which require measurements along the entire split beam because CTDI from the low- and high-energy portion of the split beam separately is not obtainable. Although CTDI is the most common used metric in clinics, it is not physically appropriate way to estimate patient dose [78]. CTDI is measured with a 10 cm pencil ionization chamber which actually underestimates the dose deposited in the phantom [76]. In addition, the response of the chamber can vary up to 20% over its length [79], which would affect the measurement of CTDI. This is especially crucial for SF DECT where the fluence and energy of the spectra changes more than any other DECT modality. Overall, dose to a specific depth is the best way to determine dose allocation for SF DECT.

The accuracy of DECT dosimetry depends on the knowledge of the effective energies of the low- and high-energy photon beams [64], as the most commonly method of dosimetry for CT machines is with an ionization chamber. CT specific ionization chambers can have up to a 5% energy response within kilo-voltage x-ray energies and are, therefore, calibrated based on the effective energy of the beam [64]. Ion chambers used for CT

dosimetry are calibrated at a primary or secondary standards lab using x-ray beams that are well characterized with known effective energies. The resulting calibration coefficient is then used to interpolate a new coefficient specific to the effective energy of the clinical CT beam. In other words, the knowledge of the effective energy of the clinical CT beam is required for accurate dosimetry. A poly-energetic beam's effective energy is defined as the energy of a mono-energetic photon beam with the same half-value layer (HVL). The effective energy is different than the mean energy but both are used to characterize a poly-energetic photon spectra. The HVL is the thickness of a certain material that attenuates an x-ray beam to half its original value. The attenuation coefficient, μ/ρ determined using Equation 3.3 is used to interpolate the effective energy from a list of known values specific to the attenuating material [65].

$$\begin{aligned} \frac{1}{2} &= e^{-(\frac{\mu}{\rho})\cdot \mathrm{HVL}\cdot\rho} \\ (\frac{\mu}{\rho}) &= \frac{ln(2)}{\rho \cdot \mathrm{HVL}} \mathrm{cm}^2/\mathrm{g} \end{aligned} \tag{3.3}$$

Aluminum and copper or a combination of the two are the most common materials used to measure HVL. The effective energies of the low- and high-energy beams of TwinBeam have not been determined but are required for any type of dosimetric investigation.

This work investigates spectral separation, dose allocation, and effective energy for the SF DECT system as its current clinical design of TwinBeam with a 120 kVp initial photon spectrum and removable SF made of gold and tin. As previously stated, other single- and dual-source DECT modalities have been optimized in the literature to operate with

a peak tube voltages much higher than 120 kVp. Therefore, the impact of SF DECT with an increased peak tube voltage will also be investigated, as it has the potential to provide a more optimal SF DECT system. These important parameters will be determined using physical measurements and simulations with equivalent Monte Carlo source models.

3.1.1 Equivalent source model

An equivalent source model is defined as a computational model that creates an equivalent spectrum that has identical attenuation properties as the actual spectrum of a given x-ray system [80]. For this work, two equivalent source models of split-filter DECT at two peak tube voltages were created to analyze the spectra as opposed to being directly measured. Directly measuring the kilo-voltage x-ray photon spectrum from CT is a difficult and time consuming task due to the high flux of x-rays generated from the CT source. It is difficult to directly measure a CT photon spectra because conventional photon counting detectors cannot operate with these high fluence beams. [2, 81–84]. In specific settings, the count rate can be reduced by adding collimators, decreasing the tube current, and increasing the distance between source and detector, but these adjustments are unachievable with conventional clinical CT due to geometric limitations of the gantry and current settings of the x-ray tube. Fortunately, other researchers have found modeled-based techniques to determine the equivalent photon spectrum from clinical CT scanners.

Modeled-base techniques are based on theoretical, empirical, or semi-empirical considerations and have been intensely validated against direct measurements [2, 80, 82, 85, 86]. Ay et al. assessed different computational methods of determining x-ray spectra and

found no statistically significant difference from measured spectra [82]. Although, Monte Carlo is the gold standard in determining the equivalent spectrum of an x-ray source [87], there is another common code that can be used to generate an x-ray spectrum from CT scanners based on empirical analytical calculations. Spektr is a MATLAB toolkit that calculates x-ray spectrum based on the tungsten anode spectral model using interpolating cubic splines (TASMICS) or based on the tungsten anode spectral model using interpolating polynomials (TASMIP). Spektr was used to determine the initial soft tungsten spectra of the equivalent source models [88].

In order to accurately determine the x-ray spectrum from a clinically used CT scanner using solely modeled-base techniques, confidential scanner-specific information from the manufacturer is needed. Scanner-specific information such as filtration design, bowtie filter and x-ray tube specifications are proprietary and require vendor cooperation and non-disclosure agreements. Unfortunately, the specifications of the Siemens SOMATOM Definition Edge is proprietary and has not been supplied by the manufacturer. Several methods have been developed to overcome the need of manufacturer cooperation and still create equivalent source models of clinical CT scanners. Turner et al. presented a methodology to create an equivalent source model based on spectra created in Spektr and measurements of half value layer (HVL) and bowtie-filter profile [2]. This method was validated by comparing simulated and measured CTDI values. The results from the equivalent source models more accurately matched physical measurements than the results from models created using the manufacturer provided specifications. The methodology of Turner was also implemented in the work of Dr. Qing where she used an

equivalent source model to determine CT dose to organs [83].

As a reminder, the TwinBeam split beam is generated using the single-energy beam from the Siemens SOMATOM Definition Edge scanner and a removable SF. This work created two single-energy equivalent source models of the Siemens SOMATOM Definition Edge scanner at a 120 kVp and 140 kVp based on HVL and profile measurements. The TwinBeam SF was then added to create the DECT equivalent source models and simulations were performed to determine the equivalent SF spectra and dose to the center of a water phantom.

3.2 Methods and materials

3.2.1 Measurements to determine equivalent source model

3.2.1.1 HVL measurements

HVL measurements were performed with the Siemens SOMATOM Definition Edge single-energy beam in order to create an equivalent single-energy source model with the same beam quality. Beam quality refers to the penetration abilities of an x-ray beam defined by a beam's HVL. The HVL will be used to determine the thickness of material in mm of aluminum with the same attenuating properties of any permanent filtration in the useful SOMATOM Definition Edge single-energy beam. This permanent filtration may include the window of the x-ray tube and any permanent enclosure for the tube. For this work, the thickness of material will be referred to as the inherent filtration.

HVL measurements were performed in static maintenance mode with the following specifications: 120 kVp, 700 mAs, 87 kW, body bowtie filter, and 64 x 0.6 mm collimation and although the reconstruction parameters were turned on, the images were not used. A schematic of the HVL measurement set up is shown in Figure 3.1. For these measurements, the gantry was parked at 90 degrees (aka 6 o'clock). The ion chamber was placed along the center ray using the inter-bore lasers and fixed to the table, which was removed from the beam line. The aluminum filters were placed on the gantry using a custom built holder. The aluminum filters were of 99.9 % purity made by PTW (Freiburg, Germany) with different thicknesses. Exposure measurements were taken by adding the alloy aluminum filters of thicknesses ranging from 0 to 9 mm.

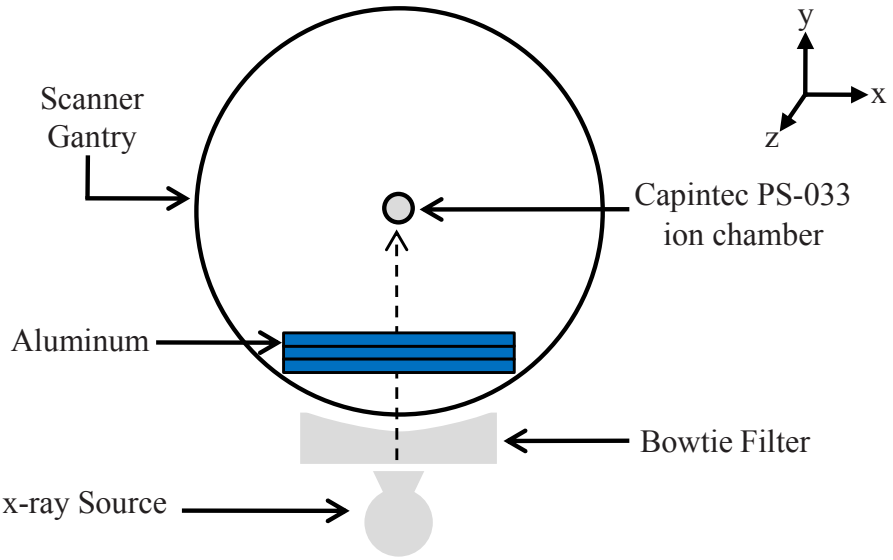

Figure 3.1: Set up for HVL measurements with the Capintec PS-033 ion chamber and aluminum filters. Image altered from Turner et al. [2].

The HVL measurements were performed with a Capintec PS-033 ion chamber (Serial number: CII337975, Capintec Inc., New Jersey) and a SuperMax 4000 (Serial number:

E001225) electrometer. This specific ion chamber was chosen because of its high spatial resolution and thin mylar window. The ion chamber has a 0.5 cm^3 active volume, 1.6 cm active volume diameter, and 2 cm cavity diameter. The energy response of this ion chamber was assessed by Dr. Qing Liang for her Doctoral Thesis. The University of Wisconsin Accredited Dosimetry Calibration Laboratory (UWADCL) Gulmay CP 320 generator and a COMET 320/26 tungsten anode tube was used to determine the air-kerma calibration coefficient, N_k of the Capintec PS-033 ion chamber at four different beam qualities. It was concluded that there is no energy dependence of this ion chamber, therefore it is an acceptable chamber for measuring HVL [83].

3.2.1.2 Fan beam profile measurements

Beam profile measurements were then performed in order to model an equivalent bowtie filter with the same attenuating properties as body bowtie filter used for abdominal scans with the Siemens SOMATOM Definition Edge. The equivalent bowtie filter should attenuate the x-ray spectrum similarly to how the actual bowtie filter attenuates the actual x-ray beam. The purpose of a bowtie filter in CT scanners is to homogenize and shape the x-ray intensity measured by the detectors to improve the image quality and reduce the dose to the patient because of the preferential filtering near the periphery of the fan beam [89]. The thickness of the equivalent bowtie filter was determined as a function of angle, θ. The angle, θ was determined based on the location of each measurement as shown in Figure 3.2 and Equation 3.4. The profile along the fan beam was measured with an Exradin A28 scanning ionization chamber (Standard Imaging, Middleton WI).

This ion chamber has a small 0.125 cm^3 collecting volume and a small energy dependence making it well suited for fan beam profile measurements. A schematic of the measurement set up is shown in Figure 3.2.

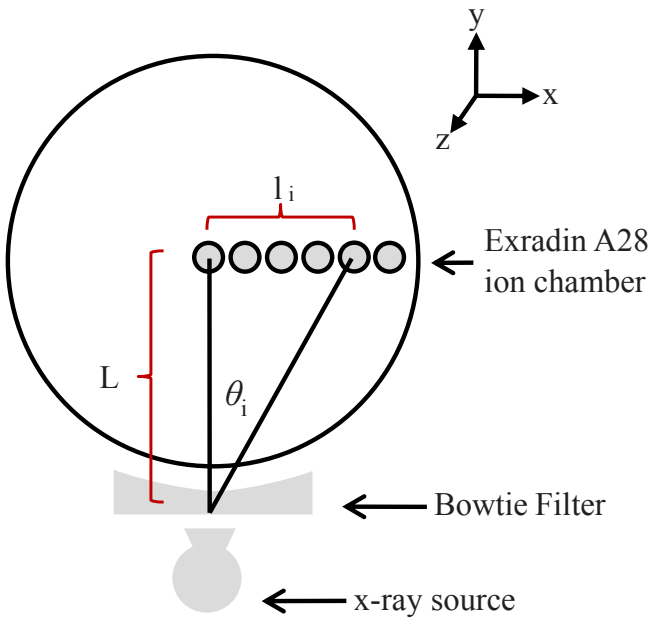

Figure 3.2: Set up for profile measurements with the Exradin A28 ion chamber. Image altered from Turner et al. [2].

The ion chamber was mounted on the couch and initially aligned to isocenter using the inner-bore lasers. The ion chamber was then incrementally shifted to one direction while still maintaining alignment to the lateral laser. It was assumed that the attenuation about the central ray was symmetric; therefore, only one direction of measurements were performed. The angle for each lateral displacement was calculated using the manufacturer-provide distance L, which is the focal spot to isocenter distance, and the distance from the central ray l_i, as shown in Equation 3.4. The ratio of each measured kerma at l_i and the center ray was calculated and used to determine the equivalent bowtie

filter.

$$\theta_i = tan^{-1}\left(\frac{l_i}{L}\right) \tag{3.4}$$

3.2.2 Simulations to determine equivalent source model

3.2.2.1 Soft tungsten spectrum

A soft x-ray spectrum was used as the source of the equivalent source model. As previously mentioned, Spektr determines an x-ray spectrum based on either TASMIP or TASMICS calculations. TASMIP is the original calculation method used in Spektr version 2.0. TASMICS calculation method was introduced in version 3.0 and offers higher spectral resolution, broader energy range, and improved overall spectral characteristics with respect to modern x-ray tubes [88]. Therefore, TASMICS was chosen for this work to calculate a spectrum leaving an anode target, also known as the soft x-ray spectrum. The user interface of Spektr is showed in Figure 3.3.

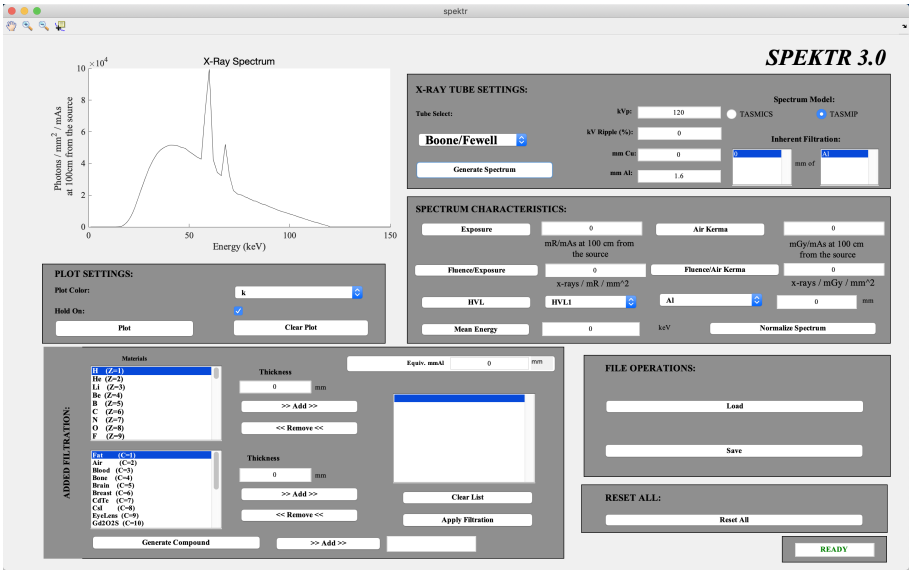

Figure 3.3: Screenshot of the Spektr interface.

The soft x-ray spectrum was calculated while assuming zero inherent filtration and 4% ripple. The x-ray generator used for the Siemens SOMATOM Definition Edge is high-frequency, which is comparable to a three-phase 12 pulse system that has about a 4% ripple [65, 90, 91].

Figure 3.4 shows the 120 kVp soft tungsten anode spectrum calculated in Spektr using TASMICS. This soft spectrum was used as the main photon source of the equivalent source model of the Definition Edge 120 kVp x-ray beam.

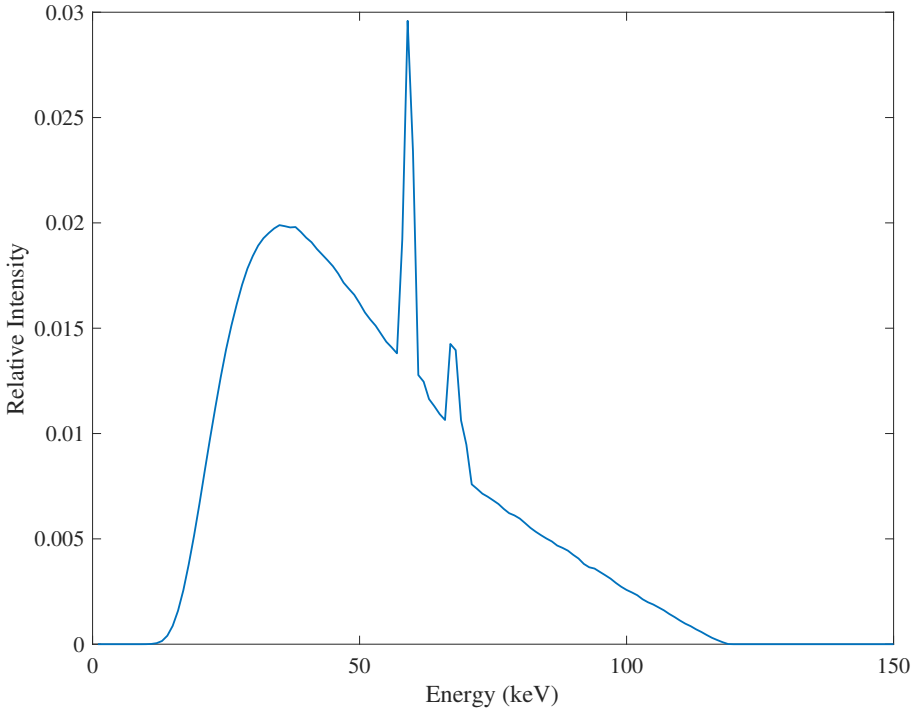

Figure 3.4: Soft 120 kVp tungsten anode spectrum calculated in Spektr with TASMICS.

3.2.2.2 Equivalent single-energy spectra

The equivalent source model was created using Monte Carlo N-particle transport (MCNP) code version 6 and simulations were performed on the University of Wisconsin Medical

Radiation Research Center (UWMRRC) computing cluster. MCNP6 was chosen because it was most familiar to the user and based on the literature, it performs well at simulating dose from kilo-voltage x-ray sources [2]. Simulations were performed using only photons with a cut off energy of 1 keV, as lower photons will not be able to penetrate and contribute information. MCNP6 assumes that all deposited energy is absorbed at the photon interaction site also known as charged particle equilibrium (CPE). For CPE, collision kerma is equal to the absorbed dose. Therefore, all simulations of air kerma or dose to water were calculated by tallying the photon energy fluence and converting to collision kerma or dose, by using the mass energy-absorption coefficients, μ_{en}/ρ of air or water obtained by Hubbell and Seltzer [92].

Several MCNP tallies were used in this study. A F1* tally determines the current across a plan and has units of MeV. A F4* tally calculates the average fluence in a volume and has units of MeV/cm^2. A F5* tally calculates the average fluence at a point and also has units of MeV/cm^2. A TMESH tally determines the fluence and bins the results based on a user defined 3D lattice and has units of MeV/cm^3.

The equivalent single-energy spectrum at the center of the beam was determined using simulations of air kerma with the inherent filtration and center portion of the bowtie filter modeled in MCNP. Figure 3.5 shows the individual components used to determine the equivalent single-energy spectra. This figure includes everything but the lead collimators which were used to shape the beam. The collimators were placed about 8 cm from the source to create a longitudinal beam width equal to 3.8 cm at isocenter. The longitudinal beam width was determined based on Siemens user manual drawings of the x-ray tube

and the measured full-width half max (FWHM) of the dose profile in air for the 64 x 0.6 mm collimation setting. The soft tungsten spectrum determined in Spektr was the source of the model. Downstream from the source was the inherent filtration, followed by the bowtie filter. The thickness of along the center of the bowtie filter was modeled as 0.05 mm of aluminum, similar to the work of Turner et al. [2]. The thickness of the inherent filtration was determined as the thickness of aluminum that when simulated to harden the initial soft tungsten spectrum, results in an equivalent single-energy spectrum (at point A) with the same HVL as measurements. Therefore, simulations of air kerma were performed with the measured HVL in thickness of aluminum located the same distance from isocenter as the measurement set up, 39 cm. Simulations were iteratively performed while increasing the thickness of the inherent filtration until the air kerma at point A was reduced by half. Air kerma was simulated using an *F5 point flux tally and calculated using the mass energy-attenuation coefficient of air from Hubbell and Seltzer [92].

Once the thickness of inherent filtration was determined, the equivalent single-energy spectrum of the Siemens SOMATOM Definition Edge beam was then sampled exiting the inherent filtration of the MCNP model. The variance reduction techniques that were used to acquire this spectrum included varying the importance, as well as forcing collisions within the inherent filtration. The resulting tally used to sample the spectra passed all statistical tests. The mean energy and effective energy of the equivalent spectra was determined.

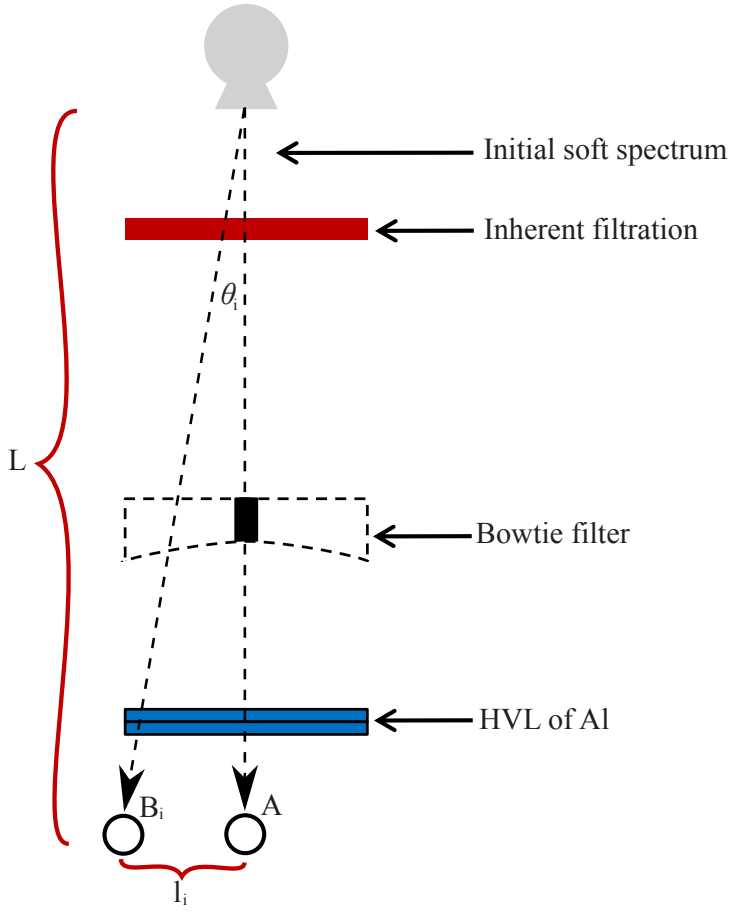

Figure 3.5: Schematic of the MCNP6 model to determine the equivalent SE spectra and fan beam (excluding collimators). L = 59.5 cm. Image altered from Turner et al. and not drawn to scale [2].

3.2.2.3 Single-energy fan beam

After the equivalent single-energy spectrum was determined, the thickness of the bowtie filter at each angle, θ from Figure 3.2 was calculated to determine the equivalent single-energy fan beam. This was done by first transmitting the equivalent x-ray spectrum through the center portion of the equivalent bowtie filter. Then, while assuming exponential attenuation, the thickness of the bowtie filter at θ was iteratively increased and the x-ray spectrum was transmitted through until the difference in ratio of simulated kerma

and the measured kerma was minimized. The single-energy equivalent source model was considered complete once the bowtie filter was determined. A flowchart showing the steps and additions to the model used to determine the equivalent SF source model is shown in Figure 3.6.

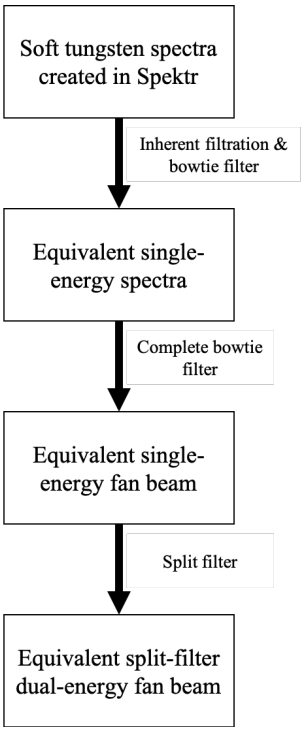

Figure 3.6: Flowchart showing the steps used to determine the equivalent source model as an equivalent SF fan beam.

3.2.2.4 Equivalent split-filter DECT spectra

The TwinBeam SF was then modeled in MCNP at the same location from isocenter as the actual scanner. The SF was placed 11.6 cm downstream from the photon source before the bowtie filter. The actual SF thickness is constant along the fan beam; therefore, it was oriented in MCNP so the 0.05 cm of gold was located in the superior direction and the 0.6 mm of tin was in the inferior direction. Air kerma measurements within the

center of the low- and high-energy region of the split-beam were measured and compared to simulations to determine the overall uncertainty in the equivalent MCNP SF model.

Measurements of air kerma were performed with the A28 ionization chamber aligned at isocenter and then shifted 1 cm in the superior and inferior directions. Air kerma was measured with a 700 mAs and the appropriate N_k values based on the HVLs of each low- and high-energy spectra were applied. Simulations were performed using an F4* tally with the same volume as the collecting volume of an A28 ionization chamber, 0.125 cm^3. The simulated air kerma was determined by summing the product of simulated energy fluence given by the simulated *F4 volume tally and the mass energy-attenuation coefficient of air from Hubbell and Seltzer [64]. The MCNP equivalent SF model was used to determine the DECT parameters of spectral separation, effective energy, and dose allocation.

3.2.3 DECT parameters

3.2.3.1 Spectral Separation

In order to determine the spectral separation, the individual low- and high-energy spectra were captured separately using two *F1 surface current tallies placed exiting the SF. Variance reduction techniques such as varying cell importance and forced collisions were used. The photon spectra were discretely sampled with 150 energy bins from 1 keV to 150 keV. Since the spectra were discretized, Equation 3.1 was modified to calculate the spectral separation,

$$\Delta E = \sum_{i=1}^{b} E_i \cdot p_{high}(E_i) - \sum_{i=1}^{b} E_i \cdot p_{low}(E_i) \tag{3.5}$$

where b is the maximum energy bin and $E_i \cdot p_{high/low}(E_i)$ are the mean energies or expected values of the low- and high-energy spectra. From the mean energy equation, $p_{high/low}(E_i)$ are the normalized photon distributions which were calculated for each spectra in Excel based on the energy bin widths and the number of photons tallied within each bin.

3.2.3.2 Effective Energy

As previously mentioned, the effective energy is an energy of a mono-energetic beam with the same attenuating properties as a poly-energetic beam. In order to compare the low- and high-energy beams to other poly-energetic beams, the HVLs were analytically determined separately for the low- and high-energy components of the beam using the equivalent photon spectra leaving each component of the split-filter. As a reminder, the amount of aluminum filtration that reduces the air kerma by half is a beam's HVL. By assuming CPE, and since the energy spectra were discretized, collision air kerma was calculated using Equation 3.6. This method of calculating HVL neglects the small amount of attenuation due to air between the split filter and isocenter.

$$Kerma = \sum_{i=1}^{E_{max}} E_i \Phi_i (\frac{\mu_{en}}{\rho})_i, \tag{3.6}$$

where E_{max} is the maximum energy of the polyenergetic spectra, Φ is the number of photons at energy E, and $(\frac{\mu_{en}}{\rho})$ is the mass energy absorption coefficient of air at energy E. The HVL of the combined split-beam was also calculated. The resulting HVL was then used to solve for the mass attenuation coefficient in Equation 3.3. The mass attenuation coefficient was then used to interpolate the effective energy from NIST reported values

of attenuation coefficients for aluminum. Any uncertainty associated with differences in attenuation coefficients caused by the 0.1% impurity of the PTW aluminum filters were negligible.

3.2.3.3 Dose allocation

For this work, the dose allocation was calculated using dose to the center of a phantom and analyzed as a function of phantom thickness. Different phantom thicknesses were investigated because literature and previous thesis Chapters suggests that quality and benefit of DECT images depend on patient size [51]. A cylindrical water phantom was placed within the model to assess the difference in relative dose of the low-energy beam to the total dose (dose allocation) as a function of phantom thickness. The dose at the center of the phantom was tallied separately for the low- and high-energy components of the split beam. While assuming charge particle equilibrium, the dose was calculated by summing the product of simulated energy fluence (MCNP *F4 tally) and the mass energy-attenuation coefficient of water from Hubbell and Seltzer [64]. The dose allocation was calculated using Equation 3.2 for a range of phantom radii ranging from 10 - 20 cm and compared to the recommended 30% [59, 61–63].

Prior to dose simulations and the calculation of dose allocation, mAs-to-dose conversion factors (CF) were calculated to convert the simulated phantom doses to dose for a specified mAs [83]. The CFs were calculated individually for the 120 kVp and 140 kVp

beams using Equation 3.1 and used for the corresponding split filter models.

$$\text{mAs-to-dose CF}_{120\text{kVp},140\text{kVp}} = \left(\frac{d_{\text{meas}}[\text{mGy/mAs}]}{d_{\text{sim}}}\right)_{120\text{kVp},140\text{kVp}} \tag{3.7}$$

The dose measured, d_{meas} was the collision air kerma at isocenter for 700 mAs using the A28 ionization chamber. Under CPE, collision air kerma is equal to dose, D and is defined as

$$D = K_C = \Psi(E)\left(\frac{\mu_{en}}{\rho}\right)_{E,Z}, \tag{3.8}$$

where Z is the atomic number of the absorbed material, Ψ is the energy fluence of the photon beam with energy E, and $(\frac{\mu_{en}}{\rho})$ is the mass absorption coefficient in units of cm^2/g. Kerma can only be measured directly with absolute dosimetry methods as the precise mass of air is required. Unfortunately, the methods available for direct kerma measurements are time intensive and require specific measurement devices such as free-air ionization chambers. Therefore, secondary measurements were performed with an ionization chamber calibrated from a secondary calibration laboratory. The calibrated ionization chamber is equipped with an air-kerma calibration coefficient. The calibration coefficient, N_k is determined for an ion chamber, j calibrated for a certain beam quality, BQ_i using the NIST ionization chamber calibration coefficient $N_{k,NIST}$,

$$N_{k,j,BQ_i} = N_{k,NIST}\frac{Rdg_{j,BQi}}{Rdg_{NIST,BQi}}. \tag{3.9}$$

where N_k for both the NIST ion chamber and the ion chamber of question is given in

cGy/nC. This work interpolated corresponding N_k values based on the beam quality in terms of measured HVLs for the 120 kVp and 140 kVp beams. The use of mAs-to-dose conversion factors from air to phantom dose has been validated by Qing [83]. The A28 N_k values from Table 3.10 were used to convert charge collected to air kerma. The measured air kerma, simulated air kerma, and resulting mAs-to-dose conversion factors for the 120 kVp and 140 kVp beams are shown in Table 3.1.

Table 3.1: mAs-to-dose conversion factors used to convert simulation results to dose.

Beam	Measurements (mGy)	σ (%)	mAs	d_{meas} (mGy/mAs)	d_{sim}	σ (%)	mAs to dose conversion factor
120 kVp	114.8	0.09	700	0.164	7.35×10^{-16}	0.015	2.23×10^{14}
140 kVp	165.6	0.05	700	0.237	1.02×10^{-15}	0.015	2.31×10^{14}

3.3 120 kVp and 120 kVp + SF source model results

3.3.1 HVL and inherent filtration

Table 3.2 lists the measurements used to determine the HVL of the Definition Edge 120 kVp beam. The values in Table 3.2 were fitted to an exponential curve using the MATLAB fit command with the exponential fit type. The values and curve are shown in Figure 3.7. The exponential fit parameters shown in Figure 3.7 were then used to calculate the HVL of the beam using the calculation shown in Equations 3.10. The uncertainty budget in the calculated HVL is shown in Table 3.3.

Table 3.2: The average and relative error of charge collected and resulting relative air kerma measured at each aluminum thickness. Values are plotted in Figure 3.7.

Al (mm)	Charge (nC)	σ (%)	Relative air kerma	σ (%)
0	2.08	0.03	1.00	1.001%
2.983	1.60	0.04	0.765	1.001%
4.949	1.36	0.05	0.651	1.001%
5.987	1.25	0.03	0.600	1.001%
8.002	1.07	0.04	0.513	1.001%
8.992	0.99	0.06	0.476	1.002%

$$
\begin{aligned}
\frac{1}{2} &= e^{-0.0839\frac{1}{\text{mm Al}}\times\text{HVL(mm Al)}} \\
ln(\frac{1}{2}) &= -0.0839\frac{1}{\text{mm Al}}\times\text{HVL(mm Al)} \\
\text{HVL(mm Al)} &= \frac{ln(2)\text{mm Al}}{0.0839} \\
\text{HVL} &= 8.26(\text{mm Al}) \qquad (3.10)
\end{aligned}
$$

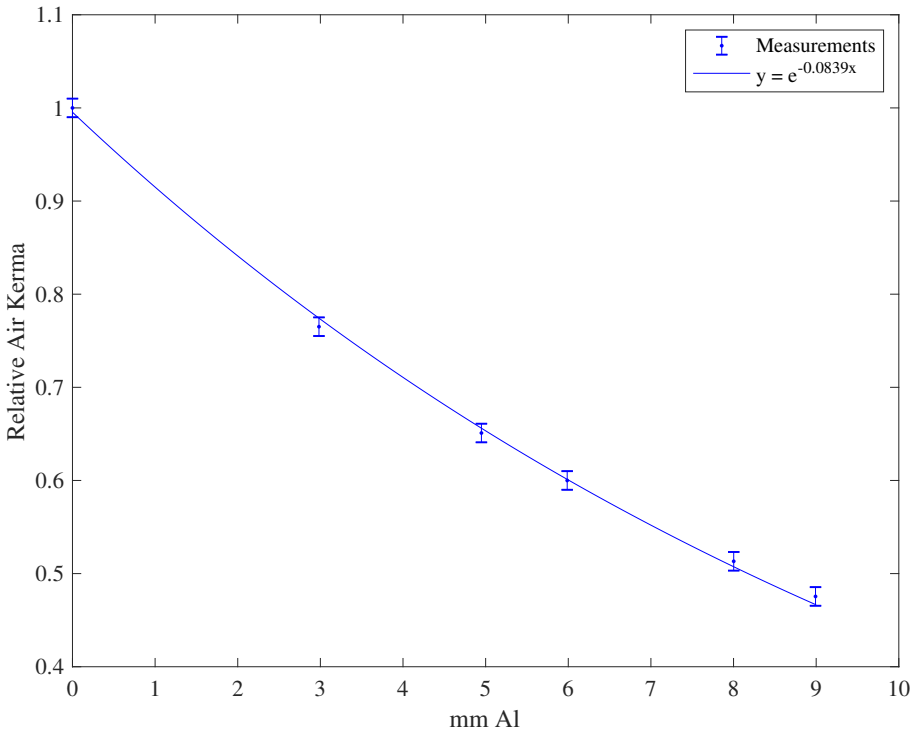

Figure 3.7: Graph showing the relative measurements listed in Table 3.2 and fitted exponential curve used to calculate the effective HVL of the Siemens SOMATOM Definition Edge 120 kVp beam.

Table 3.3: Uncertainty budget in determining the HVL.

	Relative Standard Uncertainty (%)	
Parameter	Type A	Type B
Air Kerma Measurement	0.0551	1.00
Set up Reproducibility	0.405	-
Thickness of aluminum	1.21	-
Combined uncertainty	1.30	1.00
Total uncertainty (k=1)	1.64	
Expanded uncertainty (k=2)	3.28	

The uncertainty in the air kerma measurement was determined using the greatest uncertainty in a single measurement from Table 3.2 and the uncertainty in the calibration of the ion chamber reported by the UWADCL. This uncertainty stems primarily from the uncertainty of the NIST calibration of the reference chamber. The uncertainty associated with thickness of aluminum was determined as ratio of the thinnest aluminum filter used

(0.1 mm) and the measured HVL (8.26 mm). The measured HVL was compared to the CT scanner's user manual, which states that the HVL of the 120 kVp beam is 8.3 mm. This represents a 0.6% difference compared to the measured HVL and is well within the uncertainty in our measurement. Based on this calculated HVL, the effective energy of the 120 kVp equivalent x-ray beam determined from the measured HVL was 55.4 ± 0.91 keV.

The inherent filtration was then determined which as a reminder is the amount of aluminum that hardens the soft tungsten spectrum to create a beam with the same HVL as the Siemens SOMATOM Definition Edge 120 kVp beam. The inherent filtration was 8.83 mmAl.

3.3.2 Equivalent single-energy spectrum

The equivalent single-energy 120 kVp spectrum with the same attenuating properties as the Siemens SOMATOM Definition Edge 120 kVp beam is shown in Figure 3.8. This equivalent x-ray spectrum was tallied exiting the inherent filter using a MCNP *F1 tally. The mean energy of this equivalent spectrum was 62.8 keV, which is of course higher than the mean energy of the soft spectrum determined in Spektr, 51.4 keV. In order to validate the model and the inherent filtration, the HVL was also solved analytically using the tallied equivalent spectra. The HVL solved analytically from the equivalent 120 kVp x-ray spectrum was 8.23 ± 0.01 mmAl. This is within the uncertainty of the measured HVL of 8.26 ± 0.14 mmAl.

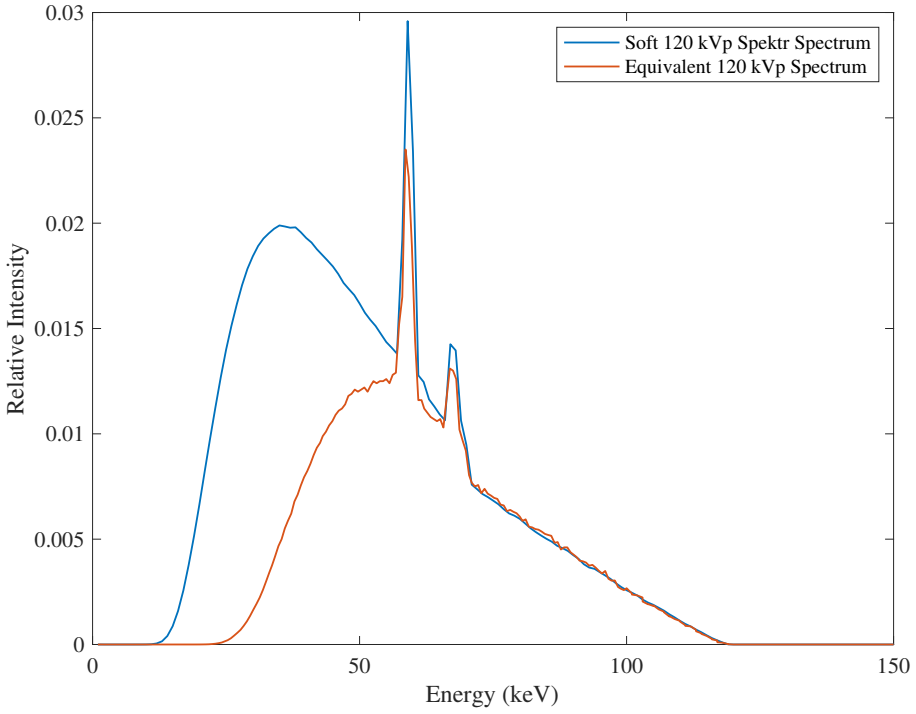

Figure 3.8: Soft 120 kVp spectra and the equivalent 120 kVp spectra to the Siemens SOMATOM Definition Edge 120 kVp beam based on HVL.

3.3.3 Equivalent bowtie filter

The measurements taken along the fan beam that were used to characterize the bowtie filter for the equivalent source model are shown in Figure 3.9. These results are normalized to the central point and extend to ±32.5 cm. These measurements were performed twice to determine the uncertainty in overall set up. The total uncertainty in each point measurement was determined with the uncertainty budget shown in Table 3.4. A schematic of the MCNP model of the resulting equivalent bowtie filter is shown in the Figure 3.10.

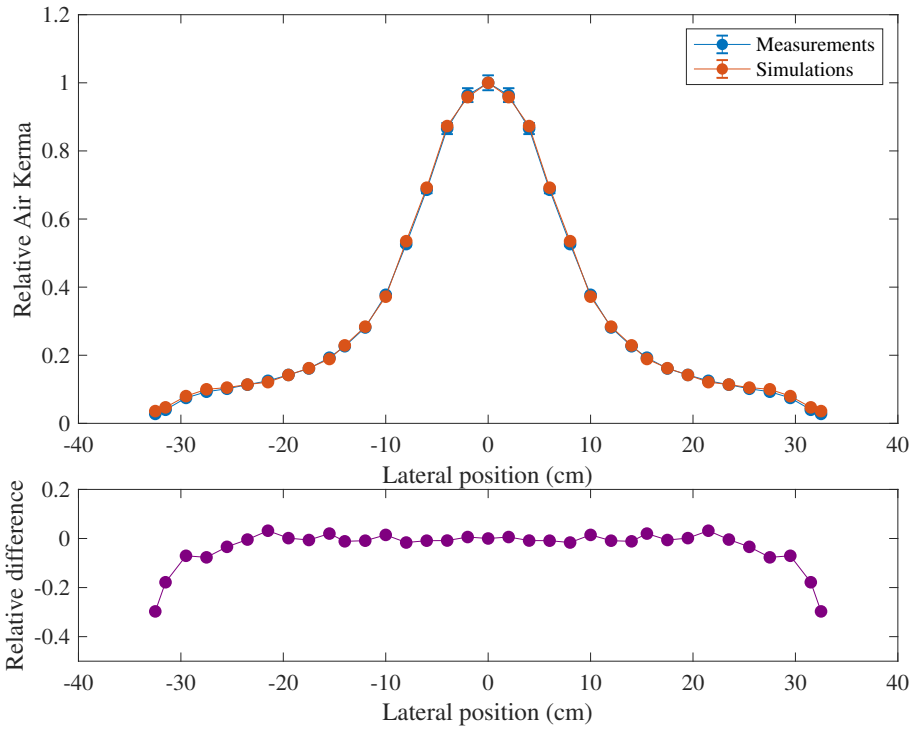

Figure 3.9: Relative air-kerma measurements performed with an A28 ion chamber along the fan beam of the Siemens SOMATOM Definition Edge 120 kVp beam and simulated air-kerma from MCNP.

Table 3.4: Uncertainty budget in measuring the fan beam profile along the bowtie filter.

	Relative Standard Uncertainty (%)	
Parameter	Type A	Type B
Air Kerma Measurement	0.013	1.00
Set up Reproducibility	2.10	-
Combined uncertainty	2.13	1.00
Total uncertainty (k=1)	2.35	
Expanded uncertainty (k=2)	4.71	

3.3.4 Equivalent split-filter DECT model

The measured air kerma and simulated air kerma within the low- and high-energy region of the split beam are shown in Table 6.2. The root-mean-squared error from the low- and high-energy region was used to determine the overall uncertainty in the SF MCNP

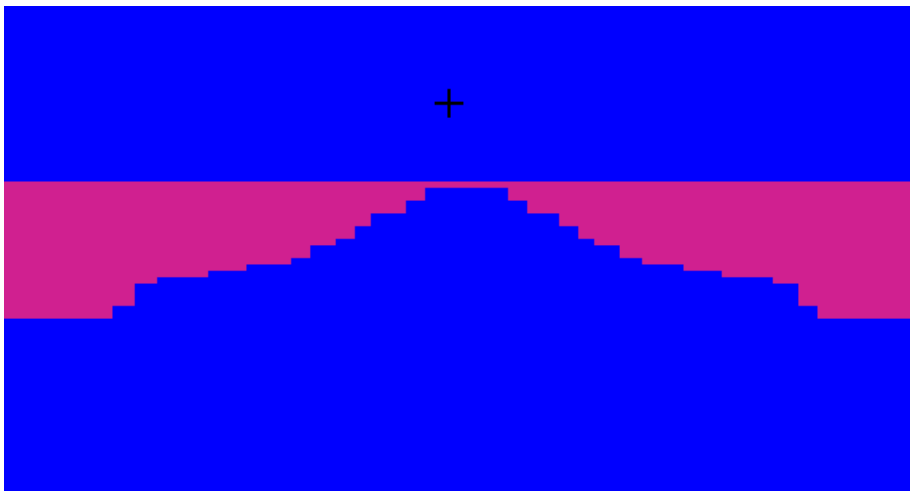

Figure 3.10: MCNP model of the equivalent bowtie filter with the same attenuating properties as the actual Siemens SOMATOM Definition Edge bowtie filter. The plus sign is just where the cursor was when the screen shot was taken.

simulations.

Table 3.5: Results used to compare the Split-filter Monte Carlo model and determine the Type B uncertainty in the MCNP model when simulating dose for the low- and high-energy regions of the split beam.

Beam	Measured Air Kerma (mGy/mAs)	σ(%)	Simulated Air Kerma (mGy/mAs)	σ(%)	Percent Difference (%)
120 kVp + 0.05 Au	0.065	1.00(%)	0.070	0.087(%)	6.8(%)
120 kVp + 0.6 Sn	0.023	1.02(%)	0.022	0.059(%)	3.3(%)

There was slight disagreement in the final air kerma results. One reason for this disagreement was the uncertainty associated with the HVL measurements used to create the original 120 kVp model. Another reason for the disagreement is the misalignment in the measured and simulated profile along the split beam. The profile of the split beam was measured using film and compared to the simulated profile. Figure 3.11 shows the overlap of the two profiles. Unfortunately, the gradient from the high- to low-energy region do not directly overlap. The simulated profile was steeper than the measured profile. The split filter is modeled in MCNP with the gold and tin simply abutted next to one another. The actual manufacturing of the split filter is unknown but the type of welding may have caused the less steep gradient between the two regions of the profile and the difference in the values listed in Table 6.2.

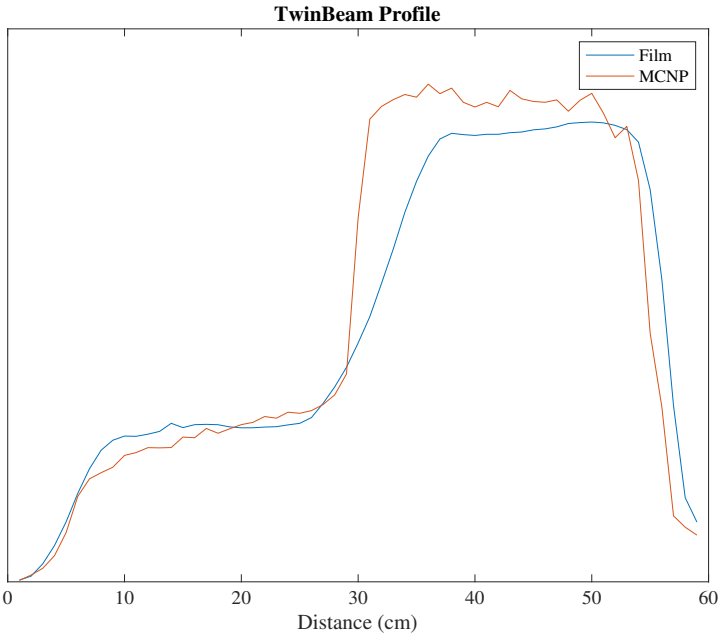

Figure 3.11: Profile along the split beam measured using film of the actual TwinBeam scanner and simulated using MCNP.

3.3.4.1 Spectral separation

Once the SF was placed within the model, the individual low- and high-energy spectra leaving the SF were tallied. Figure 3.12 shows the normalized initial 120 kVp equivalent spectra, plus the spectra leaving the gold and tin. The mean energy of the low-energy component of the split beam created from the gold was 66.2 ± 0.10 keV. The mean energy of the high-energy component of the split beam created from the tin was 82.7 ± 0.18 keV. For the TwinBeam 120 kVp + SF design, the spectral separation between the low- and high-energy beams was 16.5 ± 0.04 keV. The error in the spectral separation calculation was determined based on the Type A relative uncertainty in the *F1 tally.

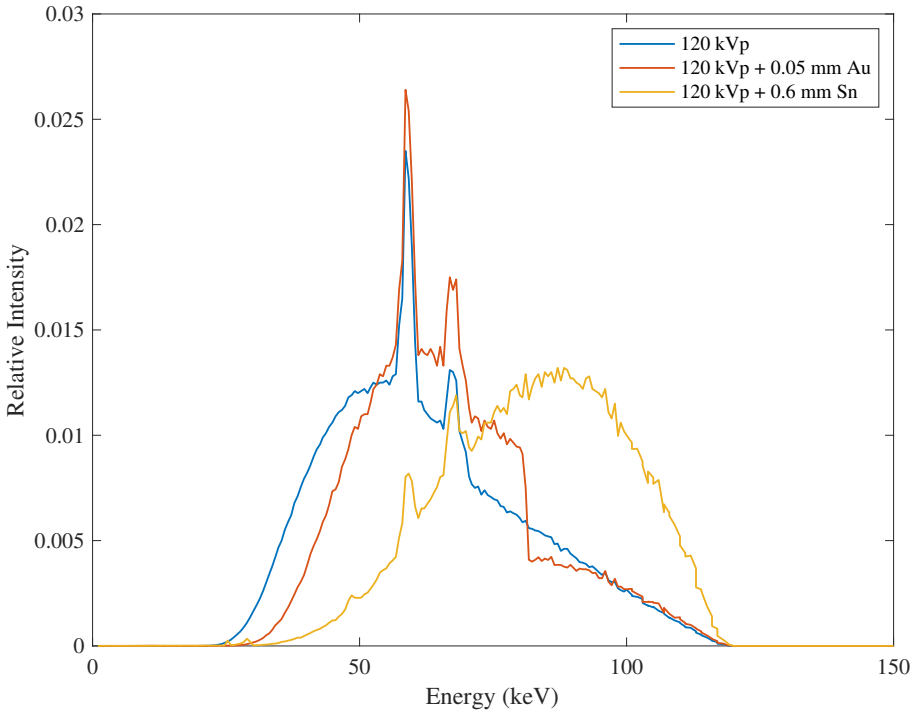

Figure 3.12: Normalized spectra determined from MCNP equivalent 120 kVp source model, the low-energy spectrum from the gold (Au) component , and the resulting high-energy spectrum from the tin (SN) component from the 120 kVp + SF source model.

3.3.4.2 Effective energy

The effective energy of the low- and high-energy portion of the split-filter were determined using analytical calculations of HVL using the spectra leaving the split-filter. The HVLs were 9.20 ±0.01 and 12.3 ± 0.03 mmAl for the low- and high-energy components of the 120 kVp + SF model, respectively. The corresponding effective energies were 59.8 ± 0.09 keV and 77.7 ± 0.17 keV. The uncertainty in the calculated HVL and effective energy was propagated from the Type A relative uncertainty in the simulated results of each energy bin tallied.

A comparison of the mean energy and effective energies of the split beam leaving the split filter and at isocenter was performed to quantify the physical overlap of the two beams. The split-beam profile was tallied at isocenter using a FMESH 13 tally (Figure 3.11). Based on the tallied profile and the relative flatness around ± 1 cm, two *F1 tallies were placed 1 cm from the central axis.

The mean energies of the tallied spectra at isocenter were, 66.7 ±1.03 keV and 81.7 ± 1.69 keV for the low- and high-energy components of the split beam, respectively. There were higher relative uncertainties when tallying the spectra at isocenter but based on the results and the mean energies listed in Table 3.9, there was no difference in mean energy when calculated at isocenter versus exiting the split-filter. There was also no difference in the analytical calculation of HVL. The HVLs determined using the spectra tallied at isocenter were 9.40 ± 0.15 mmAl and 12.45± 0.26 mmAl for the low- and high-energy beam, respectively. The corresponding effective energies were 60.8 ± 0.9 keV and 78.4 ± 1.6 keV. The HVLs and calculated effective energies determined using the spectra at

isocenter were within the uncertainty of the results using the spectra leaving the split filter. Therefore, the low- and high-energy beams do not change as a function of distance from the split-filter.

3.3.4.3 Dose allocation

The dose and dose allocation from the low- and high-energy components of 120 kVp + SF equivalent source model were determined using the mAs-to-dose conversion factor of the 120 kVp beam listed in Table 3.1. The dose and calculated dose allocation to the center of cylindrical water phantoms of varying radii ranging from 10-20 cm are listed in Table 3.6.

Table 3.6: Dose and dose allocation calculated using Equation 3.2 to a 0.5 cm^3 volume at the center of cylindrical water phantoms of varying radii from the equivalent TwinBeam 120 kVp + SF MCNP source model.

Phantom Radius (cm)	120 kVp + 0.05 cm Au Dose (mGy)	120 kVp + 0.6 mm Sn Dose (mGy)	Dose allocation ± (%)
10	0.024	0.013	0.65 ± 0.017 %
12	0.018	0.011	0.63 ± 0.017 %
15	0.012	0.0074	0.62 ± 0.017 %
17	0.0089	0.0056	0.61 ± 0.018 %
20	0.0057	0.0038	0.60 ± 0.020 %

The percent uncertainty in the dose allocation shown in Table 3.6 was the root-mean-squared error of the relative uncertainty in the *F4 tallies from the low- and high-energy components of the split beam. The uncertainty budget for the final dose allocation results is shown in Table 3.7. The error in the dose allocation from the largest phantom was used for the Type A relative standard uncertainty in the SF simulation results. The Type B

relative uncertainty in the SF simulation results was the root-mean-squared error of the percent differences listed in Table 6.2.

Table 3.7: Uncertainty budget in determining the dose allocation for the 120 kVp + SF equivalent beam model.

	Relative Standard Uncertainty (%)	
Parameter	Type A	Type B
Inherent filtration	1.64	-
Bowtie filter	2.35	-
SF Simulation results	0.020	7.56
Combined uncertainty	2.86	7.56
Total uncertainty (k=1)	8.08	
Expanded uncertainty (k=2)	16.2	

The k=1 uncertainty or in other words the 68% confidence level for the dose allocation was 8.08% which includes the uncertainty in the half value layer, the bowtie filter, and the overall accuracy of the split-filter model.

3.4 140 kVp and 140 kVp + SF source model results

It was hypothesized that the spectral separation and dose allocation of a SF DECT design will increase with a 140 kVp initial x-ray spectra by increasing the mean energy of the high-energy portion of the beam. This work created an equivalent source model of a 140 kVp + SF in MCNP in order to investigate this hypothesis. The source of the initial model was a soft 140 kVp spectrum created in Spektr with a 4% ripple and 0 inherent filtration. This model was created based on measurements using the Siemens SOMATOM Definition Edge 140 kVp beam. HVL measurements were used to determine the equivalent inherent filtration to create an equivalent spectrum with the same HVL as the Siemens SOMATOM Definition Edge 140 kVp beam. Profile measurements were used to confirm

the same bowtie filter created for the 120 kVp beam. Measurements were taken using the same set up configuration shown in Figure 3.1 and Figure 3.2. The split-filter with the same specifications as the one used for TwinBeam was inserted into the model and the spectral separation, effective energy, and dose allocation were then calculated using the same methodology as described above for the 120 kVp + SF model.

3.4.1 HVL, inherent filtration, and equivalent x-ray spectrum

The equivalent spectrum of the Siemens SOMATOM Definition Edge 140 kVp beam was determined using the same steps described in Section 3.2.1.1. A soft 140 kVp spectrum created in Spektr was hardened by increasing the amount of inherent filtration until its HVL was equal to that of measurements. The HVL measurements are shown in Figure 3.13. Based on measurements and Equation 3.10, the HVL of the Siemens SOMATOM Definition Edge 140 kVp beam was 9.67 $\pm$ 0.16 mmAl. The uncertainty in the HVL was propagated from the uncertainty in the measurements and the resulting exponential fit to the measured data. The total uncertainty is shown in Table 3.3. The reported HVL within the Siemens manual is 9.5 mmAl, which is well within the uncertainty in the measured HVL.

The amount of aluminum to harden the soft 140 kVp tungsten spectrum to the same HVL as measurements was 10.4 mm. The inherent filtration was modeled and the equivalent spectrum was then tallied exiting the inherent filtration. Figure 3.14 shows the soft spectrum determined in Spektr and the resulting equivalent 140 kVp spectrum. The mean energy of the equivalent 140 kVp beam was 68.7 $\pm$ 0.09 keV. This is within 1% of the user

manual reported mean value of the Siemens SOMATOM Definition Edge 140 kVp beam. The HVL was also solved analytically from this tallied spectra in order to validate the inherent filtration. The HVL solved analytically was 9.50 ± 0.02 mmAl which is within the uncertainty of the measured HVL.

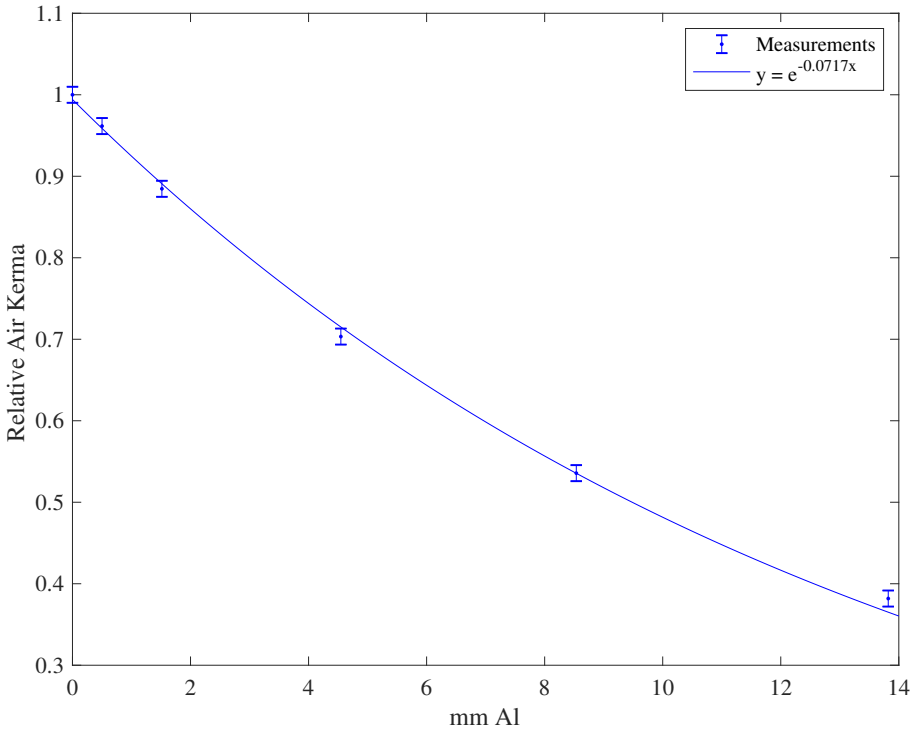

Figure 3.13: Graph showing the measurements and fitted exponential curve used to calculate the effective HVL of the Siemens SOMATOM Definition Edge 140 kVp beam.

3.4.2 Equivalent bowtie filter

Profile measurements along the 140 kVp fan beam were collected and are shown in Figure 3.15 in comparison to the 120 kVp results. Not every point that was measured for the 120 kVp was repeated, as the small subset of points showed no difference in relative output between the 120 kVp and 140 kVp beams. The same bowtie filter was used for

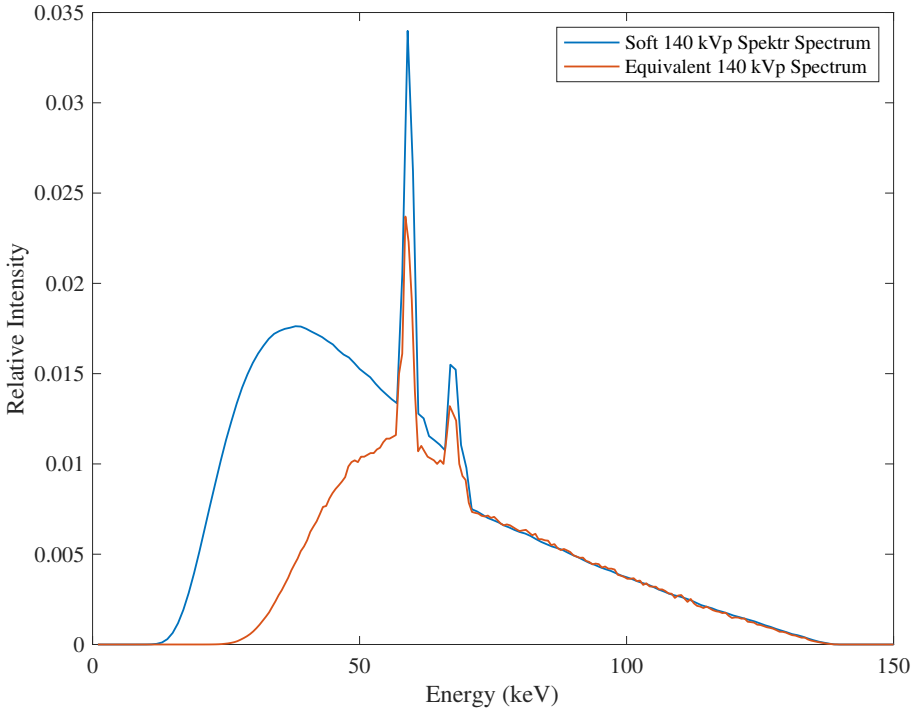

Figure 3.14: Soft 140 kVp spectra and the equivalent 140 kVp spectra to the Siemens SOMATOM Definition Edge 140 kVp beam based on HVL.

each energy. Each measurement point was within the total k=1 uncertainty of each other. Therefore, no alterations to the initial MCNP model of the bowtie filter were made. The total uncertainty in each point are shown in Table 3.4.

3.4.3 Spectral separation, effective energy, and dose allocation

The same thickness and composition of the TwinBeam split-filter was placed within the 140 kVp MCNP model. Similar to the 120 kVp equivalent spectra, two *F1 tallies were placed exiting the split filter. Energies were tallied with 150 individual tallies from 1 keV to 150 keV. Variance reductions techniques were used to decrease the uncertainty in each tallied bin, including forced collisions and increasing the importance of the cells along the

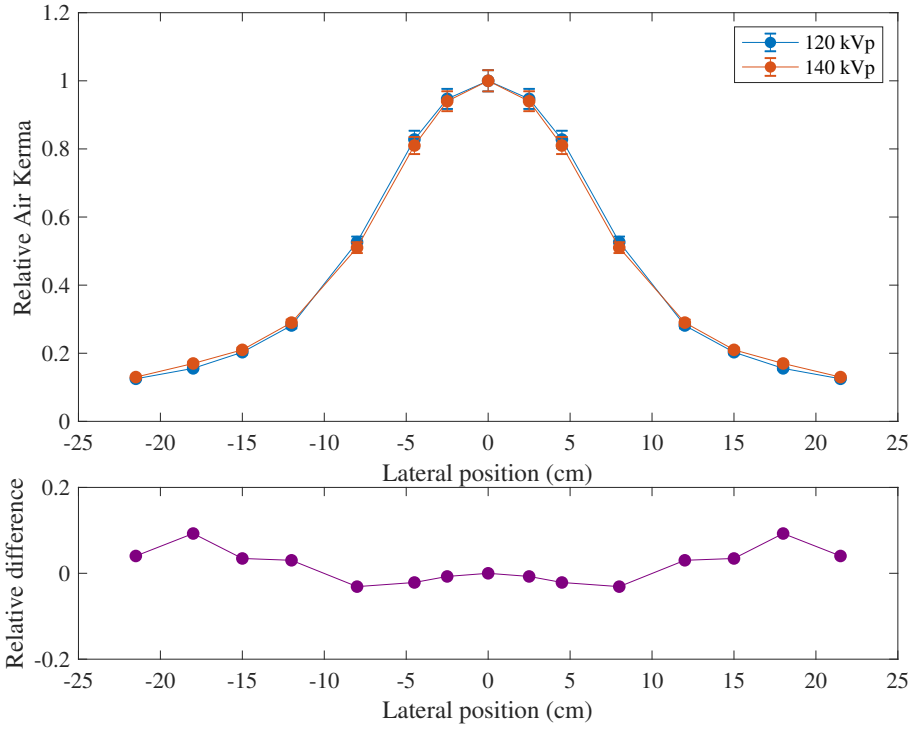

Figure 3.15: Relative air-kerma measurements performed with an A28 ion chamber along the fan beam of the Siemens SOMATOM Definition Edge at 120 kVp and 140 kVp.

beam line. The spectra of the low- and high-energy components from the 140 kVp + SF equivalent source model are shown in Figure 3.16.

The mean energy of the low- and high-energy components of the split beam were, 71.9 ± 0.72 keV and 92.9 ± 0.149 keV, respectively. The spectral separation of the equivalent SF DECT beam with a 140 kVp initial spectrum was 21.1 ± 0.04 keV. This represents a 28% increase in spectral separation compared to TwinBeam 120 kVp + SF model.

Similar to Section 3.3.4.2, the effective energy of the low- and high-energy components of the 140 kVp split beam were also determined. The HVL of each portion was analytically solved using the spectra tallied exiting the split filter. The HVLs were 11.60 ± 0.012 mmAl and 13.96 ± 0.022 mmAl for the low- and high-energy components of the split beam,

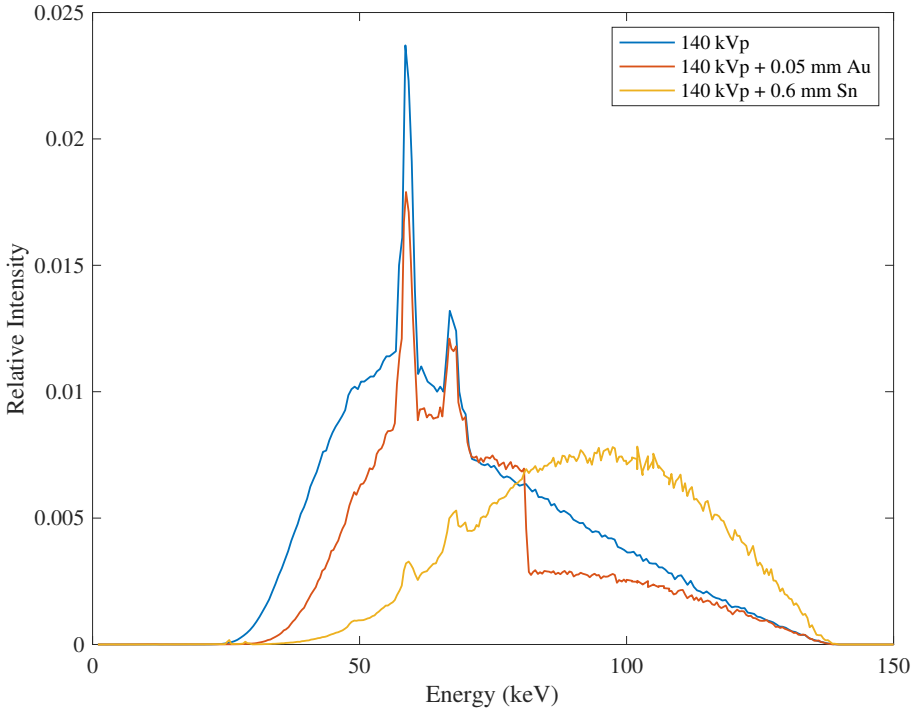

Figure 3.16: Normalized spectra determined from MCNP equivalent 140 kVp source model, the low-energy spectrum from the gold (Au) component, and the resulting high-energy spectrum from the tin (SN) component from the 140 kVp + SF source model.

respectively. The corresponding effective energies were determined using known values of the mass energy-attenuation coefficients of aluminum to be 73.1 ± 2.85 keV and 89.3 ± 6.36 keV. The HVL of the combined beam was 11.0 ± 0.014 mmAl with an effective energy of 69.5 keV.

The dose and dose allocation results determined from the 140 kVp + SF model are shown in Figure 3.8. These results were determined using simulations of dose to the center of cylindrical water phantom of varying radii and the mAs-to-dose conversion factors for the 140 kVp beam listed in Table 3.1. The total uncertainty in the dose allocation results were equivalent to the total uncertainty shown in Table 3.7 for the 120 kVp + SF model.

Table 3.8: Dose and dose allocation simulated to a 0.50 cm^3 volume at the center of cylindrical water phantoms of varying radii from the 140 kVp + SF source model.

Phantom Radius (cm)	140 + 0.05 Au Dose (mGy)	140 + 0.6 Sn Dose (mGy)	Dose allocation (%)
10	0.0423	0.0245	0.63 ± 0.017 %
12	0.0327	0.0198	0.62 ± 0.017 %
15	0.0219	0.0140	0.61 ± 0.017 %
17	0.0168	0.0111	0.60 ± 0.018 %
20	0.0112	0.0077	0.59 ± 0.020 %

3.5 Discussion and conclusions

There were several reasons why an MCNP model was used to investigate split-filter DECT. There is currently no available phantom that would be adequate enough to perform dose measurements from the low- and high-energy components of SF DECT separately. As previously mentioned, it would be very difficult and time intensive to measure the dose from SF DECT separately in a custom phantom. Also, we could not physically perform split-filter DECT scans with a 140 kVp, even in maintenance mode. For these reason, the methodology outlined in this work was chosen to best investigate SF DECT at two different tube potentials.

The importance of this work is to characterize split-filter DECT, specifically the clinically used TwinBeam DECT system to better understand what a split filter does to a polyenergetic beam based on the spectral separation, effective energy, and dose allocation. These three parameters were determined from an equivalent TwinBeam model with a 120 kVp x-ray source and a 0.05 cm Au and 0.6 mm Sn split filter. These parameters were also determined for an equivalent model with a 140 kVp x-ray source with the same split filter. Table 3.9 lists the compiled results from these two models.

Table 3.9: HVL, effective energy, mean energy, spectral separation, and dose allocation determined for each equivalent MCNP beam.

MCNP Beam	HVL (mm Al)	Effective energy (keV)	Mean energy (keV)	Spectral Separation (keV)	Dose allocation
120 kVp	8.26 ± 0.14	55.4 ± 0.91	62.8 ± 0.082	-	-
120 kVp + 0.05 mm Au	9.20 ± 0.014	59.8 ± 0.090	66.2 ± 0.10	16.5±0.04	0.62±0.03
120 kVp + 0.6 mm Sn	12.3 ± 0.027	77.7 ± 0.17	82.7 ± 0.18		
120 kVp + SF	9.60 ± 0.018	61.8 ± 0.11	69.1 ± 0.13		
140 kVp	9.67 ± 0.16	62.1 ± 1.0	68.7 ± 0.089	-	-
140 kVp + 0.05 mm Au	11.6 ± 0.017	73.1 ± 0.073	71.9 ± 0.072	21.1±0.04	0.61±0.02
140 kVp + 0.6 mm Sn	14.0 ± 0.022	89.3 ± 0.14	92.9 ± 0.15		
140 kVp + SF	12.2 ± 0.016	76.5 ± 0.099	82.4 ± 0.11		

3.5.1 HVL and spectral separation

Each equivalent model was based on inherent filtration and bowtie filter determination from HVL and profile measurements. The reported HVLs of the 120 kVp and 140 kVp beams listed in the CT scanner user manual are 8.3 mmAl and 9.5 mmAl, respectively and are within the k=2 uncertainty of the measured HVLs in this work.

The literature states that the mean energies of the low- and high-energy beams of TwinBeam split-filter are 68 keV and 86 keV, respectively [34]. Therefore, the reported spectral separation is 18 keV. This is a 8.69% difference in spectral separation compared to our calculated value. This difference in spectral separation between our calculated value and the literature reported value is most likely due to the difference in composition of the actual materials within the beam line and the modeled inherent filtration [2]. Although both the equivalent models and the Siemens SOMATOM Definition Edge have the same overall attenuating properties determined by HVL, the difference in inherent filtration material will change the actual photon spectra slightly enough to change the mean energy. In our MCNP model, the inherent filtration is strictly aluminum but the actual design of the Siemens SOMATOM Definition Edge most likely has materials such as beryllium, plastic, iron, or copper.

Several groups have investigated the spectral separation of DECT. Vilches et al. determined the spectral separation of the Siemens Flash dual-source DECT scanner which utilizes an 80 kVp and 140 kVp with 0.4 mm Sn. This dual-source has the greatest spectral separation of 43 keV [59]. Fast kVp-switching and dual-spiral with an 80 kVp and 140 kVp have also been investigated to have about a 30 keV spectral separation, which is

less than dual-source because there is no added filtration [93]. The spectral separation determined from the equivalent TwinBeam model was 17 keV, which is much less than the spectral separation of other DECT modalities. It has been established that a greater spectral separation results in more accurate DECT images [59, 61] The small spectral separation explains the low accuracy of TwinBeam DECT determined by Almeida et al. [34]. Split-filter DECT with a 140 kVp initial spectrum increased the spectral separation to 21 keV. For that reason, a split-filter DECT with 140 kVp may lead to more accurate DECT images compared to TwinBeam. The spectral separation and effective energies were determined both exiting the SF and at isocenter. It was concluded that for the 120 kVp + SF system, there was no difference in spectral separation at isocenter. Future work may involve correlating the calculated spectral separation from this work with the difference in HU of low- and high-energy images of the same scan, as HU is directly correlated to the spectra of the imaging beam.

3.5.2 Ion chamber calibration

This work investigated the effective energy of SF DECT to determine how the change in beam quality across the field effects dosimetric measurements with CT ionization chambers. When an ion chamber gets calibrated, a N_k value is provided, which is used to convert collected current to dose. The N_k value is specific to the effective energy of the beam during calibration. Therefore, the physicist is recommended to interpolate a new N_k value using the HVL of the clinical beam.

The HVL of the 120 kVp and the individual components of the split beam were used to calculate corresponding ion chamber calibration coefficients for common CT ionization chambers: a Capintec PS-033, Exradin A28, and Exradin A101. These ionization chambers were first calibrated to several moderately filter x-ray beams at the UWADCL. The calibration results are listed in Table 3.10. The calibration coefficients were then determined for the beams created in this work by interpolating to their corresponding HVLs. Table 3.11 lists the all of the resulting calibration coefficients for each of the three ionization chambers.

Table 3.10: Calibration coefficients, N_k for each of the listed ion chambers from corresponding M-series UWADCL beams.

UWADCL Beam	HVL (mm Al)	PS-033 (Gy/C)	A28 (Gy/C)	A101 (Gy/C)
M120	6.96	5.081E+07	2.276E+08	5.190E+06
M150	10.2	5.006E+07	2.274E+08	5.114E+06
M200	14.9	5.037E+07	2.283E+08	5.078E+06
% Difference		1.5%	0.3 %	2.2%

Table 3.11: Calibration coefficients, N_k for each of the listed ion chambers for each MCNP beam.

Split-filter DECT	HVL (mm Al)	PS-033 (Gy/C)	A28 (Gy/C)	A101(Gy/C)
120 kVp	8.26	5.05E+07	2.27E+08	5.15E+06
120 kVp + 0.05 cm Au	9.20	5.03E+07	2.27E+08	5.14E+06
120 kVp + 0.6 mm Sn	12.3	5.02E+07	2.28E+08	5.10E+06
120 kVp + SF	9.6	5.02E+07	2.28E+08	5.13E+06
140 kVp	9.67	5.02E+07	2.27E+08	5.13E+06
140 kVp + 0.05 cm Au	11.6	5.02E+07	2.28E+08	5.10E+06
140 kVp + 0.6 mm Sn	13.96	5.03E+07	2.28E+08	5.09E+06
140 kVp + SF	12.15	5.02E+07	2.28E+08	5.10E+06

The 0.05 mm Sn of the SF increases the effective energy by 36% within the high-energy region. This corresponds to a 1.2% difference in the calibration factor specifically for the A101 ionization chamber (Table 3.10). A101 ionization chambers measure CTDI metrics, which are used clinically to estimate CT dose. Unfortunately, CTDI metrics underestimate actual patient dose [76]. Majority of studies that have investigated CT dose, found loose agreement between simulated and measured dose values, which lead to a lax acceptable error criteria of ± 20% [94]. Although the change in beam quality is drastic across the split-beam, because of the ± 20% error criteria, no further correction is needed when using an A101 ionization chamber to measure CTDI for split-filter DECT, and the two components of the split beam do not need to be considered separately. The greatest difference in ion chamber response for the PS-033 and A28 was 0.61% and 0.12%, respectively. Although these are very small energy responses, this work established a method to determine the HVLs of split-filter DECT for proper calibration coefficient determination.

3.5.3 Dose and dose allocation

CT dose is the biggest contribution to public radiation exposure and it is suggested that 2% of all cancers in the US are caused by CT exposure [74]. Although DECT may provide better image quality compared to SECT, the dose should be equal to or less than the dose from conventional SECT. Based on the results of this study, the split filter decreases air kerma at isocenter by about 66% for the 120 kVp + SF system and 61% for the 140 kVp + SF system for the same mAs. These values were determined using simulations of

air kerma then applying the mAs-to-dose coefficients listed in Table 3.1. Unfortunately, these values only represent the total decrease in fluence due to the split-filter and not the actual difference in dose for the same image quality. According to the literature, fast kVp-switching DECT has 14-22% greater dose than conventional single-energy CT for the same image quality, this is similar for dual-source and dual-spiral [95]. On the other hand, split-filter DECT had about 14% lower dose than conventional single-energy for the same image quality based on the results of Euler et al. [44]. Euler et al. compared the objective image noise defined as the standard deviation of the CT numbers in the fat and subjective image quality of composed split-filter DECT images to conventional SECT with a retrospective study investigating contrast-to-noise ratio (CNR) of the liver [44]. Based on these findings and our results, split-filter may provide the best dose reduction of all DECT modalities for some applications in the abdomen. The point doses determined in this study are the groundwork needed to determine patient doses from SF DECT scans.

As expected, the overall dose from each component of the split beam was higher for the 140 kVp + SF model compared to the 120 kVp + SF as there were more higher energy photons. Based on the dose allocation results, it was determined that for smaller sized phantoms (20 cm diameter), the dose from the low-energy beam was 65% of the total dose for the 120 kVp + SF model, specifically. The dose allocation actually decreases to 63% for the 140 kVp + SF system. Both systems result in a 60% dose allocation for the larger 40 cm diameter phantoms. These results are much greater than the recommended dose allocation of 30% [63]. Based on this work, a 30% dose allocation is actually unachievable with split-filter DECT because the high-energy portion of the split beam contributes less

to the total dose, which is unlike the other DECT modalities. Therefore, future work investigating the optimal dose allocation for split-filter DECT needs to be investigated and this work has laid the foundation for such an investigation.

Overall, the results from this work serve as evidence to the manufacturer that it may be beneficial to perform split-filter DECT with a 140 kVp. In order to completely conclude any benefit in an increased tube potential, an investigation comparing actual DECT images created from 120 kVp + SF and 140 kVp + SF would be needed.

Chapter 4

Investigating a novel split-filter dual-energy CT technique for improving pancreas tumor visibility for radiation therapy

Chapter 3 investigated the physical characteristics of split-filter DECT and compared the results to other DECT modalities. This chapter and Chapters 5-7 investigate the limitations and clinical applications of split-filter DECT in radiation therapy through several image studies that explore the visibility of pancreas and liver tumors using TwinBeam DECT images.

The entirety of this chapter has been published in the Journal of Applied Clinical Medical Physics [96].

4.1 Introduction

Pancreatic adenocarcinoma is the fourth-leading cause of cancer death in the United States [97, 98]. Though surgery is the only established curative treatment option, 80% of patients with pancreatic cancer are not surgical candidates. Radiation therapy offers a local treatment option with recent evidence suggesting that accurately focused dose-escalated radiation therapy may increase median survival and potential for surgical resection [69, 99]. However, radiation therapy for pancreatic adenocarcinomas can be a challenge because they have poor innate contrast compared to surrounding healthy pancreatic tissue [69, 100]. For radiation therapy treatment planning, the lack of tumor contrast makes it difficult to confidently delineate the target with conventional single-energy computed tomography (SECT) even with iodine contrast. Accurate tumor delineation is crucial for successful radiation therapy [40], particularly in the pancreas where other radiation-sensitive organs are in close proximity. Recent work has shown that dose escalation can increase survival for pancreatic patients, further increasing the need to clearly visualize and accurately delineate the tumor for treatment planning [9, 101]. Fortunately, recent efforts have been dedicated to using dual-energy computed tomography (DECT) as an optimal CT modality to increase the detectability of pancreatic tumors [9–11, 23, 69, 99].

DECT is an imaging modality that utilizes two different photon spectra to image patient anatomy. Since DECT provides information about the attenuation properties of tissues at two different energies, tissues with similar density but different elemental composition can be differentiated [67]. DECT images have significant advantages over

conventional SECT specifically when imaging the abdomen; DECT applications in the abdomen include, but are not limited to, depicting small liver lesions, differentiating renal masses, and improving depiction of pancreas tumors [22]. Several studies have been published that investigate the use of DECT techniques for improving pancreas tumor contrast. In these studies, DECT offered improvements in tumor conspicuity and delineation compared to conventional 120 kVp CT [9, 11, 22, 30, 99].

A novel technique for single-source DECT was recently introduced as an additive feature to the Siemens SOMATOM Definition Edge CT scanner (Siemens Healthcare, Forchheim, Germany). The SOMATOM Definition Edge is now available with a removable gold and tin split-filter for DECT acquisition, known as TwinBeam (TwinBeam Dual Energy; Siemens). This system may offer a cost-effective solution for DECT applications in radiation therapy. The TwinBeam system is an innovative DECT modality that utilizes a split-filter to spatially separate a helical 120 kVp x-ray beam into a low- and high-energy beam along the longitudinal axis. TwinBeam allows for the low- and high-energy data of the same location in the patient to be acquired within two tube rotations. The temporal coherence between the low- and high-energy acquisition gives TwinBeam the capability to image dynamic contrast, making this modality a candidate for DECT imaging of pancreatic adenocarcinoma where iodine contrast is needed to differentiate healthy pancreatic tissue from tumor. However, in comparison to other dual-energy techniques that utilize a low-energy 80 kVp beam and high-energy 140 kVp beam, the split-filter technique of TwinBeam has inferior spectral separation [34, 35]. The effects of this limited spectral separation on image quality, specifically in the pancreas have yet to be investigated.

Though some studies have investigated the image quality of TwinBeam DECT scans [34, 47], none have investigated its utility for radiation therapy treatment planning, nor have any studies investigated the use of TwinBeam for identifying and delineating pancreatic tumors. This work investigates tumor contrast while considering the noise characteristics by calculating tumor contrast-to-noise-ratios (CNR). CNR offers a more comprehensive view of image quality as both contrast and noise play a role in tumor segmentation during the treatment planning process. To the authors' knowledge, there has not been any study to date that investigates the contrast between healthy pancreatic parenchyma and the entire gross target volume (GTV), rather a selected subsection of the GTV through a small region of interest (ROI) within the tumor. The goal of this work is to quantitatively determine if the split-filter DECT technique of TwinBeam can improve the contrast and the CNR of pancreatic GTVs with the long-term goal of improving tumor delineation for radiation therapy treatment.

4.2 Materials and methods

4.2.1 Patients and CT simulation

Following Institutional Review Board approval, a retrospective study was performed for patients who were treated for pancreatic adenocarcinoma at our institution using radiation therapy between June 2016 and November 2017. The study population included 20 patients (13 males, 7 females) with histologically proven pancreatic adenocarcinoma (mean age 69.6 years: range: 50-86, mean weight 90.3 kg: range 50.8-146.1). Biopsy

results were determined surgically or with fine needle aspiration. The study population included stage IB-IV pancreatic adenocarcinomas that were resectable, borderline resectable, or unresectable. Two tumors were located in the tail of the pancreas and 18 tumors were located in the head of the pancreas with the longest dimension ranging from about 1.5 – 4 cm. All patients were simulated on the Siemens SOMATOM Definition Edge CT scanner (Siemens Healthcare, Forchheim, Germany) for radiation therapy planning purposes. Patients were imaged during maximum inhalation breath hold guided using the Varian RMPTM system (Real-time Position Management, Varian Medical Systems, Palo Alto, CA) to minimize motion, Vac-LokTM (CIVCO Radiotherapy) cushions were used as immobilization devices. Each patient received IV nonionized iodine contrast medium, OMNIPAQUE^{TM}, during CT simulation and two phases of contrast were imaged. All patients had both the pancreatic and portal venous phase scans, except for one patient who only received a portal venous phase scan. The delays were customized on a patient-per-patient basis using a bolus tracking technique. The average delay was 32 seconds (ranged of 30.5-40 seconds) and 62 seconds (range of 54-70 seconds) for the start of the pancreatic and portal venous phase scans, respectively. The average scan time was 10 seconds with the pancreas tumor located in the center of the scan. Therefore, the center of the tumor was imaged roughly 37 and 67 seconds after iodine contrast injection for the pancreatic and portal venous phase scans, respectively.

Due to the added beam filtration of the TwinBeam system, roughly two-thirds of the x-ray beam is filtered prior to reaching the patient. As a result, large tube currents are required to achieve $CTDI_{vol}$ similar to conventional SECT acquisitions. Due to tube

current limitations, patient size, and scan length requirements for individual patients, the imaging protocol varied from patient to patient. The machine effective mAs ranged between 1350 and 1500 mAs. The automatic tube current modulation was not used, and the $CTDI_{vol}$ ranged from 21.6 to 33.6 mGy. Images were acquired with a pitch of 0.3 to 0.45, a rotation time of either 0.5 or 1 second per rotation and reconstructed at a slice thickness of 3 mm.

4.2.2 Image reconstruction

The Siemens Syngo.via software was used to reconstruct virtual monoenergetic images, called Monoenergetic Plus images, as well as images that mimic the appearance of conventional single-energy 120 kVp images, called mixed images. A mixed image is a weighted sum with of the low- and high-energy datasets to create an image with HU values equivalent to a SECT image at 120 kVp and is therefore referred to as a 120 kVp-equivalent image. On the other hand, the virtual monoenergetic images (VMIs) used in this study depict how an object would appear if it was imaged using a monoenergetic x-ray source and are reconstructed using a novel monoenergetic algorithm (nMERA) [47]. The possible reconstructed energies for a VMI range from 40 keV to 190 keV. For this study, VMIs were reconstructed at energies from 40-90 keV at 5 keV increments to investigate the change in contrast and CNR as a function of energy. Based on this preliminary analysis, the remainder of our study focused on two VMI energies: 40 keV and 57 keV. The VMI at 40 keV was chosen because it demonstrated the greatest CNR for pancreatic tumors, and the VMI at 57 keV was chosen based on physician initial preference. Due to the increase

in noise for low-energy VMIs, the role of iterative reconstruction on DECT images was investigated. In addition to filtered back projection (FBP) with the D30 reconstruction kernel, the latest generation of Siemens iterative reconstruction called Advanced Modeled Iterative Reconstruction (ADMIRE; Siemens Healthcare, Forchheim, Germany) using the Q30 reconstruction kernel was also used. ADMIRE is a model-based iterative reconstruction algorithm designed to decrease noise as well as metal and cone beam image artifacts by analyzing the data in both the Fourier and image domain [47, 98]. ADMIRE was applied to the low- and high-energy datasets individually at a strength of 2 (ADMIRE 2) out of a maximum strength of 5; level 2 represents a low to medium level of noise suppression due to iterative reconstruction. In summary, two raw datasets were acquired for each patient: a pancreatic contrast phase and a portal venous contrast phase. At each contrast phase, the raw data was reconstructed using two reconstruction methods, FBP and ADMIRE 2. For each reconstruction method, three dual-energy images were generated: a mixed 120 kVp-equivalent image, a VMI at 57 keV image, and a VMI at 40 keV image (Figure 4.1).

4.2.3 Contrast and contrast-to-noise-ratio analysis

All dual-energy images were evaluated using the MIMvista software (MIM Software Inc. Cleveland, Ohio). Three ROIs were created to evaluate tumor contrast and CNR. This study assessed the whole GTV, as defined by an experienced radiation oncologist on the pancreatic phase VMIs at 57 keV. The attenuation of healthy pancreatic parenchyma was measured using an ROI placed near the GTV that avoided stents, macroscopic vessels,

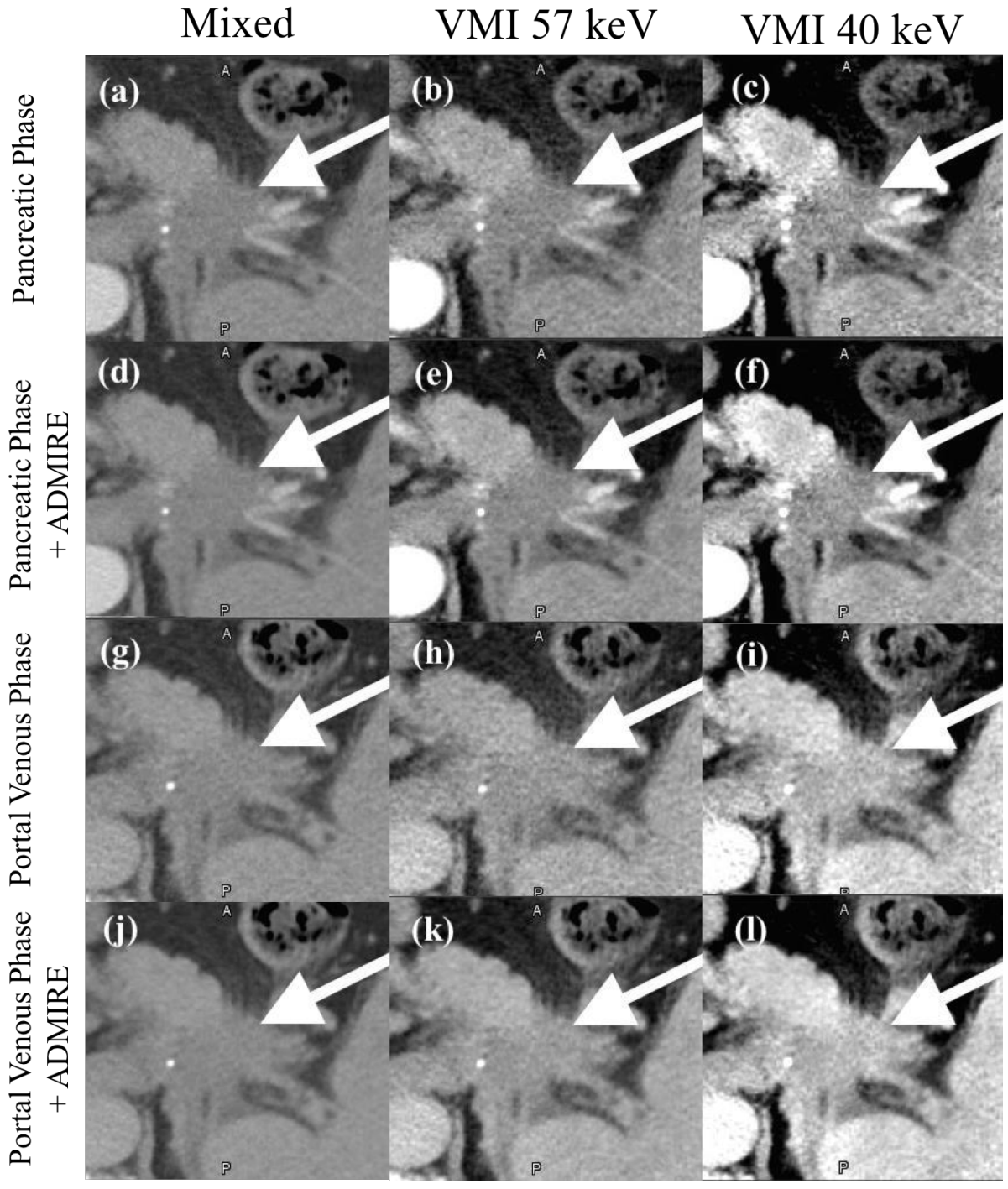

Figure 4.1: Images from the pancreatic (a-f) and portal venous phase (g-l) with FBP (a-e and g-i) and ADMIRE 2 (d-f and j-l). The arrow indicates the location of the GTV.

and the pancreatic duct. The placement of the GTV and pancreatic parenchyma ROI contours for a single patient is shown in Figure 4.2.

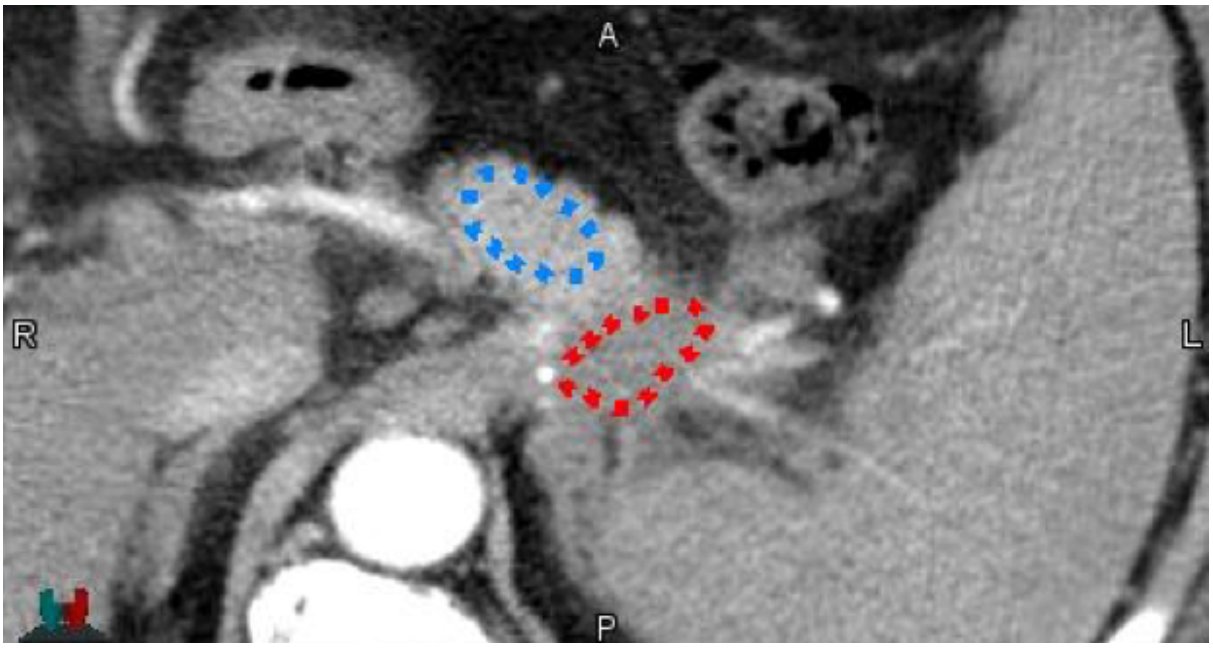

Figure 4.2: VMI at 57 keV with the pancreatic adenocarcinoma GTV contour in red and the normal pancreas tissue contour in blue.

The mean and standard deviation of the CT numbers in the GTV and the ROI in the healthy pancreatic parenchyma were calculated for each image dataset. Image noise was assessed with the standard deviation of a ROI located in the erector spinae muscle to avoid the impact of tumor heterogeneity on image noise. The size of this ROI was consistent at 10 mm^2 among all patients. GTV contrast was calculated for each image dataset as

$$GTV_{contrast} = HU_{pancreas} - HU_{GTV}, \tag{4.1}$$

where $HU_{pancreas}$ is the mean CT number of the ROI in healthy pancreatic parenchyma and HU_{GTV} is the mean CT number of the GTV. GTV CNR was also calculated for each

image dataset as

$$\mathrm{GTV}_{CNR} = \frac{\mathrm{HU}_{\mathrm{pancreas}} - \mathrm{HU}_{\mathrm{GTV}}}{\sigma}, \tag{4.2}$$

where σ is the standard deviation of CT numbers of the ROI located in the erector spinae muscle. Contrast and CNR improvement provided by VMIs in comparison to mixed 120 kVp-equivalent images was calculated.

Differences in contrast and CNR among all reconstructed datasets for a single dual-energy acquisition were statistically analyzed using analysis of variances (ANOVA). Statistical differences in contrast and CNR between the mixed 120 kVp-equivalent images and the VMIs reconstructed at 57 keV or 40 keV were analyzed using paired t-tests. A $P<.05$ was determined as statistically significant. This study analyzed a total of 39 dual-energy acquisitions, acquired from 20 patients.

4.3 Results

To determine the reconstruction energy for the VMIs that produced the greatest GTV contrast and CNR, VMIs were reconstructed at energies ranging from 40-90 keV at 5 keV increments (Figure 4.3). Among all patients, the reconstruction energy at 40 keV produced the greatest contrast and CNR. Figure 4.4 shows the GTV contrast, noise, and CNR from VMIs at energies ranging from 40-90 keV reconstructed from FBP pancreatic phase data. The remainder of our results focus on comparing VMIs at 40 keV and 57 keV against mixed 120 kVp-equivalent images, which were used to represent conventional SECT images.

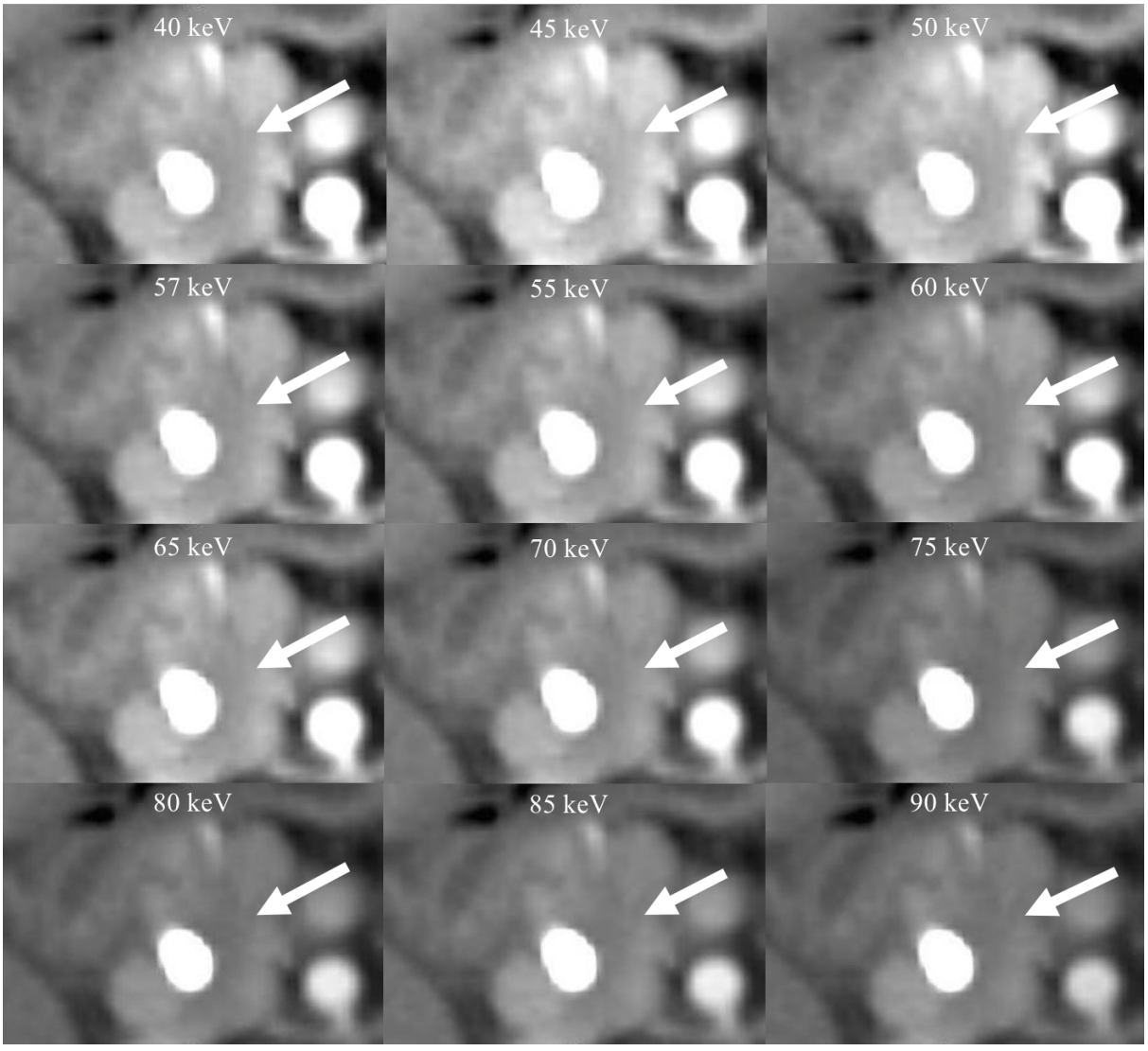

Figure 4.3: VMIs reconstructed at 40-90 keV created from the FBP pancreatic phase data. The arrow indicates the location of the GTV.

4.3.1 Contrast

The mean contrast values for the mixed 120 kVp-equivalent images, VMIs at 57 keV, and VMIs at 40 keV for both contrast phases are shown in Figure 4.5. The mean ± standard deviation (SD) GTV contrast for the pancreatic phase datasets using FBP was 15.9 ± 19.9 HU for the mixed 120 kVp-equivalent images. The VMIs at 57 keV increased the

GTV contrast to 40.7 ± 27.7 HU, which represents a 219% increase in contrast (P=.0025). The VMIs at 40 keV increased the GTV contrast to 93.7 ± 49.6 HU for a mean contrast improvement of 665% compared to the mixed 120 kVp-equivalent images (P<.0001). The mean ± SD GTV contrast for the portal venous phase datasets using FBP was 6.01 ± 15.2 HU, 16.4 ± 20.9 HU, and 41.5 ± 34.9 HU for the mixed 120 kVp-equivalent images, VMIs at 57 keV, and the VMIs at 40 keV, respectively (P<.0001). The GTV contrast was greater for all pancreatic phase images when compared to the portal venous phase images (P<.0001). On average, images reconstructed with ADMIRE had slightly greater contrast, but this improvement was statistically insignificant (P=.8717). The mean ± SD GTV contrast for the pancreatic and portal venous phase datasets reconstructed with the FBP or ADMIRE and P values are displayed in Table 4.1.

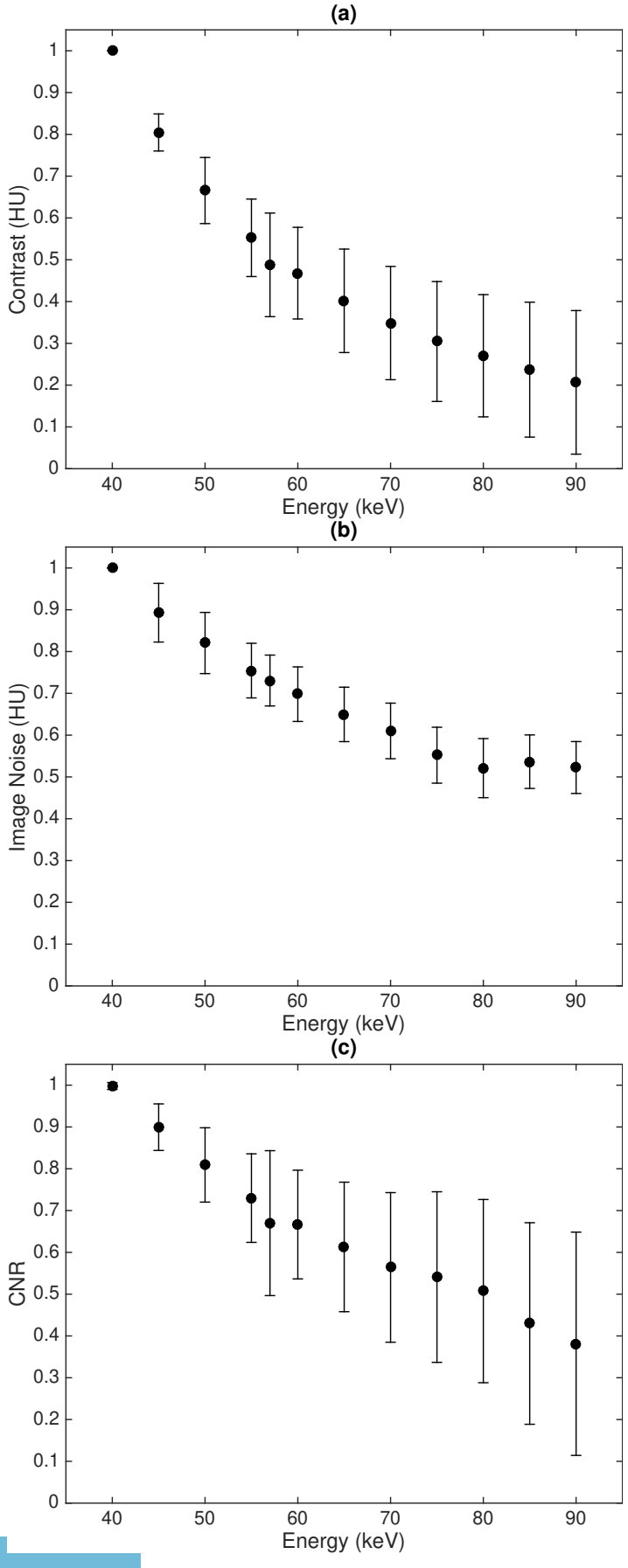

Figure 4.4: The GTV contrast (a), image noise (b), and CNR (c) for VMIs at energies ranging from 40-90 keV normalized to the values at 40 keV. These VMIs were reconstructed from FBP pancreatic phase data. Error bars represent the standard deviation amongst all patients.

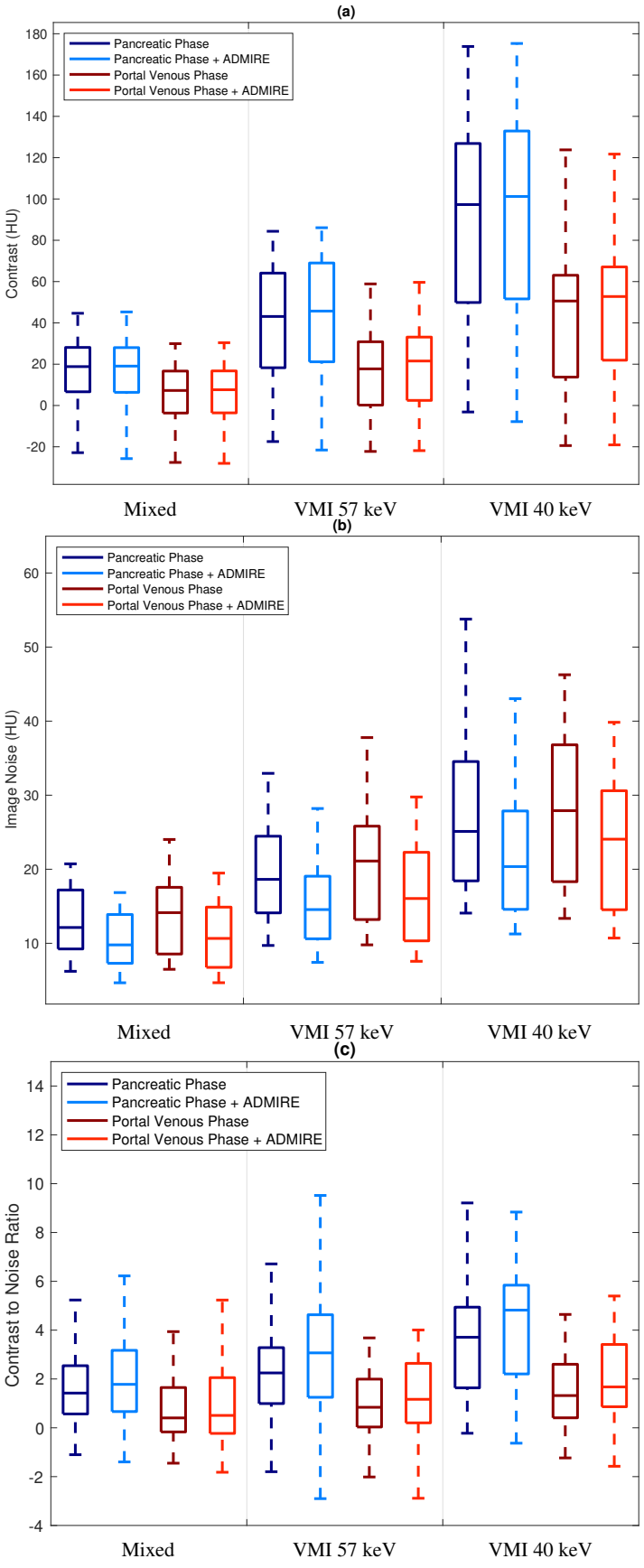

Figure 4.5: Box plots of GTV contrast (a), image noise (b), and CNR (c) from both contrast phases with FBP or ADMIRE 2 reconstructed into mixed 120 kVp-equivalent images (Mixed), virtual monoenergetic images at 57 keV (VMI 57 keV), and at 40 keV (VMI 40 keV).

Table 4.1: GTV contrast, image noise, and CNR from both contrast phases with FBP or ADMIRE 2 reconstructed into mixed 120 kVp-equivalent images (Mixed), virtual monoenergetic images at 57 keV (VMI 57 keV), and at 40 keV (VMI 40 keV).

	Mixed	VMI 57 keV	VMI 40 keV	*P* value[a]	*P* value[b]	*P* value[c]
Contrast (HU)						
Pancreatic Phase	15.9 ± 19.9	40.7 ± 27.7	93.7 ± 49.6	2.50E-03	1.12E-07	1.72E-04
Pancreatic Phase + ADMIRE	15.8 ± 19.9	43.8 ± 28.2	96.5 ± 50.4	1.05E-03	6.94E-08	1.99E-04
Portal Venous Phase	6.01 ± 15.2	16.4 ± 20.9	41.5 ± 34.9	0.0887	2.53E-04	1.08E-02
Portal Venous Phase + ADMIRE	6.23 ± 15.2	19.3 ± 19.7	46.7 ± 31.9	0.0281	1.54E-05	2.95E-03
Image Noise (HU)						
Pancreatic Phase	13.2 ± 4.38	20.3 ± 8.45	28.0 ± 12.5	1.90E-03	1.35E-05	0.0278
Pancreatic Phase + ADMIRE	10.6 ± 3.69	15.8 ± 6.09	22.2 ± 9.02	2.07E-03	4.78E-06	0.013
Portal Venous Phase	13.4 ± 5.17	20.6 ± 8.90	27.7 ± 10.6	4.40E-03	6.50E-06	0.0315
Portal Venous Phase + ADMIRE	10.9 ± 4.43	16.5 ± 7.03	23.5 ± 9.37	5.68E-03	7.81E-06	0.0155
CNR						
Pancreatic Phase	1.37 ± 2.05	2.41 ± 2.15	3.86 ± 2.78	0.14	2.61E-03	0.0671
Pancreatic Phase + ADMIRE	1.69 ± 2.63	3.16 ± 2.83	4.94 ± 3.61	0.105	2.37E-03	0.0856
Portal Venous Phase	0.674 ± 1.65	1.15 ± 1.80	1.85 ± 2.30	0.402	0.075	0.292
Portal Venous Phase + ADMIRE	0.822 ± 2.11	1.52 ± 2.22	2.42 ± 2.72	0.326	0.0479	0.262

All values are giving in mean ± SD except for *P* values
[a] paired t-test comparing columns Mixed and VMI 57 keV
[b] paired t-test comparing columns Mixed and VMI 40 keV
[c] paired t-test comparing columns VMI 57 keV and VMI 40 keV

4.3.2 Noise

The mean ± SD image noise of the mixed 120 kVp-equivalent images, VMIs at 57 keV, and VMIs at 40 keV with the FBP was 13.2 ± 4.38 HU, 20.3 ± 8.45 HU, and 28.0 ± 12.5 HU, respectively, averaged over the pancreatic and portal venous phase datasets (P<.0001). There was no difference in image noise between the two contrast phases (P=.919). The image noise was 52% higher for the VMIs at 57 keV and 110% higher for VMIs at 40 keV compared to the mixed 120 kVp-equivalent images. ADMIRE 2 decreased image noise to 10.6 ± 3.69 HU, 15.8 ± 6.09 HU, and 22.2 ± 9.02 HU for the mixed 120 kVp-equivalent images, VMIs at 57 keV, and VMIs at 40 keV, respectively (P<.0001). ADMIRE 2 decreased image noise by 19.3 ± 4.87% throughout all images.

4.3.3 Contrast-to-noise ratio

The mean CNR for the mixed 120 kVp-equivalent images and the VMIs reconstructed at 57 keV and 40 keV for both the pancreatic and portal venous phases are shown in Figure 4.5. The mean ± SD for GTV CNR for the pancreatic phase datasets reconstructed with FBP was 1.37 ± 2.05, 2.41 ± 2.15, and 3.86 ± 2.78 for the mixed 120 kVp-equivalent images, VMIs at 57 keV and VMIs at 40 keV, respectively (P =.0057). The pancreatic phase VMIs with the FBP at 57 keV and 40 keV increased CNR by a mean of 109% and 270%, respectively, compared to the mixed 120 kVp-equivalent images (P=.140, P=.00261). ADMIRE further improved CNR for all images. For the pancreatic phase, ADMIRE 2 increased CNR in the VMIs at 40 keV from 3.86 ± 2.78 to 4.94 ± 3.61 (P>.0001).

4.4 Discussion

In this study, TwinBeam was investigated to improve the delineation of pancreatic adenocarcinoma for radiation therapy treatment planning. VMIs acquired using TwinBeam were compared against mixed 120 kVp-equivalent images, which served as a baseline since these images represent conventional single-energy CT images. Entire pancreas GTVs were analyzed rather than small ROIs placed within the tumors because the contrast and CNR calculated from a ROI do not represent the detectability of the entire tumor volume. Significantly greater GTV contrast and CNR was achieved in the low-energy VMIs, with the greatest CNR occurring at the lowest reconstructed energy of 40 keV. CNR improvements of up to 500% were found from the VMIs at 40 keV when compared to the mixed 120 kVp-equivalent images. As expected, the noise of the VMIs increased with a decrease in energy and was the greatest for the VMIs at 40 keV. The use of iterative reconstruction (ADMIRE) at a strength of 2 decreased noise by about 20% throughout all images, and further improved the CNR of the VMIs. This is consistent with other published data which demonstrated that low-contrast detectability is increased by decreasing noise of DECT images using iterative reconstruction [39, 47, 98]. This data suggests that the best tumor visibility can be achieved by contouring on VMIs at 40 keV with ADMIRE, though this may still depend on physician preference, window and leveling. While increasing the strength of iterative reconstruction may further improve CNR [102], further investigation into the effects of ADMIRE on edge detection and tumor delineation is needed. In addition, further investigation is needed to determine the impact of increased CNR in VMIs on the accuracy of tumor delineation. DECT images were acquired at two

different contrast phases, pancreatic and portal venous. The pancreatic phase demonstrated greater GTV contrast and CNR compared to the datasets acquired during the portal venous phase, suggesting that the pancreatic phase is superior for tumor delineation. This agrees with published data [99, 100] and is expected because the timing of the pancreatic phase is designed to maximize tumor-to-parenchymal attenuation differences. DECT further improved the contrast and CNR for both contrast phases; however, the improvement for both metrics was greater for the pancreatic phase. The mean increase in CNR for the VMIs at 40 keV compared to the mixed 120 kVp-equivalent images was 8% greater for the pancreatic phase than the portal venous phase. This demonstrated that the TwinBeam system can exploit subtle differences in iodine uptake better than conventional single-energy imaging.

While the use of TwinBeam DECT for imaging pancreatic adenocarcinomas has not been previously investigated, others have reported improvements in pancreatic tumor contrast and CNR using a fast-kVp switching and dual-source DECT [11, 35, 47]. Patel et al. calculated contrast and CNR values from VMIs using a fast-kVp switching DECT. The contrast values from Patel et al. were higher than the contrast values calculated with TwinBeam for comparable VMIs. This discrepancy in contrast is likely attributed to differences in calculation techniques. Patel et al. calculated contrast values using a small ROI optimally placed inside the tumor, while our study calculated contrast using the entire GTV. Incorporating the entire GTV resulted in lower contrast values, however these values are more relevant for radiation therapy, where the entire tumor volume must be accurately segmented. Also, the image noise from TwinBeam (27.9 ± 11.5 HU for VMIs

at 40 keV) was lower than the values reported by Patel et al. (58.9 ± 16.7 HU for the VMIs at 45 keV). The reconstruction algorithm used to create the VMIs from TwinBeam data is a novel monoenergetic reconstruction algorithm (nMERA) that performs regional spatial frequency-based recombination of high attenuation at low photon energy images and lower image noise at higher photon energies to obtain the best possible image noise level. This algorithm is different than the standard monoenergetic reconstruction algorithm (sMERA) [47]. The difference in noise characteristics between the DECT systems results in different VMI energies producing the greatest CNR. The VMI energy that produced the greatest CNR was 40 keV for the TwinBeam system, while the optimal energy varied by patient (52.5 ± 7.7 keV) for the kVp-fast switching technique [11]. Overall, comparable values of CNR were found between TwinBeam and fast-kVp switching DECT techniques, especially at the optimal energy for each system (3.86 ± 2.78 for TwinBeam and 3.09 ± 2.0 for kVp fast-switching).

Frellesen et al. also investigated contrast and CNR values from VMIs for pancreatic tumors but for a dual-source DECT technique. Frellesen et al. also used a small ROI placed within the pancreatic adenocarcinoma, rather than the entire GTV as used in this study. In comparison to their work, the image noise of mixed 120 kVp-equivalent images from TwinBeam with ADMIRE 2 (10.7 ± 4.02 HU) is comparable to image noise values from dual-source DECT (10.69 ± 3.57 HU) [47]. TwinBeam demonstrated inferior CNR values for pancreatic adenocarcinomas when compared to the dual-source technique for VMIs at 40 keV calculated with nMERA (4.94 ± 3.61 for TwinBeam and 26.29 ± 16.83 for dual-source). This discrepancy in CNR may be attributed to the difference in

calculating contrast between using a small ROI and the entire GTV. This comparison is significant as it quantifies CNR values that are achievable with the limited spectral separation inherent in the TwinBeam system when compared to DECT systems with greater spectral separation. This work also demonstrated comparable image noise of mixed 120 kVp-equivalent images between TwinBeam and dual-source systems. This comparison highlights that in addition to the spectral separation between different dual-energy CT systems, the gain in CNR also depends on the algorithm used to generate monoenergetic images.

4.5 Conclusion

TwinBeam is a new single-source DECT, which may aid in tumor delineation for radiation therapy treatment planning. TwinBeam shows promise for DECT simulations, which aim to capture a dynamic bolus of contrast. This work demonstrates that VMIs reconstructed using the TwinBeam system provide greater CNR between pancreatic tumors and healthy pancreatic parenchyma than virtual single-energy CT images. For pancreatic tumors which are historically difficult to differentiate, this increase in CNR may increase the ability to accurately segment these tumors for radiation therapy treatment planning, which has the potential to lead to more effective radiation therapy treatment. However, definitive improvements in tumor delineation cannot be stated without further investigation of pancreas GTV segmentation reproducibility and accuracy.

Chapter 5

Investigating a novel split-filter dual-energy CT technique for improving liver tumor visibility for radiation therapy

The entirety of this chapter has been published in the Journal of Applied Clinical Medical Physics [103].

5.1 Introduction

Liver cancer is one of the leading causes of cancer-related deaths in the United States. Unfortunately, at the time of diagnosis, the majority of cases are advanced and not candidates for curative treatment. Surgical resection is the established curative treatment but

because of the extent of the majority of liver tumors and their venous involvement at diagnosis, they are unresectable. Radiation therapy is the most common localized treatment option for unresectable liver cancers, and recent studies have shown that dose-escalated stereotactic body radiotherapy (SBRT) improves local control and may decrease tumor size for resection [24]. However, dose-escalated SBRT requires precision targeting which can be challenging due to inaccurate liver tumor delineation on conventional computed tomography (CT) images [24]. Several studies have demonstrated that dual-energy CT (DECT) greatly improves the delineation and conspicuity of liver tumors [7, 22].

DECT is the acquisition of two 3-dimensional attenuation datasets using both a low- and high-energy photon spectra during a single CT protocol. The low and high energy spectra are commonly achieved through fast kVp switching, two sequential scans, dual-layer detector, or two x-ray sources. The low- and high- energy spectra are also achievable by placing filters within the beam to alter the mean energy of the spectra. DECT allows for the differentiation of tissues with the same density but different elemental composition. DECT has significant advantages over conventional SECT, specifically when imaging the abdomen [22]. When imaging the liver, low-energy images created from sequential scanning and fast kVp-switching DECT have been shown to increase iodine conspicuity and increase contrast of hyper-vascular liver tumors, including hepatocellular carcinomas (HCC) and metastases [7, 70, 71, 104].

When considering the type of DECT modality, greater spectral separation results in better tissue differentiation, and greater temporal coherence between the low- and high-energy acquisitions reduces the impact of artifacts for dynamic contrast imaging.

In addition to the previously mentioned techniques, single-source DECT can also be achieved using a split-filter technique available on the Siemens SOMATOM Defintion Edge CT scanner (Siemens Healthcare, Forchheim, Germany). The Edge has an acquisition technique known as TwinBeam which introduces a gold and tin split-filter for DECT acquisition. TwinBeam is a cost-effective and innovative DECT system with high temporal coherence compared to other DECT modalities such as Dual Spiral. The low- and high-energy datasets are acquired within two tube rotations making this modality applicable for dynamic contrast imaging. Therefore, TwinBeam may also be beneficial for abdominal cancer imaging since studies have shown that two-phase imaging increases the detection of liver tumors [105]. However, a disadvantage of TwinBeam is a lower spectral separation and, consequently, an inferior ability to differentiate tissues in comparison to other DECT techniques [7, 106, 107]. DECT techniques that utilize a low-energy 80 kVp and high-energy 140 kVp beams have been shown to increase liver tumor detection, but there has not been any study investigating the benefits of TwinBeam DECT on liver tumor delineation for radiation therapy applications. Much like a recent study that investigated the delineation of pancreas tumors using TwinBeam, this work investigates the gross target volume (GTV) contrast and contrast-to-noise ratio (CNR) [96]. This work investigates several types of liver tumors, unlike recent DECT studies that have solely investigated hypo- or hyper-vascular liver tumors [7, 24, 70, 71, 105]. Liver metastases, hepatocellular carcinomas (HCC), and cholangiocarcinomas are all included for investigation in this work. The goal of this work is to quantitatively determine if TwinBeam DECT can improve the contrast and CNR of liver tumors, in comparison to conventional

single-energy CT imaging methods, with the long-term goal of improving the delineation of these tumors for radiation therapy treatment planning purposes.

5.2 Methods

5.2.1 Patient population and CT simulation

Patient information was collected for this study after Institutional Review Board approval for patients who received dual-energy imaging at CT simulation for radiation therapy at our institution between June 2016 and August 2018. Of the 20 patients with liver cancer that were included in this study, 14 were male and 6 were female. The mean ± SD (range) of age was 67.1 ± 10 years: (39-83) year. The mean ± SD (range) of weight was 82.5 ±12 (56.8-107.9) kg. On the basis of either histopathologic analysis or imaging follow up, 6 tumors were diagnosed as intrahepatic cholangiocarcinoma, 10 as metastatic liver cancer, and 4 as hepatocellular carcinoma. The study population included Stage I-IV liver cancer and Stage IV cancer of the esophagus, colon, and rectum that metastasized to the liver. The longest tumor dimension ranged from 1-14 cm.

The image acquisition has been thoroughly described in a previous study investigating pancreas tumors [96]. For this study, all patients were imaged with a dual-phase imaging protocol. The arterial and venous phase scans were acquired using patient-specific delays based on automatic bolus tracking of the abdominal aorta. Once the iodinated contrast medium was administered, a 15 seconds timer initiated the monitoring of mean HU within the descending abdominal aorta. Once the threshold of 75 HU was reached, the set delay

times were adjusted based on the duration of each scan so that the center of each scan was 6 and 16 seconds post trigger for the arterial and portal venous phase, respectively. The effective mAs for the scans ranged between 1350 and 1500 mAs. Automatic tube current modulation was not used, and the $CTDI_{vol}$ ranged from 20.06 to 27.73 mGy. Images were acquired with a pitch ranging from 0.25 to 0.45, a rotation time of either 0.5 or 1 second per rotation, and reconstruction slice thickness of 3 mm. The arterial and venous phase datasets were acquired for all patients with the exception of one where only the venous phase was acquired.

Prior to radiation treatment planning, all patients were simulated on the Siemens SOMATOM Definition Edge with TwinBeam during maximum inhalation breath hold using the Varian RPMTM guided system (Real-time Position Management, Varian Medical Systems, Palo Alto, CA) to minimize motion. Vac-LokTM (CIVCO Radiotherapy) cushions were used as immobilization devices. All patients were scanned with a dual-phase imaging protocol with the same amount of OMNIPAQUE^{TM} IV nonionized iodine contrast medium regardless of patient weight. A bolus tracking technique was used to achieve the appropriate delay times.

5.2.2 Image reconstruction

Each raw dataset was reconstructed using the Siemens iterative reconstruction algorithm, ADMIRE, at a strength of 2 out of 5. ADMIRE 2 was used because it has shown to decrease image noise by 20% and is preferred strength by clinicians [96]. A mixed 120 kVp-equivalent image, a virtual monoenergetic image (VMI) at 57 keV, and a VMI

at 40 keV were then generated for each phase, for a total of 6 different image sets for each liver tumor case (Figure 5.1). The VMIs at 57 keV and 40 keV were generated using the Siemens Monoenergetic + application as opposed to the tradition monoenergetic reconstruction.

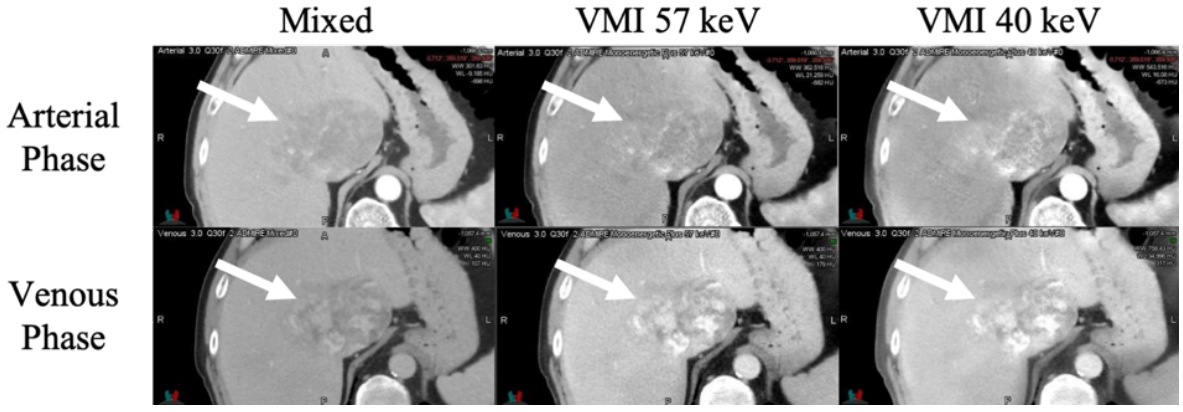

Figure 5.1: Mixed 120 kVp-equivalent image, virtual monoenergetic image at 57 keV (VMI 57 keV), and VMI at 40 keV from the arterial and venous phase, illustrating the six datasets analyzed for each patient. The arrow indicates the location of the GTV.

5.2.3 Contrast and contrast-to-noise ratio

The MIMvista software (MIM Software Inc. Cleveland, Ohio) was used to analyze each image. The entire liver gross target volume (GTV) was segmented by an experienced radiation oncologist on the arterial phase VMI at 57 keV, similar to what is done for radiation treatment planning at our institution. To investigate liver tumor GTV contrast, the surrounding healthy liver tissue was assessed using a nearby region of interest (ROI) placed within a homogenous region of healthy liver parenchyma avoiding any vessels and bile ducts. A 10 mm^2 ROI placed within a homogeneous region of the erector spinae muscle was used to assess image noise. GTV contrast was calculated as the absolute

difference in HU between the healthy liver parenchyma and GTV,

$$\mathrm{GTV}_{contrast} = |\mathrm{HU}_{\mathrm{liver}} - \mathrm{HU}_{\mathrm{GTV}}|. \tag{5.1}$$

GTV contrast was divided by the standard deviation of the ROI located in the erector spinea muscle to calculate GTV CNR,

$$\mathrm{GTV}_{CNR} = \frac{|\mathrm{HU}_{\mathrm{liver}} - \mathrm{HU}_{\mathrm{GTV}}|}{\sigma}. \tag{5.2}$$

The absolute contrast difference was used to calculate GTV contrast and CNR in order to analyze hypo-attenuating and hyper-attenuating liver tumors using the same methodology.

MATLAB was used for all statistical analyses. Variance component analysis (ANOVA) was used to assess the difference in contrast, noise, and CNR among the three different DECT images. ANOVA is used to determine whether a responsible variable (contrast, noise, or CNR) varies among different groups (mixed, VMI 57 keV, and VMI 40 keV) by returning a resulting P value. The difference in GTV contrast and CNR between the mixed 120 kVp-equivalent images and VMIs was analyzed using paired t-tests. Statistical significance was determined using a P value less than 0.05.

5.3 Results

5.3.1 Absolute contrast

Table 5.1 lists the mean liver GTV contrast from the mixed 120 kVp-equivalent images, VMIs at 57 keV, and VMIs at 40 keV for both arterial and venous phases. The mean ± standard deviation (SD) GTV contrast for the arterial phase and venous phase from all datasets was 12.1 ± 10.0 HU and 19.5 ± 13.4 HU for the mixed 120 kVp-equivalent images, respectively. The VMIs at 57 keV had a greater GTV contrast of 21.5 ± 15.4 HU and 30.9 ± 18.7 HU for the arterial and venous phase respectively, representing a 77% and 58% increase (P=.04 and .03). The VMIs at 40 keV showed the greatest GTV contrast of 43.1 ± 32.3 HU and 54.3 ± 32.6 HU for the arterial and venous phase respectively, which represent a 255% and 179% increase from the mixed 120 kVp-equivalent images (P<.001). Although on average the venous phase showed the greatest GTV contrast, some cases had a greater GTV contrast during the arterial phase.

Table 5.1: Mean ± SD (Range) GTV absolute contrast, image noise, and CNR of all cases from both contrast phases with ADMIRE 2 reconstructed mixed 120 kVp-equivalent images (Mixed), virtual monoenergetic images at 57 keV (VMI 57 keV), and at 40 keV (VMI 40 keV).

	Mixed	VMI 57 keV	VMI 40 keV	P value[a]	P value[b]	P value[c]
Contrast (HU)						
Arterial Phase + ADMIRE	12.1 ± 10.0	21.5 ± 15.4	43.1 ± 32.3	0.039	0.000	0.013
Venous Phase + ADMIRE	19.5 ± 13.4	30.9 ± 18.7	54.3 ± 32.6	0.033	0.000	0.008
Images Noise (HU)						
Arterial Phase + ADMIRE	8.1 ± 1.6	12.4 ± 2.0	17.5 ± 2.7	0.000	0.000	0.004
Venous Phase + ADMIRE	8.4 ± 1.0	13.0 ± 1.5	18.5 ± 2.2	0.000	0.000	0.000
CNR						
Arterial Phase + ADMIRE	1.6 ± 1.5	1.7 ± 1.4	2.4 ± 1.7	0.798	0.131	0.141
Venous Phase + ADMIRE	2.4 ± 1.7	2.4 ± 1.5	2.9 ± 1.8	0.977	0.307	0.485

All values are giving in mean ± SD except for P values
[a] paired t-test comparing columns Mixed and VMI 57 keV
[b] paired t-test comparing columns Mixed and VMI 40 keV
[c] paired t-test comparing columns VMI 57 keV and VMI 40 keV

5.3.2 Noise

There was no statistical difference in noise between the arterial and venous phase across all images (P>.05). The mean ± SD image noise of the mixed 120 kVp-equivalent images, VMI at 57 keV, and VMIs at 40 keV was 8.1 ± 1.6 HU, 12.7 ± 2.0 HU, and 18.0 ± 2.7 HU, respectively (P<.001). Image noise was about 50% higher for the VMIs at 57 keV and 120% higher for the VMIs at 40 keV compared to the mixed 120 kVp-equivalent images.

5.3.3 Contrast-to-noise ratio

The mean ± SD of GTV CNR across all tumor cases investigated are listed in Table 5.1. The arterial phase datasets showed an 8% and 50% increase in mean GTV CNR for the VMIs at 57 keV and 40 keV compared to the from mixed 120 kVp-equivalent. This gain in CNR was statistically insignificant (P=.80, P =.13). For the venous phase datasets, there was no statistical difference in GTV CNR between the mixed 120 kVp-equivalent images and VMIs at 57 keV (2.4 ± 1.7 and 2.4 ± 1.5). There was however a 24% increase in GTV CNR from the mixed 120 kVp-equivalent images to the VMIs at 40 keV (P=.31).

Although there was no statistical difference in mean GTV CNR, there were cases where the VMIs showed much greater GTV CNR compared to the mixed 120 kVp-equivalent images. Figure 5.2 and 5.3 show two specific cases where the VMIs provided gain in GTV CNR. For the arterial phase of case 1, the GTV CNR was increased from 0.85 to 3.41 and 6.00 for VMI at 57 keV and 40 keV compared to the mixed 120 kVp-equivalent image. For the venous phase of case 2, the GTV CNR was increased from 1.97 to 2.61 and 3.78 for VMI at 57 keV and 40 keV compared to the mixed 120 kVp-equivalent image.

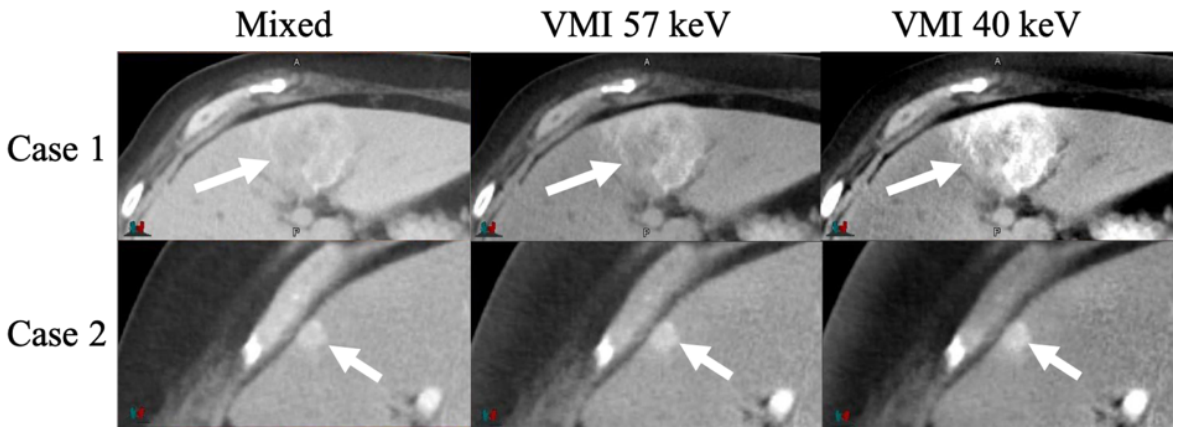

Figure 5.2: Mixed, VMI at 57 keV, and VMI at 40 keV of two tumor cases that showed the greatest tumor contrast during the arterial phase (Case 1) and during the venous phase (Case 2). The arrow indicated the location of the tumor.

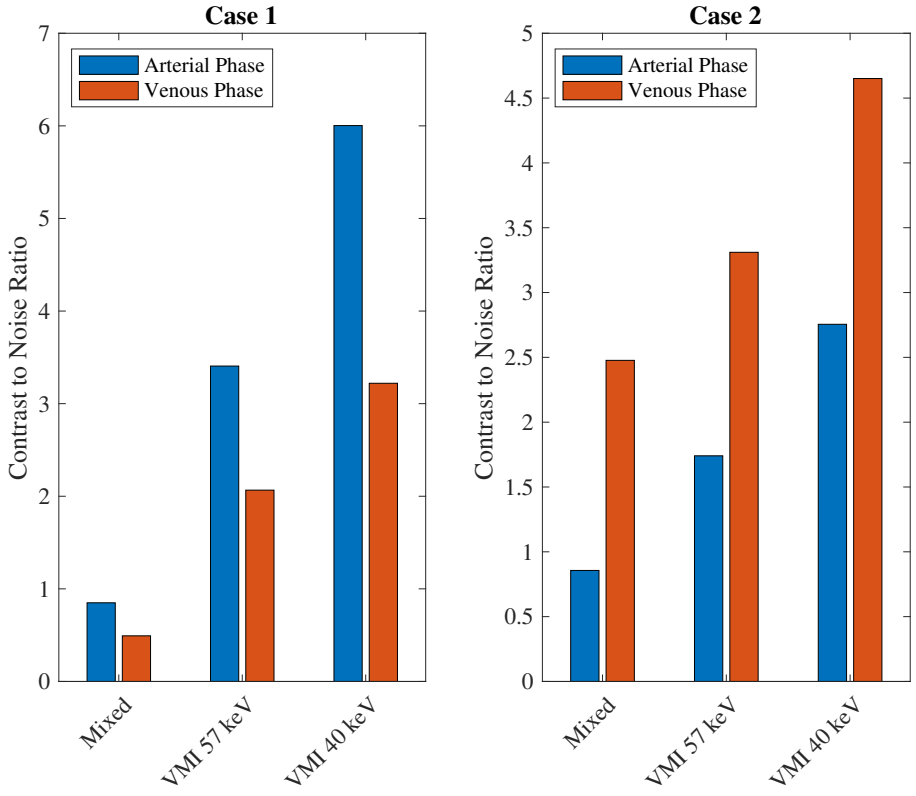

Figure 5.3: GTV CNR from Case 1 and Case 2 illustrated in Figure 5.2.

5.4 Discussion

This study investigated TwinBeam DECT images with the goal of improving the delineation of liver tumors for radiation therapy purposes. Virtual monoenergetic images from TwinBeam dual-energy data were compared to mixed 120 kVp-equivalent images by quantifying changes in GTV contrast and CNR for liver tumors. Mixed 120 kVp-equivalent images created from TwinBeam DECT data represent the baseline GTV contrast and CNR expected from conventional single-energy CT images.

On average, VMIs at 57 keV increased GTV contrast by 68% compared to mixed 120 kVp-equivalent images. VMIs at 40 keV increased GTV contrast by 215% compared to mixed 120 kVp-equivalent images. This is as expected because the attenuation of iodine increases with deceasing energy. Although on average the venous phase demonstrated greater GTV contrast, not all tumor cases followed this trend. Different liver tumors have different enhancement properties [24, 105], which is illustrated by the fact that some cases showed greater GTV contrast during the arterial phase compared to the venous phase (Figure 5.2 and 5.3). These results support other studies which say that dual-phase imaging is crucial for liver tumor detection as both phases may aid in tumor visualization [7].

This is one of the first studies to investigate the conspicuity of entire liver tumors with dual-energy CT [7, 70, 71, 104]. The investigation of contrast and CNR of the entire liver GTV rather than just a small ROI is relevant to radiation therapy as the entire tumor needs to be segmented for accurate treatment, and optimally placed ROIs do not represent the detectability of the entire GTV. Other studies have investigated the

use of DECT images for liver tumor detection using optimally-placed small ROIs and found that lower energy images provide greater tumor conspicuity [7, 70]. Robinson et al. investigated the conspicuity of hypo-vascular liver metastases using 80 kVp images and virtual 120 kVp images from sequential scanning DECT [71]. Since Robinson et al. used small ROIs placed within the liver lesion rather than the entire GTV to calculate contrast, the resulting values were much higher compared to our study (78.37 ± 24.6 HU for the 80 kVp image and 56.89 ± 17.9 HU for the virtual 120 kVp image compared to 54.9 ± 32.2 HU for the VMIs at 40 keV and 19.5 ± 13.4 HU for mixed 120 kVp-equivalent images in our study). Sequential scanning DECT has greater spectral separation and lower image noise compared to TwinBeam DECT [34]. Therefore, the superior DECT technique and the use of optimally-placed ROIs are likely factors that resulted in the Robinson et al. study achieving statistically greater CNR values while our study did not.

Marin et al. investigated hyper-vascular liver tumors on 80 kVp and 140 kVp images from sequential scanning DECT. Marin et al. also calculated CNR using a small ROI placed within the liver lesion and found higher CNR values than in our study. Marin et al. CNR values were 6.4 ± 1.0 and 8.2 ± 1.0 for the 140 kVp and 80 kVp images, respectively which is greater than the mean ± SD GTV CNR of 2.9 ± 1.8 for the VMIs at 40 keV from our study. Marin et al. investigated a total of 83 hyper-vascular liver tumors and Robinson et al. investigated 44 hypo-vascular tumors. One limitation of our study is that only 20 tumor cases of varying diagnosis and enhancement properties were investigated. A greater subject population of a single tumor type may improve the statistics of our study. Another limitation of our study is that the mean HU within the

GTV and healthy tissue ROI was used rather than median HU. This could have caused our results to be subject to outliers and not truly represent detectability. The use of median HU may improve contrast and CNR values and better represent detectability.

As expected, image noise was the greatest for the VMIs at 40 keV even with the use of ADMIRE at a strength of 2. This agrees well with published data [96]. Although the GTV contrast was significantly greater in the VMIs than the mixed 120 kVp-equivalent images, the gain in contrast did not completely overcome the increase in image noise for every case. One potential explanation as to why the low-energy VMIs on average did not provide statistically greater CNR is that this study investigated entire liver GTVs to calculate CNR rather than small optimally-placed ROIs. Liver tumors can be very heterogenous due to vascular heterogeneity causing regions of hypoxia or regions of greater enhancement. These hypo- or hyper-intense regions will then get averaged out when considering the GTV as a whole. Figure 5.4 shows examples of heterogenous tumors from our study. For these specific cases, the VMIs at 40 keV did not have a greater GTV CNR than the mixed 120 kVp-equivalent images. We did however, separate the cohort based on tumors that were not visually heterogenous, and although the sample size was small, we did see significant improvements in CNR with the VMI at 40 keV for these specific cases. This included both hypo- and hyper-attenuating tumors.

The heterogeneity of the GTV and the use of a small ROI was further investigated for Case 5. Figure 5.5 shows the histograms of the GTV of Case 5. These histograms provide a quantitative depiction of the heterogeneity of the tumor and one can conclude that an ROI placed in a high contrast region will provide different CNR values than the average

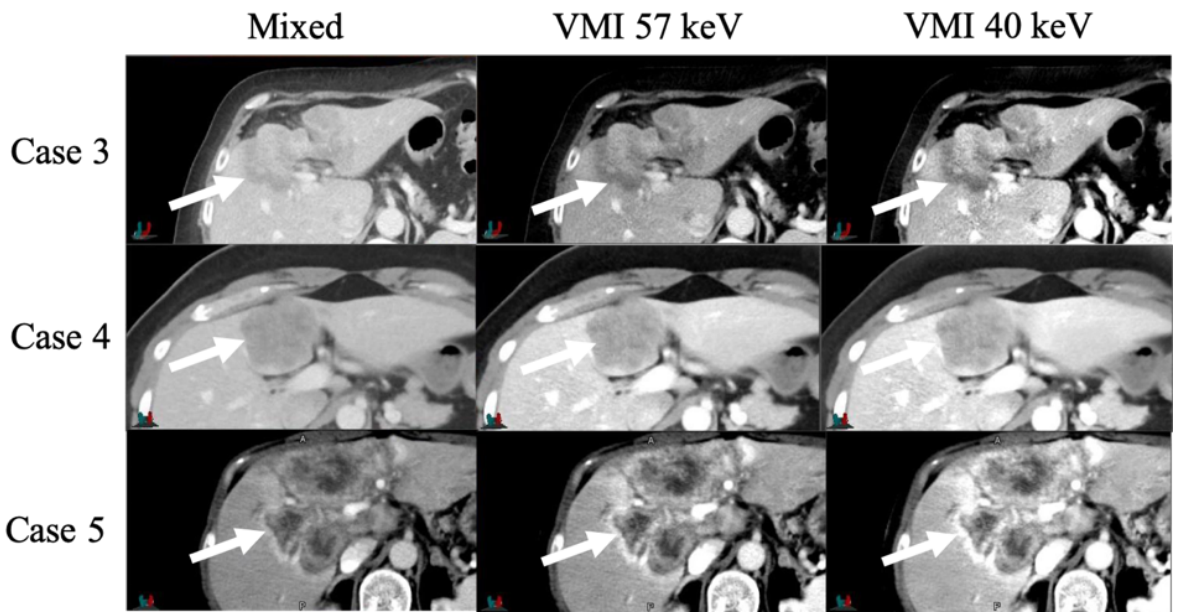

Figure 5.4: Mixed, VMI at 57 keV, and VMI at 40 keV of heterogenous tumors during the phase with the greatest GTV contrast. The arrow indicates the location of the GTV.

value of the entire GTV. The CNR calculated from the GTV of Case 5 was 1.93 and 0.25 for the mixed 120 kVp-equivalent and VMI at 40 keV image, respectively. When an optimally-placed ROI was used to calculated CNR, the values increased to 8.37 and 9.53 for the mixed and VMI at 40 keV, respectively. This example demonstrates that the VMIs at 40 keV can provide a greater CNR than the mixed 120 kVp-equivalent image when an optimally-placed ROI is used. Therefore, it is hypothesized that if ROIs were used to calculate contrast and CNR for all cases similar to previous studies, then the calculated CNR would be significantly greater for TwinBeam low energy VMIs. As previously stated, the use of small ROIs to determine tumor conspicuity is not as meaningful for radiation therapy applications.

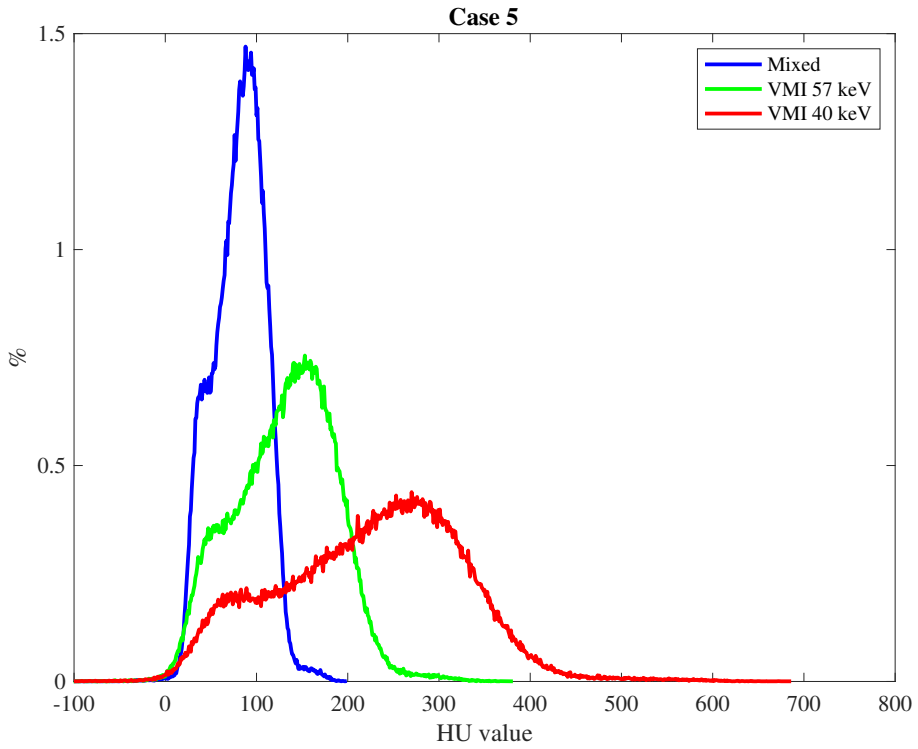

Figure 5.5: Histograms of the liver GTV from the mixed 120 kVp-equivalent image, VMI at 57 keV, and VMI at 40 of Case 5 of Figure 5.4. The y-axis is the percent of the total number of pixels within the GTV with that specific HU value with 1 HU bin widths. This graph illustrates the increase in GTV heterogeneity with low-energy VMIs.

5.5 Conclusion

Overall, TwinBeam is a cost effective, single-source DECT that can be used for dynamic contrast imaging. TwinBeam VMIs at 40 keV demonstrated greater contrast of liver tumors, and for some cases, these images provided greater CNR than conventional single energy CT images (Figure 5.2 and Figure 5.3). This was not true for all cases investigated, which is why on average there was not a statistically significant increase in CNR for low-energy VMIs. The tumors investigated for this study were very heterogeneous, so a texture analysis study of these cases is suggested, as results may lead to other methods

of using TwinBeam DECT for radiation therapy purposes. Texture analysis may reveal that for cases where TwinBeam DECT imaging does not improve CNR, it may improve the edge detection for liver tumors or enhance other imaging features that may aid in tumor delineation. A contouring study investigating the reproducibility and accuracy of GTV contours is also suggested as it may determine other clinical implications Twin-Beam DECT images have in the field of radiation therapy. Results from a contouring study may also determine if the quantitative increase in absolute contrast correlates with improvements in lesion detectability and a decrease in contour variability.

Chapter 6

Iodine quantification and texture analysis in tumor and healthy tissue of the pancreas and liver using split-filter DECT images

6.1 Iodine quantification accuracy from split-filter DECT iodine-enhanced images

The low- and high-energy images acquired with DECT are used as inputs for material decomposition algorithms to create clinically relevant images, two of which are virtual non-contrast and iodine-enhanced images. As explained in Chapter 1, these images are

paired images created by decomposing the injected iodine contrast medium and underlying soft tissue using a three material decomposition of iodine, fat, and liver soft tissue. Iodine-enhanced images from DECT are of high interest within the field of radiation oncology and radiology as they have been proven as alternatives to perfusion imaging and aid in the detection of hyper-vascular liver lesions [108, 109]. The accuracy of iodine material decomposition has been investigated using a single large phantom with six different commercially available DECT scanners: fast kilovolt peak–switching, dual-source, split-filter, sequential-scanning, and dual-layer detector [51]. It was concluded that iodine accuracy varies among systems, but dual-source and fast kilovolt-switching generally provided the most accurate results and that the accuracy depends on phantom size. Across all systems investigated, iodine quantification was accurate to within 10% of the expected value [51]. Jacobsen et al. (2018) mentions that the accuracy of TwinBeam split-filter depends on additional calibration and without it, iodine error can be up to 37% at low iodine concentrations of 2 mgI/mL. The "calibration" mentioned in this study involved altering the default CT number for water on the high-energy (tin-filter) image to 3 HU within the Syngo.via vendor software. This alteration was advised by the manufacturer but no validation of its origin is provided nor its application to different phantom sizes. The inaccuracy in TwinBeam iodine material decomposition, the lack of guidance in the calibration to improve accuracy, and the lack of knowledge of its accuracy as a function of size are the main motivations for this work.

This work will create a methodology to accurately determine the iodine concentration

from TwinBeam iodine-enhanced images and is the first study to accurately determine iodine concentration in-vivo from patient images. First, the accuracy of the vendor software, Syngo.via (VB30; Siemens Healthineers), to determine concentration within a region of interest (ROI) within a head and abdomen phantom will be determined. Due to limitations of the Syngo.via software at the time of this work, concentration values were limited to a 2D ROI on an axial slice. Therefore, a method to calculate concentration within volumetric contours was developed and the accuracy of this method was investigated. This was also performed for sequential scan DECT to compare the accuracy of the two DECT modalities and to compare to the results of Jacobsen et al. (2018) [51]. Siemens sequential scan DECT modality is referred to as Dual Spiral, while Siemens split-filter DECT modality is referred to as TwinBeam.

The second part of this work will determine patient size-specific iodine concentration calibration curves from TwinBeam DECT images. This information is important to investigate, since iodine concentration in-vivo is hypothesized to be dependent on patient size [51]. This methodology has never been done before and will provide information to correlate concentration of iodine with tumor contrast.

6.1.1 Introduction

Siemens' commercially available post-processing software, Syngo.via gives the user the ability to determine the iodine concentration within a specified circular 2D region of interest (ROI) from an axial slice of an iodine-enhanced image reconstructed from the low- and high-energy DECT data. This work investigates iodine-enhanced images with

respect to phantom size and determines the calibration curves needed to correlate iodine-enhanced image value in a volumetric contour to iodine concentration. Iodine-enhanced images are a type of dual-energy post-processing image where the uptake of iodine contrast medium is mapped separate from the underlying soft tissue.

The main aims of this project are to investigate the accuracy of iodine concentration from a 2D ROI in Syngo.via and to develop a methodology to calculate iodine concentration in a volumetric contour from an iodine-enhanced image that accounts for patient size. This methodology will include creating size-specific calibration curves that can be applied to iodine-enhanced image values (HU) to derive concentration (mg I/ml).

6.1.2 Methods

6.1.2.1 Phantoms

Gammex solid iodine plugs of concentrations ranging from 2-15 mg/mL were validated against liquid vials of iodine and water with nominal concentrations ranging from 1-15 mg/mL. The iodine vials and iodine plugs were imaged within the Gammex Multi-Energy CT (MECT) (Gammex, Middleton, WI) head (20 cm diameter) and abdomen (40 cm x 30 cm dimension) phantom separately [3, 110]. An image of this phantom is shown in Figure 6.1.

6.1.2.2 Scan protocols

Scans were performed with a $CTDI_{vol}$ of 25 mGy using the Siemens SOMATOM Definition Edge Dual Spiral and TwinBeam DECT modality at the University of Wisconsin-Madison

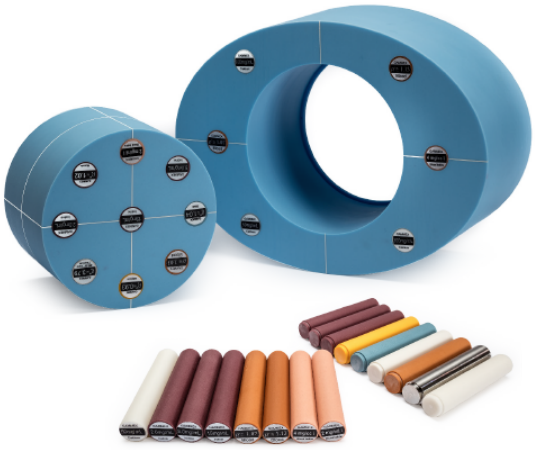

Figure 6.1: Gammex MECT head (20 cm diameter) and abdomen (40 cm x 30 cm dimension) phantom [3].

Department of Human Oncology. The average image value in Hounsfield Units (HU) within each vial and plug was collected from the low- and high-energy images in MIMvista. The average HU was determined in a long cylindrical region of interest located in the center of the rods. The results from the low-energy images were plotted as a function of high-energy value. The difference in each dataset was analyzed using an unpaired two-sample t-test with a significance value of 0.05. To isolate the effects of image noise in the size-dependency of our DECT images, an additional DECT scan was performed of the head phantom at a lower $CTDI_{vol}$ to create an image with the same image noise as the abdomen scan. This scan will be referred to as the noise equivalent head scan.

6.1.2.3 Iodine quantification in a 2D ROI

Syngo.via was then used to determine the iodine concentration of each solid iodine insert using manually created circular 2D ROIs placed on an axial slice in the center of each rod.

The values in each 2D ROI were collected and compared to the nominal concentrations for each scan and phantom size. The iodine bias of the TwinBeam and Dual Spiral DECT modalities was calculated using Equation 6.1.

$$\text{IB} = \sum_{i=2,5,10,15} ([I_i] - i), \tag{6.1}$$

where i is the nominal iodine concentration in milligrams of iodine per milliliters (mg I/mL) and $[I_i]$ is the iodine concentration determined from Syngo.via.

6.1.2.4 Iodine quantification in a 3D contour

The reconstructed iodine-enhanced images were then sent to MIMvista where manually placed 3D cylindrical ROIs were created along the entire rod to encompass 2/3 of the entire rod while avoiding the periphery. The mean value and standard deviation of HU within each cylindrical ROI were recorded and analyzed. These results and the corresponding nominal concentrations were used to generate calibration curves correlating iodine-enhanced image value (HU) to iodine concentration (mg I/ml) for each scan and phantom size.

The image values as a function of iodine concentration were fitted using the weighted linear fit command in MATLAB with individual slopes and y-intercepts for each scan type and phantom size. The weights used for the fit were the standard deviation of HU within each cylindrical ROI to weight each concentration based on the standard deviation with each ROI. A total of six calibration curves were created, three for each TwinBeam and Dual Spiral modality corresponding to the abdomen phantom, head phantom, and

noise equivalent head scan. An interpolation was performed to determine the calibration curve for a phantom size in between that of the head and abdomen phantoms (27.32 cm effective diameter) and will be referred to as the averaged calibration curve. Lastly, the iodine concentration was determined by converting the iodine-enhanced image to iodine concentration using the averaged calibration curve and the corresponding head and abdomen calibration curve.

The error in determining iodine concentration from each solid plug insert was calculated from Syngo.via and from each calibration curve. To assess the overall accuracy of each method, the root-mean-squared error across each insert was calculated.

6.1.3 Results

6.1.3.1 Gammex iodine plug validation

The mean HU values from the noise matched scans were insignificantly different than the head scan. Therefore, image noise was ruled out as a significant cause of the size-dependent HU value differences seen in the iodine-enhanced images.

The HU from the low- and high-energy datasets of the iodine and water vials and solid iodine plugs from the validation study are plotted in Figure 6.2. The goodness of fit of each curve was assessed using its r^2 value which were each greater than 0.990. These results provide evidence that the solid water plugs are equivalent to liquid iodine and water as both insert types fall on the same curve for each specified scan.

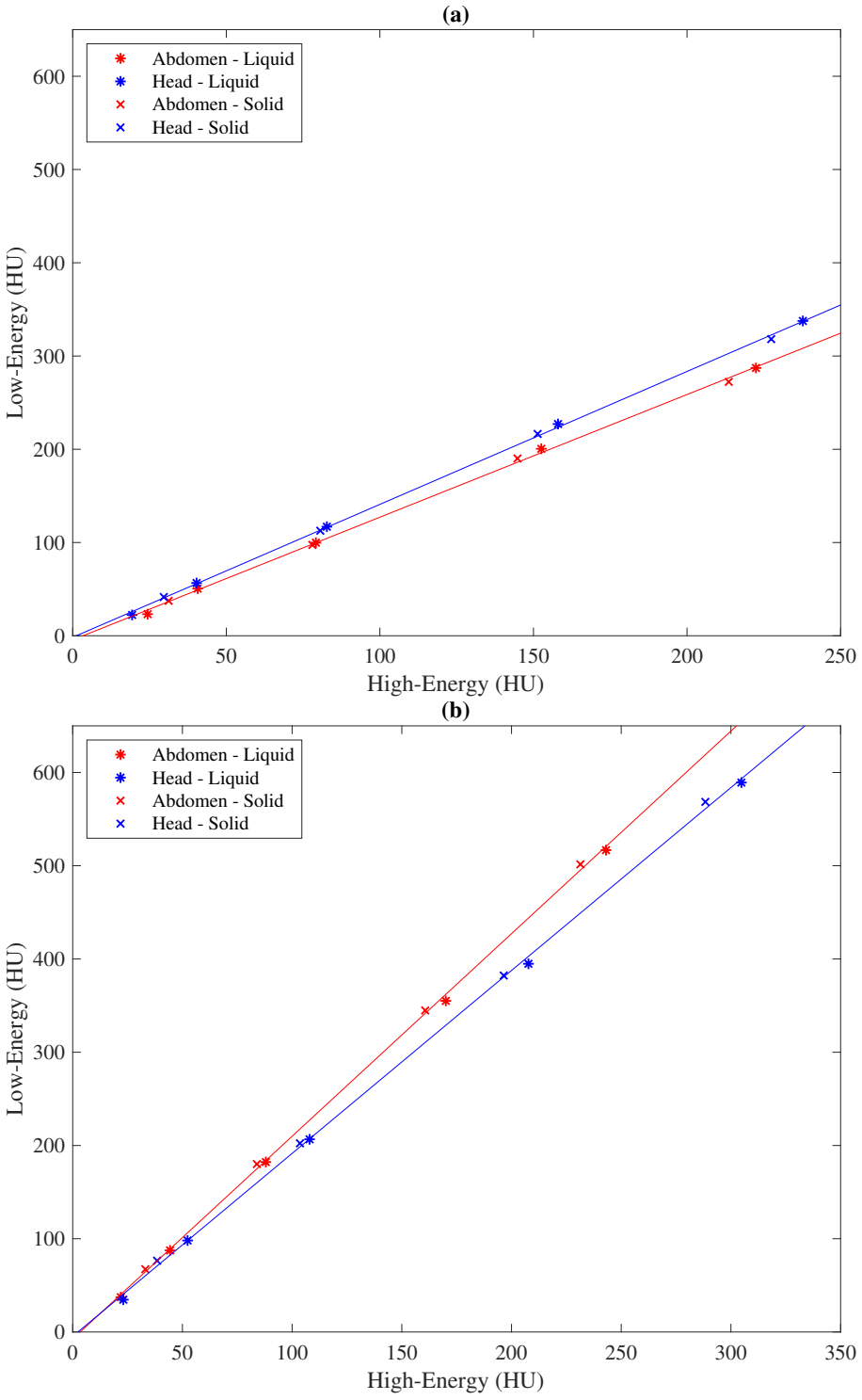

Figure 6.2: Graph showing the relationship between the low- and high-energy datasets generated from the iodine liquid vials and the iodine plug inserts within the abdomen and head phantoms for both TwinBeam (a) and Dual Spiral (b) scans.

6.1.3.2 Syngo.via iodine quantification in 2D ROI

The iodine concentration collected from 2D ROIs in Syngo.via are plotted as bar graphs in Figure 6.3 and listed in Table 6.1 for the head and abdomen phantom. The iodine concentration determined in Syngo.via deviated less from the nominal concentration for the plugs located within the head phantom compared to the abdomen phantom as the iodine bias was the lowest for these samples. The iodine bias was also lower for the Dual Spiral scans compared to the TwinBeam scans.

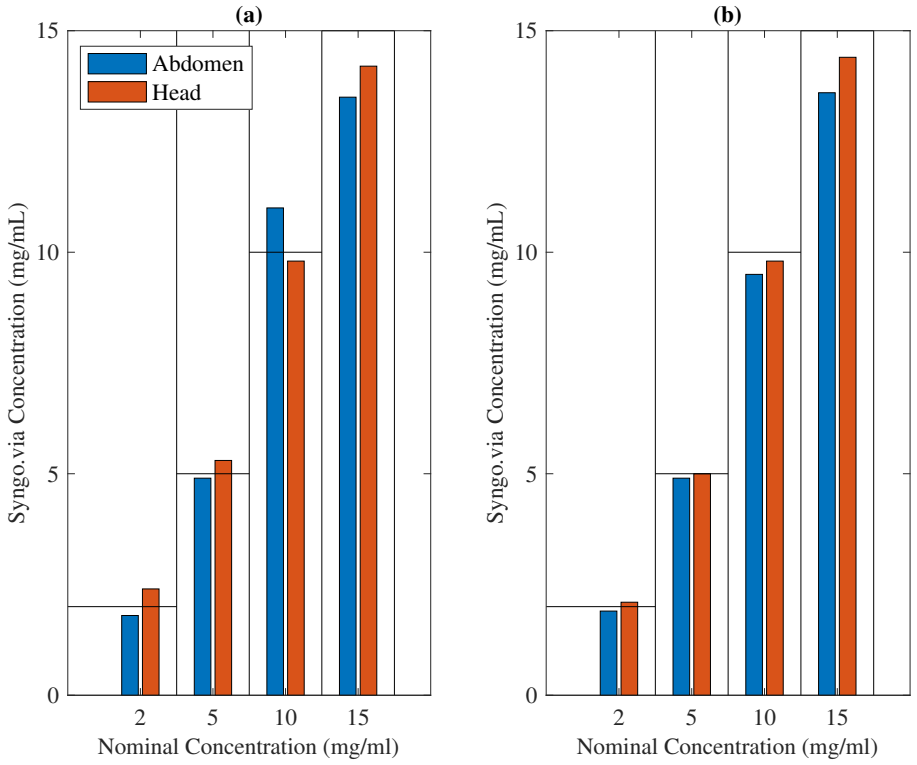

Figure 6.3: Iodine concentration determined using Syngo.via for TwinBeam (a) and Dual Spiral (b) DECT in the abdomen and head phantom that corresponds to the data listed in Table 6.1.

Table 6.1: Table listing the iodine concentration determined from Syngo.via for TwinBeam and Dual Spiral DECT in the abdomen and head phantom for each solid iodine plug with the listed nominal concentrations. This data is graphed in Figure 6.3.

		2 (mg I/mL)	5 (mg I/mL)	10 (mg I/mL)	15 (mg I/mL)	Iodine Bias
Dual spiral	Head	2.1	5	9.8	14.4	-0.7
	Abdomen	1.9	4.9	9.5	13.6	-2.1
TwinBeam	Head	2.4	5.3	9.8	14.2	-0.3
	Abdomen	1.8	4.9	11	13.5	-0.8

6.1.3.3 Iodine quantification in 3D contour

The iodine-enhanced image value given in HU collected from the 3D ROIs in MIMvista for each DECT modality and phantom size are plotted as bar graphs in Figure 6.4.

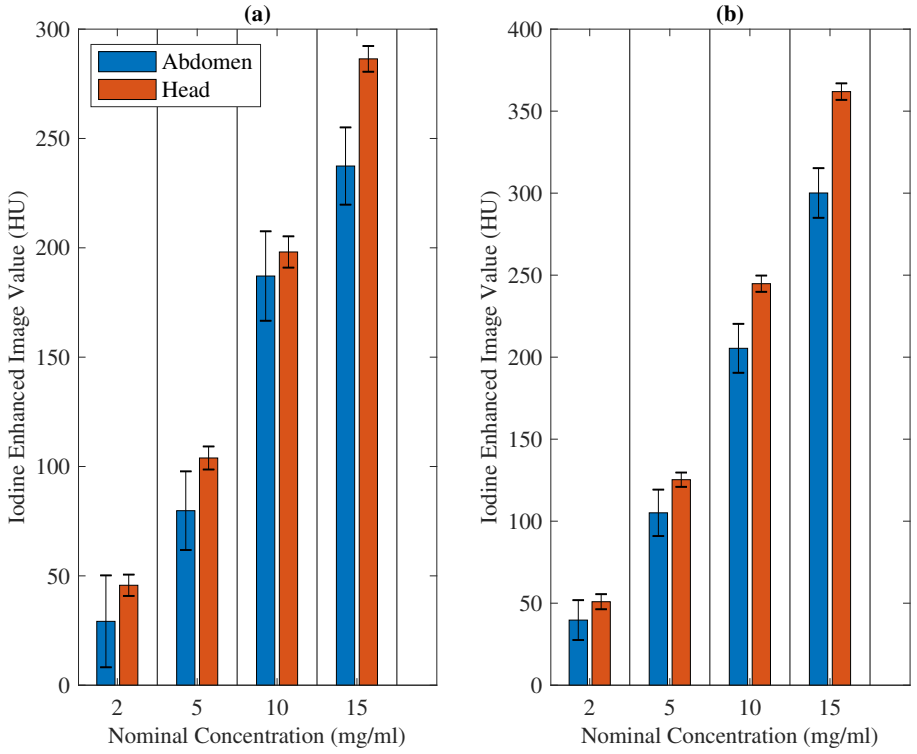

Figure 6.4: Bar graph showing the image value ($HU_{\mathbf{iodine}}$) from the iodine-enhanced images for each solid iodine insert for TwinBeam (a) and Dual Spiral (b) DECT in the abdomen and head phantom.

There was a significant difference in HU determined from the head phantom iodine-enhanced images compared to the abdomen phantom images; this difference increased with increasing iodine concentration. For each solid iodine plug, the HU from the head phantom were higher than the HU determined from the abdomen phantom. The standard deviation in HU within each 3D ROI was greater for the abdomen phantom and overall greater for the TwinBeam iodine-enhanced images compared to Dual Spiral.

The values shown in Figure 6.4 were used to create calibration curves correlating iodine-enhanced image value (HU) to iodine concentration (mg I/mL). These calibration curves for each DECT scan type and phantom size are shown in Figure 6.5. All calibration curves had a goodness of fit assessed using an r^2 value of greater than 0.90. The linear fit given in $y = mx + b$ are also listed, with m being the slope and b being the y-intercept of each curve.

Tables 6.2 and 6.3 show the percent errors in iodine concentration between the nominal concentration of each solid iodine insert and the three methods to determine iodine concentration: Syngo.via, the average interpolated calibration curve, and the size-specific (head and abdomen) calibration curve. The total root-mean-squared error for each method is also listed.

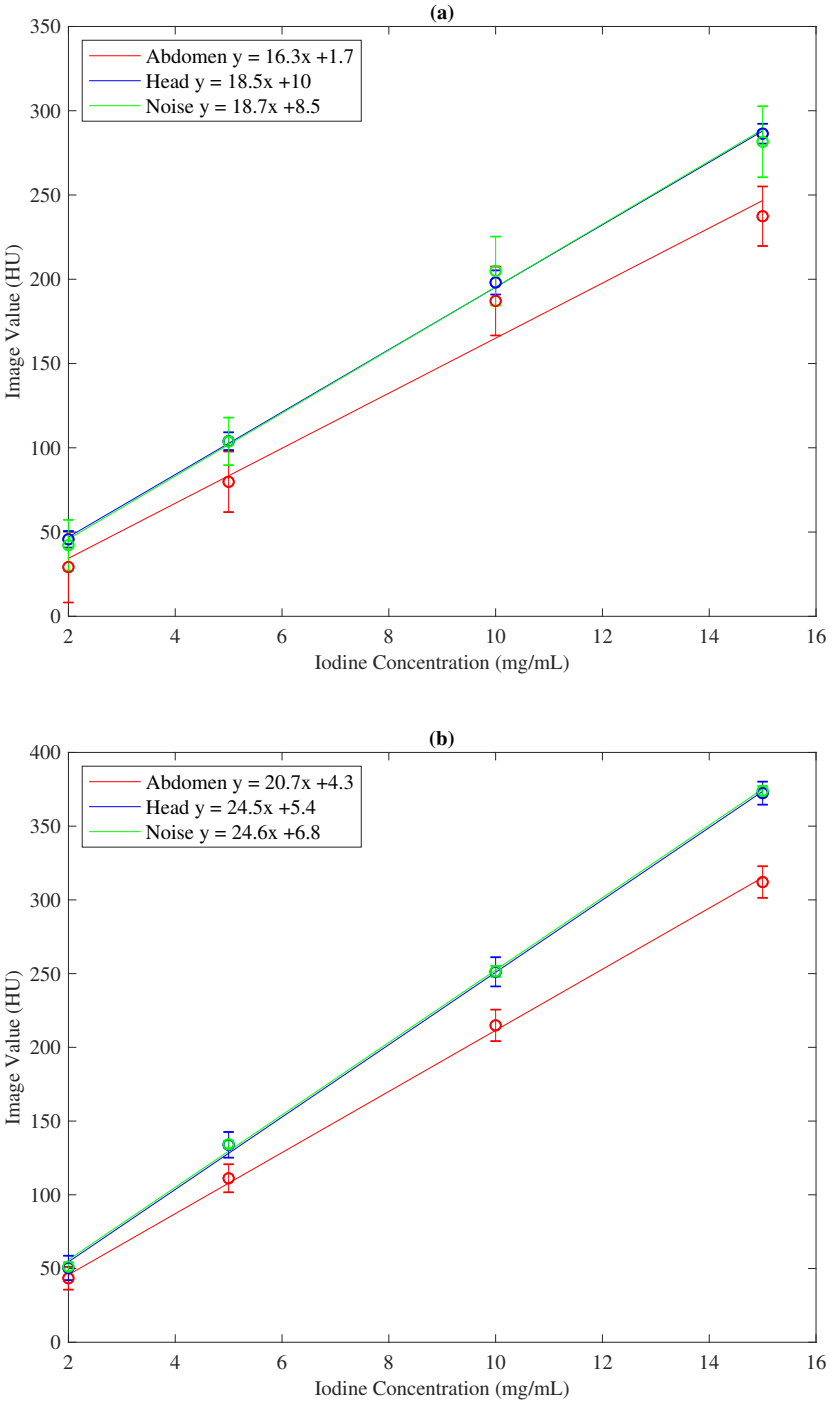

Figure 6.5: Calibration curves correlating iodine concentration (mg I/ml) and iodine-enhanced image value (HU_{iodine}) for TwinBeam (a) and Dual Spiral (b) using the abdomen phantom (red) and the head phantom (blue) scanned with the 25 mGy $CTDI_{vol}$ and the head phantom scanned with a lower $CTDI_{vol}$ to achieve the same image noise as the abdomen scan (green).

Table 6.2: Percent error between the nominal concentrations and the iodine concentrations determined from Syngo.via, the averaged calibration curve from the head and abdomen phantom, and the corresponding calibration curve for the Dual Spiral data. The root-mean-squared error (RMSE) is also shown.

Dual-Spiral		2 (mg I/ml)	5 (mg I/ml)	10 (mg I/ml)	15 (mg I/ml)	RMSE
Syngo.via	Head	5.0%	0.0%	-2.0%	-4.0%	6.7%
	Abdomen	-5.0%	-2.0%	-5.0%	-9.3%	11.9%
Average Cal. Curve	Head	14.7%	13.4%	10.3%	9.0%	24.1%
	Abdomen	-7.3%	-5.6%	-7.7%	-9.6%	15.4%
Size-Specific Cal. Curve	Head	5.0%	5.5%	3.2%	2.2%	8.4%
	Abdomen	2.4%	2.1%	-0.9%	-3.2%	4.6%

Table 6.3: Percent error between the nominal concentrations and the iodine concentrations determined from Syngo.via, the averaged calibration curve from the head and abdomen phantom, and the corresponding calibration curve for the TwinBeam data. The root-mean-squared error (RMSE) is also shown.

TwinBeam		2 (mg I/ml)	5 (mg I/ml)	10 (mg I/ml)	15 (mg I/ml)	RMSE
Syngo.via	Head	20.0%	6.0%	-2.0%	-5.3%	21.6%
	Abdomen	-10.0%	-2.0%	10.0%	-10.0%	17.4%
Average Cal. Curve	Head	15.5%	12.9%	10.4%	6.9%	23.7%
	Abdomen	-27.1%	-12.7%	4.5%	-10.5%	32.1%
Size-Specific Cal. Curve	Head	-0.8%	2.2%	1.6%	-1.1%	3.0%
	Abdomen	-11.6%	-2.3%	14.1%	-2.6%	18.5%

6.1.4 Discussion

The Gammex solid iodine plugs are equivalent to liquid mixtures of iodine and water as they both present the same attenuating properties when imaged with TwinBeam and Dual Spiral DECT. There was no statistical difference between the low- and high-energy datasets from the solid iodine inserts and liquid iodine vials for both the head and abdomen phantoms and TwinBeam and Dual Spiral imaging modality as the P value was greater than 0.8.

The head phantom was scanned with TwinBeam and Dual Spiral to 25 mGy and rescanned at a lower dose to achieve the same image noise as the abdomen phantom at 25 mGy. Overall image noise had no effect on the image value from the head phantom as the low dose and 25 mGy images resulted in the same averaged image value within each iodine plug. Therefore, it was determined that image noise was not a significant factor in the size-dependency of the HU values measured in the iodine-enhanced images. Differences in values due to phantom size can likely be attributed to beam hardening artifacts.

This work investigated the accuracy of determining iodine concentration in milligrams of iodine per milliliter (mg I/mL) from iodine-enhanced images. Solid iodine plugs were placed within a head and abdomen phantom and scanned using two different DECT modalities. The current clinical method in determining iodine concentration from TwinBeam and Dual Spiral iodine-enhanced images is from Syngo.via. The deviation of iodine concentration determined from Syngo.via to the nominal concentrations was quantified using the iodine bias. Jacobsen et al. (2018) also investigated the accuracy of iodine

quantification from Syngo.via using an abdomen phantom and calculated an iodine bias to be -0.78 for Dual Spiral and -2.60 for TwinBeam [51]. Jacobsen et al. (2018) only used 2 mgI/mL, 5 mgI/mL, and 15 mgI/mL inserts while this study used 2 mgI/mL, 5 mgI/mL, 10 mgI/mL, and 15 mgI/mL; this could be one reason for the slight discrepancy between the two studies. Another reason for the discrepancy could be the version of Syngo.via (VB10 for Jacobsen et al. (2018) versus VB30 for this study).

Since the finalization of this work, Jacobsen et al. (2019) performed a very similar investigation by creating calibration curves in the low iodine concentration range of 0.03 - 2.0 milligrams of iodine per milliliter for different DECT modalities including TwinBeam but excluding Dual Spiral [4]. The same two phantoms were scanned with a $CTDI_{vol}$= 25 mGy with inserts containing centrifuged tubes of iohexol solutions. The calibration curves parameters from this thesis and the work of Jacobsen et al. (2019) are listed in Table 6.4.

Table 6.4: Slope and y-intercept of the calibration curves for TwinBeam DECT determined in this thesis work and the work of Jacobsen et al. (2019) [4].

	This study		Jacobsen et al.	
Phantom	Slope (HU per mg/mL)	y-intercept (HU)	Slope (HU per mg/mL)	y-intercept (HU)
Abdomen	16.3	1.7	14.2	1.85
Head	18.5	10	19.8	-2.5

The Jacobsen et al. (2019) calibration curves were created using iodine-enhanced images similar to this thesis work but the Syngo.via parameters including dual-energy ratio and HU values used to post process the images were not reported. The Syngo.via version was also different than out study (VB20 vs VB30). Therefore, the creation of the images

may have been different, which may be the cause of the discrepancy in calibration curves between the two studies. Another possible reason for the differences in the calibration curves are the placement of the inserts. For this thesis study the inserts were placed within the center region of the phantom but Jacobsen et al. (2019) placed them along the periphery of the phantoms. The limit of detection (LOD) and limit of quantification (LOQ) was determined and it was concluded that TwinBeam had to highest limit in both categories compared to other modalities (head: LOD = 0.163 mgI/mL and LOQ = 0.50 mgI/mL, abdomen: LOD = 0.410 mgI/mL and LOQ = 0.50 mgI/mL). Future work, repeating this thesis work at the low concentrations for better compare to the published work is encouraged.

Overall, when Syngo.via was used to determine the iodine concentration of solid iodine plugs placed within an abdomen phantom, the total iodine error was 11.9% and 17.4% for Dual Spiral and TwinBeam, respectively. The inaccuracy of iodine quantification from Syngo.via increased with increasing nominal concentrations. This trend was also apparent in the work of Jacobsen et al. (2018) [51]. Fortunately, the clinical impact of this error at high concentrations may be less significant because studies that have used dual-energy CT to quantify the iodine concentration to differentiate different diseases found that concentrations were less than 5 mg/mL [111, 112].

The iodine-enhanced image values were greater when collected from the head phantom compared to the abdomen phantom. This difference ranged from 14-22% for the Dual Spiral images and 5-36% for the TwinBeam images but had no trend as a function of iodine concentration. This is most likely due to the beam hardening that occurs with the

larger abdomen phantom.

An abdomen, head, and averaged calibration curve were used to correlate image value to iodine concentration. The accuracy in determining iodine concentration from the averaged calibration curve was the least accurate method as the total iodine error was 32% for TwinBeam and 24.1% Dual Spiral. Size-specific calibration curves increased the accuracy of iodine quantification from iodine-enhanced images to within 3.2% for Dual Spiral and 14.1% for TwinBeam for the abdomen phantom.

As expected, TwinBeam images resulted in greater standard deviation of HU within the solid iodine plugs from the iodine-enhanced images due the lower spectral separation. TwinBeam images also resulted in greater inaccuracy of iodine quantification. Although the Dual Spiral DECT resulted in more accurate determination of iodine concentration within stationary phantoms, this performance is unlikely to be replicated due to patient motion and contrast timing between the low- and high-energy datasets.

6.1.5 Conclusion

This work developed a methodology to calculate iodine concentration in a volumetric contour using two calibration curves that may be used to interpolate size-specific calibration curves to correlate iodine concentration from iodine-enhanced image value. Further validation of the overall accuracy of the size specific calibration curves using an intermediate phantom size rather than using an average is suggested because although there were cases where the size-specific calibration curves performed superiorly to Syngo.via, it was not across the board for all concentrations.

6.2 Iodine quantification in the tumor and healthy tissue of the pancreas and liver from split-filter DECT iodine-enhanced images

6.2.1 Introduction

Iodine-enhanced dual-energy CT images can be used to improve tumor visibility for radiation therapy treatment planning. Unfortunately, for Siemens dual-energy CT scanners, the post-processing software Syngo.via is limited in its ability to report iodine concentration. At the time of this work, the software only allowed the user to obtain the mean concentration within a circular 2D ROI. The results of Section 6.1 have shown that for accurate iodine quantification from the iodine-enhanced images, size-specific calibration curves correlating image value to iodine concentration is required for 3D ROI information and can in some cases improve accuracy.

This study presents the novel use of patient size-specific calibration curves to convert HU values from iodine-enhanced images to iodine concentration in mg I/mL. This methodology was then applied to quantify iodine uptake in pancreas and liver tumors for patients scanned using TwinBeam split-filter DECT at the University of Wisconsin-Madison Department of Human Oncology for radiation therapy purposes. With this data, tumor visibility (as quantified by contrast-to-noise ratio (CNR)) has been correlated with iodine concentration for pancreas and liver tumors. The iodine uptake was also investigated as a function of patient size.

6.2.2 Methods

For this study, 19 pancreas cancer tumors and 20 liver cancer tumors were imaged prior to radiation treatment planning with a biphasic imaging protocol with TwinBeam split-filter DECT system. All pancreas cases were pancreatic adenocarcinomas, the liver cohort consisted of hepatocellular carcinomas, cholangiocarcinomas, and liver metastases. All pancreas and liver cancer patients receive a constant volume of IV nonionized iodine contrast during CT simulation. The injected contrast medium was monitored via-bolus tracking for patient specific delay times. During the bi-phasic imaging protocol, the pancreatic phase and portal venous phase was acquired for each pancreas case and the arterial phase and venous phase was collected for each liver case. An example of the first and second scan corresponding to a pancreas and liver case is shown in Figure 6.6 where the difference in iodine enhancement is illustrated.

The low- and high-energy datasets were reconstructed using the ADMIRE algorithm at a strength of 2. ADMIRE is an iterative reconstruction algorithm used to decrease noise while preserving fine details. Iodine-enhanced and mixed 120 kVp-equivalent images were reconstructed in Syngo.via and sent to MIMvista for analysis.

The same GTV contours and healthy tissue ROIs created in Chapters 4 and 5 were used for this study. Figure 6.7 shows the GTV contour of a pancreas and liver tumor on a mixed 120 kVp-equivalent and iodine-enhanced image.

The mean HU value within each healthy tissue ROI was collected for each case. Tumor visibility was assessed using the GTV contrast-to-noise ratio (CNR) on the mixed 120 kVp equivalent images. The GTV CNR was defined by Equation 6.2, where noise was defined

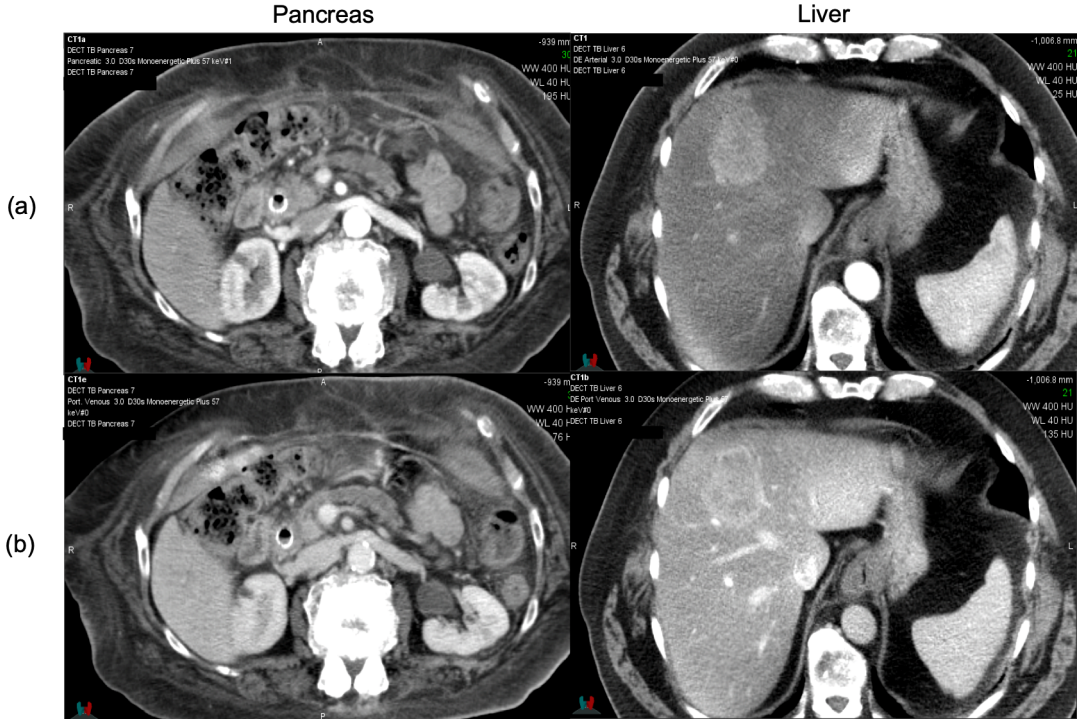

Figure 6.6: Pancreatic (a) and portal venous phase (b) image of a pancreas case and the arterial (a) and venous phase (b) image of a liver case. These examples show the difference in iodine-enhanced during each dual-phase contrast imaging.

as the standard deviation of a region of interest located in a homogenous region of the back muscle.

$$\mathrm{GTV}_{CNR} = \frac{\mathrm{HU}_{\mathrm{ROI}} - \mathrm{HU}_{\mathrm{GTV}}}{\sigma}, \tag{6.2}$$

To quantify the effects of patient size, the effective diameter (ED) of each patient was also determined using the lateral and anterior-posterior dimension of the abdomen on an image slice that encompassed the tumor. An image exemplifying the lateral (LAT) and anterior-posterior (AP) dimensions are shown in Figure 6.8.

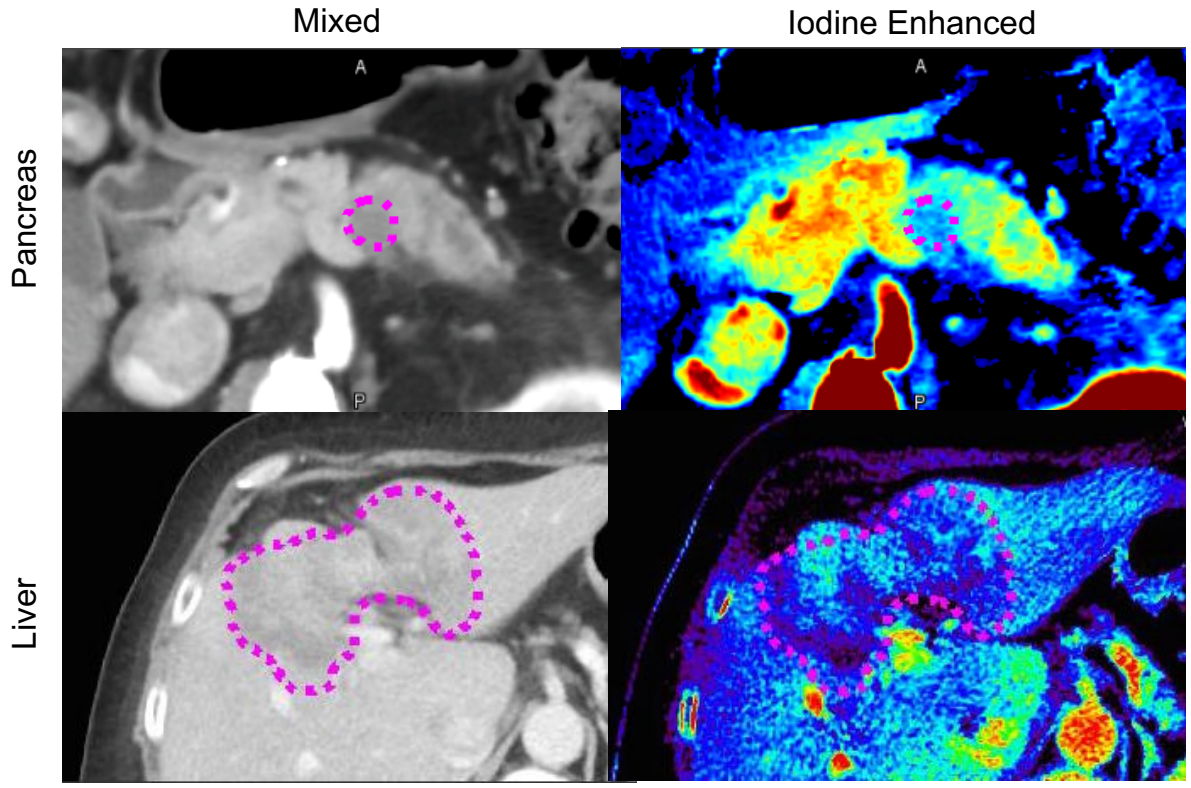

Figure 6.7: Mixed 120 kVp-equivalent (Mixed) and iodine-enhanced image reconstructed with ADMIRE 2 of a pancreas and liver tumor during the pancreatic and venous phase respectively. The magenta represents the contoured GTV.

The ED was calculated using Equation 6.3 [113]. The ED of all patients investigated in this study ranged from 23.5 cm to 40.2 cm.

$$\text{ED} = \sqrt{LATxAP} \tag{6.3}$$

The calibration curves correlating iodine-enhanced image value to iodine concentration determined in Section 6.1 were used to determine the patient size-specific calibration curves. Since the ED of the head and abdomen phantom are known (20 cm and 34.6 cm), interpolation was used to determine the slope and y-intercept of each calibration curve

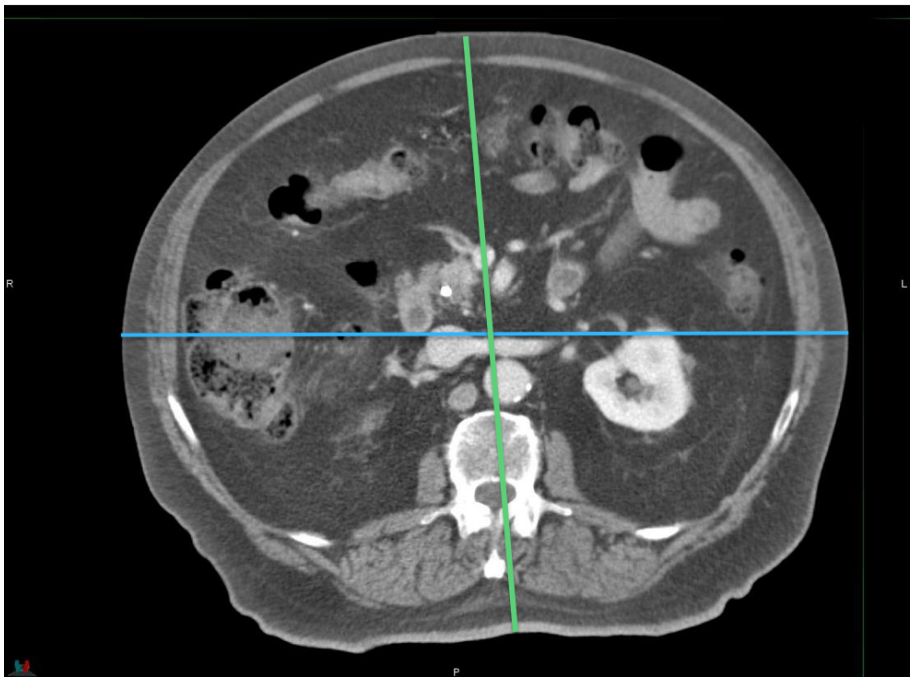

Figure 6.8: Image showing the lateral (blue) and anterior-posterior (green) dimensions used to calculate the effective diameter of each patient.

for patients with EDs within 20 cm and 34.6 cm. Extrapolation was used to determine the slope and y-intercept of each calibration curve for patients with EDs < 20 cm or ED > 34.6 cm. Size-specific calibration curves were created to correlate the iodine-enhanced mean HU value within each GTV and healthy tissue ROI to iodine concentration in milligrams of iodine per milliliter.

Since the calibration curves can extend to negative concentrations, there were some cases where the HU resulted in a negative iodine concentration value. This is physically impossible, therefore, for those cases, a zero iodine concentration was determined.

The difference in iodine concentration between the tumors and surrounding healthy tissue across all patients was analyzed using an unpaired two sample t-tests with a significance value of 0.05. Iodine concentration was also analyzed as a function of patient

ED.

For analysis, the liver tumors were categorized as hyper-attenuating and hypo-attenuating tumors based on whether the GTV CNR on the mixed 120 kVp-equivalent images was positive or negative. There were 6 hyper-attenuating tumors and 14 hypo-attenuating tumors. This type of categorical analysis was not performed with the pancreas cases as they all had similar enhancement properties.

6.2.3 Results

Figure 6.9 shows the iodine concentration in milligrams of iodine per milliliters determined within each pancreas GTV and healthy tissue ROI from the pancreatic phase iodine-enhanced images. These values were determined using size-specific calibration curves. This graph illustrates the distribution and divide in iodine concentration between the two tissues. Although Figure 6.9 only shows the results from the pancreatic phase iodine-enhanced images, the average iodine concentration with each pancreas GTV and healthy tissue ROI was determined for both the pancreatic and portal venous phase images.

The average and standard deviation over all 19 pancreas tumor cases are shown in Figure 6.10. The average iodine uptake within the pancreas GTVs was about 1.3 mgI/mL for both the pancreatic and portal venous phases. The iodine uptake within the healthy pancreas tissue decreased from 2.2 to 1.7 mg/mL for the pancreatic to the portal venous phase. For both phases, there was a statistically greater iodine uptake within the healthy pancreas tissue compared to pancreas GTV ($P<<.005$).

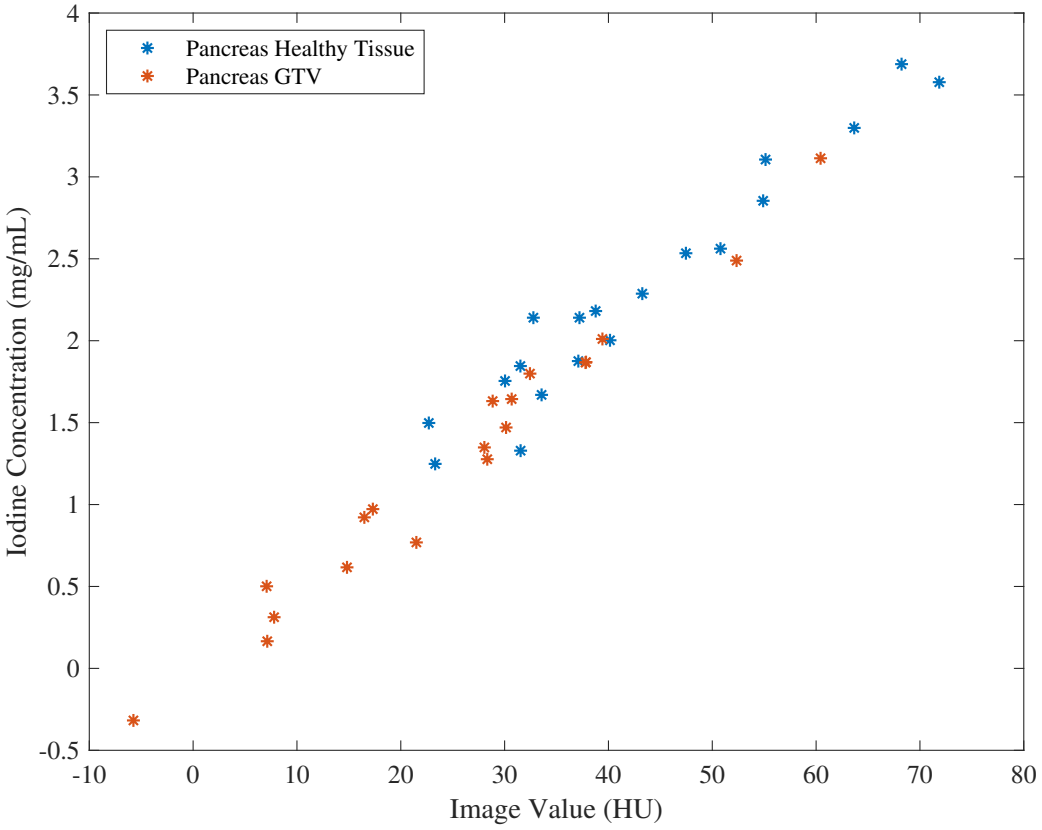

Figure 6.9: Iodine concentration (mg I/ml) within each pancreas GTV and healthy tissue ROI determined from pancreatic phase iodine-enhanced images using size-specific calibration curves.

The iodine concentration within the liver GTVs and healthy tissue ROIs from the arterial phase images are illustrated in Figure 6.11. Similar to the pancreas results, the iodine concentration within the liver GTVs and healthy tissue ROIs was determined from iodine-enhanced images using size-specific calibration curves based on each patient's ED. Due to the difference in enhanced properties of the liver tumors investigated, the average values were analyzed by dividing the tumors into either hypo- and hyper-attenuating categories.

The average and standard deviation from the arterial and venous phase scans are

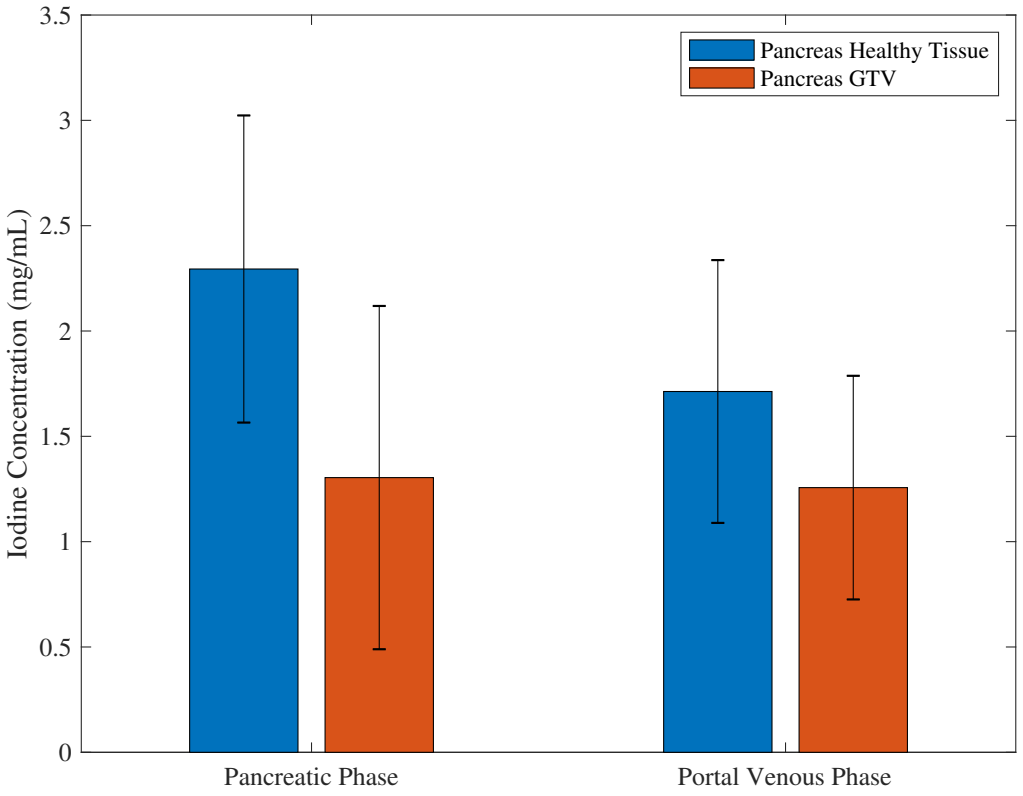

Figure 6.10: Average iodine concentration (mg I/ml) within each pancreas healthy tissue ROI and GTV determined for all pancreas cases investigated from the pancreatic and portal venous phase iodine-enhanced images.

shown in Figure 6.12. There was a statistical difference in iodine uptake between the liver GTVs and healthy tissue ROIs ($P<.05$). For both the arterial and venous phase images, the healthy liver tissue had more iodine uptake than the hypo-attenuating liver GTVs (arterial phase: 0.86 vs 0.41 mg/mL; venous phase: 1.88 vs 1.58 mg/mL). On the other hand, there was more iodine uptake within the hyper-attenuating liver GTVs than surrounding healthy liver tissue (arterial phase: 0.26 vs 0.41 mg/mL; venous phase: 1.22 vs 1.58 mg/mL). Overall, there was more iodine uptake in both tumor and healthy tissue during the venous phase compared to the earlier arterial phase scans.

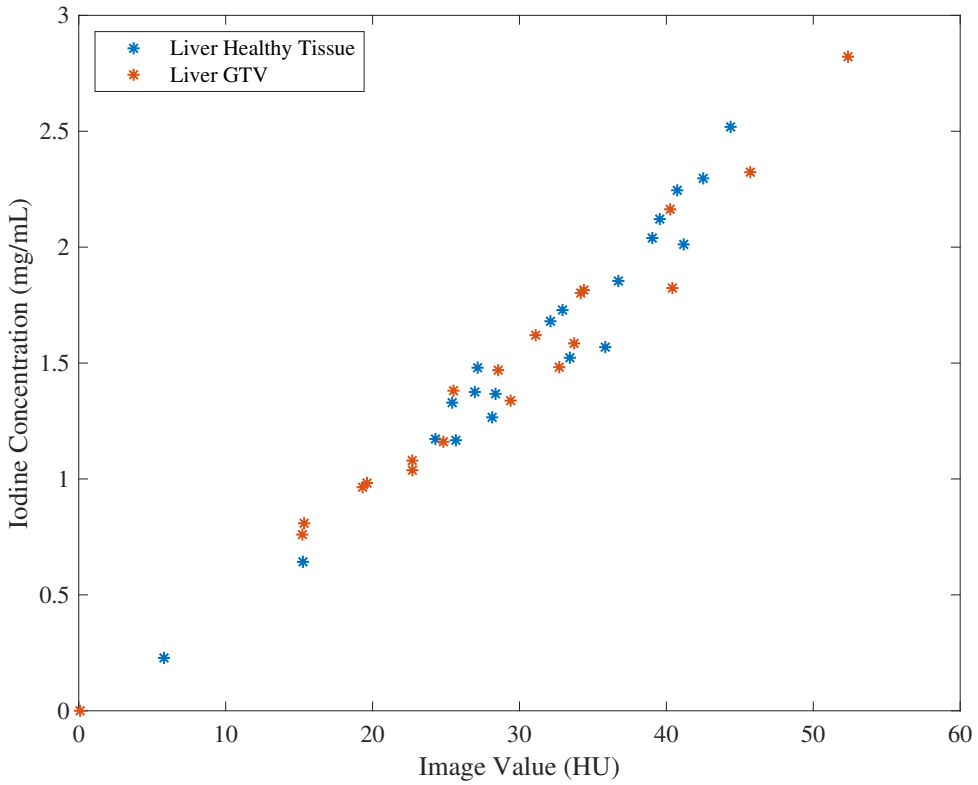

Figure 6.11: Iodine concentration (mg I/ml) within each liver GTV and healthy tissue ROI determined from venous phase iodine-enhanced images using size-specific calibration curves.

The iodine concentration was then investigated as a function of patient ED. As the patient effective diameter increased, the iodine concentration within the pancreas GTV and healthy tissue ROI also decreased. The goodness of the linear fit was evaluated using r^2 values which were 0.31 and 0.16 for the pancreas GTV and healthy tissue data, respectively. The iodine concentration as a function of ED for the pancreas GTV is shown in Figure 6.13a and healthy tissue is shown in Figure 6.13b .

On the other hand, there was no correlation between patient size and iodine uptake in the liver GTVs or healthy tissue ROIs as the r^2 values were less than 0.1 for both liver GTV and healthy tissue (Figures 6.14a and 6.14b).

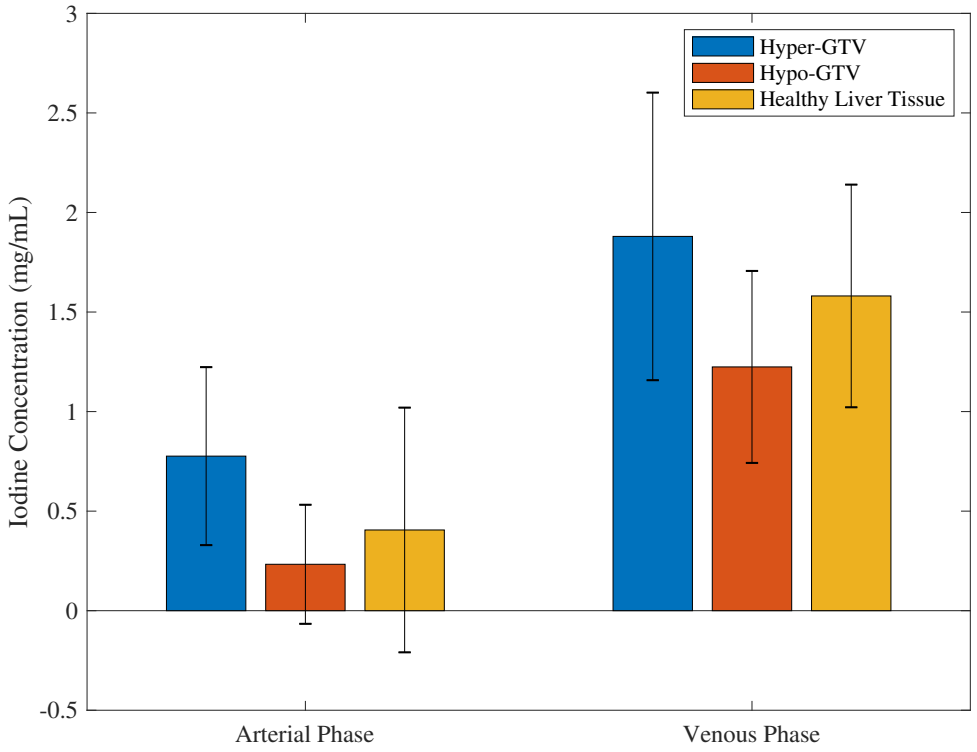

Figure 6.12: Average iodine concentration (mg I/ml) within each healthy tissue ROI and GTV of all liver tumors investigated from the arterial and venous phases iodine-enhanced images.

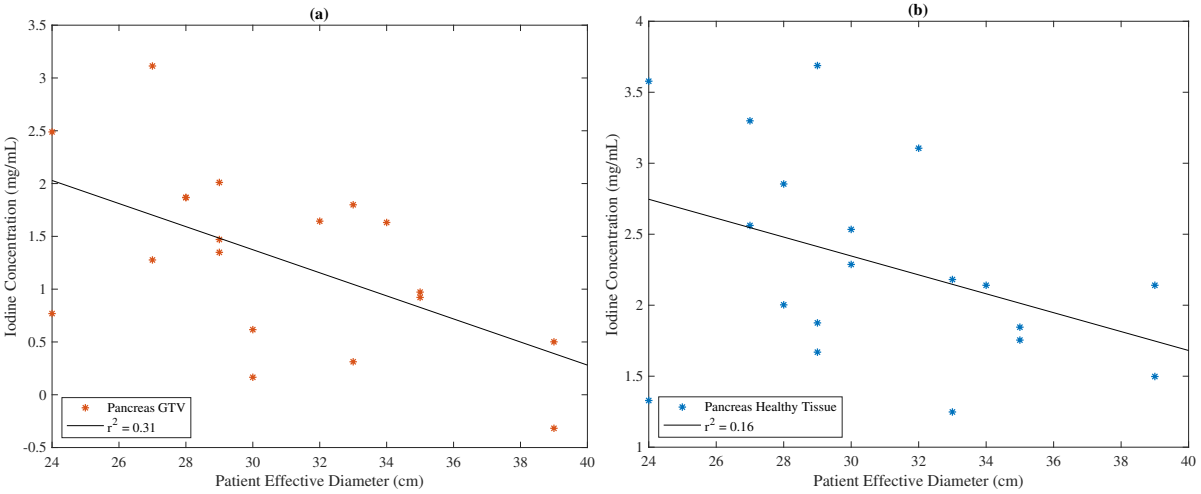

Figure 6.13: Average iodine concentration (mg I/ml) within each pancreas GTV (a) and pancreas healthy tissue (b) as a function of patient effective diameter.

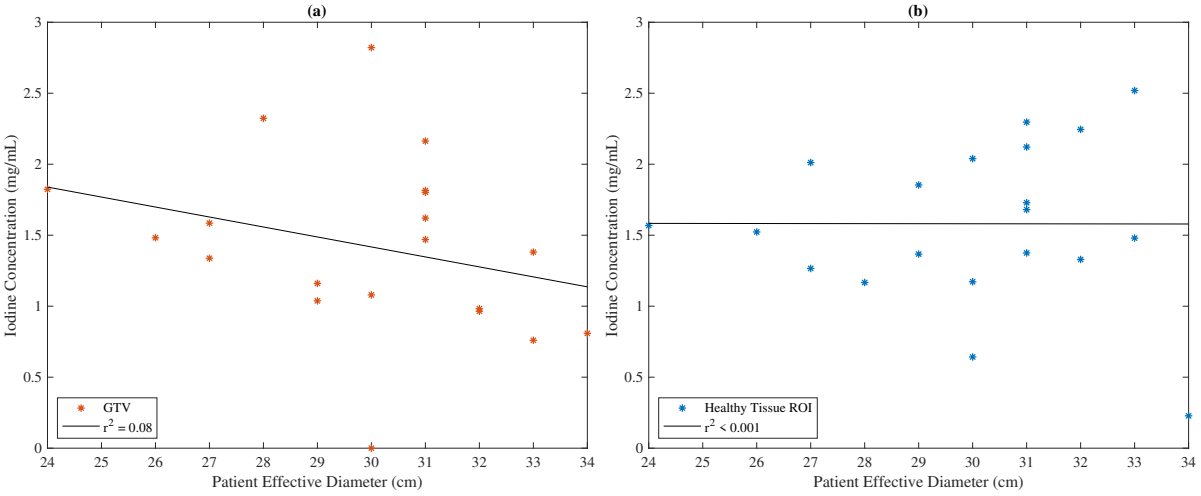

Figure 6.14: Average iodine concentration (mg I/ml) within each liver GTV (a) and liver healthy tissue (b) as a function of patient effective diameter.

The iodine concentration data was then analyzed as a function of tumor visibility. As a reminder, tumor visibility was assessed as the GTV CNR calculated on the mixed 120 kVp-equivalent images. For the pancreas cases, since the healthy tissue was found to have more iodine uptake than pancreas tumor during the pancreatic phase, the iodine concentration within the healthy pancreas tumor was analyzed as a function of GTV CNR. Figure 6.15 plots tumor visibility against iodine concentration during the pancreatic phase. There was a positive correlation between pancreas healthy tissue iodine uptake and tumor visibility, as seen from the graph and listed r^2 value of 0.47. When GTV CNR was analyzed as a function of difference in iodine uptake between the GTV and healthy tissue ROI, there was no correlation ($r^2 << 0.01$).

The iodine concentration in the liver GTVs and healthy tissue ROIs were also analyzed as a function of tumor visibility. Because this liver cohort included both hypo- and hyper-attenuating tumors, the absolute GTV CNR from the mixed 120 kVp-equivalent images

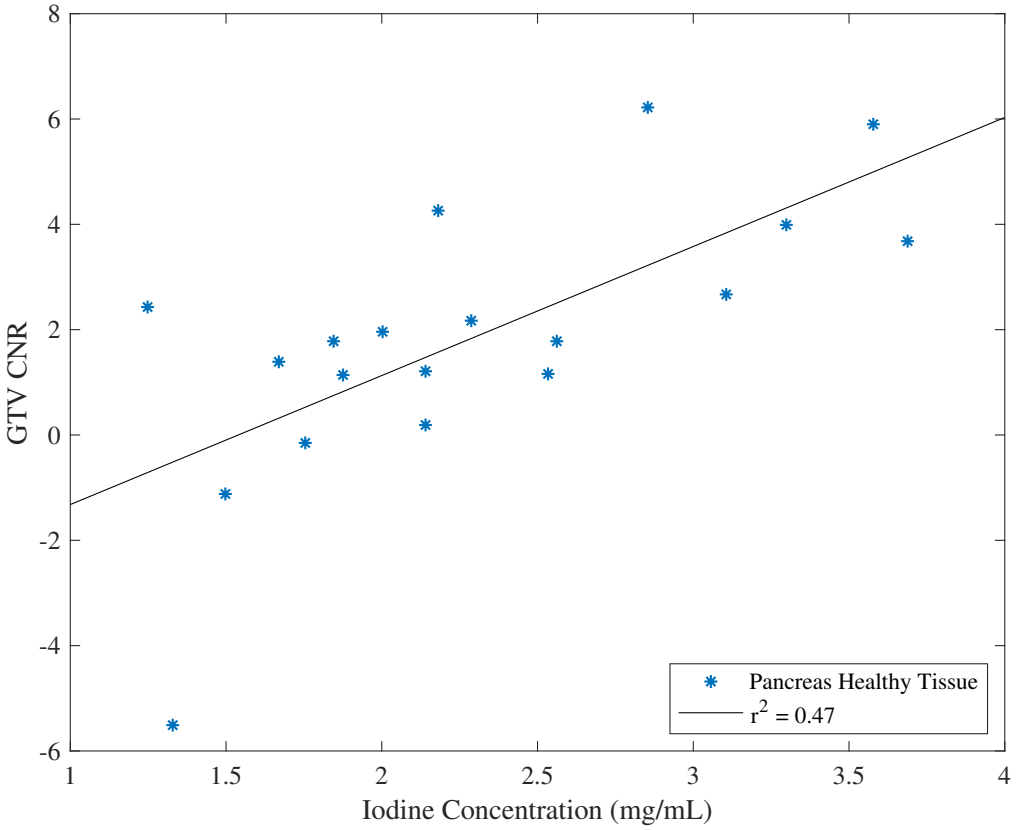

Figure 6.15: Iodine concentration (mg I/ml) within each pancreas healthy tissue as a function of GTV CNR from the mixed 120 kVp-equivalent images.

was plotted as a function of iodine concentration. The data was not categorized by enhancing properties as a linear correlation would not be possible to determine because of the lack of data points within each sub-group. Unlike the pancreas cases, there was no evident correlation between iodine uptake and tumor visibility for neither the arterial phase nor venous phase data. Figure 6.16 shows the GTV CNR as a function of iodine concentration determined from each liver healthy tissue ROI. Although there is a slight negative slope in the fitted curve, the goodness of fit was 0.11, concluding a very low correlation.

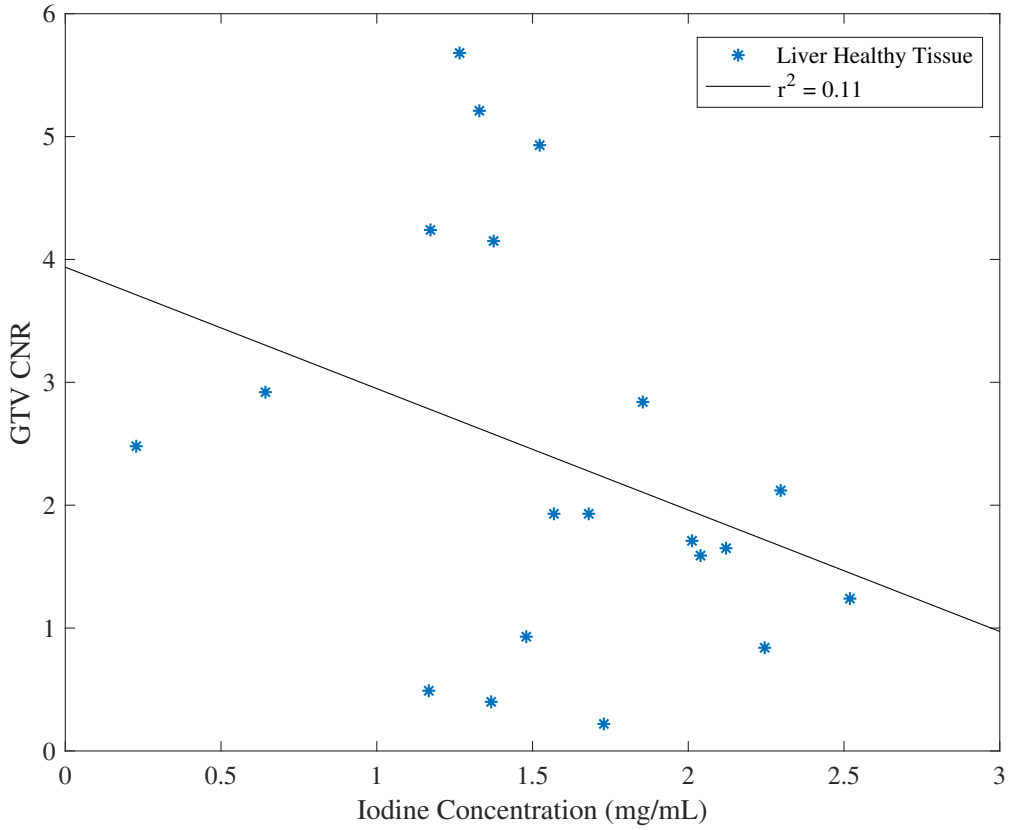

Figure 6.16: Iodine concentration (mg I/ml) within each liver healthy tissue as a function of GTV CNR from the mixed 120 kVp-equivalent images.

6.2.4 Discussion

Iodine concentration was analyzed as a function of patient size. Iodine concentration was also analyzed as a function of tumor visibility using the GTV CNR calculated on TwinBeam mixed 120 kVp-equivalent DECT images. For the pancreas cases, the difference in iodine uptake between the pancreas GTV and healthy tissue was greater during the pancreatic phase than the portal venous phase. This is as expected as the pancreatic phase is the time after intravenous injection of the iodine contrast where the difference in normal parenchyma and adenocarcinomas is maximized [114]. Based on the results of

this study, greater patient size was correlated with less iodine uptake in healthy pancreas tissue. This makes sense as Bae et al. concludes that the body weight is the most important factor affecting parenchyma contrast enhancement [115]. This means that the same amount of bolus administered to each patient during radiation therapy simulation and monitored via bolus tracking does not account patient size only cardiac output.

The lack of correlation between GTV visibility and difference in iodine concentration between tumor and healthy tissue was not as expected as the visibility of the GTVs on the mixed 120 kVp-equivalent images should depend on the iodine uptake. This null result was not due to the inaccuracy of the calibration curves as there was also no correlation between GTV CNR and difference in iodine-enhanced image value (HU) between GTV and healthy tissue ROI (Figure 6.17). Rather, it is hypothesized to be due to the manufacturer calculation of the iodine-enhanced image, specifically the dual-energy (DE) ratio. The DE ratio is used to decompose iodine and soft tissue to create the iodine-enhanced image and the virtual non-contrast (VNC) image. The DE ratio is the slope of the line when the low- and high-energy dataset value are plotted for different iodine concentrations. During the creation of iodine-enhanced and VNC images, there is only one DE ratio used regardless of patient size but as Figure 6.2 shows, the points fall on two different lines for the head and abdomen phantom, implying that there is a size dependence. Therefore, the manufacturer DE ratio may not be the most accurate value to properly decompose iodine and soft tissue. Future work investigating the effect of different DE ratio values on the points plotted in Figure 6.17 is desired.

For the liver cases investigated, 6 were hyper-attenuating and 14 were hypo-attenuating

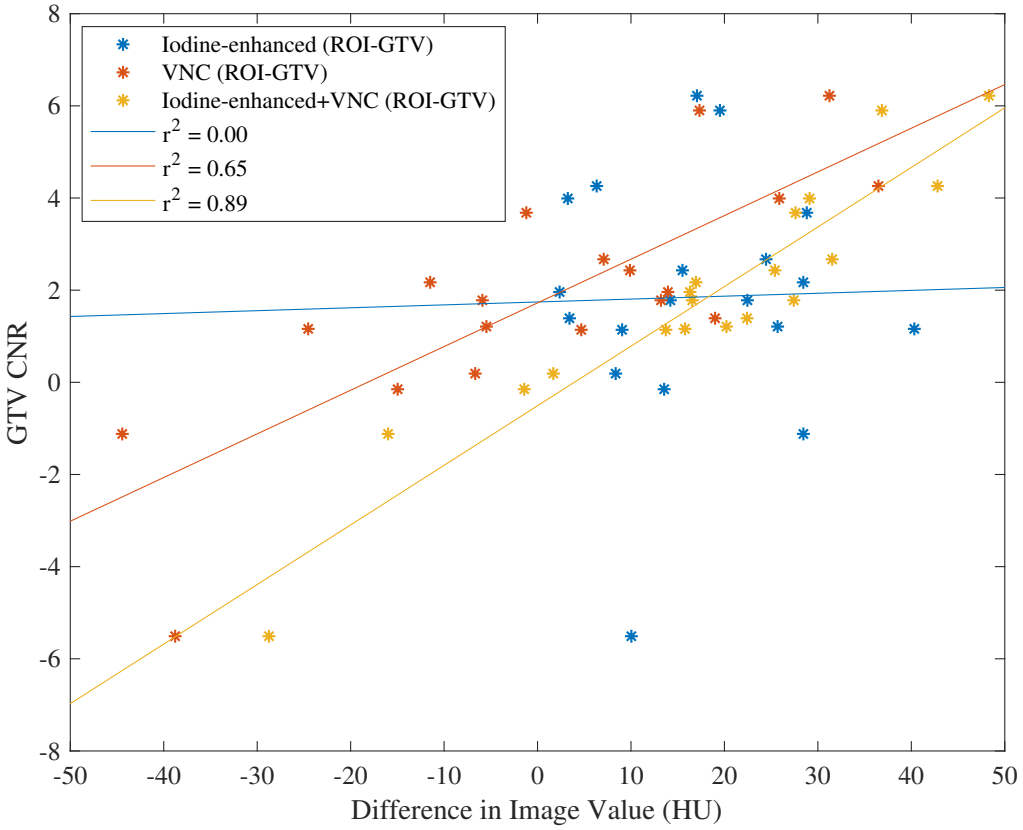

Figure 6.17: Difference in image value (HU) between the healthy tissue ROI and GTV from the iodine-enhanced image (blue), virtual non-contrast image (VNC) (red), and the summation of the results from the two images (yellow) plotted as a function of GTV CNR from the mixed 120 kVp-equivalent images.

based on whether the GTV CNR on the mixed 120 kVp-equivalent images was positive or negative. As expected, the hypo-attenuating tumors had less iodine uptake than surrounding healthy liver tissue and the hyper-attenuating tumors had greater iodine uptake than surrounding healthy liver tissue. This means that the differences in attenuation that were seen on the mixed 120 kVp-equivalent images corresponded to iodine uptake rather than just differences in underlying soft tissue of the tumor and surrounding parenchyma. We did not see any correlation between iodine concentration and patient size, or tumor

visibility for the liver cases. One possible reason for this was because of the different types of liver tumors investigated because hepatocellular carcinomas, cholangiocarcinomas, and liver metastases all have different enhancing properties. Therefore, it becomes difficult to find any correlation of iodine concentration with the entire group, and unfortunately each subgroup was too small for accurate analysis. Future work investigating the iodine uptake in tumor specific cases with a bigger sample size would be beneficial.

6.2.5 Conclusion

This study determined iodine concentration within pancreas and liver tumors and healthy tissue using iodine-enhanced images reconstructed from TwinBeam dual-phase DECT scans. Iodine concentration was determined using size-specific calibration curves correlating image value to concentration in milligrams of iodine per milliliter. Overall, TwinBeam DECT images were able to differentiate pancreas and liver tissue from healthy tissue based on iodine concentration differences.

6.3 Texture analysis of pancreas and liver tumors and healthy tissue

6.3.1 Introduction

As a reminder, virtual monoenergetic images (VMIs) are a type of post-processing DECT images created as if they were acquired from a series of monochromatic x-ray beams. Siemens VMIs can be reconstructed into energies ranging from 40-190 keV.

CTTA of fast kVp switching, dual source, and Dual Spiral DECT images have been investigated for pancreas tumors and other locations of the abdomen [12, 13, 56, 116, 117]. Results from these studies have shown that DECT images perform superiorly compared to single energy CT and that texture analysis metrics are enhanced at lower energy VMIs. Forghani et al. investigates CTTA information extracted with fast kVp-switching DECT images to differentiate regions within the head and neck that was not achievable with conventional SECT [117]. Bayliyan et al. investigated the impact on reconstruction energy of fast kVp-switching DECT VMIs on CTTA parameters and found that reconstruction energy has variable impact on the different CTTA parameters investigated [13]. Skewness and kurtosis showed no change as a function of energy while entropy, mean positive pixel value, and standard deviation decreased with increasing energy [13]. Noid et al. investigated the radiation-induced image CTTA changes from Dual Spiral VMIs and found that low-energy VMIs are superior at identifying radiation-induced CTTA changes compared to SECT [12].

Although the spectral separation and overall accuracy of split-filter DECT is inferior compared to the previously mentioned DECT modalities [34], CTTA of split-filter DECT images is still of importance as there has not been any investigation of CTTA with this system. Efforts in determining the ability of split-filter DECT to differentiate CTTA parameters similarly to other DECT modalities is beneficial to the field of radiology and radiation oncology, as CTTA can be performed retrospectively and is an objective way to assess lesion heterogeneity and characteristics beyond what is possible with subjective visual interpretation [57]. This work investigates the texture analysis features of pancreas

and liver tumors as these tumors are hard to visualize with conventional SECT due to the poor innate contrast, and any additional information that can be collected to differentiate these tumors from healthy tissue is helpful, specifically for radiation therapy. The purpose of this work is to investigate the effect of energy on CTTA of pancreas and liver tumors and healthy tissue using VMIs generated from split-filter DECT.

6.3.2 Methods

Split-filter DECT data from 16 of the pancreas and 17 of the liver cancer patients from Chapters 4 and 5 were used for this investigation. The pancreatic phase from the pancreatic cases and the venous phase of the liver cases were used for this study because based on previous investigation of tumor contrast, these phases represent the highest tumor contrast on average. The raw DECT datasets were used to reconstruct VMIs at energies ranging from 40-90 keV in 5 keV increments in Siemens Syngo.via (VB30) software. The texture analysis of pancreas and liver tumor and healthy tissue was assessed using the entire gross target volume and healthy tissue contours created in Chapters 4 and 5. First order CTTA parameters of the pancreas and liver tumor and healthy tissue were extracted from MIMvista. First order CTTA parameters analyze the histogram of pixels within a given region of interest (ROI). The first order parameters analyzed in this study were mean CT number (MCTN), standard deviation (SD), skewness, and kurtosis.

Skewness is a value relating to the symmetry of a histogram, while kurtosis assess the sharpness of the histogram peak. As Figure 6.18 shows, a positive skewness values means that the histogram is skewed to the right and vice versa, and a positive kurtosis value

means that the histogram has a sharper peak compared to a normal curve. MCTN and SD are simply the average and standard deviation in HU as defined by the histogram of HU within a defined ROI.

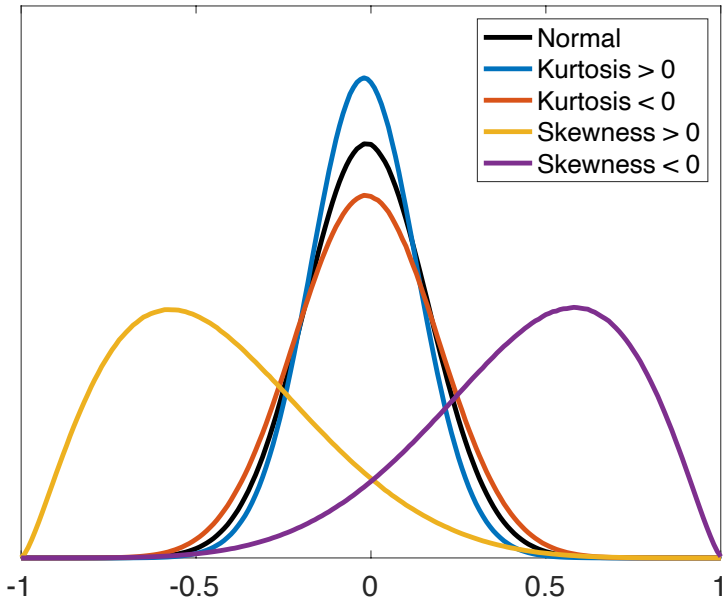

Figure 6.18: Example curves showing the difference in kurtosis and skewness relative to a normal Gaussian curve.

Statistical analysis was performed using unpaired two sample t-tests and analysis of variances (ANOVA). T-tests were used to analyze the difference in CTTA parameters between tumor and healthy tissue while ANOVA was used to analyze the difference in CTTA parameters as a function of energy.

6.3.3 Results

6.3.3.1 Liver results

The kurtosis, skewness, MCTN, and SD of the GTV and healthy tissue ROI for each reconstructed energy averaged over all liver cases are shown in Figure 6.19. The kurtosis of the liver healthy tissue ROIs were all close to zero and did not change as a function of energy as seen by the red curve of Figure 6.19a (P=.91). On the other hand, the GTV kurtosis varied by liver case but there was no statistical trend as a function of VMI energy (P=.10). There was no statistical difference in kurtosis or skewness between the liver GTVs and healthy tissue (P>.05). There was also no trend as a function of energy (P=.879 for kurtosis and P=.461 for skewness).

This study analyzed both hypo- and hyper-attenuating liver tumors based on whether the difference in MCTN between the liver GTV and healthy tissue was positive or negative on the VMI at 40 keV. An example of a hypo- and hyper-attenuating tumor is shown in Figure 6.20.

The MCTN of liver GTVs and healthy tissue increased at lower energies with the (P<<.01). Based on this type of analysis, there were 4 hyper-attenuating liver tumors and 13 hypo-attenuating liver tumors. The average MCTN is shown Figure 6.19c. This type of categorical trend was not apparent for any other type of texture analysis metric. The hyper-attenuating liver GTVs had greater MCTN than the surrounding healthy tissue and vice versa for the hypo-attenuating liver GTVs. VMI at 40 keV also provided the greatest difference in MCTN between liver GTVs and healthy tissue.

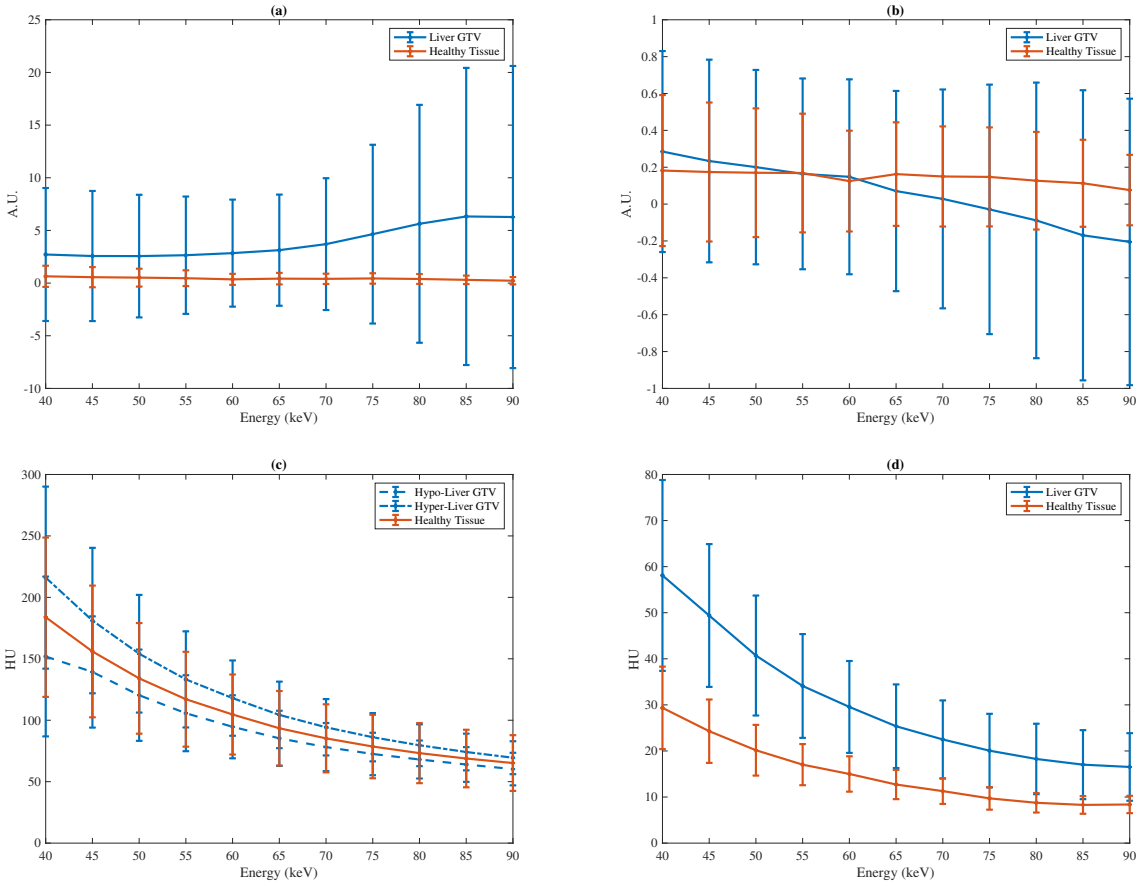

Figure 6.19: Results of kurtosis (a), skewness (b), mean CT number (c), and standard deviation of the liver GTVs and healthy tissue ROIs as a function of VMI energy averaged over all liver cases.

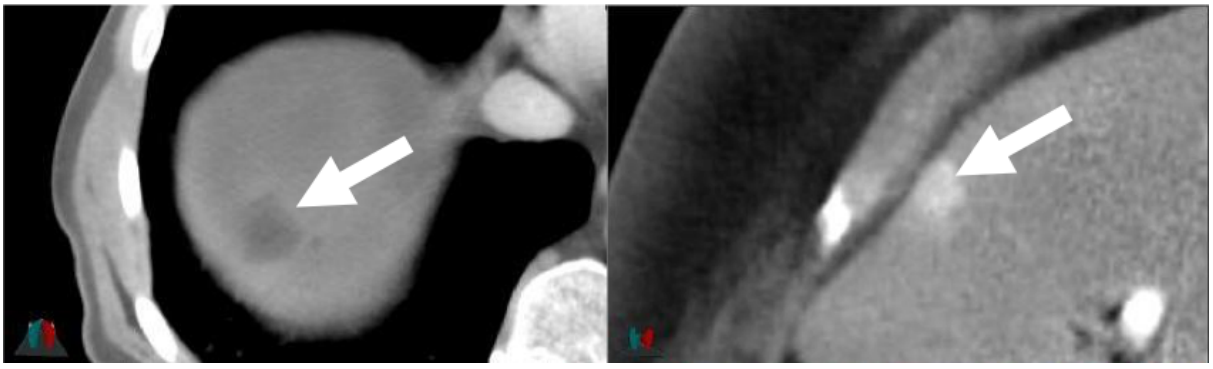

Figure 6.20: An example of a hypo-attenuating (left) and hyper-attenuating (right) liver tumor indicated by the white arrow.

The liver GTVs were more heterogenous than the surrounding healthy tissue ROIs as seen by SD values of Figure 6.19d. To further analyze GTV SD, liver GTV volume was plotted as a function of GTV SD. Figure 6.21 shows the correlation between GTV volume and SD from the VMIs at 40 keV (r^2=0.29). The r^2 value decreases to 0.04 when the same data is plotted from VMI at 90 keV (Figure 6.22).

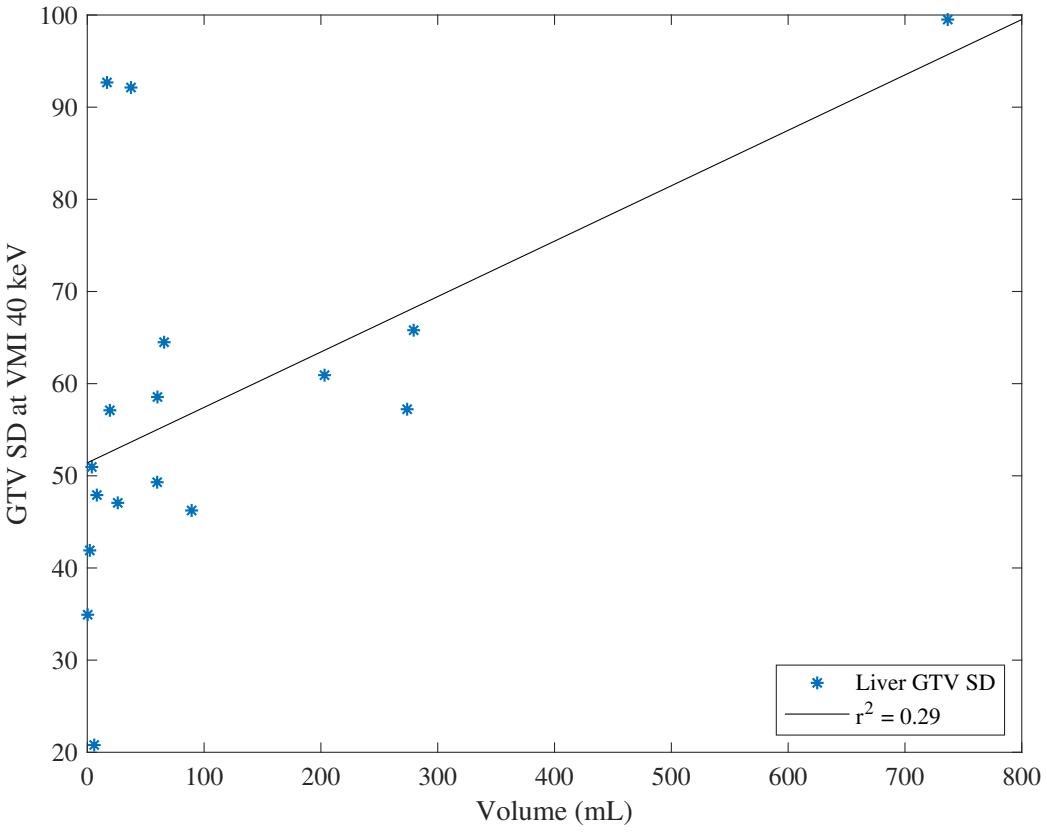

Figure 6.21: The standard deviation (SD) of the image value within the liver GTV from the VMI at 40 keV plotted as a function GTV volume.

To further investigate the histograms of the GTVs and healthy tissue ROIs, the histogram results of a specific liver case was plotted for different VMI energies. Figure 6.23 shows the histogram of the liver GTV and healthy tissue ROI from the VMI at 40 keV, 60 keV and 90 keV. An axial slice from the corresponding VMIs are shown in Figure 6.24.

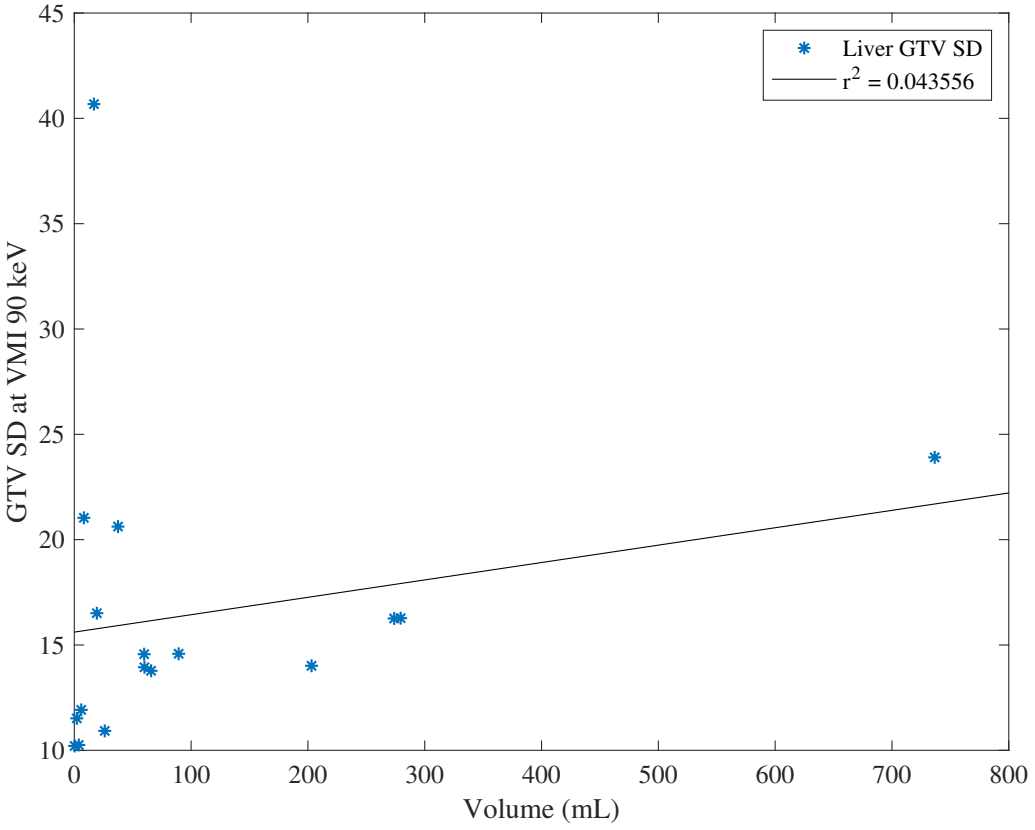

Figure 6.22: The standard deviation (SD) of the image value within the liver GTV from the VMI at 90 keV plotted as a function GTV volume.

These graphs visually show the difference in the CTTA metrics as a function of energy with both the MCTN and SD increasing with decreasing energy. The GTV kurtosis for this specific case at each reconstructed energy was 1.51, 0.648, and 1.789 for the VMIs at 40 keV, 60 keV and 90 keV, respectively. The healthy tissue ROI kurtosis was 0.55, 0.105, and -0.121 and the skewness was 0.157, 0.129, and 0.04 for the VMIs at 40 keV, 60 keV and 90 keV, respectively.

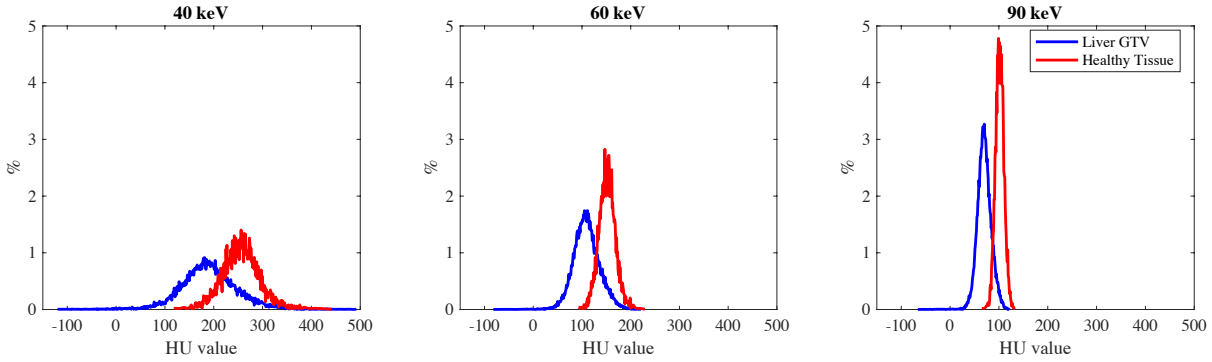

Figure 6.23: Histogram of image values within a liver GTV shown (blue) and parenchyma (red) from the VMIs at 40 keV, 60 keV, and 90 keV shown in Figure 6.24.

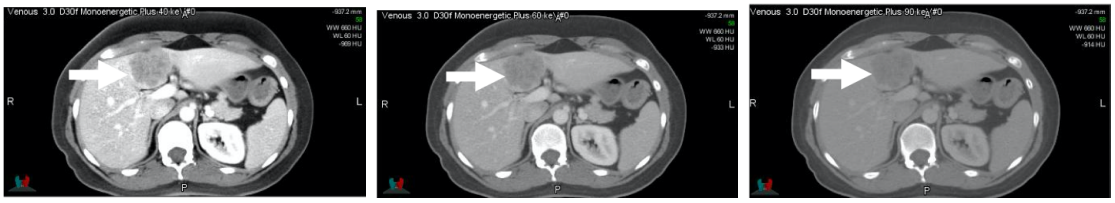

(a) **(b)** **(c)**

Figure 6.24: VMIs at 40 keV (a), 60 keV (b), and 90 keV (b) of a hypo-attenuating liver tumor indicated by the arrow. The histograms of this liver GTV for each image set are shown in Figure 6.23.

6.3.3.2 Pancreas results

Figure 6.25 shows the average kurtosis, skewness, MCTN, and SD for the GTV and healthy tissue at each VMI reconstructed energy averaged over all pancreas cases. The kurtosis and skewness from the pancreas GTVs and healthy tissue ROIs were similar to the liver results. There was a small variation in kurtosis among the pancreas cases and no trend as a function of energy (P=.95). Similar to the liver cases, the GTV kurtosis varied by pancreas case but there was no apparent trend as a function of VMI energy (P=.91).

There was no difference in skewness between the pancreas GTVs and healthy tissue

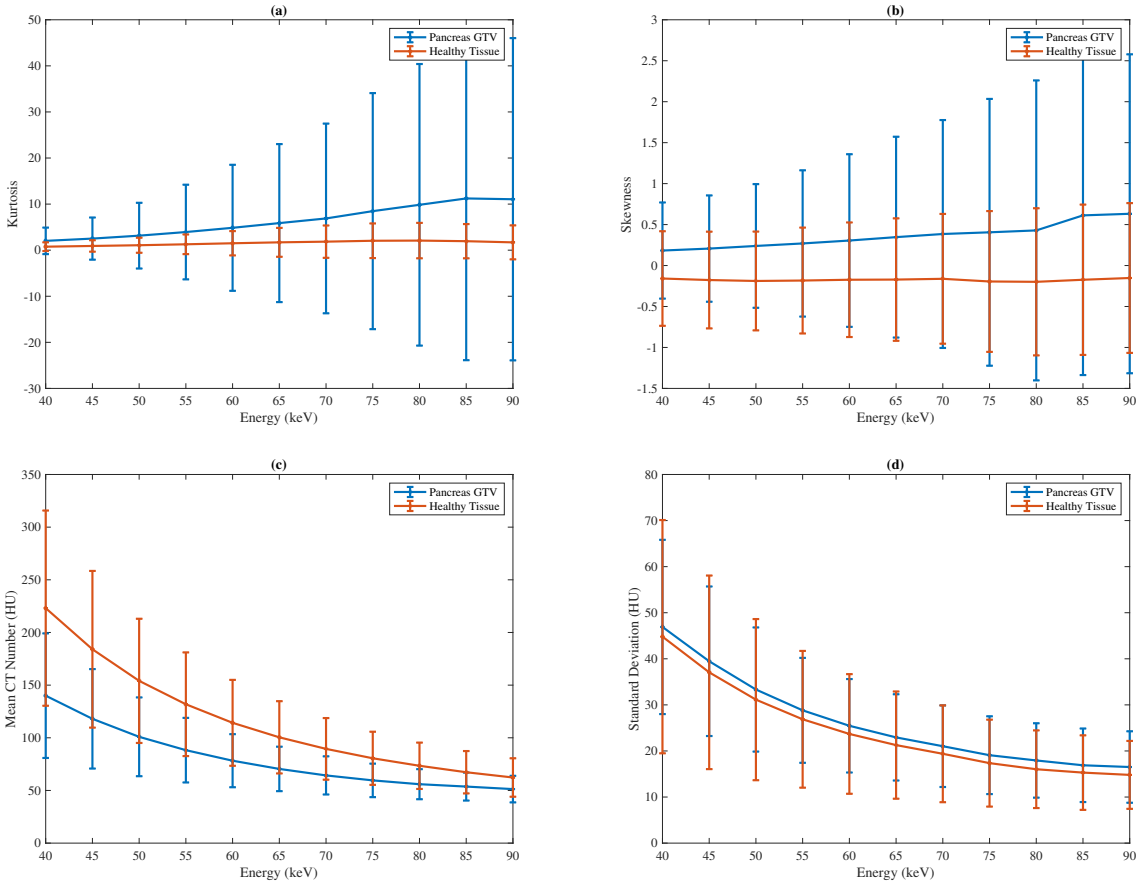

Figure 6.25: Results of kurtosis (a), skewness (b), mean CT number (c), and standard deviation of the pancreas GTVs and healthy tissue ROIs as a function of VMI energy averaged over all pancreas cases.

ROIs. MCTN increased with decreasing energy for both regions (P<.001) and the difference in MCTN was the greatest for VMIs at 40 keV (P=<.001). Unlike the liver results, there was no difference in SD between the GTVs and healthy tissue ROIs (P=1), but the overall SD did increase at low-energy VMIs (P>.001). This was due to the increase in image noise rather than the increase in tumor heterogeneity.

Histograms of one pancreas GTV and surrounding healthy tissue ROI is shown in Figure 6.26 with the VMI corresponding to each graph shown in Figure 6.27. The difference in MCTN at each reconstructed energy is visible from the plotted histograms. The

kurtosis of the healthy tissue ROI for this pancreas case was -0.102, -0.115, and 0.524 and the skewness was -0.273, -0.188, and -0.028 for the VMIs at 40 keV, 60 keV and 90 keV, respectively. The kurtosis of the GTV was -0.348, -0.541, and -0.37 for the VMIs at 40 keV, 60 keV and 90 keV, respectively. The corresponding skewness was 0.274, 0.032, and -0.271.

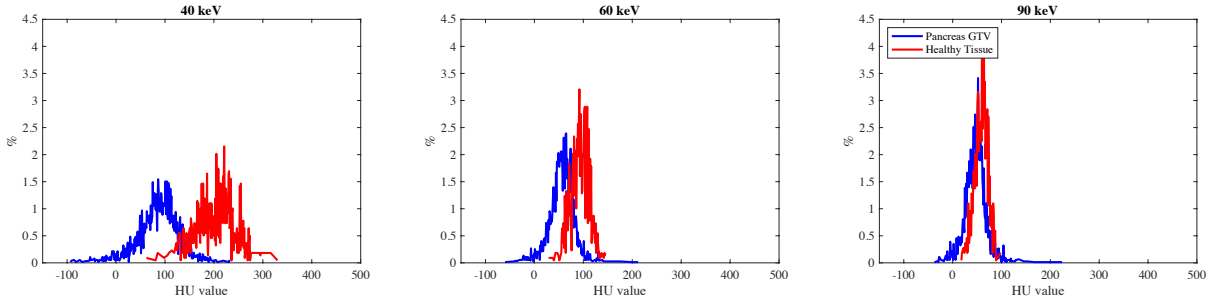

Figure 6.26: Histogram of image values within a pancreas GTV (blue) and healthy tissue ROI (red) from the VMIs at 40 keV, 60 keV, and 90 keV shown in Figure 6.27.

(a) **(b)** **(c)**

Figure 6.27: VMIs at 40 keV (a), 60 keV (b), and 90 keV of a pancreas tumor indicated by the arrow. The histograms of this pancreas GTV for each image set are shown in Figure 6.26.

6.3.4 Discussion and conclusion

This work investigated the first order CTTA parameters of pancreas and liver GTVs and surrounding healthy tissue ROIs. The CTTA parameters were analyzed as a function of VMI reconstructed energy. The kurtosis of the healthy tissue ROIs did not change

with VMI energy and did not greatly vary among patients for both the pancreas and liver cases. On the other hand, the kurtosis from the pancreas and liver GTVs did vary among patients but there was no trend as a function of reconstruction energy. Overall, there was no statistical difference in skewness or kurtosis between tumor and healthy tissue; therefore, neither parameter provided statistically significant information that can be used to differentiate GTV and healthy tissue. This agrees with previous work that also found no statistical difference in kurtosis or skewness as a function of energy [13].

There were cases where the trend of kurtosis and skewness for the GTV was visually apparent when plotted as a function of energy. An examples is shown in Figure 6.28.

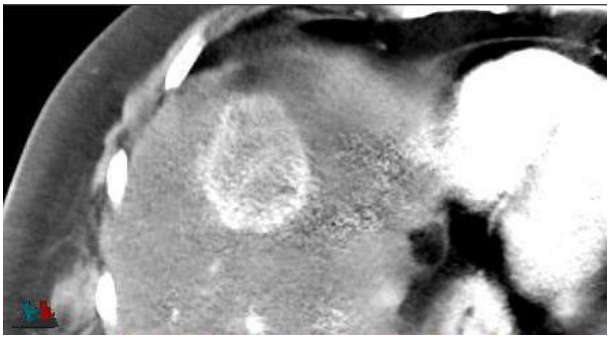

(a)

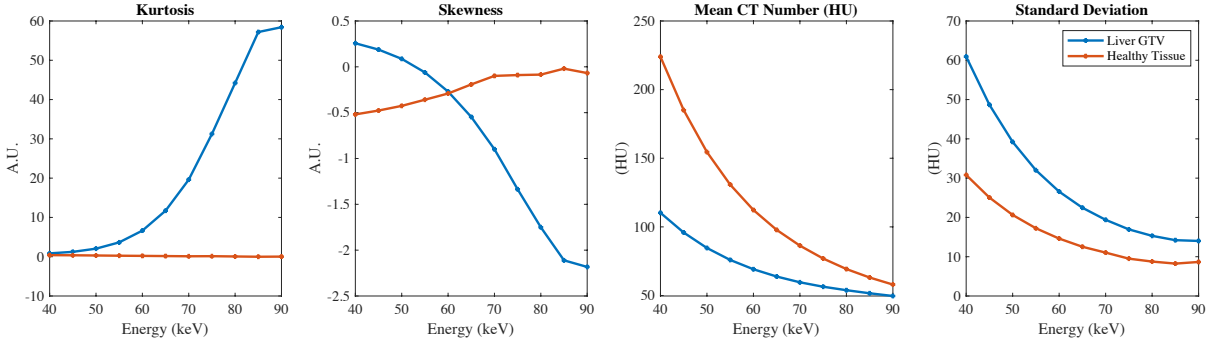

(b)

Figure 6.28: VMI at 40 keV of a liver metastasis (a) and the CTTA parameters at different VMI energy (b).

The average MCTN from both types of GTVs and healthy tissue ROIs increased at

lower energies. This suggests that there was iodine uptake within both regions. Iodine has an atomic number of 53 and exhibits significant changes in attenuation at different energies. This is unlike soft tissue which has a relatively constant attenuation as a function of energy. The iodine uptake in both regions agree with Section 6.2 that quantified the actual iodine concentration within pancreas and liver tumors and healthy tissue. VMIs at 40 keV showed the greatest difference in MCTN between pancreas tumor and healthy tissue. This agrees with Chapters 4 and 5.

Hypo-attenuating liver tumors had statistically lower MCTN compared to surrounding normal tissue. On the other hand, the hyper-attenuating tumors showed no statistical difference in MCTN because of the small subset of hyper-attenuating tumor cases included in this study (n=4). If more cases were included in this group, the statistical significance may increase.

VMI energy had the same impact on the standard deviation of both pancreas tumor and healthy tissue, which increased at lower energies. The increase in SD at low energies was due to the inherent increase in image noise of the split-filter VMIs [34, 96]. There was, on the other hand, a difference in SD between liver GTVs and healthy tissue ROIs. The correlation between tumor volume and heterogeneity was more prevalent for the low-energy VMIs than the high-energy VMIs.

One initial goal of this work was to also quantify second and third order texture analysis parameters of these pancreas and liver cases using a third party software. Unfortunately, the software did not have the ability to import and analyze previously segmented contours, and would not allow for the comparison of the same GTV contour and healthy

tissue ROI across all VMIs from a single case. Hopefully, within the near future, this software will have the capabilities to perform this type of analysis.

The first order texture analysis results of this study serve as a foundation for future studies assessing the applicability of TwinBeam to distinguish radiation-induced changes to the texture of pancreas and liver tumors.

Chapter 7

Electron density and atomic number of pancreas and liver tumor and healthy tissue

7.1 Introduction

Chapters 4 and 5 of this thesis found that VMIs from TwinBeam DECT provided greater contrast and contrast-to-noise ratios (CNR) of pancreatic adenocarcinomas and some liver tumors when compared to virtual single-energy CT (SECT) images. Other DE post-processing images include relative electron density, and effective atomic number. The goal of this chapter is to see if these images created from TwinBeam DECT can provide additional information to aid in the delineation of pancreas and liver tumors. The impact of ADMIRE's iterative reconstruction algorithm on these additional DE post-processing

images will also be investigated.

A material's attenuation, $\mu(E)$ is a contribution of both Compton scatter and photoelectric effect. Therefore, the attenuation is dependent on the electron density, ρ_e and atomic number, Z of the material:

$$\mu(E) \approx a_1 \rho_e f(E) + a_2 \rho_e \frac{Z^n}{E^3} \tag{7.1}$$

where E is energy, n is approximately equal to 3, $f(E)$ is an almost flat function of photon energy, and a_1 and a_2 are proportionality factors [118]. Maps of the relative electron density, $\rho_e/\rho_{e,w}$ and effective atomic number, Z_{eff} can be reconstructed from the low- and high-energy data of DECT as attenuation coefficients are obtained at two different energies. The mathematical derivation to individually determine $\rho_e/\rho_{e,w}$ and Z_{eff} from DECT is thoroughly explained in Hunemohr et al. [118].

The relative electron density and atomic number images are of high interest to the proton therapy realm as they can be used to estimate the stopping power ratio used for dose calculations for proton therapy. These images can be created simply by a click of a button so we wanted to investigate if there is any benefit in examining these images during radiation treatment planning of pancreas and liver tumors.

7.2 Methods

The same raw data used to reconstruct the mixed 120 kVp-equivalent images and VMIs in the previous chapters were also used to reconstruct relative electron density and atomic

number images in Syngo.via. Both the ADMIRE and non-ADMIRE data were used for post-processing. Figure 7.1 and 7.2 are examples of the atomic number and electron density images of a pancreas and liver tumor.

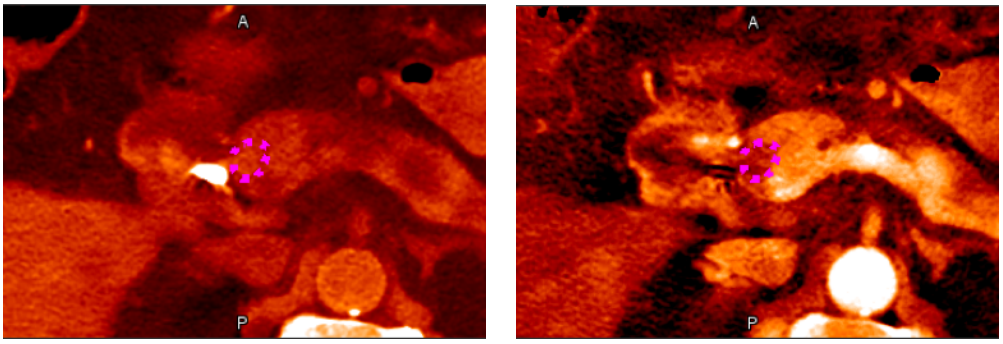

(a) **(b)**

Figure 7.1: Relative electron density (a) and effect atomic number (b) images of a pancreatic adenocarcinoma located in the head of the pancreas. The pancreas GTV is outlined in magenta. Both images are reconstructed with ADMIRE 2.

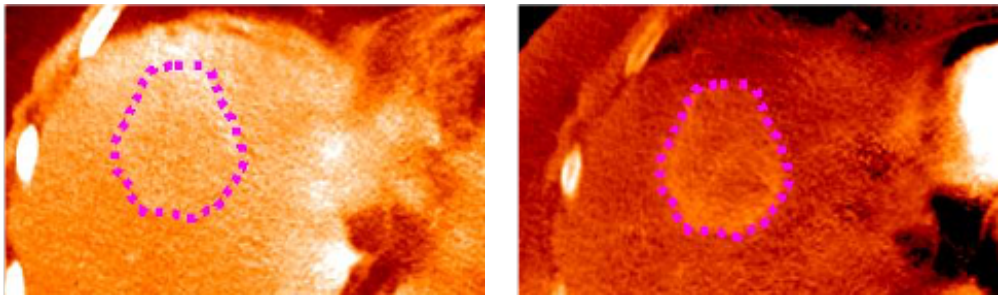

(a) **(b)**

Figure 7.2: Relative electron density (a) and effective atomic number (b) images of a liver tumor. The liver GTV is outlined in magenta. Both images are reconstructed with ADMIRE 2.

The same gross target volumes (GTVs) and healthy tissue regions of interest (ROIs) contoured by an experienced radiation oncologist on the VMI at 57 keV were fused to the relative electron density and effective atomic number images. The contouring and fusions were performed in MIMvista. The mean effective atomic number and relative electron density were collected for each GTV and healthy tissue ROI. Statistical analysis

was performed to assess the difference in electron density and atomic number of the GTV and healthy tissue ROI using an unpaired two sample t-test with a significance P value of 0.05.

7.3 Results

Table 7.1 shows the relative electron density results from the dual-phase image sets reconstructed with and without ADMIRE. The results are given in mean ± standard deviation (SD) average over all pancreas or liver cases. The resulting P values comparing the GTV and healthy tissue ROIs are also listed [119].

Table 7.1: Mean ± SD relative electron density within each pancreas or liver GTV ($\rho_{e,GTV}/\rho_w$) and surrounding healthy tissue ROI, ($\rho_{e,HT}/\rho_w$). P values assessing the difference in the GTV and healthy tissue are also listed.

	$\rho_{e,GTV}/\rho_w$	$\rho_{e,HT}/\rho_w$	P value
Pancreas			
Pancreatic Phase	34.9 ± 11.3	37.0 ± 12.8	0.59
Pancreatic Phase + ADMIRE	35.0 ± 11.6	35.5 ± 13.2	0.89
Portal Venous Phase	40.8 ± 9.1	42.2 ± 13.8	0.71
Portal Venous Phase + ADMIRE	40.8 ± 9.6	40.7 ± 14.2	0.98
Liver			
Arterial Phase	41.03 ± 7.87	46.65 ± 11.66	0.09
Arterial Phase + ADMIRE	40.77 ± 7.81	46.61 ± 11.57	0.08
Venous Phase	45.33 ± 7.97	55.56 ± 15.51	0.01
Venous Phase + ADMIRE	45.45 ± 7.78	55.62 ± 15.21	0.01

The relative electron density of the pancreas GTVs and healthy tissue ROIs was greater during the later portal venous phase. This same trend was apparent for the liver cases, where the greatest electron density in both regions was during the later venous phase. There was no difference in electron density determination between the ADMIRE and non-ADMIRE images (P>.05). There was also no statistical difference in electron

density between the pancreas GTV and healthy tissue ROIs. On the other hand, there was a statistical difference in electron density between the liver tumors and healthy tissue ROIs but only during the venous phase data sets (P=.01).

Table 7.2 shows mean ± SD effective atomic number of the pancreas and liver GTVs and healthy tissue ROIs.

Table 7.2: Effective atomic number within each pancreas or liver GTV ($Z_{eff,GTV}$) and surrounding healthy tissue ROI ($Z_{eff,HT}$). P-values assessing the difference in the GTV and healthy tissue are also listed.

	$Z_{eff,GTV}$	$Z_{eff,HT}$	P value
Pancreas			
Pancreatic Phase	8.03 ± 0.54	8.48 ± 0.47	0.01
Pancreatic Phase + ADMIRE	8.06 ± 0.52	8.56 ± 0.42	0.00
Portal Venous Phase	8.02 ± 0.38	8.29 ± 0.51	0.07
Portal Venous Phase + ADMIRE	8.05 ± 0.36	8.38 ± 0.43	0.02
Liver			
Arterial Phase	7.77 ± 0.36	7.83 ± 0.34	0.65
Arterial Phase + ADMIRE	7.78 ± 0.34	7.80 ± 0.30	0.87
Venous Phase	8.25 ± 0.31	8.34 ± 0.31	0.38
Venous Phase + ADMIRE	8.29 ± 0.29	8.40 ± 0.24	0.21

Unlike the electron density results, there was a significant difference in the effective atomic number of the pancreas GTVs and healthy tissue ROIs from both the pancreatic phase with and without ADMIRE (P<.05). The portal venous phase datasets with ADMIRE also showed a statistical difference in atomic number (P<.05). On the other hand, there was no statistical difference in effective atomic number between liver GTVs and healthy tissue ROIs.

7.4 Discussion

The effective atomic number images demonstrated a statistically significant difference between the healthy pancreas tissue ROIs and pancreatic adenocarcinoma GTVs ($P<.05$). This was not true for the liver cases, as there was no statistical difference in effective atomic number between the two regions. The effective atomic number is dependent on the iodine uptake as greater iodine concentration correlates with greater effective atomic number. Chapter 6 shows that all pancreatic adenenocarcinomas have significantly less iodine uptake than surrounding healthy tissue, while the enhancements of the liver tumors are different for each case. To further analyze the effective atomic number for this liver cohort, the absolute difference in effective atomic number between the liver GTVs and healthy tissue ROIs was calculated and averaged over all cases. The resulting values were statistically greater than zero (Table 7.3, ($P<.001$)), concluding that the effective atomic number of some liver GTVs was smaller relative to surrounding healthy tissue while other cases had greater effective atomic number values relative to surrounding healthy tissue. Overall, the determination and differentiation of effective atomic number for pancreas and liver tumor and healthy tissue agrees with the iodine results of Chapter 6.

Table 7.3: Absolute difference in effective atomic number between the liver GTVs and healthy tissue ROIs ($|Z_{eff,GTV}\text{-}Z_{eff,HT}|$) from each raw DECT dataset averaged over all liver cases. P-value showing statistical significance is also shown.

	$\lvert Z_{eff,GTV}\text{-}Z_{eff,HT}\rvert$	P
Arterial Phase	0.33 ± 0.23	< 0.001
Arterial Phase + ADMIRE	0.33 ± 0.24	< 0.001
Venous Phase	0.25 ± 0.21	< 0.001
Venous Phase + ADMIRE	0.24 ± 0.20	< 0.001

For the relative electron density results, there was no difference between pancreas GTVs and healthy tissue ROIs while there was a statistical difference for the liver cases. This means that the enhancements that are seen in CT images of pancreas tumors are only due to the differences in iodine uptake and that there is inherently no difference in attenuation properties between pancreas tumor and healthy tissue. This was not true for the liver cases included in this study. Although iodine contrast does aid in the visualization of these liver tumors, the underlying soft tissue between the tumor and healthy tissue is different making the GTVs easily identifiable on the relative electron density and virtual non-contrast images. Figure 7.3 shows relative electron density images and virtual non-contrast image of three liver cases. In the virtual non-contrast images the iodine has been subtracted leaving behind the underlying soft tissue.

7.5 Conclusion

In conclusion, electron density DE images could aid in the delineation of pancreatic adenocarcinomas when used in conjunction with VMIs for radiation therapy applications by providing better qualitative and quantitative information of iodine enhancement compared to mixed 120 kVp-equivalent images. On the other hand, the relative electron density images may provide additional information during tumor delineation of liver tumors for radiation treatment planning because the differentiation of liver tumors and healthy tissue is greatly affected by differences in underlying soft tissue and not just iodine uptake.

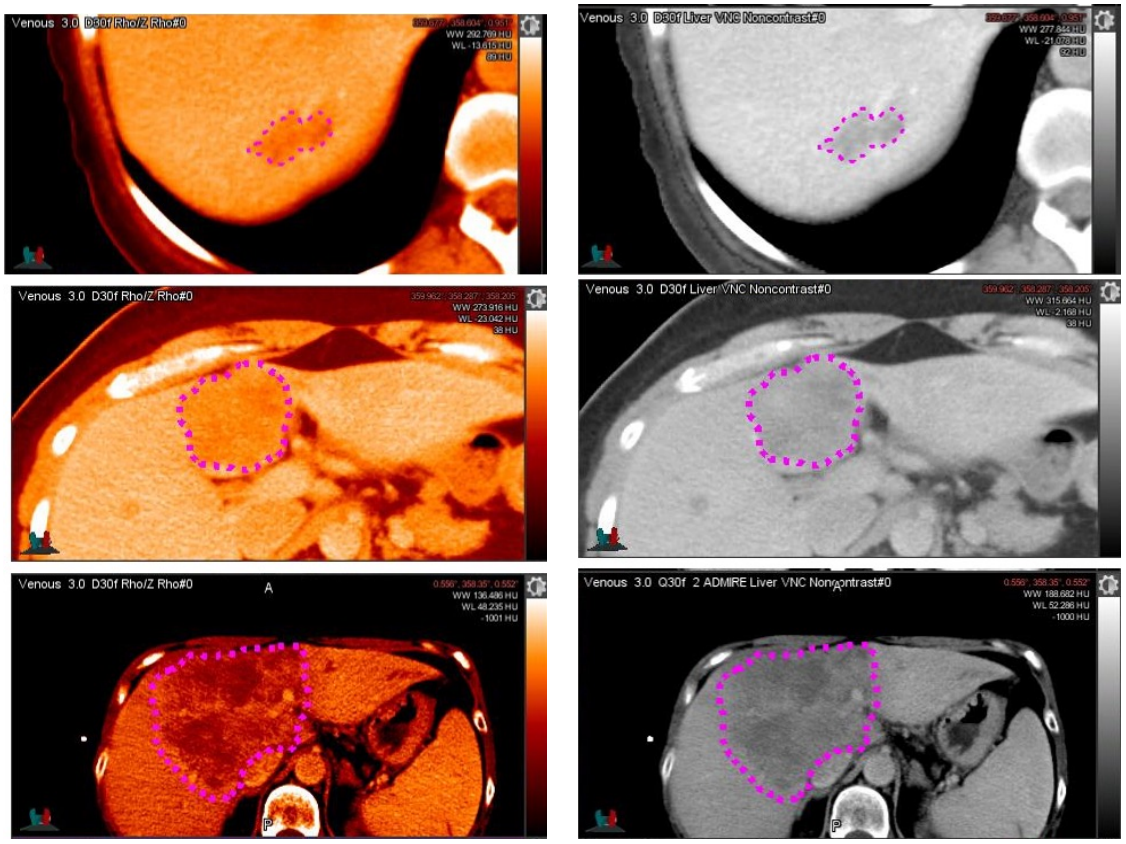

(a) **(b)**

Figure 7.3: Relative electron density (a) and virtual non-contrast (b) images of three liver tumors. The liver GTVs are outlined in magenta.

Chapter 8

Inter-clinician agreement of pancreas and liver gross target volumes using TwinBeam DECT images and virtual SECT images

8.1 Introduction

During radiation therapy treatment planning, the radiation oncologist contours what they visualize to be the gross disease or gross target volume (GTV). The GTV is essentially the gross demonstrable location and extent of the tumor [120]. The GTV is supposed to correspond to where the tumor cell density is the highest and is used to determine the radiotherapy dose location. Once the GTV is defined, additional margins are added to

account for subclinical disease, tumor motion, and setup uncertainty. Tighter margins are necessary for dose-escalated radiotherapy in order to maintain dose constraints to surrounding organs at risk. Dose-escalated radiotherapy has shown to provide better patient outcomes, especially for liver and pancreas cancer patients [23, 29]. It is therefore important to accurately define the GTV as it sets the groundwork for all future radiation planning. The application of DECT for the detection of pancreas and liver GTVs for radiation therapy applications has not been extensively investigated.

Contouring studies are important as the geometric uncertainty associated with contouring variation is larger than that of set-up errors and organ movement for some tumor sites [121]. Several contouring studies have used DECT images to analyze the reproducibility and accuracy of tumors and ROI delineation [73, 122]. Hayden et al. used sequential scan DECT images to investigate the performance of two automatic segmentation techniques by analyzing both qualitative and quantitative metrics [122]. Qualitative metrics included scoring values on a scale of 1 to 4 based on the quality of the auto-segmented contour. Quantitative values included Dice Similarity Coefficient, Hausdorff distance, and center of mass displacement, all of which were used to assess the accuracy of the segmentations compared to manual contours from two radiation oncologists. These quantitative metrics are commonly used in contouring studies to evaluate the agreement between two contours.

Gupta et al. investigated fast kVp-switching DECT images for the reproducibility of pancreas tumor measurements [73]. Similarly to Hayden et al., this study also used qualitative metrics, including tumor conspicuity and edge sharpness on a 5-point scale

to test inter-observer agreement from three radiologists. It was concluded that planar measurements of pancreas tumors were highly reproducible on fast kVp-switching DECT images.

It is also common to collect only qualitative scores when investigating a new imaging modality to assess the overall image quality and to determine whether a clinician prefers a new image type over another. Altenbernd et al. collected subjective scores of image quality on a scale of 1 to 5 during their investigation of dual-source DECT on HCC [7]. It was concluded that low-energy DECT images were more sensitive in detecting HCC but also correlated to low subjective image quality scores [7]. Other studies also included subjective reader analysis during their investigation of the visualization of pancreas and liver tumors with a new imaging modality [38, 69].

Chapter 4 and 5 demonstrated that DECT VMIs can provide greater contrast and CNR compared to virtual single-energy CT images for pancreas and liver tumors. As a result, it was concluded that TwinBeam may improve the delineation of tumors for radiation therapy purposes. The goal of this work is to quantify the impact of TwinBeam images on the delineation of pancreas and liver GTVs by investigating the variation in GTV contours among several clinicians. This work will investigate the inter- and intra-clinician agreement of GTV contour, GTV volume, tumor conspicuity, edge sharpness, delineation confidence, and image quality across three DECT datasets. Pancreas and liver GTV contours on VMIs at 40 keV and iodine-enhanced images will be compared to mixed 120 kVp-equivalent images. This is the first contouring study analyzing both quantitative and qualitative results using TwinBeam DECT images.

Jameson et al. did a full literature review of methods of analysis for contouring studies and found that the most common metric for comparison was volume [123]. It was also concluded that each type of comparison metric had its limitations; therefore, it is beneficial to use multiple metrics when possible. For that reason, this contouring study investigated four metrics to compare GTV contours. Jameson et al. also mentions that the absolute accuracy of contours is hard to address as there is an absence of a gold standard that outlines the true extent of objects being contoured [123]. Therefore, the majority of contouring studies measure the variation of contour differences rather than accuracy. This study attempted to address both the GTV accuracy and variation as all GTV contours created in this study were compared to a reference contour as well as being compared across image sets.

8.2 Methods

8.2.1 Patient population

The pancreas patient data reported in Chapter 4 and the liver data reported in Chapter 5 were used in this contouring study.

8.2.2 Imaging technique and reconstruction

The imaging protocols discussed in Chapter 4 Section 4.2.1 were used to acquire all images in this study. For each individual liver patient, the contrast phase which demonstrated the max CNR value in Chapter 5 was used in the contouring study. For all pancreas

patients, the pancreatic phase was used. Of the 20 liver cases, 7 showed maximum GTV contrast during the arterial phase and 13 showed maximum GTV contrast during the portal venous phase. All datasets were reconstructed with ADMIRE at a strength of 2; representing a low to medium level of noise suppression due to iterative reconstruction.

In summary, 7 arterial phase, 13 portal venous phase, and 18 pancreatic phase raw DECT datasets were reconstructed using ADMIRE 2. From those DECT datasets, three images were then generated: a mixed 120 kVp-equivalent image, a VMI at 40 keV, and an iodine-enhanced image.

8.2.3 Image interpretation

Two separate contouring studies were performed, one for the pancreas cases and one for the liver cases. For each study, the images were evaluated in a randomized order for independent interpretation of the mixed 120 kVp-equivalent image, VMI at 40 keV, and the iodine-enhanced image fused with the mixed 120 kVp-equivalent image. The fusion of the iodine-enhanced image with the mixed 120 kVp-equivalent image was used because the iodine-enhanced images are thought to provide complementary information to anatomical images as opposed to being stand-alone images that can be used independently. For the rest of this paper, this fusion (mixed 120 kVp-equivalent image and iodine-enhanced image pair) will only be referred to as the "iodine-enhanced image". Three radiation oncologists and one radiologist independently contoured the liver and pancreas tumors and analyzed the images in three sessions separated by at least 7 days to reduce recall bias. Clinicians 1, 2, and 3 were the same for the pancreas and liver studies while

Clinician 4 was two different physicians. One clinician from the pancreas study did not finish the third contouring session so there was less than 18 complete datasets for that clinician, but this was taken into account during analysis. The images were not batched by reading session but were rather completely randomized. Four clinicians for each study was determined to be an adequate number of readers based on the number of readers used in past similar contouring studies, which ranged from 1-11 readers [7, 73, 122, 124–126]. Vinod et al. did an extensive literature search of contouring studies between 2000-2014 and found that the number of observers ranged from 3 to 50 with the median being 7 [127].

Each clinician was asked to contour the liver GTV using provided diagnostic information including tumor type, size determined during diagnosis, liver lobe location, and vascular involvement. For the pancreas study, the information provided to the clinicians included the overall location of the tumor (head or tail of the pancreas), the size at diagnosis, the resectability, and a CT slice number of where the tumor is present. Clinicians contoured using the tools in MIMvista software (MIM Software Inc. Cleveland, Ohio) and were allowed to window the images as needed.

Qualitative assessment of GTV contours and image type was assessed using scaling questions. The clinicians were also asked to answer 5 questions on a 5 or 6 point scale evaluating tumor conspicuity, tumor edge sharpness, contouring confidence, and image quality. Tumor conspicuity was rated from 0 = not visible to 5 = easily visible. Tumor edge sharpness was rated from 0 = very poor sharpness to 5 = very sharp. Confidence in tumor contour was rated as 0 = no confidence to 5 = very confident. Overall image

quality was rated from 1 = very poor quality to 5 = very good quality.

8.2.4 Contour comparison

Three evaluation metrics were used to assess the variation in tumor segmentation: Jaccard coefficient (JC), Dice similarity coefficient (DSC), and Hausdorff distance (HD). The DSC calculates the overlap between datasets which in this case were two 3D contours. The DSC is defined using Equation 8.1,

$$\mathrm{DSC} = \frac{2|X \cap Y|}{|X| + |Y|} \tag{8.1}$$

where $|X|$ and $|Y|$ are the volumes of each GTV. A resulting DSC value equal to one corresponds to perfect overlap and a resulting value equal to zero corresponds to no overlap. The JC is also used to gauge the similarity of two sample sets but the calculation is different as shown in Equation 8.2,

$$\mathrm{JC} = \frac{|X \cap Y|}{|X| + |Y| - |X \cap Y|} \tag{8.2}$$

a resulting value of 1 means the two datasets are identical, while a value equal to 0 means the two datasets are completely distinct. The DSC and JC are similar but DSC is more intuitive because it can be seen as the percent overlap between the two contours. The HD measures the distance between two outer surfaces and is extensively described in Rogel et al. [128]. Two identical surfaces have a HD equal to 0 mm and increasing distances indicate more disagreement in contouring surfaces. For this work, the minimum, mean,

and maximum HD between two outer surfaces were collected. The quantitative metrics were calculated in MIMvista, where a workflow was created to compare two ROIs. The metrics were then exported and analyzed in MATLAB.

8.2.4.1 Inter-clinician agreement

Quantitative assessment of GTV contour accuracy and inter-observer variability was performed by calculating the three metrics between the treatment GTV contour, GTV_{treat} and the new GTV contours, GTV_{clin}. GTV_{treat} is the treatment planning GTV that were created on VMIs at 57 keV using all available diagnostic information, diagnostic MRIs, and all CT simulation images. MRI images are the gold standard for diagnosing and delineating pancreas and liver tumors, which is why the treatment planning GTV was chosen as a reference to assess the accuracy and variation of GTV_{clin}.

8.2.4.2 GTV volume

Although volume does not indicate location or shape of a contour, it can be used for GTV comparison. GTV volume was collected for each GTV_{clin} and served as an inter-comparison metric to determine the variability of GTV_{clin} across the different image sets. The volume of each GTV_{clin} from a single image set for each tumor case was averaged across all four clinicians. The coefficient of variation (CV) was then calculated and averaged across all tumor cases and was used to determine whether a single image set provided lower variability than another as a lower CV would indicate less variability in GTV_{clin} volumes.

8.2.4.3 Intra-clinician agreement

The GTV contours were also intra-compared to assess the repeatability in GTV contouring across two image sets from a single clinician. The intra-clinician quantitative metrics were calculated using the GTV_{clin} from two different image sets (Mixed 120 kVp-equivalent vs iodine-enhanced image, Mixed 120 kVp-equivalent vs VMI at 40 keV, and VMI at 40 keV vs iodine-enhanced image). These results were used to determine if two image pairs resulted in more reproducible contours than another image pair.

8.2.5 Statistical analysis

Statistical analysis was performed in MATLAB. Variance component analysis (ANOVA) was used to estimate whether an image set or clinician provided statistically different results than another. ANOVA is a statistical analysis used to determine whether a responsible variable varies among two or more different groups by returning a resulting P value. All statistical tests were two-sided and statistical significance was determined using a P value less than 0.05.

Linear mixed modeling was used to compare the qualitative scores among the three images and between clinicians. Linear mixed modeling is a type of analysis that allows for both fixed and random effects. Kappa statistics were used to determine the inter- and intra-observer agreement of qualitative scoring of tumor conspicuity, tumor edge sharpness, contouring confidence, and overall image quality. Kappa is a statistical analysis used to determine whether a group of scores are in agreement or not in agreement based on the resulting kappa value. Table 8.1 shows the different levels of agreement.

Table 8.1: Scale showing the level of agreement associated with the resulting value for kappa statistics.

κ	Agreement
<0	poor
0-0.2	slight
0.21-0.4	fair
0.41-0.6	moderate
0.61-0.8	substantial
0.81-1	perfect

8.3 Liver Results

8.3.1 Qualitative results

The results illustrated in Figure 8.1 show the distribution of qualitative scores from each clinician for each category and image type for the liver cases. This plot along with the mean values from each clinician (Table 8.2) provide insight on the type of scorer each clinician was. For example, Clinician 1 used the whole scale when rating each image and had a large standard deviation of scored values. Clinicians 2 and 3, on the other hand, had a smaller standard deviation of scoring and tended to rate each image highly. Table 8.2 shows the average results of the qualitative scores across all liver cases and clinicians. The average image quality score was the greatest for the mixed 120 kVp-equivalent image at 3.40, which corresponds to above average image quality, while the average corresponding score for the VMI at 40 keV was 3.33.

The accuracy of the qualitative scores was assessed to determine whether the confidence, tumor conspicuity, and tumor edge sharpness score were correlated with GTV contour accuracy. This was done by correlating each qualitative score with the quantitative metrics assessing the overlap between the GTV_{clin} with the GTV_{treat}. For cases

Table 8.2: Mean qualitative score averaged across all liver cases for each scoring category and image set for each clinician. The mean across all four clinicians is also shown.

Tumor Conspicuity

Clinician	Mixed	VMI	Iodine
1	3.12	3.44	2.69
2	4.33	4.12	3.83
3	3.88	3.29	3.76
4	3.67	3.40	3.41
Mean	3.75	3.56	3.42

Tumor Edge Sharpness

Clinician	Mixed	VMI	Iodine
1	1.53	2.13	2.38
2	3.67	3.47	3.06
3	3.76	3.29	3.41
4	2.67	3.00	2.29
Mean	2.91	2.97	2.78

Confidence

Clinician	Mixed	VMI	Iodine
1	2.29	2.88	2.63
2	3.89	3.65	3.33
3	3.71	3.24	3.41
4	2.80	2.93	2.53
Mean	3.17	3.17	2.97

Image Quality

Clinician	Mixed	VMI	Iodine
1	2.50	2.90	2.70
2	4.15	3.80	3.40
3	4.15	3.60	3.75
4	2.80	3.00	2.50
Mean	3.40	3.33	3.09

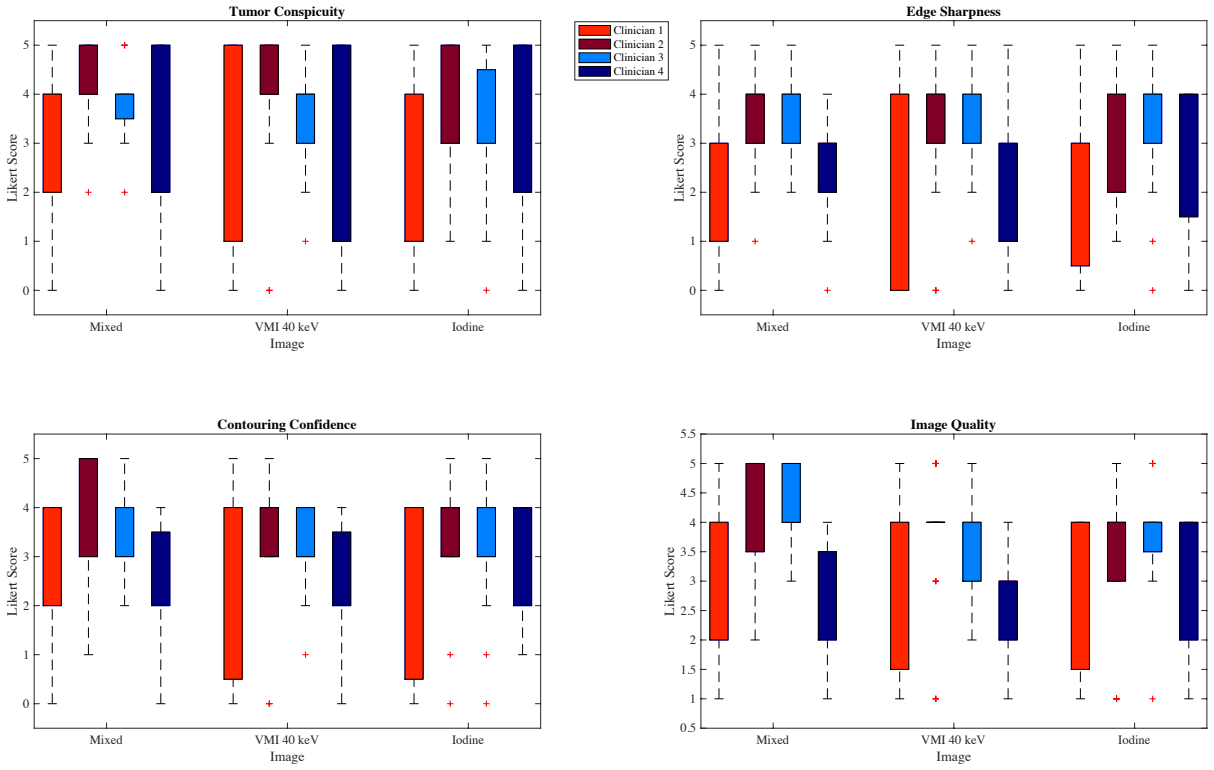

Figure 8.1: Box plots of the qualitative scores given by each clinician for each of the three types of images across all liver tumor cases.

where the minimum Hausdorff distance was greater than one and the DSC and JC were equal to zero, the GTV_{clin} was not near the GTV_{treat}. The scored values corresponded to these cases were altered to zero for all future analysis. The regions that the clinicians were scoring could have been liver cirrhosis, a tumor bed, or another tumor that was not the one specified in the diagnostic sheet.

8.3.1.1 Inter-clinician agreement

The qualitative scores were analyzed using linear mixed modeling and agreement was assessed using kappa statistics. Table 8.3 lists the kappa values resulting from Fleiss' kappa computation to assess the inter-clinician agreement of the qualitative scores. In general, these results show poor to slight agreement amongst clinicians. The reader agreement in

contouring confidence and image quality was the lowest for the mixed 120 kVp-equivalent image.

Table 8.3: Kappa values assessing the inter-clinician agreement in the qualitative scores for each category and image type for the liver contouring study. Higher kappa equates to higher agreement.

	Iodine-enhanced	Mixed	VMI 40 keV
Tumor Conspicuity	0.04	0.10	0.10
Tumor Edge Sharpness	-0.01	0.04	0.09
Confidence	0.11	-0.01	0.10
Image Quality	0.09	0.00	0.07

8.3.1.2 Intra-clinician agreement

The intra-clinician agreement across the three image sets was also investigated (Table 8.4). Clinician 1 showed the highest moderate agreement in tumor conspicuity scoring across all images ($\kappa = 0.40$), meaning that the reader saw almost no difference in tumor conspicuity across image sets. For the rest of the clinicians and qualitative scoring categories, the agreement ranged from slight to fair ($\kappa = 0.04 - 0.29$).

Table 8.4: Kappa values assessing the intra-clinician agreement in the qualitative scores across the three image sets. A greater kappa value corresponds to greater agreement.

	Clinician 1	Clinician 2	Clinician 3	Clinician 4
Tumor Conspicuity	0.40	0.18	0.22	0.22
Tumor Edge Sharpness	0.18	0.12	0.04	0.08
Confidence	0.11	0.27	0.04	0.27
Image Quality	0.06	0.28	0.20	0.29

8.3.1.3 Linear mixed modeling

The linear mixed modeling results comparing the qualitative scores of the mixed 120 kVp-equivalent images against the iodine-enhanced images and VMIs at 40 keV are shown in Table 8.5. Overall, there was no difference in the qualitative scores as all but one of the P values were greater than 0.11. One exception was Clinician 3, who scored the image quality of the VMIs at 40 keV statistically lower than the mixed 120 kVp-equivalent images (P=.03).

The qualitative scores were also analyzed per liver patient. Five out of the 20 liver cases had greater scores of tumor conspicuity, tumor edge sharpness, and contouring confidence scores on the VMIs at 40 keV compared to the mixed 120 kVp-equivalent image from two out of the four clinicians. Figure 8.2 illustrates one example of the five cases. The GTV contrast and CNR of this specific case determined in Chapter 5 was 7.46 HU and 1.14 for the mixed 120 kVp-equivalent image and increased to 12.26 HU and 1.71 for the VMI at 40 keV.

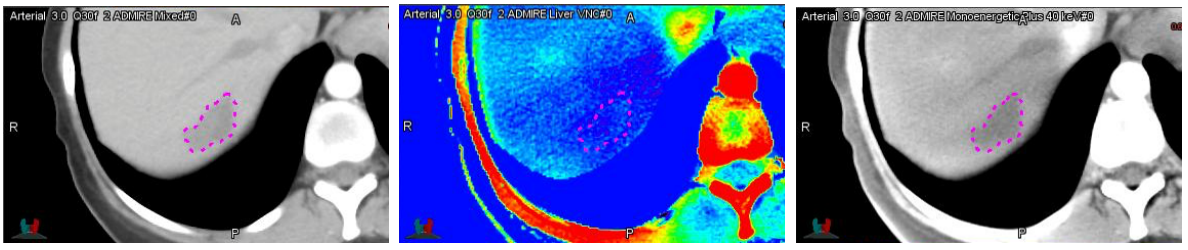

(a) **(b)** **(c)**

Figure 8.2: Mixed 120 kVp-equivalent (a), iodine-enhanced (b), and VMI at 40 keV (c) for liver Patient 17 where the tumor conspicuity, tumor edge sharpness, and contouring confidence scores were greater on the VMI at 40 keV compared to the mixed 120 kVp-equivalent image from two out of the four clinicians.

Table 8.5: Linear mixed model analysis comparing each qualitative scoring category for each image set versus the mixed 120 kVp-equivalent images by Clinician 1, 2, 3, and 4.

Qualitative scoring category		Image Set	Mean Difference Compared to Mixed 120 kVp[a]	LCL 95%	UCL 95%	*P* value
Conspicuity[b]	1	Iodine	-0.45	-1.26	0.36	0.40
		VMI 40 keV	-0.40	-1.33	0.23	0.51
	2	Iodine	-0.15	-0.92	0.62	0.82
		VMI 40 keV	0.20	-0.78	0.58	0.77
	3	Iodine	-0.10	-0.75	0.55	0.82
		VMI 40 keV	-0.50	-1.01	0.41	0.77
	4	Iodine	0.55	-0.11	1.21	0.40
		VMI 40 keV	0.00	-0.11	1.01	1.00
Edge Sharpness[b]	1	Iodine	-0.55	-1.20	0.20	0.27
		VMI 40 keV	-0.35	-1.26	-0.24	0.52
	2	Iodine	-0.10	-0.80	0.40	0.84
		VMI 40 keV	-0.10	-0.80	0.30	0.85
	3	Iodine	-0.30	-0.92	0.42	0.56
		VMI 40 keV	-0.40	-0.86	0.06	0.37
	4	Iodine	0.45	0.03	1.07	0.37
		VMI 40 keV	-0.10	-0.43	0.43	0.84
Confidence[c]	1	Iodine	-0.50	-1.14	0.34	0.32
		VMI 40 keV	-0.40	-1.08	0.38	0.48
	2	Iodine	-0.20	-0.45	0.85	0.71
		VMI 40 keV	-0.05	-0.73	0.53	0.93
	3	Iodine	-0.25	-1.17	0.17	0.44
		VMI 40 keV	-0.40	-1.04	0.24	0.11
	4	Iodine	0.55	-0.65	0.65	0.27
		VMI 40 keV	0.05	-0.77	0.57	0.92
Image Quality[d]	1	Iodine	-0.75	-1.16	0.36	0.04
		VMI 40 keV	-0.35	-0.83	0.13	0.29
	2	Iodine	-0.25	-0.44	0.34	0.51
		VMI 40 keV	-0.05	-0.49	0.39	0.90
	3	Iodine	-0.40	-0.99	0.19	0.11
		VMI 40 keV	-0.55	-0.94	-0.16	0.03
	4	Iodine	0.00	-0.53	0.63	1.00
		VMI 40 keV	-0.40	-0.79	-0.01	0.18

[a] (-) value = score is less than mean score for mixed 120 kVp-equivalent image, (+) value = score is greater than mean score for mixed 120 kVp-equivalent image
[b] 6-point Scale: 0 = barely visualized to 5 = easily visualized
[c] 6-point Scale: 0 = not confident to 5 = very confident
[d] 5-point Scale: 1 = poor to 5 = excellent
keV, kiloelectron-volts; kVp, kiloelectron voltage peak; LCL, lower confidence interval; UCL, upper confidence interval

8.3.2 Quantitative results

8.3.2.1 Inter-clinician agreement

The results of the three quantitative evaluation metrics comparing the GTV_{clin} and GTV_{treat} from each image set are presented in Table 8.6. The mean values were averaged across all liver cases. Statistically, these results showed negligible variation in the GTV_{clin} contours across the different image types ($P>.40$). In other words, there was no statistical difference in quantitative metric based on image type.

Clinician 3 had the overall greatest agreement to the reference contours with the greatest JC, greatest DSC, and smallest HD_{mean} values regardless of image set. Clinician 2 showed the overall worst agreement to the reference contours because on average, the JC, and DSC were the smallest and the HD_{mean} was the greatest for each image set.

As already mentioned, there were cases where each clinician contoured a region of interest that was completely different than the GTV_{treat} contour. But there were also cases where the agreement was almost perfect as the maximum DSC was greater than 0.90.

The quantitative results listed in Table 8.6 were then averaged across all clinicians for each image type to determine if one image correlated with GTV contours that more closely matched the reference contours. These average results are listed in Table 8.7. Although statistically insignificant, the GTV_{clin} contours created on the mixed 120 kVp-equivalent images were on average more similar to the reference contours than ones created on the iodine-enhanced images or VMIs at 40 keV.

Table 8.6: Mean, standard deviation (SD), coefficient of variation (CV), minimum, median, and maximum Jaccard coefficient (JC), Dice Similarity Coefficient (DSC), and mean Hausdorff distance (HD) calculated for each GTV_{clin} compared to the GTV_{treat} averaged across all liver cases. The mean results averaged across all clinicians are shown in Table 8.7.

	Clinician	Image	Mean	SD	CV (%)	Min	Median	Max	P value
JC	1	Mixed	0.47	0.3	62%	0.00	0.46	0.86	0.79
		VMI 40 keV	0.44	0.3	74%	0.00	0.52	0.83	
		Iodine	0.48	0.3	52%	0.00	0.45	0.86	
	2	Mixed	0.49	0.3	54%	0.00	0.52	0.83	0.41
		VMI 40 keV	0.46	0.3	62%	0.00	0.42	0.84	
		Iodine	0.48	0.3	58%	0.00	0.55	0.84	
	3	Mixed	0.42	0.3	80%	0.00	0.41	0.87	0.91
		VMI 40 keV	0.38	0.3	90%	0.00	0.36	0.83	
		Iodine	0.38	0.3	88%	0.00	0.42	0.89	
	4	Mixed	0.45	0.3	74%	0.00	0.53	0.87	0.79
		VMI 40 keV	0.49	0.3	64%	0.00	0.54	0.88	
		Iodine	0.42	0.3	79%	0.00	0.49	0.87	
DC	1	Mixed	0.58	0.3	54%	0.00	0.63	0.93	0.92
		VMI 40 keV	0.54	0.4	68%	0.00	0.69	0.91	
		Iodine	0.61	0.3	45%	0.00	0.62	0.93	
	2	Mixed	0.61	0.3	52%	0.00	0.71	0.93	0.99
		VMI 40 keV	0.58	0.3	59%	0.01	0.76	0.91	
		Iodine	0.58	0.3	57%	0.00	0.69	0.94	
	3	Mixed	0.51	0.4	72%	0.00	0.58	0.93	0.93
		VMI 40 keV	0.46	0.4	85%	0.00	0.53	0.91	
		Iodine	0.47	0.4	82%	0.00	0.59	0.94	
	4	Mixed	0.54	0.4	69%	0.00	0.69	0.93	0.80
		VMI 40 keV	0.59	0.3	59%	0.00	0.70	0.93	
		Iodine	0.51	0.4	73%	0.00	0.65	0.93	
HD_{mean} (mm)	1	Mixed	10.3	17	168%	1.48	3.57	59.98	0.44
		VMI 40 keV	15.9	25	154%	1.50	3.41	82.25	
		Iodine	8.13	14	170%	2.14	3.46	58.53	
	2	Mixed	7.05	7.6	108%	1.50	3.60	29.62	0.98
		VMI 40 keV	6.82	6.3	93%	1.31	3.97	21.11	
		Iodine	7.28	6.6	91%	1.45	4.34	23.58	
	3	Mixed	14.8	20	133%	1.50	4.14	58.22	0.83
		VMI 40 keV	16.8	21	124%	1.31	5.87	61.45	
		Iodine	19.2	26	134%	1.45	5.93	85.00	
	4	Mixed	15.0	20	135%	1.08	3.88	56.26	0.94
		VMI 40 keV	17.9	31	173%	1.22	3.40	113.4	
		Iodine	16.9	26	154%	1.26	4.48	100.4	

Table 8.7: Mean and coefficient of variation (CV) of Jaccard Coefficient, Dice Similarity Coefficient, and mean Hausdorff Distance (HD_{mean}) calculated for each liver GTV_{clin} compared to GTV_{treat} averaged across all clinicians for each image set. Results from each clinician are shown in Table 8.6.

	Image type	Mean	CV (%)	P value
Jaccard Coefficient	Mixed	0.46	6.1%	0.85
	VMI 40 keV	0.45	12%	
	Iodine	0.44	11%	
Dice Similarity Coefficient	Mixed	0.56	8.0%	0.89
	VMI 40 keV	0.54	11%	
	Iodine	0.54	12%	
HD_{mean}(mm)	Mixed	11.8	32%	0.77
	VMI 40 keV	14.4	35%	
	Iodine	12.9	47%	

8.3.2.2 Volume

Figure 8.3 shows the distribution of volumes for each liver GTV_{clin} and GTV_{treat}. Although no single image set resulted in GTV volumes that were statistically different from another (P>.1), Figure 8.3 does point out certain outliers. Clinician 1, for example contoured GTVs that were significantly different in size than the GTV_{treat} volumes as indicated by the blue +.

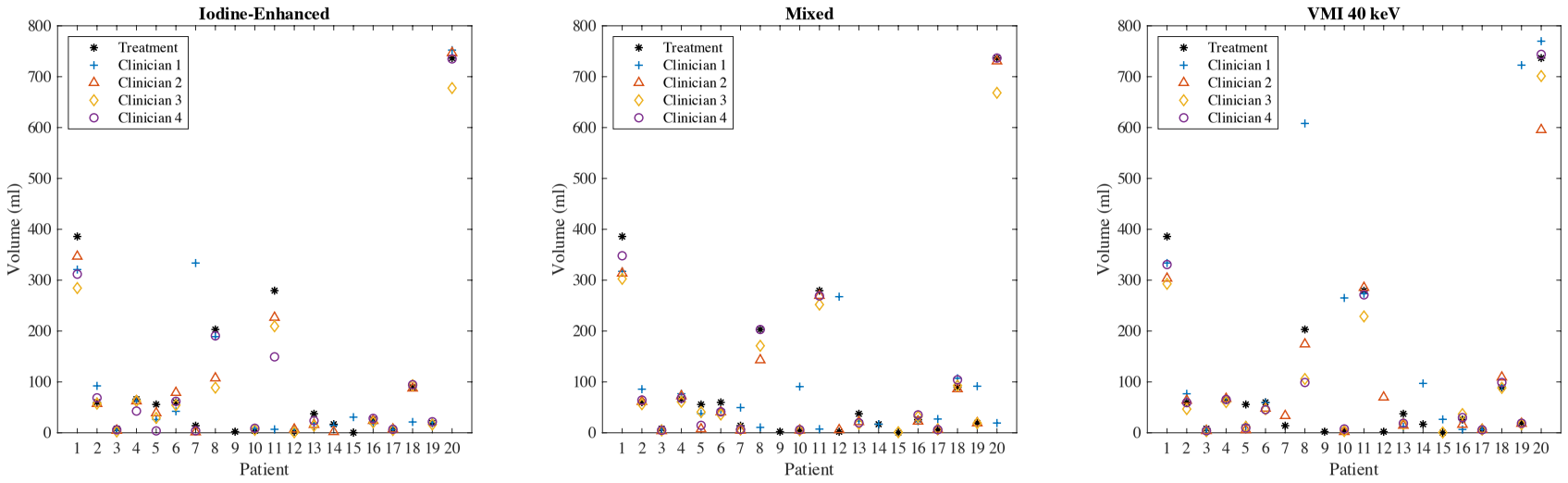

Figure 8.3: GTV_{clin} contour volume from each image set (Iodine-enhanced, Mixed, and VMI 40 keV) shown for each clinician. The referenced GTV_{treat} volume is also plotted.

Table 8.8 lists the volumes from each liver GTV_{treat}, the mean GTV_{clin} volume averaged across all four clinicians, and the corresponding CV for each image set. If there were at least three clinicians that did not accurately contour the tumor on an image set, those cases were disregarded from analysis, which is why there are only 17 cases listed in Table 8.8. Table 8.9 shows the mean CV averaged over all liver cases for each image set. Although, statistically there was no difference in the variation of the GTV_{clin} contours across the different image sets (P=.36), the smallest mean CV was 0.38 from the mixed 120 kVp-equivalent images. The mean CV was 0.58 for the iodine-enhanced images, and 0.46 for the VMIs at 40 keV.

Table 8.8: The volume of each liver GTV_{treat} as well as the mean volume from each GTV_{clin} and the CV averaged across all four clinicians from the iodine-enhanced images, mixed 120 kVp-equivalent images, and VMIs at 40 keV.

Patient	Reference (ml)	Iodine (ml)	CV	Mixed (ml)	CV	VMI (ml)	CV
1	386	316	0.08	320	0.06	315	0.06
2	60.1	68.9	0.24	66.9	0.19	61.6	0.20
3	8.15	4.69	0.32	5.05	0.25	4.39	0.29
4	66.0	57.9	0.17	69.7	0.10	65.4	0.05
5	55.7	24.5	0.61	25.1	0.66	10.6	0.39
6	59.8	59.4	0.26	40.9	0.10	49.8	0.13
7	7.50	113	1.69	16.9	1.30	33.5	0.40
8	203	144	0.37	132	0.64	247	0.99
10	3.87	7.73	0.22	26.7	1.60	69.6	1.87
11	279	148	0.67	200	0.64	265	0.09
12	2.15	4.98	0.68	136.7	1.35	69.9	0.40
13	37.4	18.3	0.23	20.6	0.12	15.6	0.19
16	26.1	22.7	0.19	28.1	0.23	22.4	0.60
17	5.95	6.41	0.12	11.7	0.88	6.28	0.04
18	89.3	74.3	0.48	97.6	0.10	97.0	0.10
19	19.3	19.5	0.14	43.3	0.97	194	1.81
20	737	728	0.05	539	0.65	703	0.11

Table 8.9: Mean CV averaged over all liver cases shown in Table 8.8 for each image type.

	CV_{mean}	P value
Mixed	0.38	
VMI 40 keV	0.58	0.36
Iodine	0.45	

8.3.2.3 Tumor edge sharpness and mean Hausdorff distance

As previously mentioned, HD is a metric used to compare the surfaces between two 3D contours. The HD_{mean} specifically is the mean distance between two surfaces and a greater distance corresponds to greater disagreement and vice versa. This study investigated whether there was a correlation between the clinician scored tumor edge sharpness and the HD_{mean} calculated between the GTV_{clin} and GTV_{treat}. Figure 8.4 shows the distribution of HD_{mean} for each tumor edge sharpness score for all four clinicians. As seen by the data, a smaller HD_{mean} correlated to larger tumor edge sharpness score ($P<<.001$)

8.3.2.4 Intra-clinician agreement

Table 8.10 shows the intra-clinician quantitative results for the liver study. These results compared the GTV_{clin} contours between two image sets (Mixed - Iodine, Mixed - VMI, and VMI - Iodine). On average, the GTV_{clin} contours were equally reproducible regardless of image type ($P>.36$).

Since the mixed 120 kVp-equivalent images served as a surrogate for conventional SECT image, the Mixed - VMI and Mixed - Iodine results were averaged across all clinicians to determine whether the VMI or iodine-enhanced image produced more similar

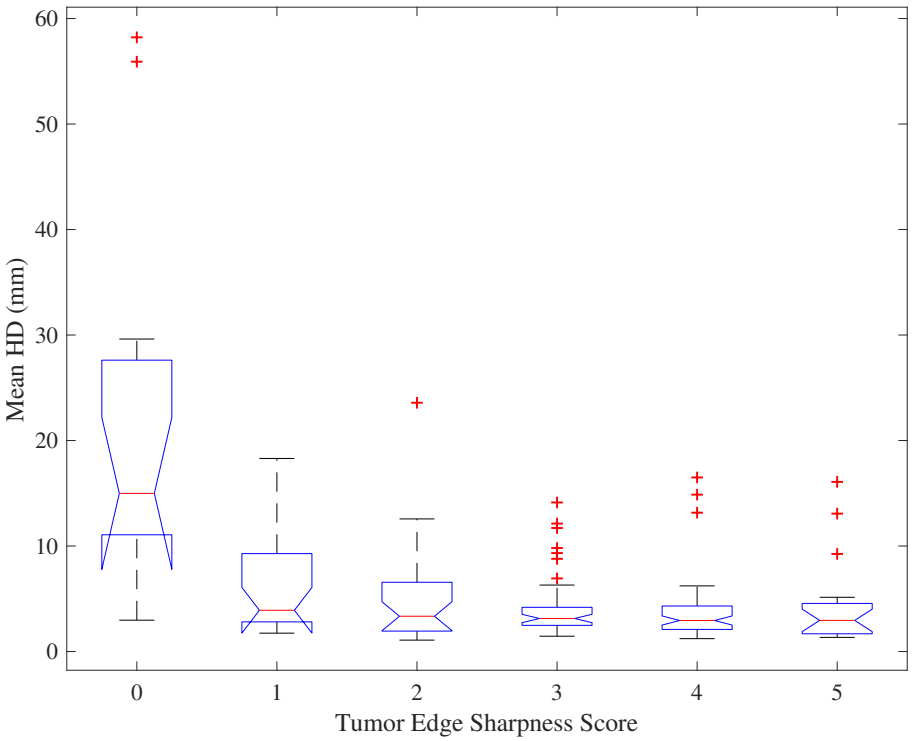

Figure 8.4: HD_{mean} for each tumor edge sharpness score from all four clinicians from all liver cases.

GTV contours by analyzing the variation in these metrics across the clinicians. Figure 8.5 illustrates the consolidated data of JC, DSC, and HD_{max} averaged for each liver patient.

There were two specific liver cases (Patient 6 and Patient 19) that showed statistically greater agreement in GTV_{clin} contours from the Mixed - VMIs at 40 keV pair than the Mixed - iodine-enhanced images. Image sets from Patient 6 are shown in Figure 8.6, where the JC for the Mixed - Iodine pair was 0.59 ± 0.07, while the JC for the Mixed - VMI pair was 0.73 ± 0.07 (P=.03). For this same patient, the DSC was 0.74 ± 0.05 for the Mixed - Iodine pair and 0.84 ± 0.05 for the Mixed - VMI pair (P=.03). The HD_{mean} was 3.49 ± 0.6 mm from the Mixed - Iodine pair and 2.14 ± 0.5 mm for the Mixed - VMI pair (P=.01). The increase in GTV_{clin} contrast and CNR of this tumor determined

from Chapter 5 went from 8.08 HU and 0.52 from the mixed 120 kVp-equivalent image to 93.98 HU and 3.38 from the VMI at 40 keV.

Table 8.10: Jaccard coefficient (JC), Dice Similarity Coefficient (DSC), and mean Hausdorff distance (HD) comparing the GTV_{clin} from the mixed 120 kVp-equivalent image to the VMI at 40 keV (Mixed - VMI), to the iodine-enhanced image (Mixed - Iodine), and the VMI at 40 keV to the iodine-enhanced images (VMI - Iodine) averaged across all liver cases for each clinician.

	Clinician	Image Comparison	Mean	SD	Min	Median	Max	P value
JC	1	Mixed - Iodine	0.59	0.28	0.00	0.63	0.88	0.60
		Mixed - VMI	0.57	0.34	0.00	0.77	0.88	
		VMI - Iodine	0.53	0.32	0.00	0.63	0.86	
	2	Mixed - Iodine	0.62	0.19	0.16	0.68	0.87	0.82
		Mixed - VMI	0.56	0.31	0.00	0.71	0.86	
		VMI - Iodine	0.53	0.30	0.00	0.59	0.85	
	3	Mixed - Iodine	0.52	0.28	0.00	0.58	0.84	0.73
		Mixed - VMI	0.57	0.24	0.00	0.63	0.84	
		VMI - Iodine	0.59	0.25	0.00	0.67	0.84	
	4	Mixed - Iodine	0.56	0.29	0.00	0.60	0.88	0.87
		Mixed - VMI	0.59	0.31	0.00	0.66	0.89	
		VMI - Iodine	0.51	0.32	0.00	0.63	0.87	
DSC	1	Mixed - Iodine	0.69	0.29	0.00	0.77	0.94	0.44
		Mixed - VMI	0.65	0.37	0.00	0.87	0.94	
		VMI - Iodine	0.62	0.35	0.00	0.78	0.92	
	2	Mixed - Iodine	0.75	0.17	0.27	0.81	0.93	0.81
		Mixed - VMI	0.65	0.34	0.00	0.83	0.93	
		VMI - Iodine	0.64	0.33	0.00	0.74	0.92	
	3	Mixed - Iodine	0.63	0.32	0.00	0.74	0.91	0.72
		Mixed - VMI	0.69	0.24	0.00	0.77	0.91	
		VMI - Iodine	0.70	0.27	0.00	0.80	0.91	
	4	Mixed - Iodine	0.67	0.31	0.00	0.75	0.94	0.77
		Mixed - VMI	0.68	0.33	0.00	0.79	0.94	
		VMI - Iodine	0.61	0.36	0.00	0.77	0.93	
HD_{mean} (mm)	1	Mixed - Iodine	8.39	16.05	0.87	2.91	56.97	0.36
		Mixed - VMI	11.05	19.70	0.96	2.15	68.09	
		VMI - Iodine	13.58	22.92	1.07	3.41	85.72	
	2	Mixed - Iodine	5.44	7.19	0.98	2.86	32.96	0.71
		Mixed - VMI	11.33	18.36	1.01	2.15	64.26	
		VMI - Iodine	12.08	19.58	0.80	2.92	71.66	
	3	Mixed - Iodine	12.82	23.06	1.68	2.79	72.69	0.65
		Mixed - VMI	6.90	16.44	1.68	2.38	74.34	
		VMI - Iodine	9.04	18.99	1.53	2.48	72.93	
	4	Mixed - Iodine	9.00	19.05	1.27	2.30	81.53	0.75
		Mixed - VMI	14.68	29.63	0.97	2.63	105.04	
		VMI - Iodine	13.07	22.35	1.31	2.75	71.84	

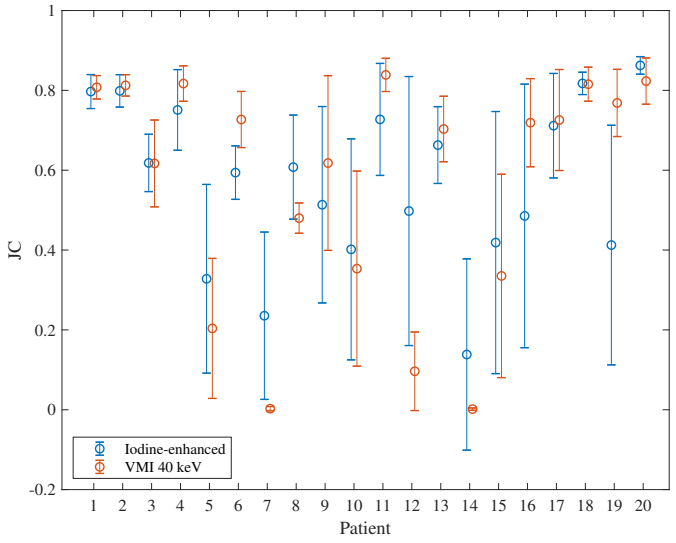

(a)

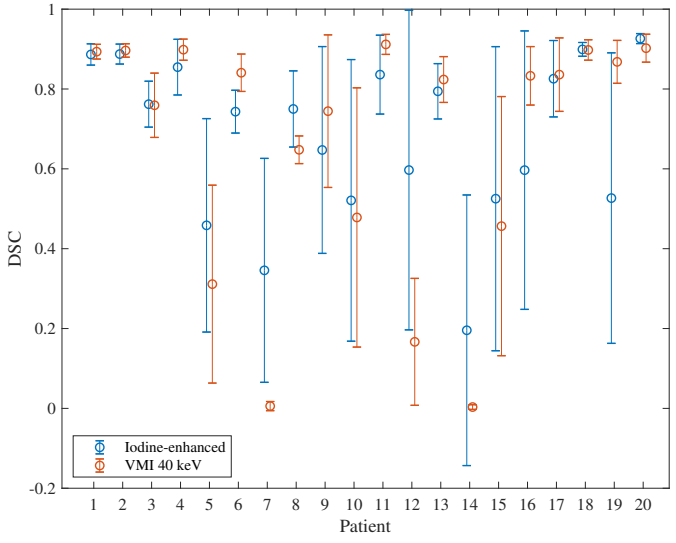

(b)

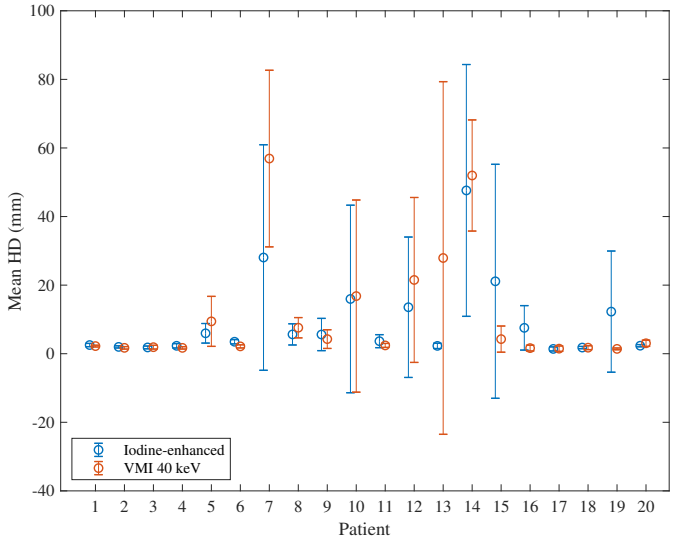

(c)

Figure 8.5: Mean and variation in Jaccard Coefficient (JC) (a), Dice Similarity Coefficient (DSC) (b), and the mean Hausdorff Distance (HD) (c) for each liver case. These metrics were calculated comparing the Mixed - Iodine and Mixed - VMI 40 keV image sets.

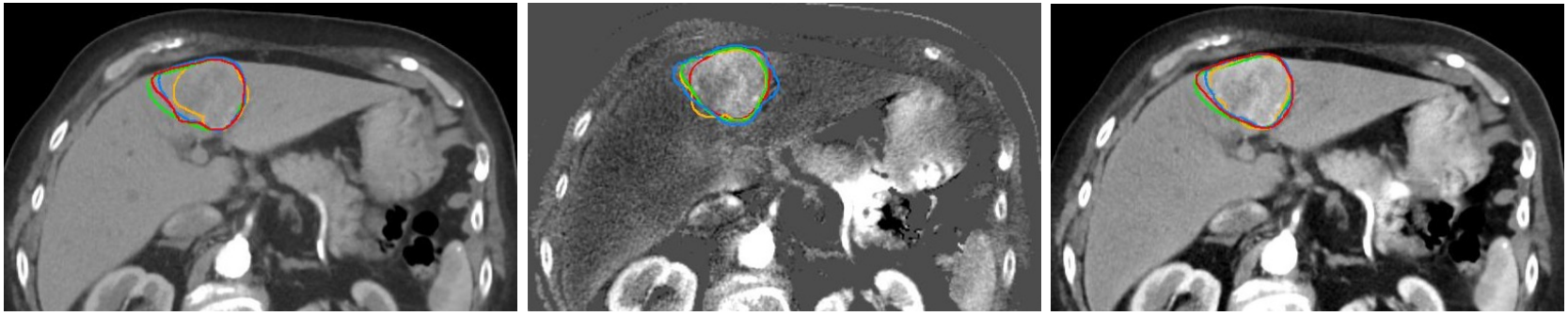

(a) (b) (c)

Figure 8.6: The GTV_{clin} contours of liver Patient 6 from all four clinicians on the mixed 120 kVp-equivalent (a), iodine-enhanced image (b), and VMI at 40 keV (c). The JC and DSC from the Mixed - Iodine was much different than the Mixed - VMI analysis. Red is Clinician 1, blue is Clinician 2, orange is Clinician 3, and green is Clinician 4.

8.4 Pancreas Results

8.4.1 Qualitative results

The qualitative scores of the pancreas cases are displayed in Figure 8.7 to visualize the distribution of scores from each clinician. Clinician 1 and 4 had a greater range of scores, while Clinician 2 and 3 did not. The qualitative scores were then averaged across all pancreas cases and are listed in Table 8.11. Similarly to the liver results, the mixed 120 kVp-equivalent images had on average the greatest image quality score of 3.54 compared to 3.30 and 2.99 for the VMIs at 40 keV and iodine-enhanced images, respectively.

There were also pancreas cases where the clinician contoured a region of interest that was not near the GTV_{treat} as determined by the HD_{max}, DSC, and JC. Therefore, the tumor conspicuity, edge sharpness, and contouring confidence was altered to zero for future analysis. For these cases, the region could have been inflammation due to the pancreas cancer, or the clinician could have been completely guessing on the tumor location did not refer to the given CT slice.

8.4.1.1 Inter-clinician agreement

Table 8.12 list the kappa values resulting from the kappa statistics assessing the inter-clinician agreement in the qualitative scores. As Figure 8.7 and Table 8.12 show, there was large variability in the qualitative scoring and was no agreement in qualitative scores for any of the categories.

Table 8.11: Mean qualitative scores averaged across all pancreas cases for each scoring category and image set. The mean across all four clinicians is also shown.

Tumor Conspicuity

Clinician	Mixed	VMI	Iodine
1	3.00	3.22	2.41
2	2.35	2.18	1.81
3	3.23	3.62	3.00
4	4.18	3.33	2.73
Mean	3.19	3.09	2.49

Tumor Edge Sharpness

Clinician	Mixed	VMI	Iodine
1	2.44	2.56	1.82
2	1.18	1.47	1.06
3	3.00	3.38	2.90
4	3.94	3.67	2.60
Mean	2.64	2.77	2.10

Confidence

Clinician	Mixed	VMI	Iodine
1	2.72	2.67	2.41
2	1.71	1.76	1.38
3	3.00	3.38	3.00
4	4.29	3.67	2.67
Mean	2.93	2.87	2.36

Image Quality

Clinician	Mixed	VMI	Iodine
1	3.83	4.06	3.11
2	2.44	2.28	1.83
3	4.00	3.69	3.80
4	3.89	3.17	3.22
Mean	3.54	3.30	2.99

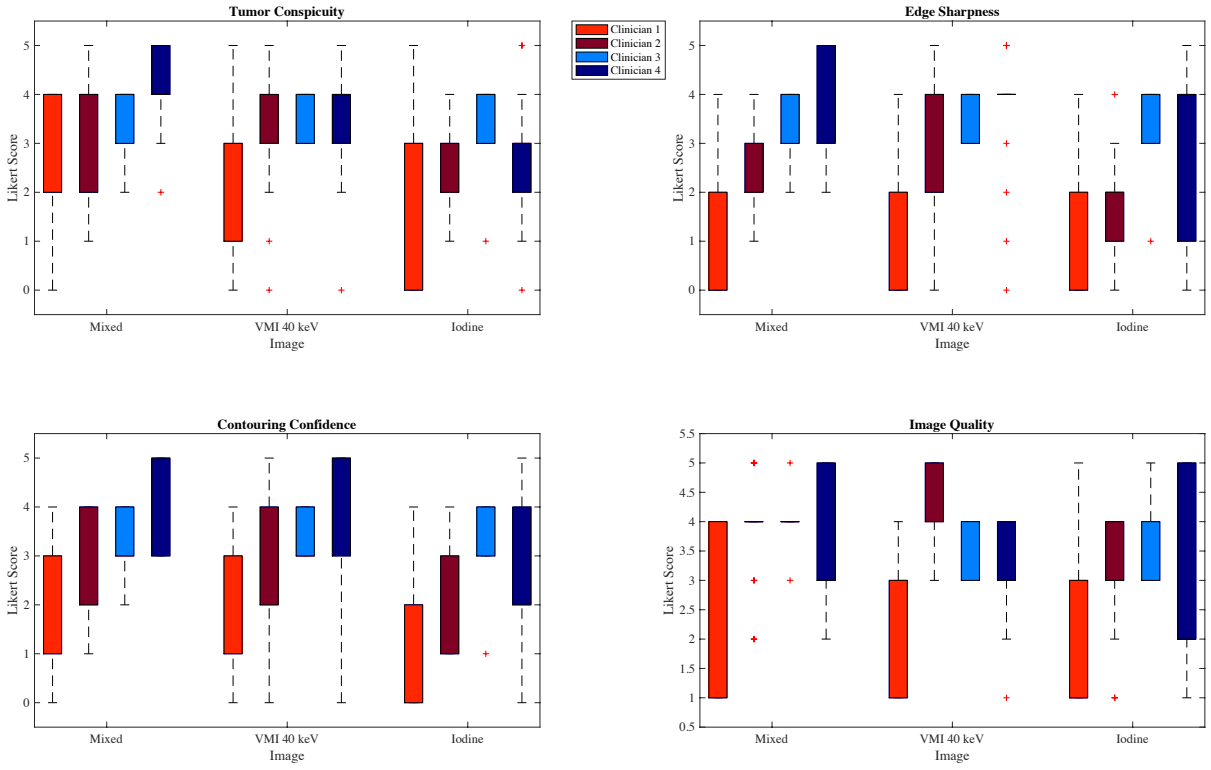

Figure 8.7: Box plots of the qualitative scores given by each clinician for each of the three types of images across all pancreas tumor cases.

Table 8.12: Kappa statistic results showing the inter-clinician agreement in the qualitative scores for each category and image type for the pancreas cases. Higher kappa value equates to higher agreement.

	Iodine-enhanced	Mixed	VMI 40 keV
Tumor Conspicuity	0.03	-0.07	0.01
Tumor Edge Sharpness	0.08	-0.08	-0.01
Confidence	-0.03	-0.09	-0.06
Image Quality	-0.05	-0.02	0.01

8.4.1.2 Intra-clinician agreement

The intra-clinician agreement in the qualitative scores were then assessed for each clinician. There was overall poor to slight agreement in the scores ($\kappa = -0.12 - 0.13$). This means that the clinicians scored differently for each image set. Clinician 3 was one exception, who scored the tumor conspicuity fairly similar across the three image sets

($\kappa = 0.22$).

Table 8.13: Kappa values assessing the intra-clinician agreement in the qualitative scores across the three image sets for the pancreas cases. A greater kappa value corresponds to greater agreement.

	Clinician 1	Clinician 2	Clinician 3	Clinician 4
Tumor Conspicuity	0.02	0.06	0.22	-0.04
Tumor Edge Sharpness	-0.10	0.01	0.04	-0.07
Confidence	0.13	0.01	0.04	-0.06
Image Quality	-0.12	0.09	0.2	-0.12

8.4.1.3 Linear mixed modeling

Table 8.14 shows the mean scoring results from the iodine-enhanced images and VMIs at 40 keV in comparison to the mixed 120 kVp-equivalent images averaged over all pancreas cases. There were several cases where the iodine-enhanced and VMI at 40 keV had statistically different scores than the mixed 120 kVp-equivalent image ($P<.05$). For Clinicians 1 and 4, the mixed 120 kVp-equivalent images scored on average higher than iodine-enhanced images in tumor conspicuity and edge sharpness ($P<0.02$). Clinician 4 also scored the mixed 120 kVp-equivalent images higher in image quality than the VMIs at 40 keV ($P=.03$).

The qualitative results were also analyzed as a function of pancreas patient. The majority of the cases had higher scores on the mixed 120 kVp-equivalent images for all four scoring categories. There were two pancreas cases where two out of the four clinicians scored the VMIs at 40 keV higher than the mixed 120 kVp-equivalent images based on tumor conspicuity, tumor edge sharpness, and contouring confidence. Figure 8.8 shows one of those cases where you can visually see the increase in tumor conspicuity from the

Table 8.14: Linear mixed model analysis comparing each qualitative scoring category for each image set against the mixed 120 kVp-equivalent images by Clinician 1, 2, 3, and 4 from the pancreas cases.

Qualitative scoring category		Image Set	Mean Difference Compared to Mixed 120 kVp[a]	LCL 95%	UCL 95%	*P* value
Conspicuity[b]	1	Iodine	-0.72	-1.29	-0.16	0.02
		VMI 40 keV	0.22	-1.37	-0.07	0.56
	2	Iodine	-0.61	-1.34	0.12	0.12
		VMI 40 keV	-0.17	-0.82	0.49	0.70
	3	Iodine	-0.64	-1.95	0.67	0.35
		VMI 40 keV	0.28	-1.89	0.72	0.65
	4	Iodine	-1.78	-2.74	-0.82	0.00
		VMI 40 keV	-0.78	-2.71	-0.51	0.08
Edge Sharpness[b]	1	Iodine	-0.72	-1.00	0.11	0.04
		VMI 40 keV	0.11	-1.27	-0.18	0.81
	2	Iodine	-0.17	-1.06	0.29	0.63
		VMI 40 keV	0.28	-1.19	-0.04	0.49
	3	Iodine	-0.58	-1.84	0.78	0.39
		VMI 40 keV	0.28	-2.34	0.78	0.63
	4	Iodine	-1.61	-3.04	-0.74	0.01
		VMI 40 keV	-0.22	-1.78	0.34	0.59
Confidence[c]	1	Iodine	-0.44	-0.51	0.96	0.13
		VMI 40 keV	-0.06	-0.80	1.02	0.89
	2	Iodine	-0.39	-0.99	0.66	0.27
		VMI 40 keV	0.06	-0.50	1.05	0.88
	3	Iodine	-0.53	-0.92	1.47	0.44
		VMI 40 keV	0.28	-0.84	1.40	0.63
	4	Iodine	-1.89	-1.59	0.04	0.01
		VMI 40 keV	-0.56	-1.01	0.56	0.20
Image Quality[d]	1	Iodine	-0.72	-0.84	0.73	0.02
		VMI 40 keV	0.22	-0.38	0.83	0.48
	2	Iodine	-0.61	-0.66	0.77	0.05
		VMI 40 keV	-0.17	-0.65	0.32	0.51
	3	Iodine	-0.78	-0.84	1.40	0.34
		VMI 40 keV	-0.19	-1.55	1.16	0.78
	4	Iodine	-0.72	-1.37	0.26	0.20
		VMI 40 keV	-0.78	-1.40	-0.15	0.03

[a](-) value = score is less than mean score for mixed 120 kVp-equivalent image, (+) value = score is greater than mean score for mixed 120 kVp-equivalent image
[b]6-point Scale: 0 = barely visualized to 5 = easily visualized
[c]6-point Scale: 0 = not confident to 5 = very confident
[d]5-point Scale: 1 = poor to 5 = excellent
keV, kiloelectron-volts; kVp, kiloelectron voltage peak; LCL, lower confidence interval; UCL, upper confidence interval

VMI at 40 keV. Based on the results of Chapter 4 the GTV contrast and CNR for this specific case increased from 35.78 HU and 5.90 for the mixed 120 kVp-equivalent image to 161.7 HU and 14.36 for the VMI at 40 keV.

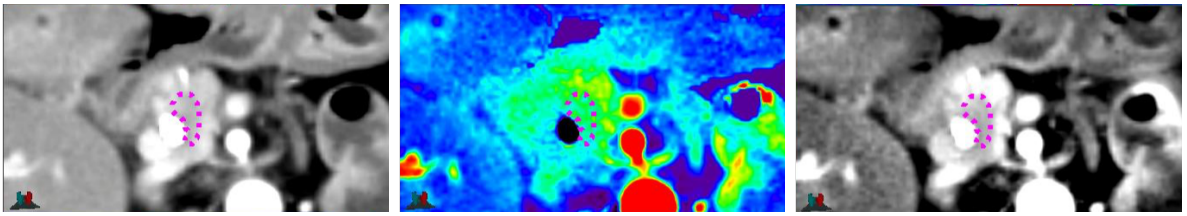

(a) (b) (c)

Figure 8.8: GTV_{treat} shown in magenta on the Mixed 120 kVp-equivalent (a), iodine-enhanced (b), and VMI at 40 keV (c) for pancreas Patient 17 where the tumor conspicuity, tumor edge sharpness, and contouring confidence scores were greater on the VMI at 40 keV compared to the mixed 120 kVp-equivalent image from two out of the four clinicians.

8.4.2 Quantitative results

8.4.2.1 Inter-clinician agreement

The quantitative results comparing the GTV_{treat} and GTV_{clin} for the pancreas cases are presented in Table 8.15. Although there was no statistical difference in the evaluation metrics across the different image types (P>.10), the VMIs at 40 keV provided the greatest JC and DSC and smallest HD_{mean}. Clinician 4 created GTV contours that were on average most similar to the reference GTV contours. On the other hand, Clinician 2 provided GTV contours that were least similar to the reference contours.

There were instances were a clinician did not accurately contour the GTV even with the provided diagnostic information as the minimum JC and DSC were zero. On the

other hand, the greatest overlap determined by the DSC was only 0.83 from the mixed 120 kVp-equivalent images of Clinician 4.

Table 8.16 shows the results of Table 8.15 averaged across all clinicians. The GTV contours created from the VMIs at 40 keV were statistically more similar to the reference contours and considered more accurate based on the HD_{mean} values (P=.04).

8.4.2.2 Volume

Table 8.17 lists the GTV_{treat} volumes, the mean GTV_{clin} volumes averaged across all clinicians, and the corresponding CV. Each GTV_{clin} volume was much greater than the reference contours except for pancreas Patient 18. Scatter plots of each GTV_{treat} and GTV_{clin} are shown in Figure 8.9.

Table 8.15: Mean, standard deviation (SD), coefficient of variation (CV), minimum, median, and maximum Jaccard coefficient (JC), Dice Similarity Coefficient (DSC), and mean Hausdorff distance (HD) calculated for each GTV_{clin} from each image set compared to the GTV_{treat} averaged across all pancreas cases. The mean results averaged across all clinicians is shown in Table 8.16.

	Clinician	Image	Mean	SD	Min	Median	Max	ANOVA P value
JC	1	Mixed	0.20	0.2	0.04	0.14	0.55	0.77
		VMI 40 keV	0.21	0.2	0.04	0.15	0.55	
		Iodine	0.17	0.2	0.00	0.13	0.65	
	2	Mixed	0.19	0.1	0.00	0.16	0.52	0.81
		VMI 40 keV	0.19	0.1	0.00	0.19	0.48	
		Iodine	0.17	0.1	0.00	0.14	0.50	
	3	Mixed	0.20	0.2	0.00	0.18	0.58	0.64
		VMI 40 keV	0.22	0.2	0.02	0.13	0.55	
		Iodine	0.15	0.2	0.00	0.10	0.47	
	4	Mixed	0.30	0.2	0.00	0.29	0.71	0.27
		VMI 40 keV	0.33	0.1	0.04	0.34	0.57	
		Iodine	0.23	0.2	0.00	0.26	0.61	
DSC	1	Mixed	0.31	0.2	0.07	0.24	0.71	0.70
		VMI 40 keV	0.32	0.2	0.07	0.27	0.71	
		Iodine	0.27	0.2	0.00	0.23	0.78	
	2	Mixed	0.30	0.2	0.00	0.28	0.68	0.79
		VMI 40 keV	0.30	0.2	0.00	0.32	0.65	
		Iodine	0.26	0.2	0.00	0.25	0.66	
	3	Mixed	0.30	0.2	0.00	0.31	0.73	0.65
		VMI 40 keV	0.33	0.2	0.04	0.23	0.71	
		Iodine	0.24	0.2	0.00	0.17	0.63	
	4	Mixed	0.42	0.3	0.00	0.44	0.83	0.20
		VMI 40 keV	0.48	0.2	0.08	0.51	0.72	
		Iodine	0.33	0.3	0.00	0.42	0.76	
HD_{mean}	1	Mixed	8.24	4.1	3.49	7.04	18.4	0.28
		VMI 40 keV	7.75	3.7	2.59	8.40	14.0	
		Iodine	10.2	6.1	2.39	9.01	26.6	
	2	Mixed	9.98	8.8	3.10	6.80	36.8	0.77
		VMI 40 keV	9.03	5.7	4.05	7.03	23.7	
		Iodine	11.0	9.9	2.78	7.03	37.5	
	3	Mixed	9.17	7.3	2.30	6.49	24.1	0.78
		VMI 40 keV	7.81	5.0	2.55	7.37	21.6	
		Iodine	9.39	5.4	3.63	9.17	20.3	
	4	Mixed	6.38	5.2	0.83	4.43	18.8	0.10
		VMI 40 keV	5.15	5.2	1.33	3.39	22.4	
		Iodine	10.4	11	1.08	6.21	41.1	

Table 8.16: Mean and coefficient of variation (CV) of Jaccard Coefficient, Dice Similarity Coefficient, and mean Hausdorff Distance calculated for each pancreas GTV_{clin} compared to GTV_{treat} averaged across all clinicians for each image set. Results from each clinician are shown in Table 8.15.

		Mean	CV (%)	P value
Jaccard Coefficient	Mixed	0.22	23%	0.30
	VMI 40 keV	0.24	26%	
	Iodine	0.18	19%	
Dice Similarity Coefficient	Mixed	0.33	18%	0.22
	VMI 40 keV	0.36	23%	
	Iodine	0.27	15%	
HD_{mean}(mm)	Mixed	8.4	18%	0.04
	VMI 40 keV	7.4	22%	
	Iodine	10.3	7.0%	

Table 8.17: The volume of each pancreas GTV_{treat} volume as well as the mean volume from each GTV_{clin} and the CV averaged across all four clinicians from the iodine-enhanced images, mixed 120 kVp-equivalent images, and VMIs at 40 keV.

Patient	Reference (ml)	Iodine (ml)	CV	Mixed (ml)	CV	VMI (ml)	CV
1	0.527	6.11	0.50	12.3	0.33	13.4	1.08
2	3.53	37.4	0.65	38.9	0.69	46.3	0.87
3	5.32	18.7	0.68	15.0	0.96	16.0	0.67
4	9.21	17.4	0.53	15.5	0.24	17.6	0.32
5	1.64	10.18	0.24	14.0	0.61	8.11	0.58
6	5.56	19.9	0.69	10.4	0.20	22.1	0.55
7	7.50	29.7	0.63	35.1	0.47	28.0	0.52
8	1.50	7.59	0.26	9.06	0.18	11.0	0.42
9	25.9	50.3	0.13	49.4	0.09	45.2	0.15
10	2.57	5.95	0.50	7.23	0.21	5.77	0.86
11	0.943	4.11	0.68	6.14	0.68	6.44	0.80
12	2.31	32.6	0.35	33.1	0.22	22.9	0.51
13	2.07	23.6	0.58	21.3	0.21	21.1	0.35
14	2.82	10.4	0.52	9.56	0.26	9.38	0.50
15	0.795	7.35	0.62	8.54	0.51	9.86	0.57
16	2.76	12.7	0.75	7.23	0.16	12.5	0.84
17	1.41	6.37	0.37	5.23	0.47	5.94	0.49
18	29.3	19.3	0.40	13.3	0.34	17.4	0.49

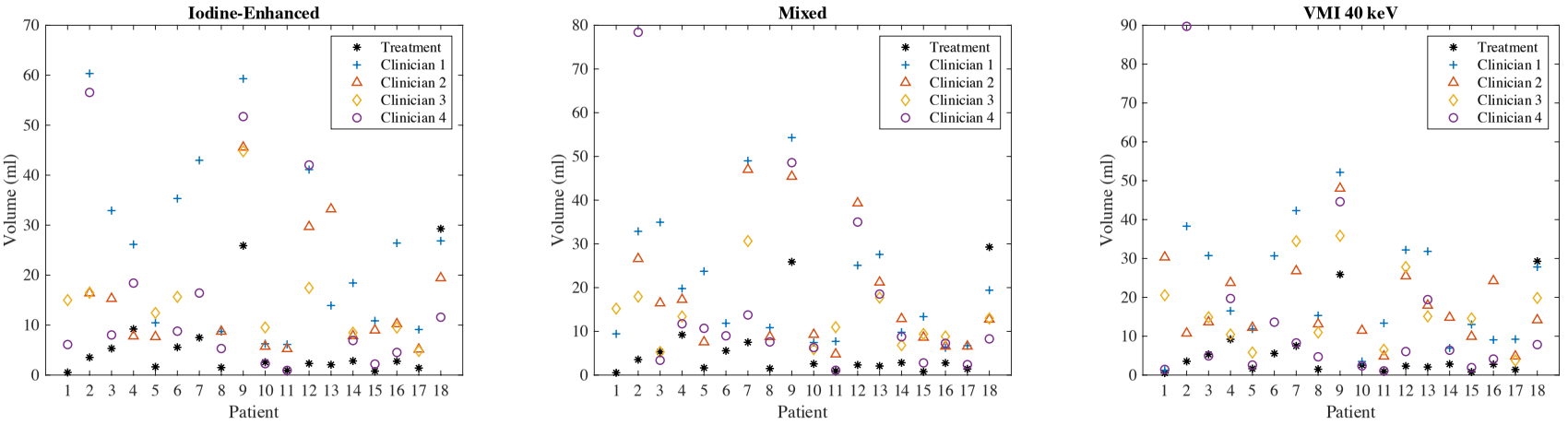

Figure 8.9: Pancreas GTV_{clin} contour volumes from each image set (Iodine-enhanced, Mixed, and VMI 40 keV) shown for each clinician. The referenced GTV_{treat} volume is also plotted.

The CV was then averaged across all patients for each image type (Table 8.18). The variation in the GTV_{clin} volumes was statistically smaller for the mixed 120 kVp-equivalent images with a CV equal to 0.38 compared the iodine-enhanced images (CV = 0.50) and VMIs at 40 keV (CV = 0.59).

Table 8.18: The average coefficient of variation (CV) of GTV_{clin} volumes contoured from each image type averaged across all pancreas cases. The P value listed is from ANOVA test.

	CV (%)	P value
Mixed	0.38	
VMI 40 keV	0.59	0.02
Iodine	0.50	

Figure 8.10 shows an axial slice of Patient 7 with the GTV_{clin} contoured by Clinician 1 on each of the three image sets as well as the reference GTV_{treat} contour. In this example, the difference in volume between the GTV_{treat} and the GTV_{clin} contours is easily apparent.

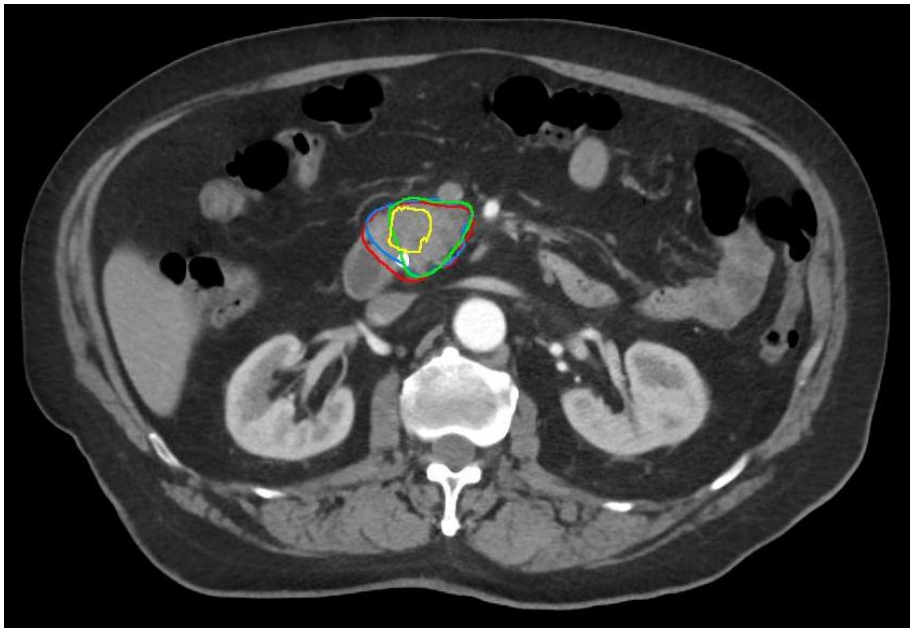

Figure 8.10: Mixed 120 kVp-equivalent of pancreas Patient 7 with the GTV_{treat} in yellow and the GTV_{clin} from the three different image sets (mixed in red, iodine-enhanced in green and VMI at 40 keV in blue) from Clinician 1.

8.4.2.3 Tumor edge sharpness and mean Hausdorff distance

The correlation between the clinician scored tumor edge sharpness and the HD_{mean} between the GTV_{clin} and GTV_{treat} was also investigated for the pancreas cases. Figure 8.11 shows the distribution of HD_{mean} for each tumor edge sharpness score. Greater tumor edge sharpness score corresponded to smaller HD_{mean} ($P<<.003$).

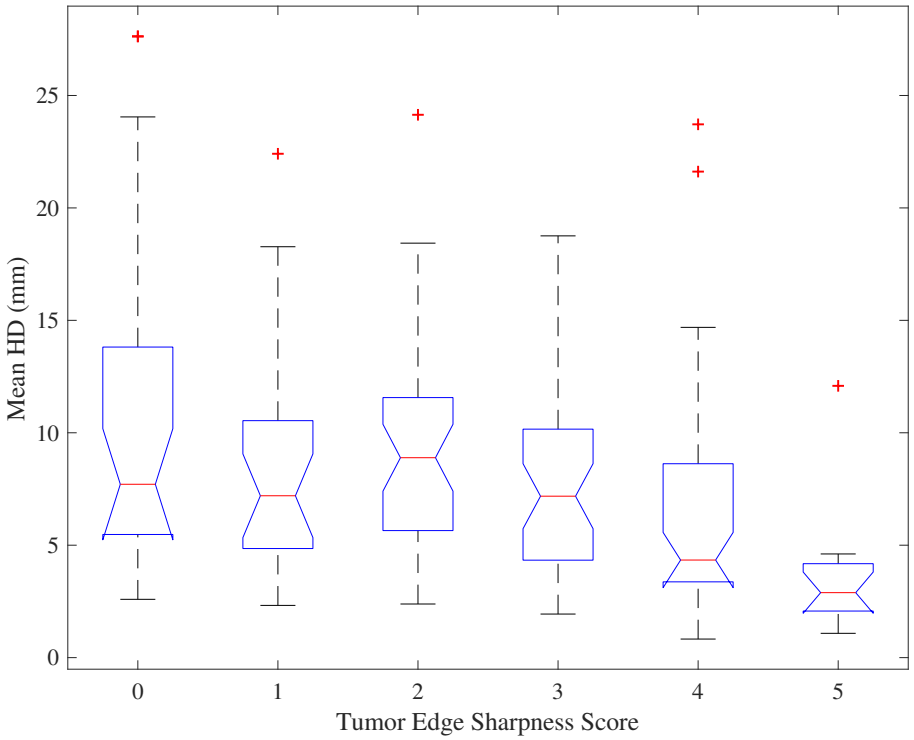

Figure 8.11: Mean Hausdorff Distance (HD) for each tumor edge sharpness score from all four clinicians for all pancreas cases.

8.4.2.4 Intra-clinician

The same intra-clinician analysis was performed for the pancreas cases. The JC, DSC, and HD_{mean} was calculated using GTV_{clin} contours from two image sets (Mixed - Iodine, Mixed - VMI, and VMI - Iodine). Table 8.19 shows these intra-clinician results. Similarly

to the liver cases, the GTV contours were equally reproducible regardless of image pair (P>.13).

The variation in the JC, DSC, and HD_{mean} from the Mixed - Iodine and Mixed - VMI data is illustrated in Figure 8.12. Overall, the variation in these metrics across the clinicians was much greater than the liver study as illustrated by the standard deviations across the four clinicians. For pancreas Patient 2, there was low variability and relatively high average values in all three metrics across the clinicians implying that the GTV was easily identifiable. This is illustrated in the three image sets in Figure 8.13.

Table 8.19: Jaccard coefficient (JC), Dice Similarity Coefficient (DSC), and mean Hausdorff distance (HD) comparing the GTV_{clin} from the mixed 120 kVp-equivalent images to the VMIs at 40 keV (Mixed - VMI), to the iodine-enhanced images (Mixed - Iodine), and the VMIs at 40 keV to the iodine-enhanced images (VMI - Iodine) for all pancreas cases for each clinician.

	Clinician	Image Comparison	Mean	SD	Min	Median	Max	P value
JC	1	Mixed - Iodine	0.44	0.20	0.08	0.42	0.81	0.88
		Mixed - VMI	0.46	0.25	0.00	0.44	0.84	
		VMI - Iodine	0.42	0.22	0.00	0.47	0.75	
	2	Mixed - Iodine	0.43	0.24	0.05	0.51	0.84	0.13
		Mixed - VMI	0.49	0.21	0.06	0.48	0.80	
		VMI - Iodine	0.34	0.21	0.00	0.33	0.76	
	3	Mixed - Iodine	0.40	0.27	0.05	0.43	0.69	0.45
		Mixed - VMI	0.45	0.20	0.09	0.50	0.69	
		VMI - Iodine	0.28	0.23	0.01	0.28	0.62	
	4	Mixed - Iodine	0.39	0.22	0.00	0.48	0.70	0.32
		Mixed - VMI	0.40	0.21	0.00	0.39	0.82	
		VMI - Iodine	0.30	0.21	0.00	0.31	0.72	
DSC	1	Mixed - Iodine	0.59	0.20	0.15	0.59	0.89	0.90
		Mixed - VMI	0.59	0.25	0.00	0.62	0.92	
		VMI - Iodine	0.56	0.26	0.00	0.64	0.86	
	2	Mixed - Iodine	0.56	0.26	0.10	0.67	0.91	0.13
		Mixed - VMI	0.63	0.20	0.11	0.65	0.89	
		VMI - Iodine	0.47	0.24	0.00	0.50	0.86	
	3	Mixed - Iodine	0.52	0.31	0.10	0.60	0.82	0.43
		Mixed - VMI	0.59	0.22	0.17	0.67	0.82	
		VMI - Iodine	0.40	0.28	0.03	0.44	0.77	
	4	Mixed - Iodine	0.53	0.25	0.00	0.65	0.82	0.32
		Mixed - VMI	0.54	0.23	0.00	0.56	0.90	
		VMI - Iodine	0.42	0.25	0.00	0.47	0.84	
HD_{mean} (mm)	1	Mixed - Iodine	4.68	2.28	1.69	4.85	10.18	0.66
		Mixed - VMI	5.52	6.27	0.92	4.98	28.87	
		VMI - Iodine	6.46	7.48	2.13	3.89	28.87	
	2	Mixed - Iodine	5.14	3.88	1.48	3.47	14.08	0.20
		Mixed - VMI	4.16	2.94	1.30	3.19	13.20	
		VMI - Iodine	6.59	5.04	1.75	5.17	21.93	
	3	Mixed - Iodine	5.13	3.77	1.42	4.37	10.47	0.32
		Mixed - VMI	4.00	2.59	2.03	3.03	9.81	
		VMI - Iodine	7.32	5.06	2.98	6.14	16.07	
	4	Mixed - Iodine	5.35	6.16	1.29	3.91	27.82	0.27
		Mixed - VMI	4.68	3.41	1.48	4.04	14.66	
		VMI - Iodine	7.68	6.75	1.53	5.57	24.32	

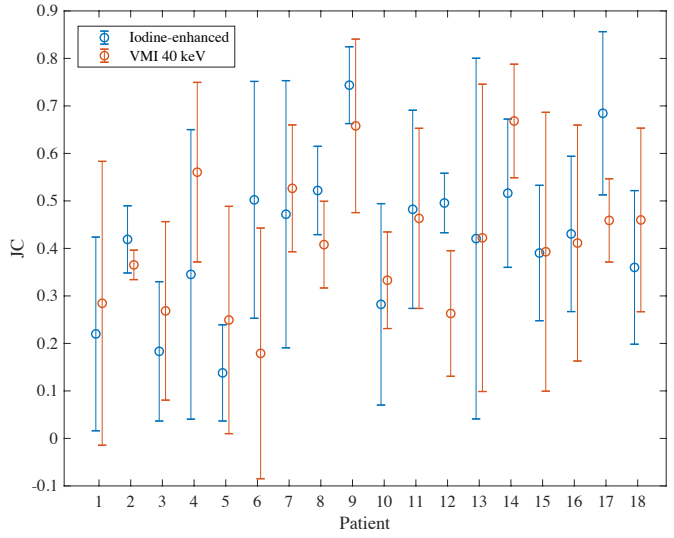

(a)

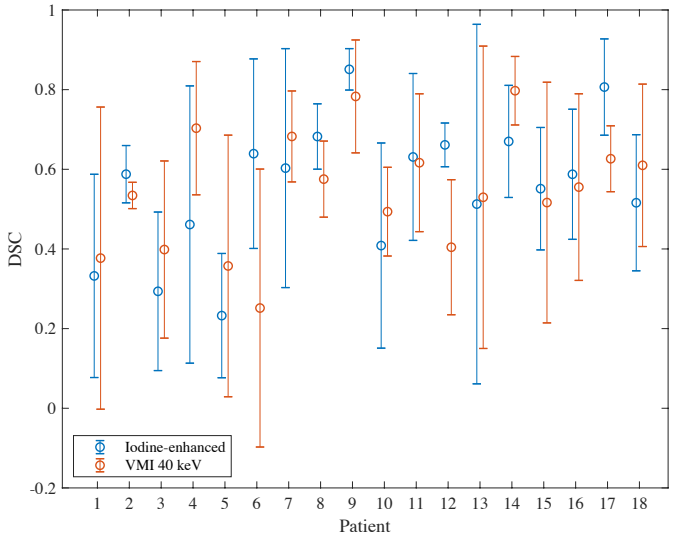

(b)

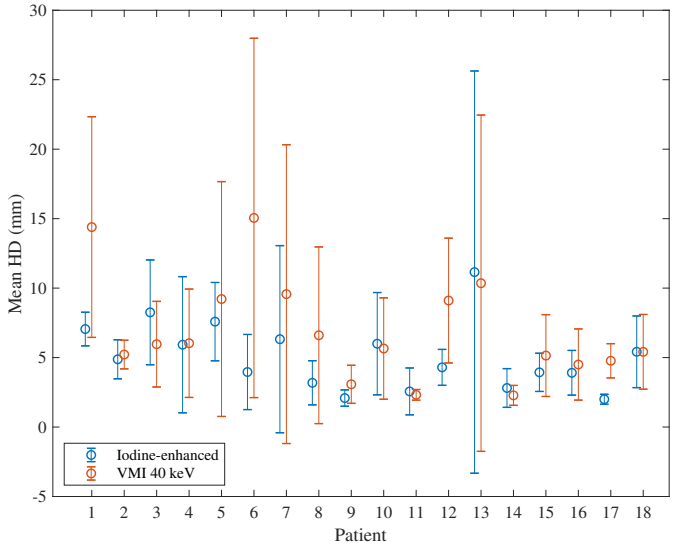

(c)

Figure 8.12: Mean and variation in Jaccard Coefficient (JC) (a), Dice Similarity Coefficient (DSC) (b), and the mean Hausdorff Distance (HD) (c) for each pancreas patient. These metrics were calculated comparing the Mixed - Iodine and Mixed - VMI 40 keV image sets.

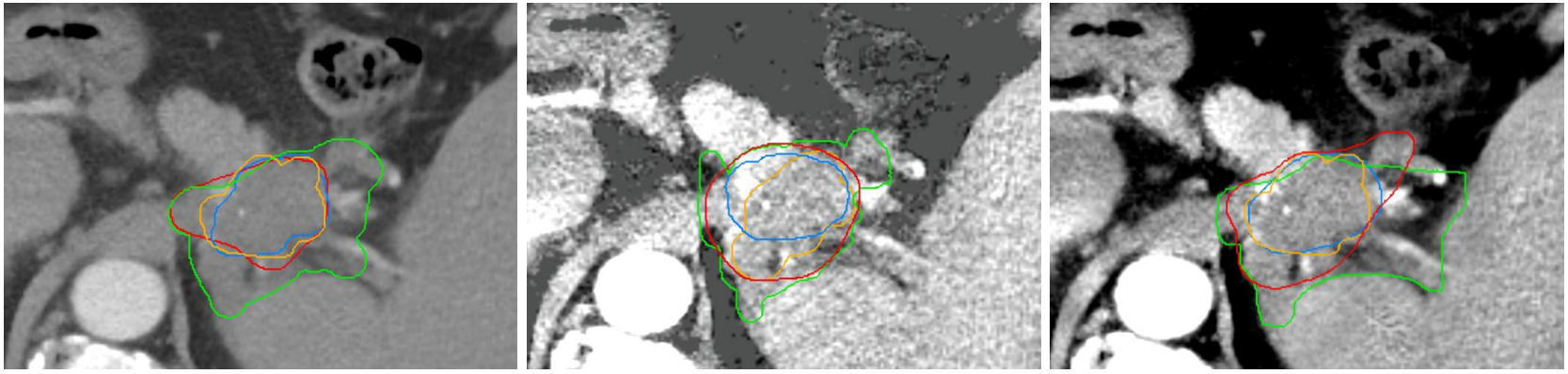

(a) (b) (c)

Figure 8.13: The GTV_{clin} from all four clinicians on the mixed 120 kVp-equivalent (a), iodine-enhanced (b), and VMI at 40 keV (c) for pancreas Patient 2. The variation in JC and DSC calculated from Mixed - Iodine and Mixed - VMI was small across the clinicians. Red is Clinician 1, blue is Clinician 2, orange is Clinician 3, and green is Clinician 4.

Overall, the reproducibility of the pancreas GTV_{clin} contours across two image sets was not as high as the liver cases. Out of the 18 pancreas cases, only 3 cases had mean JC values greater than 0.50 and DSC values greater than 0.65 (Patient 9, Patient 14, and Patient 17). There was only one specific pancreas case (Patient 12) that showed statistically greater reproducibility in GTV_{clin} contours from mixed 120 kVp-equivalent images to iodine-enhanced images than to VMIs at 40 keV based on JC and DSC values (P=.05). An axial slice of Patient 12 is shown in Figure 8.14 with the GTV_{clin} contours from all four clinicians. For all other cases, the reproducibility was the same regardless of image type because no other pancreas case showed statistically significant differences in JC, DSC, or HD_{mean}.

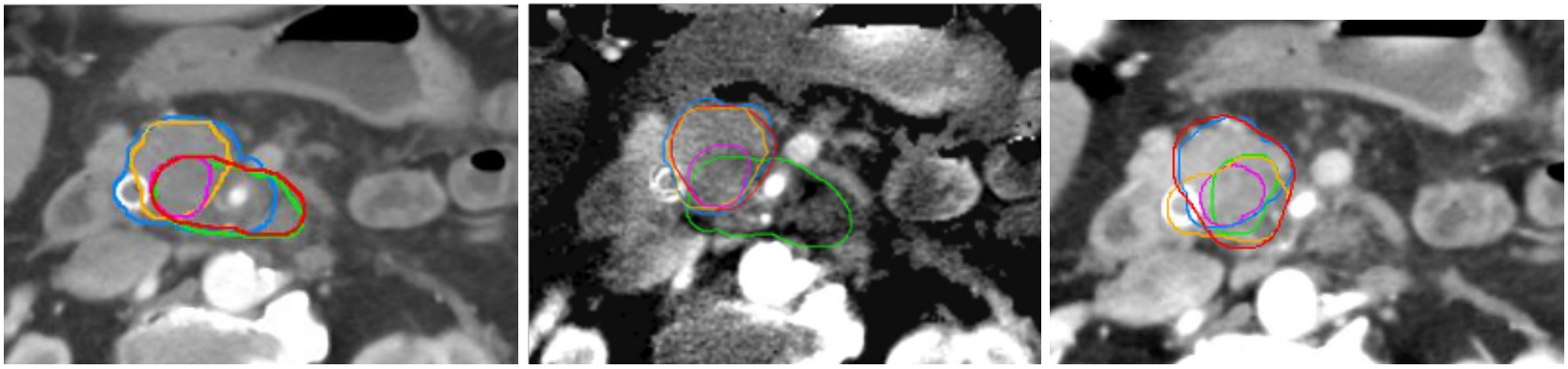

(a) **(b)** **(c)**

Figure 8.14: The GTV_{clin} from all four clinicians on the mixed 120 kVp-equivalent (a), iodine-enhanced (b), and VMI at 40 keV (c) for pancreas Patient 12 where Mixed - Iodine contours were more similar than the Mixed - VMI contours. Red is Clinician 1, blue is Clinician 2, orange is Clinician 3, and green is Clinician 4. Magenta is the GTV_{treat} contour.

8.5 Discussion

Several groups have made efforts to study the advantages of DECT imaging in radiotherapy to determine its clinical relevance, accuracy in delineating tumor from parenchyma, and implementation in a clinical workflow [22, 96, 103, 129]. However, to our knowledge, no prior work has analyzed the delineation reproducibility, accuracy, and variation of entire liver and pancreas GTV contouring on TwinBeam DECT images. Chapters 4 and 5 of this thesis analyzed the GTV contrast and CNR from TwinBeam DECT images and found that VMIs at 40 keV had higher GTV contrast and CNR of pancreas tumors and higher GTV contrast of liver tumors but equal average CNR compared to mixed 120 kVp-equivalent images [96, 103]. The results of those studies provided the motivation to investigate the effect the increased CNR and/or contrast has on the delineation of liver tumors and the increase in CNR has on the delineation of pancreas tumors for radiation therapy applications.

The liver contouring study showed that there was minimal variation in liver GTV contouring across the three image sets investigated; iodine-enhanced image, VMI at 40 keV, and mixed 120 kVp-equivalent image. Therefore, on average the difference in GTV CNR and/or contrast based on image type determined in Chapter 5 had no distinct effect on GTV contouring. The qualitative component of the liver contouring study showed that the inter-clinician agreement across the three image types for the 4 categories, tumor conspicuity, tumor edge sharpness, contouring confidence, and overall image quality was poor to slight. While the intra-clinician agreement was slight to moderate depending on the clinician. Therefore, although there was a low agreement in the qualitative scoring,

the GTV contours were still highly reproducible across image sets. Overall, this is because the liver GTVs were not difficult to visualize. The lesions included were not small (mean volume was 103 ml), which could have contributed to why the conspicuity scores were insignificantly different across all image types. Overall, the tumors were easily visible regardless of the image type.

For our pancreas contouring study, there was much more variation and less repeatability compared to the liver study, but the variation and reproducibility were statistically equal across the three image sets. Concluding that, although Chapter 4 found that on average the GTV contrast and GTV CNR increased with the VMIs at 40 keV, the tumors were still difficult to delineate. For the intra-clinician qualitative investigation of the pancreas study, there was no statistical agreement in scoring. For the inter-clinician qualitative investigation, there was more than one instance where the mixed 120 kVp-equivalent image scored much higher than the iodine-enhanced and VMI at 40 keV.

One pancreas case where the overlap of the GTV_{clin} contours with respect to the GTV_{treat} substantially increased with the VMI at 40 keV was Patient 3. The GTV contrast, and CNR of this case also substantially increased with VMI at 40 keV compared to the mixed 120 kVp-equivalent image (contrast: 25.5 HU vs 96.5 HU & CNR: 2.4 vs 4.5). Table 8.20 lists the JC, DSC, HD_{mean}, and volume averaged across all four clinicians for each of the three image sets. The VMI at 40 keV showed the greatest JC, DSC and smallest HD_{mean} meaning that the GTV_{clin} contours created on the VMIs at 40 keV more closely matched the GTV_{treat} contour. For this case, the substantial increase in GTV contrast and CNR from the low-energy VMI did correspond to more accurate GTV_{clin}

contours. The qualitative results of this same pancreas case are shown in Table 8.21. The increase in tumor conspicuity also corresponded to greater qualitative scores of tumor edge sharpness and contouring confidence. Axial slices from the three image sets for pancreas Patient 3 with the GTV_{clin} contours from each of the four clinicians are shown in Figure 8.15.

Table 8.20: Jaccard Coefficient (JC), Dice Similarity Coefficient (DSC), mean Hausdorff Distance (HD_{mean}), and volume averaged across all four clinicians for each of the three image sets for pancreas Patient 3. The P values are the results from the ANOVA test comparing the difference in the metric across the three image sets.

	JC	P	DSC	P	HD_{mean} (mm)	P	Volume (cc)	P
Mixed	0.12		0.21		9.62		15.02	
Iodine	0.12	0.01	0.21	0.01	8.77	0.09	18.74	0.93
VMI 40 keV	0.28		0.43		5.58		16.04	

Table 8.21: Qualitative scores of tumor conspicuity, tumor edge sharpness, contouring confidence, and image quality averaged across all clinicians for pancreas Patient 3.

	Conspicuity	Tumor Edge Sharpness	Contouring Confidence	Image Quality
Mixed	3.25	2.67	2.67	4.00
Iodine	3.00	2.50	2.50	3.25
VMI 40 keV	3.25	2.75	3.25	3.50

Figure 8.15: GTV_{clin} from all four clinicians on the mixed 120 kVp-equivalent (a), iodine-enhanced (b), and VMI at 40 keV (c) for pancreas Patient 3. Red is Clinician 1, blue is Clinician 2, orange is Clinician 3, and green is Clinician 4. Magenta is the GTV_{treat} contour.

As previously mentioned, there have been studies that investigated the visualization of pancreas and liver tumors using DECT. In one study including 40 hyper-vascular liver tumors, low-energy images from dual-source DECT were more sensitive in detecting the liver lesions based on values of CNR but the low-energy images also corresponded with a decrease in subjective image quality [7]. Another group investigated the CNR of pancreatic adenocarcinomas using fast kVp-switching DECT and also found that low-energy images correspond to greater CNR and overall detectability of these tumors [11]. Both of these studies suggest that DECT can play a critical role in improving the delineation of liver and pancreas lesions. In our study, we did not find a statistically favorable DECT image set based on subjective scores including tumor conspicuity and image quality. One reason for this null result was because the DECT images were not evaluated side-by-side for direct comparison. This result was similar to a previous study investigating qualitative metrics of DECT images for pancreatic adenocarcinomas [73]. Overall, tumor conspicuity depends on several factors that differ from clinician to clinician such as image noise and perceived resolution. For example, if one clinician is more accustomed to viewing low-noise diagnostic scans and hasn't frequently used DECT images, they will most likely score the image quality and tumor conspicuity lower than a clinician who constantly works with high-noise DECT images.

However, two out of the four clinicians did score tumor conspicuity, tumor edge sharpness, and contouring confidence greater on the VMIs at 40 keV than the mixed 120 kVp-equivalent images for 5 specific liver cases and 3 specific pancreas cases. As a reminder, the mixed 120 kVp-equivalent images served as a surrogate for conventional single-energy

CT images. Therefore, the results of this study suggest that the benefit of low-energy DECT images during GTV contouring can be evaluated on a patient-per-patient basis.

One might consider a limitation of this study to be the total number of patients included. According to the literature, contouring studies included total cases ranging from 2-100 [73, 123, 127, 130]. Although the total cases of this study is in the lower range, an n=18 for pancreas and n=20 for liver was determined to be an adequate number of cases for these studies. Statistical analysis was performed to determine the sample size that would have achieved statistical significance based on the qualitative results of Tables 8.5 and 8.14. Based on this post-analysis, it would require an average of 185 liver patients and 481 pancreas patients to achieve statistically significant results of the quantitative data. Therefore, a slightly greater number of cases might have altered the average values determined in this study, but it would not have affected the statistical significance of our results.

This study attempted to assess the accuracy and variation of the GTV_{clin} contours by referencing them to the treatment GTVs, GTV_{treat}. Unfortunately, the GTV_{clin} and the GTV_{treat} contours were contoured under two different circumstances. The collected diagnostic information provided to the clinicians in this study was extracted from each patient's diagnostic health records by searching for key words such as "diagnosis," "resectable," and "lobe." Due to the fact that records varied by patient and by attending physician, the collected information was not the same for each patient and in some cases was limited. This is unlike actual GTV delineation for radiotherapy as all of the possible patient information is available during contouring, including the diagnostic MRI that is

usually commented by the radiologist. The fact that the clinicians in this study did not have complete access to the patient's records, access to the MRI images, and was overall in a slightly different mindset during contouring, caused some to completely miss the tumor and possibly provide another source of inaccuracy. Therefore, future work further analyzing the variation of the GTV_{clin} contours based on image type can be done by inter-comparing them using metrics other than volume such as center of mass or longest axial and perpendicular tumor dimensions.

8.6 Conclusion

Overall, we did find that pancreas and liver GTV contouring was highly reproducible regardless of type of DECT image set. Therefore, based on the results from this study, and the results of Chapters 4 and 5, it may still be advantageous to use all available DECT images when delineating pancreas and liver tumors for radiation treatment planning as the benefits of DECT vary patient to patient and in no case were detrimental to the accuracy and repeatability of tumor visualization.

Chapter 9

Conclusions

9.1 Split-filter DECT spectra, dose allocation, and the visualization of pancreas and liver tumors

The spectra achieved with the split-filter dual-energy CT (DECT) modality of TwinBeam has been thoroughly investigated in this work. A benchmarked Monte-Carlo model was created to determine point dose differences between TwinBeam and conventional single-energy CT. The model was benchmarked based on HVL and profile measurements and created equivalent photon spectra from split-filter DECT with a 120 kVp and 140 kVp. Based on these models and the resulting equivalent spectra, the DECT spectral separation, effective energies, and dose allocation were quantified. It was concluded that the spectral separation of split-filter DECT is about 40% lower than that of other DECT modalities and that the majority of the dose deposited is from the low-energy portion of the beam. This is the opposite for other DECT modalities on the market. Fortunately,

this work also quantified the impact a 140 kVp initial photon spectra has on split-filter DECT, and it was concluded that it may be beneficial to perform split-filter DECT with a higher energy beam as the spectral-separation increased and dose allocation decreased providing a more optimal split-filter system.

Although TwinBeam has an inferior spectral separation and higher dose allocation compared to other DECT modalities, its images were still able to differentiate pancreas and liver tumors based on GTV contrast, iodine uptake, and texture analysis features. Dual energy post-processing, specifically from single-source split-filter DECT offers many advantages over conventional single-energy CT in the evaluation of pancreatic and liver cancers. The retrospective studies of this thesis work quantified the gain in gross target volume (GTV) contrast and contrast-to-noise ratio (CNR) from split-filter DECT virtual monoenergetic images (VMIs) compared to conventional SECT images. The results provided valuable guidance in integrating TwinBeam images into radiation therapy workflow. It was demonstrated that the optimal VMIs of 40 keV outperformed conventional SECT images in pancreas GTV CNR. For pancreas tumors, which are historically difficult to differentiate with SECT, this increase in CNR may increase the ability to accurately segment these tumors for radiation therapy treatment planning, leading to more effective radiation therapy treatment. The visibility of liver GTVs were also investigated. Low-energy VMIs demonstrated about 215% greater contrast than the virtual single-energy CT images and for some cases the VMIs provided much greater CNR. This unfortunately, wasn't true for all tumors investigated, leading to a non-statistical difference on average. These results paved the way for a texture analysis study that quantified the first order

texture analysis features of pancreas and liver tumor and healthy tissue.

The texture analysis of pancreas and liver tumor and parenchyma was analyzed as a function of VMI energy using TwinBeam DECT images. Two of the first order parameters (kurtosis and skewness) did not change as a function of energy and are not well suited for differentiating tumor versus tissue but has the potential to provide information for tumor treatment response. On the other hand, mean CT number (MCTN) and standard deviation (SD) increased for low-energy VMI, as expected based on the GTV contrast results. The texture analysis results provided quantitative information to explain the heterogeneity of some liver tumors.

The effective atomic number and relative electron density was determined within the tumor and healthy tissue of the pancreas and liver using TwinBeam DECT images. There was a statistical difference between the effective atomic number of pancreas GTVs and healthy tissue ROIs. On the other hand, there was no statistical difference in effective atomic number for the two regions in the liver. The opposite trend was apparent from the relative electron density images. There was a statistical difference in the relative electron density of the liver GTVs and healthy tissue ROIs but there was no difference for the pancreas cases. These results provide insight on the differences in underlying soft tissue and iodine uptake of the two anatomical regions and which of these two images can provide additional information during tumor delineation.

The accuracy of iodine quantification from Syngo.via was determined from TwinBeam iodine-enhanced images using 2D region of interests (ROIs) of a solid water phantom. Based on these results, a methodology to accurately go from image value in 3D ROIs to

iodine concentration in milligrams of iodine per milliliter was created using TwinBeam DECT iodine-enhanced images and patient specific calibration curves. Iodine concentration was quantified in pancreas and liver tumors and analyzed as a function of tumor visibility.

Two contouring studies were conducted and used to assess the subjective tumor visibility and image quality of TwinBeam DECT images. The quantitative metrics comparing pancreas and liver GTVs from several clinicians across different TwinBeam DECT images were calculated. The inter- and intra-clinician agreement of tumor segmentation was determined using the Jaccard coefficient (JC), Dice similarity coefficient (DSC), and Hausdorff distance (HD). Based on the results, it was concluded that for some pancreas and liver tumor cases, tumor conspicuity, edge sharpness, and GTV contouring confidence were greatest for low-energy VMIs compared to mixed 120 kVp-equivalent and iodine-enhanced images. The results of this study suggest that there is benefit of TwinBeam low-energy VMIs during pancreas and liver GTV contouring for specific cases.

Overall, TwinBeam is a unique technology utilizing a split beam to almost simultaneously acquire the low- and high-energy data for DECT image reconstruction. The major applications of this technology include dual-phase contrast imaging to improve the visibility of pancreas and liver tumors using low-energy VMIs, quantify iodine uptake using iodine-enhanced images, and provide texture analysis information to aid in radiation therapy treatment planning. The cost of installing dual-energy CT, especially dual-source scanners is currently significant, and may be prohibitive for some groups. Fortunately, the split-filter single-source scanner of TwinBeam has considerably lower

costs which may further motivate other radiation oncology clinics to invest in this DECT modality for simulations prior to radiation treatment planning [131].

9.2 Future work

This thesis provides the groundwork for a handful of future studies as TwinBeam DECT is still a relatively new technology with a lot of research opportunities. Much of the work completed in this thesis was preliminary for future clinical studies investigating whether TwinBeam can improve the accuracy of treatment and applicability of dose-escalated radiation therapy of pancreas and liver tumors. Liver tumor cases treated between June 2016 and August 2018 were included in this work regardless of diagnosis and tumor characteristics. As the results of this thesis show, each tumor had distinct enhancement properties, texture analysis results, contouring trends, and iodine uptake. Future work with more liver cases of similar diagnostic and enhancement characteristics may reveal information that was not apparent in these studies. The texture analysis performed was solely with first-order parameters due to time constraints and software limitations, therefore there is great motivation to investigate higher order texture analysis parameters and more knowledge may provide additional aid to tumor delineation and tumor treatment response. Syngo.via was used for the iodine quantification study and has since released updates to its software that allow for direct iodine concentrations from 3D ROIs in iodine-enhanced images. Therefore, it is of high value to compare the software update to the results of this work.

The equivalent Monte Carlo source models can be used for future simulations investigating patient dose and other possible filter configurations. The 140 kVp + split filter source model provided greater spectral separation and lower dose allocation, which should convince the manufacturer to perform split-filter DECT with a 140 kVp. Such a manipulation would allow for phantom studies to compare image quality and contrast differences between 120 kVp and 140 kVp split-filter DECT.

Bibliography

[1] Katharine L. Grant, Thomas G. Flohr, Bernhard Krauss, Martin Sedlmairr, Christoph Thomas, and Bernhard Schmidt. Assessment of an advanced image-based technique to calculate virtual monoenergetic computed tomographic images from a dual-energy examination to improve contrast-to-noise ratio in examinations using iodinated contrast media. *Investigative Radiology*, 49(9), 2014.

[2] Adam C. Turner, Di Zhang, Hyun J. Kim, John J. DeMarco, Chris H. Cagnon, Erin Angel, Dianna D. Cody, Donna M. Stevens, Andrew N. Primak, Cynthia H. McCollough, and et al. A method to generate equivalent energy spectra and filtration models based on measurement for multidetector CT monte carlo dosimetry simulations. *Medical Physics*, 36(6):2154–2164, 2009. ISSN 0094-2405. doi: 10.1118/1.3117683. URL `http://dx.doi.org/10.1118/1.3117683`.

[3] Chris Constantinou, James C. Harrington, and Larry A. DeWerd. An electron density calibration phantom for ct-based treatment planning computers. *Medical Physics*, 1992.

[4] Megan C. Jacobsen, Erik N. K. Cressman, Eric P. Tamm, Dodge L. Baluya, Xinhui Duan, Dianna D. Code, David Schellingerhout, and Rick R. Layman. Dual-energy ct: Lower limits of iodine detection and quantification. *Radiology*, 292:414–419, 2019.

[5] Mark Nicholls. Sir godfrey newbold hounsfield and allan m. cormack. *European Heart Journal*, 40(26):2101–2103, Jul 2019. ISSN 1522-9645. doi: 10.1093/eurheartj/ehz421. URL http://dx.doi.org/10.1093/eurheartj/ehz421.

[6] Cynthia H. McCollough, Shai Leng, Lifend Yu, and Joel Fietcher. Dual- and multi-energy CT: Principles, technical application, and clinical applications. *Radiology*, 276(3), 2015.

[7] Jens Altenbernd, Till A. Heusner, Adrian Ringelstein, Susanne C. Ladd, Michael Forsting, and Gerald Antoch. Dual-energy-CT of hypervascular liver lesions in patients with HCC: investigation of image quality and sensitivity. *European Radiology*, 21(4):738–743, 2010. ISSN 1432-1084. doi: 10.1007/s00330-010-1964-7. URL http://dx.doi.org/10.1007/s00330-010-1964-7.

[8] Elizabeth George, Jeremy R Wortman, Urvi P Fulwadhva, Jennifer W Uyeda, and Aaron D Sodickson. Dual energy ct applications in pancreatic pathologies. *British Journal of Radiology*, 90, 2017.

[9] Vincenza Granata, Roberta Fusco, Orlando Catalano, Sergio Venanzio Setola, Elisabetta de Lutio di Castelguidone, Mauro Piccirillo, Raffaele Palaia, Roberto

Grassi, Francesco Granata, and Francesco Izzo. Multidetector computer tomography in the pancreatic adenocarcinoma assessment: an update. *Infectious Agents and Cancer*, 11(1), 2016. ISSN 1750-9378. doi: 10.1186/s13027-016-0105-6. URL http://dx.doi.org/10.1186/s13027-016-0105-6.

[10] M. Klauss, W. Stiller, G. Pahn, F. Fritz, M. Kieser, J. Werner, H. U. Kauczor, and L. Grenacher. Dual-energy perfusion-CT of pancreatic adenocarcinoma. *European Journal of Radiology*, 82:208–214, 2013.

[11] B. N. Patel, J. V. Thomas, M.E. Lockhart, L.L. Berland, and Morgan D.E. Single-source dual-energy spectral multidetector CT of pancreatic adenocarcinoma: Optimization of energy level viewing significantly increases lesion contrast. *Clinical Radiology*, 68:148–154, 2013.

[12] George Noid, An Tai, Diane Schott, Nilesh Mistry, Liu Yu, Taly Gilat-Schmidt, Jared Robbins, and Allen Li. Technical note: Enhancing soft tissue contrast and radiation-induced image changes with dual-energy ct for radiation therapy. *Medical Physics*, 45(9):4238–4245, 2018.

[13] Vinit Baliyan, Kordbacheh, Hamed, Bimal Parameswaran, Balaji Ganeshan, Dushyant Sahani, and Avinash Kambadakone. Virtual monoenergetic imaging in rapid kvp-switching dual-energy ct (dect) of the abdomen: impact on ct texture analysis. *Abdominal Radiology*, 2018.

[14] Chong Hyun Suh, Seong Jong Yun, Wook Jin, Sun Hwa Lee, So Young Park, and Chang-Woo Ryu. Diagnostic performance of dual-energy ct for the detection of

bone marrow oedema: a systematic review and meta-analysis. *European Radiology*, 2018.

[15] Luca Saba, Massimo De Filippo, Francesco Saba, Federica Fellini, Pierre-Yves Marcy, Robert Dagan, Philippe Voituriez, Jacques Aelvoet, Gérard Klotz, Roland Bernard, Valérie Salinesi, and Serge Agostini. Dual energy ct and research of the bone marrow edema: Comparison with mri imaging. *Indian Journal of Radioly Imaging*, 29(4), 2019.

[16] Mitchell M. Goodsitt, Apeksha Shenoy, Jincheng Shen, David Howard, Matthew J. Schipper, Scott Wilderman, Emmanuel Christodoulou, Se Young Chun, and Yuni K. Dewaraja. Evaluation of dual energy quantitative CT for determining the spatial distributions of red marrow and bone for dosimetry in internal emitter radiation therapy. *Medical Physics*, 41(5):051901, 2014. ISSN 0094-2405. doi: 10.1118/1.4870378. URL `http://dx.doi.org/10.1118/1.4870378`.

[17] Andréanne Lapointe, Houda Bahig, Danis Blais, Hugo Bouchard, Édith Filion, Jean-François Carrier, and Stéphane Bedwani. Assessing lung function using contrast-enhanced dual-energy computed tomography for potential applications in radiation therapy. *Medical Physics*, 2017.

[18] Hye Jeon Hwang, Eric A Hoffman, Chang Hyun Lee, Jin Mo Goo, David L Levin, Hans-Ulrich Kauczor, and Joon Beom Seo. The role of dual-energy computed tomography in the assessment of pulmonary function. *European Journal of Radiology*, 2017.

[19] L-q Zhao, W He, B Yan, H-y Wang, and J Wang. The evaluation of haemodynamics in cirrhotic patients with spectral ct. *The British Journal of Radiology*, 86(1028): 20130228, Aug 2013. ISSN 1748-880X. doi: 10.1259/bjr.20130228. URL `http://dx.doi.org/10.1259/bjr.20130228`.

[20] Anantharaman Ayyalusamy, Subramani Vellaiyan, Shanmuga Subramanian, 1 Shyama Satpathy Arivarasan Ilamurugu, Mohammed Nauman, Gowtham Katta, and Aneesha Madineni. Auto-segmentation of head and neck organs at risk in radiotherapy and its dependence on anatomic similarity. *Radiation Oncology Journal*, 37(2), 2019.

[21] Bulat Ibragimov and Lei Xing. Segmentation of organs-at-risks in head and neck ct images using convolutional neural networks. *Medical Physics*, 44(2), 2017.

[22] Mukta D. Agrawal, Daniella F. Pinho, Naveen M. Kulkarni, Peter F. Hahn, Alexander R. Guimaraes, and Dushyant V. Sahani. Oncologic applications of dual-energy CT in the abdomen. *Radiographics*, 34:589–612, 2014.

[23] Christy Goldsmith, Patricia Price, Timothy Cross, Sheila Loughlin, Ian Cowley, and Nicholas Plowman. Dose-volume histogram analysis of stereotactic body radiotherapy treatment of pancreatic cancer: A focuson duodenal dose constraints. *Seminars in Radiation Oncology*, 26:149–156, 2016.

[24] Jun Won Kim, Jinsil Seong, Ik Jae Lee, Joong Yeol Woo, and Kwang-Hyub Han. Phase I dose-escalation study of helical intensity-modulated radiotherapy-based

stereotactic body radiotherapy for hepatocellular carcinoma. *Oncotarget*, 7(26): 40756–40766, 2016.

[25] Benjamin M Yeh, John A Shepherd, Zhen J Wang, Hui Seong Teh, Robert P Hartman, and Sven Prevrhal. Dual-energy and low-kvp ct in the abdomen. *AJR Am J Roentgenol*, 193(1):47–54, Jul 2009. doi: 10.2214/AJR.09.2592.

[26] Ravi K. Kaza, Joel F. Platt, Richard H. Cohan, Elaine M. Caoili, Mahmoud M. Al-Hawary, and Ashish Wasnik. Dual-energy CT with single- and dual-source scanners: Current applications in evaluating the genitourinary tract. *Radiographics*, 32(2): 353–369, 2012.

[27] Anno Graser, Thorsten R. C. Johnson, Hersh Chandarana, and Michael Macari. Dual energy CT: preliminary observations and potential clinical applications in the abdomen. *European Radiology*, 19(1):13–23, 2008. ISSN 1432-1084. doi: 10.1007/s00330-008-1122-7. URL `http://dx.doi.org/10.1007/s00330-008-1122-7`.

[28] Chad Tao and Li-Xi Yang. Improved radiotherapy for primary and secondary liver cancer: Stereotactic body radiation. *Anticancer Research*, 32, 2012.

[29] Michael Velec, Joanne L Moseley, Laura A Dawson, and Kristy K Brock. Dose escalated liver stereotactic body radiation therapy at the mean respiratory position. *International Journal of Radiation Oncology Biology and Physics*, 89(5):1121–1128, Aug 2014. doi: 10.1016/j.ijrobp.2014.04.051.

[30] Sunil Krishnan, Awalpreet S. Chadha, Yelin Suh, Hsiang-Chun Chen, Arvind Rao, Prajnan Das, Bruce D. Minsky, Usama Mahmood, Marc E. Delclos, Gabriel O.

Sawakuchi, Sam Beddar, Matthew H. Katz, Jason B. Fleming, Milind M. Javle, Gauri R. Varadhachary, Robert A. Wolff, and MD Christopher H. Crane. Focal radiation therapy dose escalation improves overall survival in locally advanced pancreatic cancer patients receiving induction chemotherapy and consolidative chemoradiation. *International Journal of Radiation Oncology*, 94(4):755–765, 2016.

[31] Nicholas G. Zaorsky, Eric J. Lehrer, Elizabeth Handorf, and Joshua E. Meyer. Dose escalation in stereotactic body radiation therapy for pancreatic cancer a meta-analysis. *American Journal of Clinical Oncology*, 42(1), 2019.

[32] Alexander Chi, Nam Phong Nguyen, James S. Welsh, William Tse, Manish Monga, Olusola Oduntan, Mohammed Almubarak, John Rogers, Scot C. Remick, and David Gius. Strategies of dose escalation in the treatment of locally advanced non-small cell lung cancer: Image guidance and beyond. *Frontiers in Oncology*, 4, Jun 2014. ISSN 2234-943X. doi: 10.3389/fonc.2014.00156. URL `http://dx.doi.org/10.3389/fonc.2014.00156`.

[33] Sebastian Zschaeck, Bibiana Blumke, Peter Wust, David Kaul, Marcus Bahra, Hanno Riess, Fritz Klein, Marianne Sinn, Uwe Pelzer, Volker Budach, and Pirus Ghadjar. Dose-escalated radiotherapy for unresectable or locally recurrent pancreatic cancer: Dose volume analysis, toxicity and outcome of 28 consecutive patients. *PLoS One*, 12(10), 2017.

[34] Isabel P. Almeida, Lotte E. J. R. Schyns, Michael C. Öllers, Wouter van Elmpt, Katia Parodi, Guillaume Landry, and Frank Verhaegen. Dual-energy CT quantitative imaging: a comparison study between twin-beam and dual-source ct scanners. *Medical Physics*, 44(1):171–179, 2017.

[35] André Euler, Anushri Parakh, Anna L. Falkowski, Sebastian Manneck, David Dashti, Bernhard Krauss, Zsolt Szucs-Farkas, and Sebastian T. Schindera. Initial results of a single-source dual-energy computed tomography technique using a split-filter assessment of image quality, radiation dose, and accuracy of dual-energy applications in an in vitro and in vivo study. *Investigative Radiology*, 51 (8):491–498, 2016. ISSN 0020-9996. doi: 10.1097/rli.0000000000000257. URL `http://dx.doi.org/10.1097/RLI.0000000000000257`.

[36] Deepak Kumar Bhasin, Surinder Singh Rana, Sujeet Jahagirdar, and Birinder Nagi. Does the pancreas move with respiration? *Journal of Gastroenterology and Hepatology*, 0(0):060606032707072–???, 2006. ISSN 1440-1746. doi: 10.1111/j.1440-1746.2006.04324.x. URL `http://dx.doi.org/10.1111/j.1440-1746.2006.04324.x`.

[37] Naveen Kulkarni, David Hough, Parag Tolat, Erik Soloff, and Avinash Kambadakone. Pancreatic adenocarcinoma: cross-sectional imaging techniques. *Abdominal Radiology*, 43:253–263, 2017.

[38] Michael Macari, Bradley Spieler, Danny Kim, Anno Graser, Alec Jeffrey Megibow, James Babb, and Hersh Chandarana. Dual-source dual-energy mdct of pancreatic adenocarcinoma: Initial observations with data generated at 80 kvp

and at simulated weighted-average 120 kvp. *American Journal of Roentgenology*, 194(1):W27–W32, 2010. ISSN 1546-3141. doi: 10.2214/ajr.09.2737. URL http://dx.doi.org/10.2214/AJR.09.2737.

[39] C. F. Njeh. Tumor delineation: The weakest link in the search for accuracy in radiotherapy. *Journal of Medical Physics*, 33(4):136–140, 2008.

[40] Paul E. Oberstein and Kenneth P. Olive. Pancreatic cancer: why is it so hard to treat? *Therapeutic Advances in Gastroenterology*, 6(4):321–337, 2013. ISSN 1756-2848. doi: 10.1177/1756283x13478680. URL http://dx.doi.org/10.1177/1756283X13478680.

[41] Robert Alvarez and Albert Macovski. Energy-selective reconstructions in x-ray computerized tomography. *Physics in Medicine and Biology*, 21(5):733–744, 1976.

[42] Hyun Woo Goo and Jin Mo Goo. Dual-energy ct: New horizon in medical imaging. *Korean Journal of Radiology*, 2017.

[43] Brian Rutt and Aaron Fenster. Split-filter computed tomography (CT) for routine dual energy scanning. *Application of Optical Instrumentation in Medicine IX*, 1981. doi: 10.1117/12.931816. URL http://dx.doi.org/10.1117/12.931816.

[44] André Euler, Markus Obmann, Zsolt Szucs-Farkas, Achille Mileto, Caroline Zaehringer, Anna L. Falkowski, David Winkel, Daniele Marin, Bram Stieltjes, Bernhard Krauss, and Sebastian T. Schindera. Comparison of image quality and radiation dose between split-filter dual-energy images and single-energy images in single-source abdominal CT. *European Radiology*, 28, 2018.

[45] Tonghe Wang, Beth Bradshaw Ghavidel, Jonathan J. Beitler, Xiangyang Tang, Yang Lei, Walter J. Curran, Tian Liu, and Xiaofeng Yang. Optimal virtual monoenergetic image in "twinbeam" dual-energy ct for organs-at-risk delineation based on contrast-noise-ratio in head-and-neck radiotherapy. *Journal of Applied Clinical Medical Physics*, 20(2):121–128, Jan 2019. ISSN 1526-9914. doi: 10.1002/acm2.12539. URL `http://dx.doi.org/10.1002/acm2.12539`.

[46] Lifeng Yu, Jodie A Christner, Shuai Leng, Jia Wang, Joel G Fletcher, and Cynthia H McCollough. Virtual monochromatic imaging in dual-source dual-energy CT: radiation dose and image quality. *Medical Physics*, 38(12):6371–9, 2011. doi: 10.1118/1.3658568.

[47] Claudia Frellesena, Freia Fesslera, Andrew D. Hardieb, Julian L. Wichmanna, Carlo N. De Ceccob, U. Joseph Schoepf, J. Matthias Kerla, Boris Schulza, Renate Hammerstingla, Thomas J. Vogla, and Ralf W. Bauera. Dual-energy CT of the pancreas: improved carcinoma-to-pancreas contrast with a noise-optimized monoenergetic reconstruction algorithm. *European Journal of Radiology*, 84:2052–2058, 2015.

[48] Bernhard Krauss, Katharine L. Grant, Bernhard T. Schmidt, and Thomas G. Flohr. The importance of spectral separation an assessment of dual-energy spectral separation for quantitative ability and dose efficiency. *Investigative Radiology*, 50(2), 2015.

[49] Mohammed Y.M Abujazar, Rafidah Binti Zainon, M.B Kurama, and Elaine Salmi. Optimisation of dect spectral separation for quantitative evaluation of clinical contrast agent. *Journal of Physics: Conference Series*, 1083:012013, Aug 2018. ISSN 1742-6596. doi: 10.1088/1742-6596/1083/1/012013. URL `http://dx.doi.org/10.1088/1742-6596/1083/1/012013`.

[50] Jack W Lambert, Paul F FitzGerald, Peter M Edic, Yuxin Sun, Peter J Bonitatibus, Jr, Robert E Colborn, and Benjamin M Yeh. The effect of patient diameter on the dual-energy ratio of selected contrast-producing elements. *J Comput Assist Tomogr*, 41(3):505–510, 2017. doi: 10.1097/RCT.0000000000000557.

[51] Megan Jacobsen, Dawid Schellingerhout, Cayla Wood, Eric Tamm, Myrna Godoy, Jia Sun, and Dianna Cody. Intermanufacturer comparison of dual-energy CT iodine quantification and monochromatic attenuation: A phantom study. *Radiology*, 000 (0):1–11, 2018.

[52] Michael Toepker, Thomas Moritz, Bernhard Krauss, Michael Weber, Gordon Euller, Thomas Mang, Florian Wolf, Christian J. Herold, and Helmut Ringl. Virtual non-contrast in second-generation, dual-energy computed tomography: Reliability of attenuation values. *European Journal of Radiology*, 81(3):e398–e405, 2012. ISSN 0720-048X. doi: 10.1016/j.ejrad.2011.12.011. URL `http://dx.doi.org/10.1016/j.ejrad.2011.12.011`.

[53] Nora Hunemohr, Bernhard Krauss, Christoph Tremmel, Benjamin Ackermann, Oliver Jakel, and Steffen Greilich. Experimental verification of ion stopping power

prediction from dual energy CT data in tissue surrogates. *Physics in Medicine and Biology*, 59:83–96, 2013.

[54] Caroline Caramella, Adrien Allorant, Fanny Orihac, Francois Bidault, Bernard Asselain, Sammy Ammari, Corinne Balleyguier, Nathalie Lassau, and Stephanie Pitre-Champagnat. Can we trust the calculation of texture indices of CT images? a phantom study. *Medical Physics*, 45, 2018.

[55] Andrea Ferrero, Juan Montoya, Lisa Vaughan, Alice Huang, Ian McKeag, Felicity Enders, James Williams, and Cynthia McCough. Quantitative prediction of stone fragility from routine dual energy CT: Ex vivo proof of feasibility. *Academic Radiology*, 23(12):1545–1552, 2016.

[56] A. F. Rodriguez, O. A. Jimenez del Toro, A. Platony, P. A. Polettiy, H. Henning Muller, and A Depeursinge. Benefits of texture analysis of dual energy CT for computer-aided pulmonary embolism detection. In *Engineering of Medicine and Biology Society (EMBC), 201335th Annual Internation Conference of the IEEE*, Osaka, Japan, 2013. IEEE.

[57] Meghan G. Lubner, Andrew Smith, Kumar Sandrasegaran, Dushyant Sahani, and Perry J. Pickhardt. CT texture analysis: Definitions, applications, biologic correlations, and challenges. *Radiographics*, 37:1483–1503, 2017.

[58] Meghan G. Lubner, Kyle Malecki, John Kloke, Balaji Ganeshan, and Perry J. Pickhardt. Texture analysis of the liver at MDCT for assessing hepatic fibrosis. *Abdominal Radiology*, 42(8):2069–2078, 2017. ISSN 2366-0058. doi: 10.1007/

s00261-017-1096-5. URL http://dx.doi.org/10.1007/s00261-017-1096-5.

[59] Gloria Vilches-Freixas, Jean Michel Letang, Nicolas Ducros, and Simon Rit. Optimization of dual-energy CT acquisitions for proton therapy using projection-based decomposition. *Medical Physics*, 44(9):4548–4558, 2017.

[60] Arun Kumar Gupta, Veena Chowdhury, and Niranjan Khandelwal. *Diagnostic Radiology: Recent Advances and Applied Physics in Imaging*. Jaypee Brothers Medical Publishers, 2013.

[61] S. Richard and J. H. Siewerdsen. Optimization of dual-energy imaging systems using generalized NEQ and imaging task. *Medical Physics*, 34(1):127–139, 2006.

[62] N. A. Shkumat, J. H. Siewerdsen, A. C. Dhanantwari, D. B. Williams, S. Richard, N. S. Paul, J. Yorkston, and R. Van Metter. Optimization of image acquisition techniques for dual-energy imaging of the chest. *Medical Physics*, 34(10):3904–3915, 2007. ISSN 0094-2405. doi: 10.1118/1.2777278. URL http://dx.doi.org/10.1118/1.2777278.

[63] Baojun Li, Girijesh Yadava, and Jiang Hsieh. Quantification of head and body CTDI(vol) of dual-energy x-ray CT with fast-kVp switching. *Medical Physics*, 38 (5):2595–601, 2011. doi: 10.1118/1.3582701.

[64] CMO. *Calibration of X-ray Radiation Detectors*. National Institute of Science and Technology, 4.30 edition, 2017.

[65] Frank H. Attix. *Introduction to radiological physics and radiation dosimetry*. Wiley-Interscience, 1986.

[66] American Cancer Society. Cancer facts and figures 2019. *Atlanta:American Cancer Society*, 2019.

[67] Edgar Ben-Josef, Mathew Schipper, Isaac R Francis, Scott Hadley, Randall Ten-Haken, Theodore Lawrence, Daniel Normolle, Diane M Simeone, Christopher Sonnenday, Ross Abrams, William Leslie, Gazala Khan, and Mark M Zalupski. A phase I/II trial of intensity modulated radiation (IMRT) dose escalation with concurrent fixed-dose rate gemcitabine (FDR-G) in patients with unresectable pancreatic cancer. *International Journal of Radiation Oncology*, 84(5):1166–71, 2012. doi: 10.1016/j.ijrobp.2012.02.051.

[68] Mert Erkan, Simone Hausmann, Christoph W. Michalski, Alexander A. Fingerle, Martin Dobritz, Jörg Kleeff, and Helmut Friess. The role of stroma in pancreatic cancer: diagnostic and therapeutic implications. *Nature Reviews Gastroenterology and Hepatology*, 9(8):454–467, 2012. ISSN 1759-5053. doi: 10.1038/nrgastro.2012.115. URL `http://dx.doi.org/10.1038/nrgastro.2012.115`.

[69] Daniele Marin, Rendon C. Nelson, Huiman Barnhart, Sebastian T. Schindera, Lisa M. Ho, Tracy A. Jaffe, Terry T. Yoshizumi, Richard Youngblood, and Ehsan Samei. Detection of pancreatic tumors, image quality, and radiation dose during the pancreatic parenchymal phase : Effect of a low-tube-voltage, high-tube-current ct technique—preliminary results. *Radiology*, 256(2):450–459, 2010.

[70] Daniele Marin, Rendon C. Nelson, Ehsan Samei, Erik K. Paulson, Lisa M. Ho, Daniel T. Boll, David M. DeLong, Terry T. Yoshizumi, and Sebastian T. Schindera. Hypervascular liver tumors: Low tube voltage, high tube current multidetector CT during late hepatic arterial phase for detection initial clinical experience. *Radiology*, 251(3):771–779, 2005.

[71] Emma Robinson, James Babb, Hersh Chandarana, and Michael Macari. Dual-source dual-energy MDCT: Comparison of 80 kVp and weighted average 120 kVp data for conspicuity of hypo-vascular liver metastesis. *Investigative Radiology*, 45 (7):413–418, 2010.

[72] Daniela Muenzel, Grace C. Lo, Hei Shun Yu, Anushri Parakh, Manuel Patino, Avinash Kambadakone, Ernst J. Rummeny, and Dushyant V. Sahani. Material density iodine images in dual-energy ct: Detection and characterization of hypervascular liver lesions compared to magnetic resonance imaging. *European Journal of Radiology*, 95, 2017.

[73] Shiva Gupta, Nicolaus Wagner-Bartak, Corey T. Jensen, Anthony Hui, Wei Wei, Patrick Lertdilok, Aliya Qayyum, and Eric P. Tamm. Dual-energy CT of pancreatic adenocarcinoma: reproducibility of primary tumor measurements and assessment of tumor conspicuity and margin sharpness. *Abdominal Radiology*, 41(7):1317–1324, 2016. ISSN 2366-0058. doi: 10.1007/s00261-016-0689-8. URL `http://dx.doi.org/10.1007/s00261-016-0689-8`.

[74] David J. Brenner and Eric J. Hall. Computed tomography — an increasing source of radiation exposure. *The New England Journal of Medicine*, 357(22):2277–2284, 2007.

[75] Cynthia McCollough, Dianna Cody, Sue Edyvean, Rich Geise, Bob Gould, Nicholas Keat, Walter Huda, Phil Judy, Willi Kalender, Mike McNitt-Gray, Rick Morin, Tom Payne, Stanley Stern, Larry Rothenberg, Paul Shrimpton, Jan Timmer, and Charles Wilson. Task group 23: The measurement, reporting and management of radiation dose in CT. Technical report, AAPM, 2008.

[76] Robert L. Dixon and Adam C. Ballard. Experimental validation of a versatile system of CT dosimetry using a conventional ion chamber: Beyond CTDI100. *Medical Physics*, 34(8):3399–3413, 2007. ISSN 0094-2405. doi: 10.1118/1.2757084. URL http://dx.doi.org/10.1118/1.2757084.

[77] Sebastian T. Schindera, Caroline Zaehringer, Luigia D'Errico, Fides Schwartz, Maka Kekelidze, Zsolt Szucs-Farkas, and Matthias R. Benz. Systematic radiation dose optimization of abdominal dual-energy ct on a second-generation dual-source ct scanner: assessment of the accuracy of iodine uptake measurement and image quality in an in vitro and in vivo investigations. *Abdominal Radiology*, 42(10): 2562–2570, May 2017. ISSN 2366-0058. doi: 10.1007/s00261-017-1160-1. URL http://dx.doi.org/10.1007/s00261-017-1160-1.

[78] Cynthia H. McCollough, Shuai Leng, Yu Lifeng, Dianna D. Cody, John M. Boone, and Michael F. McNitt-Gray. CT dose index and patient dose: They are not the

same thing. *Radiology*, 259(2):311–316, 2011.

[79] A Jensen, A Culberson, S Davis, J Micka, and L DeWerd. Calibration of ct ion chambers in air-kerma length. *AAPM annual meeting*, 2006.

[80] John M. Boone and J. Anthony Seibert. An accurate method for computer-generating tungsten anode x-ray spectra from 30 to 140 kv. *Medical Physics*, 24 (11), 1997.

[81] Dana Kurkova and Libor Judas. X-ray tube spectra measurement and correction using a cdte detector and an analytic response matrix for photon energies up to 160 kev. *Radiation Measurements*, 85:64–72, 2016.

[82] M. R. Ay, S. Sarkar, M. Shahriari, D. Sardari, and H. Zaidi. Assessment of different computational models for generation of x-ray spectra in diagnostic radiology and mammography. *Medical Physics*, 32(6Part1):1660–1675, 2005. ISSN 0094-2405. doi: 10.1118/1.1906126. URL `http://dx.doi.org/10.1118/1.1906126`.

[83] Qing Liang. *Patient-specific CT dose determination from CT images using Monte Carlo simulations*. PhD thesis, University of Wisconsin - Madison, 2013.

[84] L. Abbene, G. Gerardi, F. Principato, S. Del Sordo, R. Ienzi, and G. Raso. High-rate x-ray spectroscopy in mammography with a cdte detector: A digital pulse processing approach. *Medical Physics*, 37(12):6147–6156, Nov 2010. ISSN 0094-2405. doi: 10.1118/1.3512804. URL `http://dx.doi.org/10.1118/1.3512804`.

[85] G Poludniowski, G Landry, F DeBlois, P M Evans, and F Verhaegen. Spekcalc: a program to calculate photon spectra from tungsten anode x-ray tubes. *Physics in Medicine and Biology*, 54:N433–N438, 2009.

[86] R Birch and M Marshall. Computation of bremsstrahlung x-ray spectra and comparison with spectra measured with a ge(li) detector. *Physics in Medicine and Biology*, 24(3):505–517, 1979.

[87] Mohammad Reza Ay and Habib Zaidi. Development and validation ofmcnp4c-based monte carlo simulator for fan- and cone-beam x-ray ct. *Physics in Medicine and Biology*, 50:4863–4885, 2005.

[88] J. Punnoose, J. Xu, A. Sisniega, W. Zbijewski, and J. H. Siewerdsen. Technical note: spektr 3.0—a computational tool for x-ray spectrum modeling and analysis. computaional tool 8, Johns Hopkins University, 2016.

[89] R Kramer, V F Cassola, M E A Andrade, M W C de Araújo, D J Brenner, and H J Khoury. Mathematical modelling of scanner-specific bowtie filters for monte carlo ct dosimetry. *Physics in Medicine and Biology*, 62(3):781–809, Jan 2017. ISSN 1361-6560. doi: 10.1088/1361-6560/aa5343. URL `http://dx.doi.org/10.1088/1361-6560/aa5343`.

[90] Siemens. Siemens computed tomography (ct) systems comparison chart.

[91] The Center of Evidence-based Purchasing. Comparitive specifications: 128 to 320 scanner technical specifications, March 2009.

[92] J. H. Hubbell and S. M. Seltzer. Tables of x-ray mass attenuation coefficients and mass energy-absorption coefficients. 2004. URL http://physics.nist.gov/PhysRefData/XrayMassCoef/cover.html.

[93] Andrew N. Primak, Juan Carlos Ramirez Giraldo, Christian D. Eusemann, Bernhard Schmidt, Birgit Kantor, Joel G. Fletcher, and Cynthia H. McCollough. Dual-source dual-energy CT with additional tin filtration: Dose and image quality evaluation in phantoms and in vivo. *American Journal of Roentgenology*, 195 (5):1164–1174, 2010. ISSN 1546-3141. doi: 10.2214/ajr.09.3956. URL http://dx.doi.org/10.2214/AJR.09.3956.

[94] X. Li, E. Samei, and W. P. Segar. Patient-specic radiation dose and cancer risk estimation in ct: Part i. development and validation of a monte carlo program. *Medical Physics*, 2011.

[95] Usman Mahmood, Natally Horvat, Joao Vicente Horvat, Davinia Ryan, Yiming Gao, Gabriella Carollo, Rommel DeOcampo, Richard K Do, Seth Katz, Scott Gerst, C Ross Schmidtlein, Lawrence Dauer, Yusuf Erdi, and Lorenzo Mannelli. Rapid switching kvp dual energy ct: Value of reconstructed dual energy ct images and organ dose assessment in multiphasic liver ct exams. *European Journal of Radiology*, 102:102–108, May 2018. doi: 10.1016/j.ejrad.2018.02.022.

[96] Lianna D. DiMaso, Jessie Huang, Michael F. Bassetti, Larry A. DeWerd, and Jessica R. Miller. Investigating a novel split-filter dual-energy ct technique for improving pancreas tumor visibility for radiation therapy. *Journal of Applied Clinical*

Medical Physics, 19(5):676–683, 2018. ISSN 1526-9914. doi: 10.1002/acm2.12435. URL http://dx.doi.org/10.1002/acm2.12435.

[97] Thorsten R. C. Johnson. Dual-energy CT: General principles. *American Journal of Roentgenology*, 199(5 supplement):S3–S8, 2012. ISSN 1546-3141. doi: 10.2214/ajr.12.9116. URL http://dx.doi.org/10.2214/AJR.12.9116.

[98] Justin Solomon, Achille Mileto, Juan Carlos Ramirez-Giraldo, and Ehsan Samei. Diagnostic performance of an advanced modeled iterative reconstruction algorithm for low-contrast detectability with a third generation dual-source multidetector CT scanner: Potential for radiation dose reduction in multireader study. *Radiology*, 275 (3):735–745, 2015.

[99] Priya Bhosale, Ott Le, Aprana Balachandran, Patricia Fox, Eric Paulson, and Eric Tamm. Quantitative and qualitative comparison of single-source dual-energy computed tomography and 120-kVp computed tomography for the assessment of pancreatic ductal adenocarcinoma. *Journal of Computed Assistant Tomography*, 39 (6):907–13, 2015. doi: 10.1097/RCT.0000000000000295.

[100] Fabian Morsbach, Moritz Wurnig, Daniel Müller, Bernhard Krauss, Johannes Georg Korporaal, and Hatem Alkadhi. Feasibility of single-source dual-energy computed tomography for urinary stone characterization and value of iterative reconstructions. *Investigative Radiology*, 49(3):125–130, 2014.

[101] Avani D. Rao, Ziwei Feng, Eun Ji Shin, Jin He, Kevin M. Waters, Stephanie Coquia, Robert DeJong, Lauren M. Rosati, Lin Su, Dengwang, Juan Jackson, Stephen

Clark, Jeffrey Schultz, Danielle Hutchings, Seong-Hun Kim, Ralph H. Hruban, Theodore L. DeWeese, John Wong, Amol Narang, Joseph M. Herman, and Kai Ding. A novel absorbable radiopaque hydrogel spacer to separate the head of the pancreas and duodenum in radiation therapy for pancreatic cancer. *International Journal of Radiation Oncology*, 99(5):1111–1120, 2017.

[102] Pavan Tummala, Omer Junaidi, and Banke Agarwal. Imaging of pancreatic cancer: An overview. *Journal of Gastrointestinal Oncology*, 2(3):168–74, 2011. doi: 10.3978/j.issn.2078-6891.2011.036.

[103] Lianna D. DiMaso, Jessica R. Miller, Michael Lawless, Michael F. Bassetti, Larry A. DeWerd, and Jessie Huang. Investigating split-filter dual-energy ct for improving liver tumor visibility for radiation therapy. *Journal of Applied Clinical Medical Physics*, 2020.

[104] Kazuhiro Matsumoto, Masahiro Jinzaki, Yutaka Tanami, Akihisa Ueno, Minoru Yamada, and Sachio Kuribayashi. Virtual monochromatic spectral imaging with fast kilovoltage switching: Improved image quality as compared with that obtained with conventional 120-kvp ct. *Radiology*, 259(1):257–262, 2011.

[105] Yong Eun Chung, Myeong-Fin Kim, Young Nyun Park, Fin-Young Choi, Fu Yeon Pyo, Young Chul Kim, Hyeon Fe Cho abd Kyung Ah Kim, and Sun Young Choi. Varying appearances of cholangiocarcinoma: Radiologicpathologic correlation. *Radiographics*, (29):683–700, 2009.

[106] R L Baron, J H Oliver, G D Dodd, M Nalesnik, B L Holbert, and B Carr. Hepatocellular carcinoma: evaluation with biphasic, contrast-enhanced, helical ct. *Radiology*, 199(2), 1996.

[107] Florence Keane, Jennifer Wo, Andrew Zhu, and Theodore Hong. Liver-directed radiotherapy for hepatocellular carcinoma. *Liver Cancer*, 5:198–206, 2016.

[108] Daniela Muenzel, Grace C. Lo, Hei Shun Yu, Anushri Parakh, Manuel Patino, Avinash Kambadakone, Ernst J. Rummeny, and Dushyant V. Sahani. Material density iodine images in dual-energy ct: Detection and characterization of hypervascular liver lesions compared to magnetic resonance imaging. *European Journal of Radiology*, 95:300–306, 2017.

[109] Stephan Skornitzke, Franziska Fritz, Philipp Mayer, Marco Koell, Jens Hansen, Gregor Pahn, Thilo Hackert, Hans-Ulrich Kauczor, and Wolfram Stiller. Dual-energy ct iodine maps as an alternative quantitative imaging biomarker to abdominal ct perfusion: determination of appropriate trigger delays for acquisition using bolus tracking. *British Journal of Radiology*, 91, 2018.

[110] Gammex Sun Nuclear. Multi-energy ct phantom. URL `https://www.sunnuclear.com/products/multi-energy-ct-phantom`.

[111] Achille Mileto, Daniele Marin, Marcela Alfaro-Cordoba, Juan Carlos Ramirez-Giraldo, Christian D. Eusemann, Emanuele Scribano, Alfredo Blandino, Silvio Mazziotti, and Giorgio Ascenti. Iodine quantification to distinguish clear cell from

papillary renal cell carcinoma at dual-energy multidetector ct: A multireader diagnostic performance study. *Radiology*, 273(3), 2014.

[112] Jessica G. Zarzour, Desmin Milner, Roberto Valentin, Bradford E. Jackson, Jennifer Gordetsky, Janelle West, Soroush Rais-Bahrami, and Desiree E. Morgan. Quantitative iodine content threshold for discrimination of renal cell carcinomas using rapid kv-switching dual-energy ct. *Abdominal Radiology*, 42, 2017.

[113] John M. Boone, Keith J. Strauss, Dianna D. Code, Cynthia H. McCollough, Michael F. McNitt-Gray, and Thomas L. Toth. Size-specific dose estimates (SSDE) in pediatric and adult body CT examinations. *AAPM*, Task Group(204), 2011.

[114] Keith Quencer, Avinash Kambadakone, Dushyant Sahani, and Alexander S. R. Guimaraes. Imaging of the pancreas: Part 1. *Applied Radiology*, 2013.

[115] Kyongtae T. Bae. Intravenous contrast medium administration and scan timing at ct:considerations and approaches. *Radiology*, 2009.

[116] Eiman Ajmi, Behzad Forghani, Caroline Reinhold, Maryam Bayat, and Reza Forghani. Spectral multi-energy ct texture analysis with machine learning for tissue classification: an investigation using classification of benign parotid tumours as a testing paradigm. *European Radiology*, 28:2604–2611, 2018.

[117] Reza Forghani, Ashok Srinivasan, and Behzad Forghani. Advanced tissue characterization and texture analysis using dual- energy computed tomography horizons and emerging applications. *Neuroimaging Clinics of North America*, 27(3), 2017.

[118] Nora Hünemohr, Harald Paganetti, Steffen Greilich, Oliver Jäkel, and Joao Seco. Tissue decomposition from dual energy CT data for MC based dose calculation in particle therapy. *Medical Physics*, 41(6):061714, 2014. ISSN 0094-2405. doi: 10.1118/1.4875976. URL http://dx.doi.org/10.1118/1.4875976.

[119] Lianna D. DiMaso, Jessie Huang, Michael F. Bassetti, Larry A. DeWerd, and Jessica R. Miller. Investigation of dual-energy post-processing techniques using twinbeam dect modality for radiation therapy applications of pancreas adenocarcinoma. *AAPM annual meeting*, (WE-C930-GePD-F2-2), 2018.

[120] Neil G. Burnet. Defining the tumour and target volumes for radiotherapy. *Cancer Imaging*, 4(2):153–161, 2004. ISSN 1470-7330. doi: 10.1102/1470-7330.2004.0054. URL http://dx.doi.org/10.1102/1470-7330.2004.0054.

[121] Elisabeth Weiss and Clemens F. Hess. The impact of gross tumor volume (gtv) and clinical target volume (ctv) definition on the total accuracy in radiotherapy. *Strahlentherapie und Onkologie*, 179(1):21–30, Jan 2003. ISSN 0179-7158. doi: 10.1007/s00066-003-0976-5. URL http://dx.doi.org/10.1007/s00066-003-0976-5.

[122] Brent van der Heyden, Patrick Wohlfahrt, Daniëlle B. P . Eekers, Christian Richter, Karin Terhaag, Esther G. C. Troost, and Frank Verhaegen. Dual-energy ct for automatic organs-at-risk segmentation in brain-tumor patients using a multiatlas and deep-learning approach. *Scientific Reports*, 2019.

[123] Michael G Jameson, Lois C Holloway, Philip J Vial, Shalini K Vinod, and Peter E Metcalfe. A review of methods of analysis in contouring studies for radiation oncology. *Journal of Medical Imaging and Radiation Oncology*, 54(5): 401–410, 2010. ISSN 1754-9477. doi: 10.1111/j.1754-9485.2010.02192.x. URL http://dx.doi.org/10.1111/j.1754-9485.2010.02192.x.

[124] Tobias Heimann et al. Comparison and evaluation of methods for liver segmentation from ct datasets. *IEEE Transactions in Medical Imaging*, 28(8), 2009.

[125] Hideya Yamazaki, Yoshinori Ito, and Satoko Arahira. Dummy run for a phase II multi-institute trial of chemoradiotherapy for unresectable pancreatic cancer: Inter-overserver variance in contour delineation. *Anticancer Research*, 27:2965–2972, 2007.

[126] Heidi T. Lotz, Floris J. Pos, Maarten C.C.M. Hulshof, Marcel van Herk, Joos V. Lebesque, Joop C. Duppen, and Peter Remeijer. Tumor motion and deformation during external radiotherapy of bladder cancer. *International Journal of Radiation Oncology Biology and Physics*, 64(5):1551–1558, 2006. ISSN 0360-3016. doi: 10.1016/j.ijrobp.2005.12.025. URL http://dx.doi.org/10.1016/j.ijrobp.2005.12.025.

[127] Shalini K. Vinod, Michael G. Jameson, Myo Min, and Lois C. Holloway. Uncertainties in volume delineation in radiation oncology: A systematic review and recommendations for future studies. *Radiology and Oncology*, 2016.

[128] Peter Rogel, Robert Hudej, and Primoz Petric. Distance deviation measure of contouring variability. *Radiology and Oncology*, 47(1), 2013. ISSN 1318-2099. doi: 10.2478/raon-2013-0005. URL `http://dx.doi.org/10.2478/raon-2013-0005`.

[129] Wouter Elmpt, Guillaume Landry, Marco Das, and Frank Verhaegen. Dual-energy ct in radiotherapy: Current application and future outlook. *Radiotherapy and Oncology*, 119:137–144, 2016.

[130] J P Logue, C L Sharrock, R A Cowan, G Read, J Marrs, and D Mott. Clinical variability of target volume description in conformal radiotherapy planning. *International Journal of Radiation Oncology Biology and Physics*, 41(4):929–31, 1998.

[131] Joel G. Fletcher, Naoki Takahashi, Robert Hartman, Luis Guimaraes, James E. Huprich, David M. Hough, Lifeng Yu, and Cynthia H. McCollough. Dual-energy and dual-source CT: Is there a role in the abdomen and pelvis? *Radiologic Clinics of North America*, 47(1):41–57, 2009. ISSN 0033-8389. doi: 10.1016/j.rcl.2008.10.003. URL `http://dx.doi.org/10.1016/j.rcl.2008.10.003`.